UNIVERSIDAD DE GRANADA

Tesis Doctoral
Mayo 2012

High Energy Phenomena in Clusters of Galaxies

Ph.D. Thesis

Fabio Zandanel
Instituto de Astrofísica de Andalucía (CSIC)

Memoria de Tesis
presentada en la Universidad de Granada
para optar al grado de Doctor en Astrofísica

Director de Tesis:
Dr. Francisco Prada Martínez

Editor: Editorial de la Universidad de Granada
Autor: Fabio Zandanel
D.L.: GR 206-2013
ISBN: 978-84-9028-283-0

Alla mia Famiglia che ha reso tutto questo possibile.

Ad Alessandra per esistere.

To Isaac Asimov and Albert Einstein,
if I am here today is also your fault!

It was the tension between these two poles - a restless idealism on one hand and a sense of impending down on the other - that kept me going.

Hunter S. Thompson

Resumen

Esta tesis doctoral se ha centrado en el estudio de la emisin no-térmica debida a rayos cósmicos y materia oscura en los cúmulos de galaxias. Mi actividad ha combinado tanto observaciones, gracias a mi participación en el experimento Major Atmospheric Gamma Imaging Cherenkov (MAGIC), como trabajo teórico. MAGIC es un sistema de dos telescopios Cherenkov (Imaging Athmospheric Cherenkov Telescopes, IACTs) que observan el cielo a energías superiores a 50 GeV situado en la isla Canaria de La Palma.

En muchos cúmulos de galaxias se observa, en frecuencias radio, la presencia de emisión de sincrotrón difusa en forma de alones o mini-alones que demuestran la presencia de electrones de alta energía. La explicación de este fenómeno es muy complicada y, al día de hoy, es todavía una cuestión abierta entre dos modelos principales: el hadrónico y el de re-aceleración. Este ultimo prevé que turbulencias re-aceleran una población pre-existentes de electrones hasta energías lo bastante altas como para producir la emisión observada. El modelo hadrónico prevé que esta emisión sea debida a las interacciones hadrónicas entre los protones de los rayos cósmicos, que pueden acumularse en los cúmulos por tiempos cosmológicos, y los protones del gas en el cúmulo. En estas interacciones hadrónicas se forman piones que se disintegran en electrones y fotones de alta energía. Esta población, llamada secundaria, de electrones puede generar la emisión difusa observada en radio. Una manera para poder discriminar entre estos modelos es la búsqueda de la emisión en frecuancias gamma de los fotones producidos por la disintegración de los piones dado que ésta se espera solo en el modelo hadrónico. Un parte fundamental de esta tesis doctoral ha sido dedicada a la búsqueda de emisión gamma en cúmulos. He liderado una campaña de observación del cúmulo de Perseus con los telescopios MAGIC que ha resultado ser la observación más larga (85 horas) de un cúmulo a altas energías. Por primera vez estas observaciones han permitido poner a prueba la física adoptada en las simulaciones hidro-dinámicas de formación de cúmulos sugiriendo que la eficiencia de la aceleración de los rayos cósmicos es menor de la esperada ó que los fenómenos de transporte de rayos cósmicos en los cúmulos son particularmente relevantes. Durante esta campaña de observación de Perseus han sido detectadas también dos fuentes del cúmulo: las galaxias IC 310 y NGC 1275.

El nuevo observatorio radio LOFAR jugará un papel fundamental en el estudio de la emisión radio difusa de los cúmulos porque uno de sus proyectos principales es hacer un survey de cúmulos. LOFAR nos proporcionará una larga población de cúmulos con emisión radio hasta distancias de $z \approx 1$. Se espera que el estudio de esta población permita la caracterización del mecanismo base que genera los alones y mini-alones radio. He estudiado esta posibilidad para el caso del modelo hadrónico. He desarrollado un modelo fenomenológico que me ha permitido

crear, desde la simulación con sólo materia oscura MultiDark, un catálogo que reproduce las características principales de los cúmulos tal como son observadas en rayos X. He construido un nuevo modelo hadrnico, desde anteriores resultados analíticos y de simulaciones, y he calculado la emisión en radio y en rayos gamma de los cúmulos del catálogo. He investigado cómo la emisión radio se relaciona con la emisión en otras frecuencias así como la función de luminosidad radio de los cúmulos. Al mismo tiempo he investigado el papel de diferentes parámetros como el campo magnético, la presión de los rayos cósmicos y térmica y los fenómenos de transporte de los rayos cósmicos en los cúmulos. De esta forma he podido ver cómo las futuras observaciones de LOFAR podrán ayudar a identificar el mecanismo base que genera los alones y mini-alones radio.

Una parte importante de esta tesis doctoral ha sido dedicada a la búsqueda indirecta de materia oscura. La naturaleza de la materia oscura es una cuestión científica vital que concentra muchos esfuerzos de investigación tanto teóricos como experimentales. Los productos secundarios de la disintegración o aniquilación de materia oscura pueden generar un espectro muy complejo desde frecuencias radio hasta gamma. Sabemos que un 80% de la masa total de los cúmulos es materia oscura y, por esta razón, son candidatos excelentes donde buscar este tipo de emisión. He utilizado las observaciones del telescopio MAGIC del cúmulo de Perseus para investigar la naturaleza de la materia oscura. También he investigado las posibilidades de que el satélite de la NASA *Fermi* (20 MeV–300 GeV) pueda detectar emisión debida a la disintegración o aniquilación de materia oscura en estructuras extra-galácticas. La mayor ventaja de *Fermi* sobre los IACTs existentes es que observa constantemente todo el cielo y puede tratar sin problemas con fuentes muy extensas. Utilizado una simulación cosmológica del Universo local, hecha por el proyecto CLUES, se ha determinado que *Fermi* podría detectar indicios de emisión debida a materia oscura, en particular por el caso de disintegración, en los cúmulos más cercanos y también en los filamentos del Universo local.

Summary

The main research activities of my PhD thesis are focused on the study of non-thermal emission coming from cosmic rays (CR) and dark matter (DM) in clusters of galaxies. My research work combines both observational and theoretical approaches, the former thanks to my participation in the Major Atmospheric Gamma Imaging Cherenkov (MAGIC) experiment. MAGIC is a system of two Imaging Athmospheric Cherenkov Telescopes (IACTs) located on the Canary Island of La Palma (Spain), which observes the sky at energies above 50 GeV.

Extended radio synchrotron emission is observed in some galaxy clusters, the so-called radio halos and mini-halos (RHs), probing the presence of high-energy CR electrons. The explanation of this phenomenon is very challenging and currently debated between the re-acceleration and the hadronic models. In the first one, turbulences are thought to re-accelerate a pre-existing population of electrons up to emitting energies. In the hadronic model, the CR protons, accumulated in the cluster over cosmic times, interact hadronically with the protons of the intra-cluster medium giving pions, which then decay to electrons and high-energy photons. This so-called secondary electron population can generate the observed RHs. A clear way to disentangle between the two models is to search for the high-energy gamma-ray emission coming from the CR hadronic interactions, which is not expected in the re-acceleration model. I devoted a large part of this thesis exploring this possibility by leading a deep observation campaign of the Perseus galaxy cluster with the MAGIC telescopes. This campaign resulted in the longest observation ever (85 hours) of a cluster at very high energies (VHE). For the first time, this permits to probe the underlying physics of cosmological hydrodynamic simulations of cluster formation by putting the strongest constraint to date to the CR-to-thermal pressure. This suggests the CR acceleration efficiency at structure formation shocks is lower than expected or the presence of non-negligible CR transport processes such as diffusion and streaming. Additionally, during the Perseus cluster MAGIC observation campaign, VHE emission was detected for the first time from the head-tail galaxy IC 310 and the central radio galaxy NGC 1275.

The next generation radio observatory, LOFAR, will play a fundamental role providing us with a galaxy cluster survey up to redshift $z \approx 1$. RHs population studies will then permit the characterisation of the underlying physical mechanisms. I explore this possibility for the hadronic model case. I develop a phenomenological model that permits to create a complete cluster mock catalog from the MultiDark N-body simulation which well reproduces the observed X-ray cluster properties and statistics. I then construct a new hybrid hadronic model, merging previous simulation and analytical results, and compute the synchrotron radio and gamma-ray emission due to CR interactions with the ICM. Using the mock catalog, I then investigate the

radio scaling relations and the cluster radio luminosity function. I explore the role of different parameters like the magnetic field, the CR-to-thermal pressure, and the CR transport properties. In this way, I show how future LOFAR observations can constrain the physical mechanism generating RHs.

I devoted part of my PhD activities also to DM indirect searches. The nature of DM is a pressing scientific question and it is the object of many theoretical and experimental efforts. The secondary products of the decay or self-annihilation of many DM particle candidates can generate a complex spectrum from radio up to gamma-ray frequencies. About 80% of the mass of a galaxy cluster is in the form of DM; therefore they are good candidates for DM indirect searches. I use the VHE MAGIC (single telescope) observations of the Perseus galaxy cluster to test the DM nature. In addition, I investigate the potentiality of the NASA gamma-ray satellite *Fermi* (20 MeV–300 GeV) in detecting DM annihilation or decay in extragalactic structures. *Fermi* has the advantage over the existing IACTs of a full-sky survey and the ability to deal with extended region. Using a constrained N-body cosmological simulation of the local Universe from the CLUES project, I show that indeed *Fermi* might detect DM induced gamma-ray emission from nearby galaxy clusters as well as from filaments of the cosmic web, particularly for some DM decay models.

Contents

Chapter 1

Introduction: Non-Thermal Signatures of Structure Formation

My profession is to be forever journeying, to travel
about the Universe so that I may know all its conditions.
Abu Ali ibn Sina *aka* Avicenna

Modern cosmology has reached an important point where a wide variety of observations support a single model for the structure formation and evolution. According to the so-called concordance model, the cosmological hierarchic clustering model, large-scale structures grow through merging and accretion of smaller systems into larger ones. The geometry of the Universe is indistinguishable from a flat geometry which implies that the total energy density is similar to the critical density needed to close the Universe. The Universe seems to have two dominant components: a non-baryonic form of matter - the dark matter - whose gravity is actually responsible for the structure formation, and an unknown form of energy - the dark energy - responsible for the current acceleration of the Universe. The total matter density is composed by approximately 15% of baryonic matter, just a tiny fraction of the total matter-energy content of the Universe. Baryonic matter is visible only because of the dark matter gravitational attraction that drawn it into deep potential wells to form the structures we observe nowadays.
The concordance model is supported by many observations ranging from cosmic microwave background radiation, big bang nucleosynthesis, and cluster abundances, to the Universe accelerated expansion as observed by type Ia supernovae. This is complemented by numerical simulations of cosmological structure formation which are a powerful tool to study the non-linear evolution of structure formation and the baryonic physical processes in clusters of galaxies. According to the hierarchic model, clusters are the latest and most massive gravitational bound systems that form in the Universe. They provide us with the unique opportunity to study an ecosystem, a volume that is a high-density microcosm of the rest of the Universe. Clusters of galaxies are indeed a powerful tool to study the latest phase of the structure formation and have therefore an important cosmological impact.
The work in this thesis represents an effort to answer some of the still many remaining open questions in our view of the cluster formation and therefore of the Universe evolution. This

goal is pursued through the study of the non-thermal emission in galaxy clusters, investigating both the role of cosmic rays and of dark matter in the cluster eviroment. This is done both from a theoretical and an observational point of view, the last thanks to my participation in the Major Atmospheric Gamma-ray Imaging Cherenkov (MAGIC) experiment, at the Roque de los Muchachos observatory (La Palma, Spain), observing the sky at energies above 50 GeV. This chapter provides an introduction to the thesis scientific case outlined above, and to the gamma-ray astronomy, and it is partially inspired to Pfrommer (2005), Zandanel (2007), Sánchez-Conde (2009) and Prandini (2011).

1.1 The ΛCMD Cosmological Model

The scientific community seems to agree in a standard cosmological picture of the Universe, the so-called Λ Cold Dark Matter (ΛCDM) paradigm. This scenario, based on General Relativity, emerged after more than 80 years of continuos work and it is now capable to explain the observations in general terms, as well as to reconcile them with a congruent theoretical picture of the Universe and its evolution. In the ΛCDM model, the geometry of the Universe is flat, meaning euclidean, and its energy-matter density is distributed in $\sim$ 4% of baryonic matter, $\sim$ 23% of still unknown non-baryonic dark matter (DM) and approximately 73% of the even more mysterious dark energy. The model arose from the Big Bang scenario in which the Universe evolved from a highly compressed state existing about 10^{10} years ago. This whole scenario has survived to all kinds of tests and observations up to now and permits to explain in a satisfactory way the thermal history, relic background radiation, abundance of elements, large scale structure and many other properties of the Universe. However, our knowledge is partial, and the are still many open questions that we have to face.

1.1.1 An Introduction

The fundamental equation of the ΛCDM paradigm encloses the symmetry of the problem, i.e. the metric, the physical properties of energy-matter content, i.e. the equation of state, and, more important, relates the geometry of the Universe with its energy-matter content. This is known as the Einstein equation which can be written as:

$$R_{ij} - \frac{1}{2} g_{ij} R - \Lambda g_{ij} = \frac{8\pi G}{c^4} T_{ij} \tag{1.1}$$

where G is the gravitational constant, c the speed of light and R_{ij} and R are the Ricci tensor and scalar respectively, obtained by contraction of the Riemann curvature tensor. The quantity g_{ij} is the metric tensor that describes the geometry of space-time, Λ is the so-called cosmological constant, and T_{ij} is the energy-momentum tensor that describes the distribution of energy-matter. This equation has the important meaning, which is also the key concept of the General Relativity, that *the geometry of space-time is affected by the matter and the matter distribution is influenced by the space-time geometry*.

The cosmological constant Λ represents a *vacuum energy* - the so-called dark energy - associated with space-time itself and is a source of gravitational field. The contribution of this factor to the total energy of the Universe seems to be crucial according to the analyses of type Ia supernovae and the estimations of the cosmological parameters from the cosmic microwave background (CMB). Indeed, the evidence of the Universe accelerating expansion raised the possibility that it contains a bizarre form of matter or energy that is gravitationally repulsive. The cosmological constant is an example of this type of energy.

The concordance cosmological model is based upon two fundamental postulates: the *Cosmological* and *Copernican* principles. The first states that *on sufficient large scales the Universe is both isotropic and homogeneous*. Isotropy is the property of looking the same in every direction, while homogeneity is the property of being identical everywhere in space. Isotropy is supported by observations of galaxy populations on the largest scales (much larger than the scale of a galaxy cluster). Another strong argument in favor of isotropy is the extremely low CMB anisotropy level, around 10^{-5} on all measured angular scales. However, isotropy does not necessarily imply homogeneity without the additional assumption of the Copernican principle: *the observer is not in a preferential place*.

The Robertson-Walker metric describes an isotropic and homogeneous space-time. In spherical polar coordinates, the line element for this metric is:

$$ds^2 = g_{ij}dX^i dX^j = c^2dt^2 - a(t)^2\left[\frac{dr^2}{1-Kr^2} + r^2(d\vartheta^2 + sin^2\vartheta d\varphi^2)\right] \tag{1.2}$$

where $a(t)$ is the *cosmic scale factor* (or *expansion parameter*), and K is the *curvature parameter* that takes values 1, 0 or -1, which means open, flat and closed universe, respectively. Given this metric, it is possible to solve the Einstein equation and get the Friedmann equation:

$$H^2 = \left(\frac{\dot{a}}{a}\right)^2 + \frac{K}{a^2} = \frac{8\pi G}{3}\rho_{tot} + \frac{\Lambda}{3} \tag{1.3}$$

where the dot on the scale parameter represents the derivation with respect to cosmological proper time, ρ_{tot} is the total average energy density of the universe and H is the Hubble parameter. The Hubble parameter value at present time is $H_0 \approx 70$ km s^{-1} Mpc^{-1}. In equation 1.3, the Universe is flat provided that the energy density equals the critical density:

$$\rho_c = \frac{3H^2}{8\pi G} \tag{1.4}$$

or, alternatively, the space is closed ($K = 1$), open ($K = -1$) or flat ($K = 0$) according to whether the density parameter $\Omega = \rho_{tot}/\rho_c$ is greater than, less than, or equal to unity. The abundance of a substance in the Universe (matter, radiation or vacuum energy) is usually expressed in units of ρ_c. One can define the density of a given substance $\Omega_i = \rho_i/\rho_c$ such as $\Omega = \Sigma_i\Omega_i$. At the present epoch, we have for the matter, cosmological constant, radiation and curvature, $\Omega_m = 8\pi G\rho_m/3H_0^2$, $\Omega_\Lambda = \Lambda/3H_0^2$, $\Omega_r = 8\pi G\rho_r/3H_0^2$ and $\Omega_K = -K/a_0^2H_0^2$, respectively. Therefore, the Friedmann equation can be written for the present epoch simply as $1 = \Omega_m + \Omega_\Lambda + \Omega_K$ where the radiation contribution is typically neglected due to its tiny value today ($\sim 10^{-5}$). The latest results (Jarosik et al., 2011) suggest that:

- $\Omega_b = 0.0456 \pm 0.0016$
- $\Omega_{dm} = 0.227 \pm 0.014$
- $\Omega_\Lambda = 0.728^{+0.015}_{-0.016}$

where Ω_b is the baryon density, Ω_{dm} is the DM density and $\Omega_m = \Omega_b + \Omega_{dm}$. This means that about 23% of the Universe content is non-baryonic DM, and DM and dark energy make about 96% of the total density of the Universe.
On the other side, the expansion of the Universe means that the scale factor $a(t)$ has been increasing since the earliest times after the Big Bang. This affects the light emitted by distant objects. In particular, for an emitted wavelength λ_{emit} and an observed wavelength λ_{obs}, the redshift is defined $z = \frac{\lambda_{obs}}{\lambda_{emit}} - 1$. Finally, a general expression for the expansion rate of the Universe is:

$$H(z)^2 = H_0^2 \left[\Omega_m (1+z)^3 + \Omega_\Lambda\right] \tag{1.5}$$

where the radiation contribute is again neglected as well as the curvature contribute, which is null.
A complete mathematical derivation of the ΛCMD model and an extensive discussion on these topics can be found in e.g. Weinberg (1972), de Felice & Clarke (1990) and Coles & Lucchin (2002).

1.1.2 Structure Formation

In the hierarchical scenario, structures grow via gravitational instability from initial density fluctuations within a very homogeneous and isotropic background distribution. The small primordial density fluctuations grow due to non-linear gravitational evolution and finally become the first virialized structures called halos. Gravitation is the dominant interaction governing the evolution and dynamics of galaxies, clusters and large scale structures due to the long range of its interaction. The importance of gravitation for cosmology is supported by the growing evidence for DM constituting the major fraction of matter in our Universe. The most stringent argument in favour of this matter to be dark, i.e. not interacting electromagnetically, is the fact that the time elapsed since the decoupling of pure baryonic density perturbations from the primordial photon-baryon plasma is not long enough to produce all the structures observed today with the size of density perturbations inferred from the CMB anisotropies (see e.g. Bergström, 2000; Bertone et al., 2005). Furthermore, indirect DM evidences can be inferred for example by the gravitational effect on visible matter or radiation such as discrepancies of mass estimates for galaxy clusters by the gravitational lensing effect on background galaxies (see e.g. figure 1.1), flat rotation curves in spiral galaxies, and by the analysis of peculiar velocity fields of galaxies averaged over very large scales (see e.g. Bergström, 2000; Bertone et al., 2005).
DM is thought to be composed of yet undiscovered elementary particles which primarily interact by gravity; they carry neither an electromagnetic nor a strong charge while they can possibly interact through the weak nuclear force (see also section 1.2.2). If the DM particle is non-relativistic, trans-relativistic or relativistic at the time of decoupling from weak interactions it is named cold, warm or hot, respectively. Light particles, like neutrinos, are representative of hot

Figure 1.1: The 1E 0657-56 galaxy cluster, also known as the *bullet* cluster. The hot X-ray emitting gas is shown in red. The blue hues show the matter distribution mapped by observations of gravitational lensing of background galaxies. The clear discrepancy between the gravitational lensing result and the gas distribution is a direct evidence that DM exists (Markevitch, 2006; Clowe et al., 2006).

DM and seem to be ruled out since they would predict a scenario in which large structures form early and smaller ones (such as galaxies) form some time later by fragmentation. This would contradict observational evidences that structure formed bottom up leading to the hierarchical model of structure formation as, for example, shown in figure 1.2. This scenario is corroborated by cold DM (CDM) models, with its most promising candidate the lightest super-symmetric particle (see e.g. Bertone et al., 2005; see also section 1.2.2). Indeed, massive particles (with ~GeV masses or more), which are moving with non-relativistic velocities when they decoupled from radiation in the early Universe, can clump on smaller scales. However it has to be noticed that even though particle physics and structure formation mechanism do not favour both hot and warm DM candidates, they could exist and partially contribute to Ω_m.

Although the large scale structure picture seems very clear nowadays, our understanding is still far from being complete. In particular, the description of the evolution of structures from primordial density fluctuations is complicated by the action of many physical processes. The most widely adopted approach to the problem of large scale structure formation involves the use of N-body cosmological simulations (see Bagla, 2005 for a review). The structure evolution is often approximated with non-linear gravitational clustering from specified initial conditions of DM particles and can be refined by introducing the effects of gas dynamics, chemistry, radiative transfer and other astrophysical processes. The main problem of simulations is the huge number of particles, N, as the number of interactions needing to be computed is proportional to N^2. The highest resolution simulations at present include many millions of particles, see for example fig-

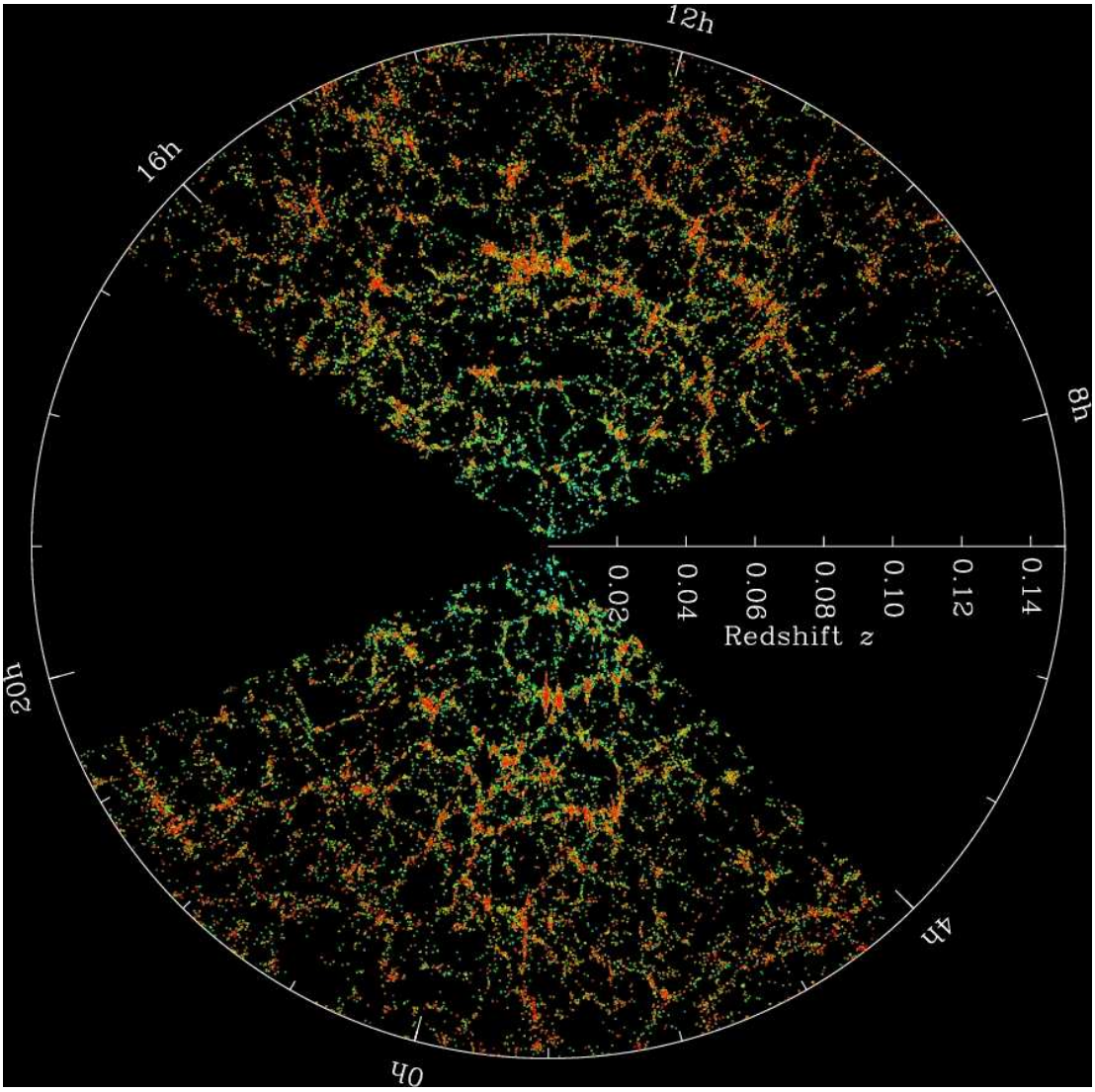

Figure 1.2: The large scale structure of the Universe, as observed by the Sloan Digital Sky Survey (Eisenstein et al., 2011). Each point represents a galaxy. The center of the image is the observer position, namely the Earth. Image taken from www.sdss3.org.

ure 1.3. Many simulations only work with CDM, as it makes up to about 5/6 of the total matter content of the Universe, and therefore include only the gravitational force. In fact, incorporating baryons in simulations dramatically increases their complexity.

N-body cosmological simulations based on the ΛCDM paradigm are in good agreement with a wide range of observations, such as the abundance of clusters at $z \leq 1$ and the galaxy-galaxy correlation functions (see e.g. Primack, 2001 for a review). Note that there are also some important discrepancies (see e.g. Taoso et al., 2008 for a discussion). For example, the so-called *missing satellite problem*: the number of satellite halos in Milky Way-sized galaxies as predicted by simulations exceeds the number of observed dwarf galaxies (Klypin et al., 1999). However,

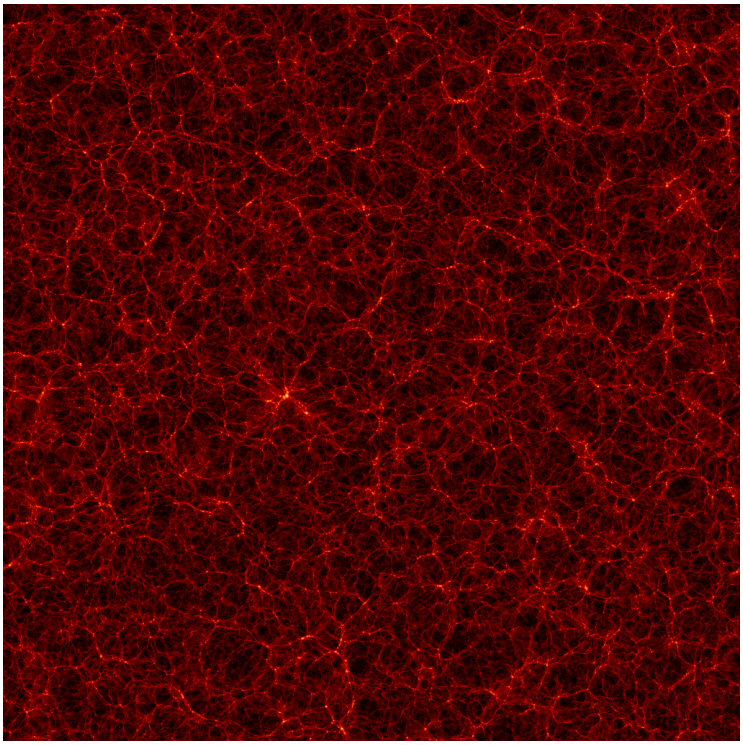

Figure 1.3: A recent example of N-body cosmological simulation: the MultiDark Run 1 (Prada et al., 2011). It is a simulation of 2048^3 particles in a box of 1 h^{-1} Gpc on a side. The brightest visible spot corresponds to the most massive galaxy cluster present in the entire simulation box. Image taken from www.multidark.org.

new ultra-faint dwarf galaxies recently detected with the Sloan Digital Sky Survey (SDSS) seem to importantly alleviate the discrepancy between CDM predictions and observations (Simon & Geha, 2007).

1.1.3 Clusters of Galaxies

As explained in the previous section, structures form through a hierarchical process in which gravity is continuously drawing matter together to form increasingly larger structures. Clusters of galaxies are the latest and most massive gravitationally bound systems in the Universe. With radii of few Mpc and total masses of $\sim (10^{14} - 10^{15})\ M_{\odot}$, they represent the the top stage of the hierarchical structure formation. The total cluster mass is divided up in about 5, 15 and 80% of galaxies, gas and DM, respectively (see e.g. Sarazin, 1988 and Voit, 2005 for a general overview). The hot gas, called intra-cluster medium (ICM), has been detected in galaxy cluster cores through its thermal bremsstrahlung X-ray emission. This plasma shows typical temperatures of 1 to 10 keV and has typical electron densities of 10^{-2} to 10^{-3} cm^{-3}.
Clusters of galaxies are constantly growing through mergers and accretion shocks (collectively called "structure formation shocks"). Recently, high resolution X-ray observations by *Chandra* and *XMM-Newton* orbiting telescopes have provided confirmation of this picture (e.g. Rosati

et al., 2002; Voit, 2005). During the course of cluster assembly, energies of order of the final gas binding energy $\sim 3 \times (10^{61} - 10^{63})$ erg should be dissipated through these structure formation shocks as well as turbulence. Therefore, even a small fraction of this energy channeled into non-thermal particles can have a major observable consequence. In fact, relativistic electrons, emitting synchrotron radiation in the presence of magnetic fields, have been observed as extended radio relics in the cluster outskirts, clearly tracing shock waves (see e.g. figure 1.4). Shocks and turbulence are likely to accelerate non-thermal electrons and protons to high energies (e.g. Jaffe, 1977; Schlickeiser et al., 1987; Miniati, 2002, 2003; Brunetti & Lazarian, 2007; Pfrommer et al., 2007, 2008; Pfrommer, 2008). Clusters are also home to different types of energetic outflows and the ICM can function as an efficient energy reservoir. Most clusters are seen to harbour radio galaxies around their central regions, whose large, powerful jets of relativistic plasma are interacting vigorously with the ICM (Heinz et al., 1998; Forman et al., 2003; Fabian et al., 2006a, 2011a). Although rarely seen in present-day clusters, other sources which should have been active in the past are galactic winds, i.e. outflows driven by the joint action of numerous supernovae (Völk et al., 1996). Along with dumping energy, these sources can inject substantial quantities of non-thermal particles into the ICM, or could have done so in the past. Therefore, it is clear that non-thermal phenomena provide complementary information for the formation and evolution history of galaxy clusters.

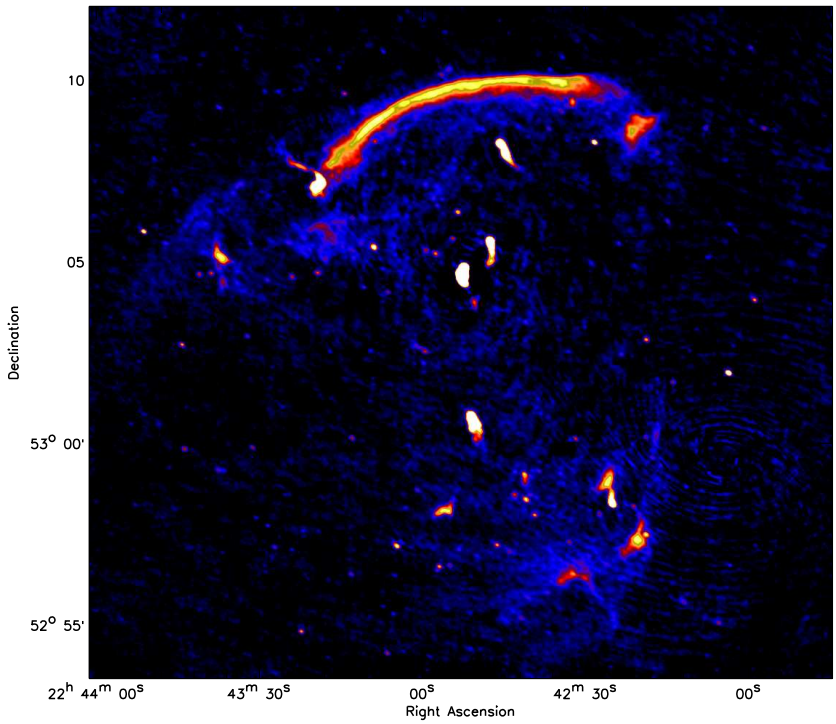

Figure 1.4: GMRT 610 MHz observation of the radio relic of the CIZA J2242.8+5301 cluster from van Weeren et al. (2010). The radio relic has an extension of about 2 Mpc and it is clearly tracing a merging shock.

1.2 Non-thermal Phenomena in Clusters of Galaxies

Many galaxy clusters show large scale diffuse synchrotron radio emission in the form of so-called radio halos which prove the existence of magnetic fields and relativistic electrons permeating the ICM (e.g. Feretti, 2003; Ferrari et al., 2008). Similar populations of electrons but with harder spectra may produce gamma-rays efficiently via inverse Compton (IC) up-scattering of the cosmic microwave background (Loeb & Waxman, 2000; Totani & Kitayama, 2000; Miniati, 2002, 2003; Petrosian et al., 2008). Observations in the hard X-ray regime may suggest the presence of a non-thermal component due to the IC scattering of cosmic microwave photons by relativistic electrons (see Rephaeli et al., 2008 for a recent review). However, recently Ajello et al. (2009) have found no evidence of a hard tail above the thermal emission in a large sample of clusters.
Faraday rotation measurements also provide a powerful tool to probe the strength of the intracluster magnetic fields (Kim et al., 1991) and even their distribution (Clarke et al., 2001). Thus the ICM is now being known to be permeated by magnetic fields with strengths $B \sim (1 - 10)\,\mu$G (Carilli & Taylor, 2002; Vogt & Enßlin, 2005), which allow for particle acceleration in shocks up to gamma-ray emitting energies.
In analogy with shocks within our Galaxy, such as those in supernova remnants, galaxy clusters should also be acceleration sites for relativistic protons and heavier relativistic nuclei. Due to their higher masses compared with the electrons, protons and nuclei are accelerated more efficiently to relativistic energies and are expected to show a ratio of the spectral energy flux of cosmic ray (CR) protons to CR electrons above 1 GeV of about 100 as it is observed in our Galaxy (Schlickeiser, 2002). CR protons also have radiative cooling times that are larger than the corresponding cooling times of CR electrons by the square of the mass ratio, and hence can accumulate for cosmological times in a galaxy cluster (Völk et al., 1996). The magnetic fields play another crucial role by confining non-thermal protons within the cluster volume for longer than the Hubble time (Völk et al., 1996; Berezinsky et al., 1997). The ICM gas should provide ample target matter for inelastic proton-proton collisions leading to pion-decay gamma-rays (Völk et al., 1996; Enßlin et al., 1997; Pfrommer & Enßlin, 2003, 2004a; Pfrommer et al., 2008; Pfrommer, 2008) as well as secondary electron injection (Dennison, 1980; Vestrand, 1982; Blasi & Colafrancesco, 1999; Dolag & Enßlin, 2000; Pfrommer & Enßlin, 2004a; Fujita et al., 2007; Pfrommer, 2008).
As explained above, galaxy clusters present very large mass-to-light ratios. In fact, DM makes up about 80% of their mass. DM annihilation or decay could therefore generate non-thermal emission from radio up to gamma-ray frequencies (Colafrancesco et al., 2006; Pinzke et al., 2009; Jeltema et al., 2009; Cuesta et al., 2011; Dugger et al., 2010; Pinzke et al., 2011; Sánchez-Conde et al., 2011; Gao et al., 2012).

1.2.1 Cosmic Rays

The diffuse radio emission observed in many galaxy clusters can be separated in two classes: radio relics and radio halos (see e.g. Kempner et al., 2004; Ferrari et al., 2008). Radio halos (RHs) are located at the center of clusters and are characterized by a regular and un-polarized morphology with clear similarities with the thermal X-ray emission (see figure 1.5). On the

contrary, radio relics typically lie at the cluster outskirts, have a irregular morphology, and often show a high degree of polarization. While relics seem to directly trace structure formation shocks (see e.g. figure 1.4 and van Weeren et al., 2010), the explanation for the RHs phenomenon is challenging and still an open question.

Two principal models have been proposed to explain RHs. In the "hadronic model" the radio emitting electrons are produced in CR proton-proton interactions with the ICM, requiring only a very modest fraction of a few percent of CR-to-thermal pressure (see e.g. Enßlin et al., 1997; Miniati et al., 2001; Pfrommer & Enßlin, 2003, 2004a,b; Blasi et al., 2007; Pfrommer et al., 2008; Pfrommer, 2008; Kushnir et al., 2009; Donnert et al., 2010a,b; Keshet & Loeb, 2010; Keshet, 2010; Enßlin et al., 2011). As explained above, CR protons have radiative cooling times larger than electrons by the square of the mass ratio and can accumulate in clusters for cosmological times. Indeed, CR electrons suffer more severe energy losses via synchrotron and IC emission at GeV energies, and bremsstrahlung and Coulomb losses below 100 MeV. In the "re-acceleration model", RHs are thought to be the result of electrons accelerated during powerful states of ICM turbulence, as after a cluster merger (see e.g. Giovannini et al., 1993; Gitti et al., 2002; Brunetti & Blasi, 2005; Brunetti & Lazarian, 2007, 2011; Brunetti et al., 2009). This, however, requires a sufficiently long-lived CR electron population at energies around 100 MeV which might be maintained by re-acceleration at a rate faster than the cooling processes. A detailed discussion on the strengths and weaknesses of these two models can be found in Enßlin et al. (2011).

RHs can be divided in two classes. Radio halos are typically associated with merging clusters and have very large extensions, e.g. the Coma cluster halo have an extension of about 2 Mpc (see figure 1.5). Radio mini-halos are associated with very relaxed clusters, having a cool core harboring the halo and typical extension of few hundred kpc, e.g. the Perseus cluster mini-halo has an extension of about 0.2 Mpc (see figure 1.5). The observed morphological similarities with the thermal X-ray emission suggest RHs may be of hadronic origin. Indeed, the hadronic model would naturally explain the RHs generation mechanism and, moreover, directly predict the existence of radio halos and mini-halos depending on the cluster dynamical state. In fact, cool-core clusters (CCCs) are characterized by very high thermal X-ray emissivity and very peaked ICM densities with respect to the non cool-core clusters (NCCCs) (see e.g. Croston et al., 2008). This dramatic difference in the ICM density of CCCs and NCCCs would reflect in the two observed classes of RHs as the hadronic model emissivity is proportional to the gas density squared.

The RH luminosity seems strongly correlated also with the clusters thermal X-ray emissivity (see e.g. Brunetti et al., 2009; Enßlin et al., 2011 and chapter 6). However, a large fraction of clusters do not exhibit significant diffuse synchrotron emission of any kind. Galaxy clusters with the same thermal X-ray luminosity show an apparent bimodality with respect to their radio luminosity. Either they harbor a RH or they do not have any detectable diffuse radio emission. This suggests the existence of a switch-on/switch-off mechanism able to change the radio luminosity by more than one order of magnitude. While such a mechanism could be easily realized in the framework of the re-acceleration model (Brunetti et al., 2009), the *classical* hadronic model predicts the presence of RHs in all clusters. The failure to reproduce the observed cluster radio-to-X-ray bimodality was one of the main criticisms against the hadronic model. Another criticism to the *classical* hadronic model is the the fact that it does not reproduce some spectral features

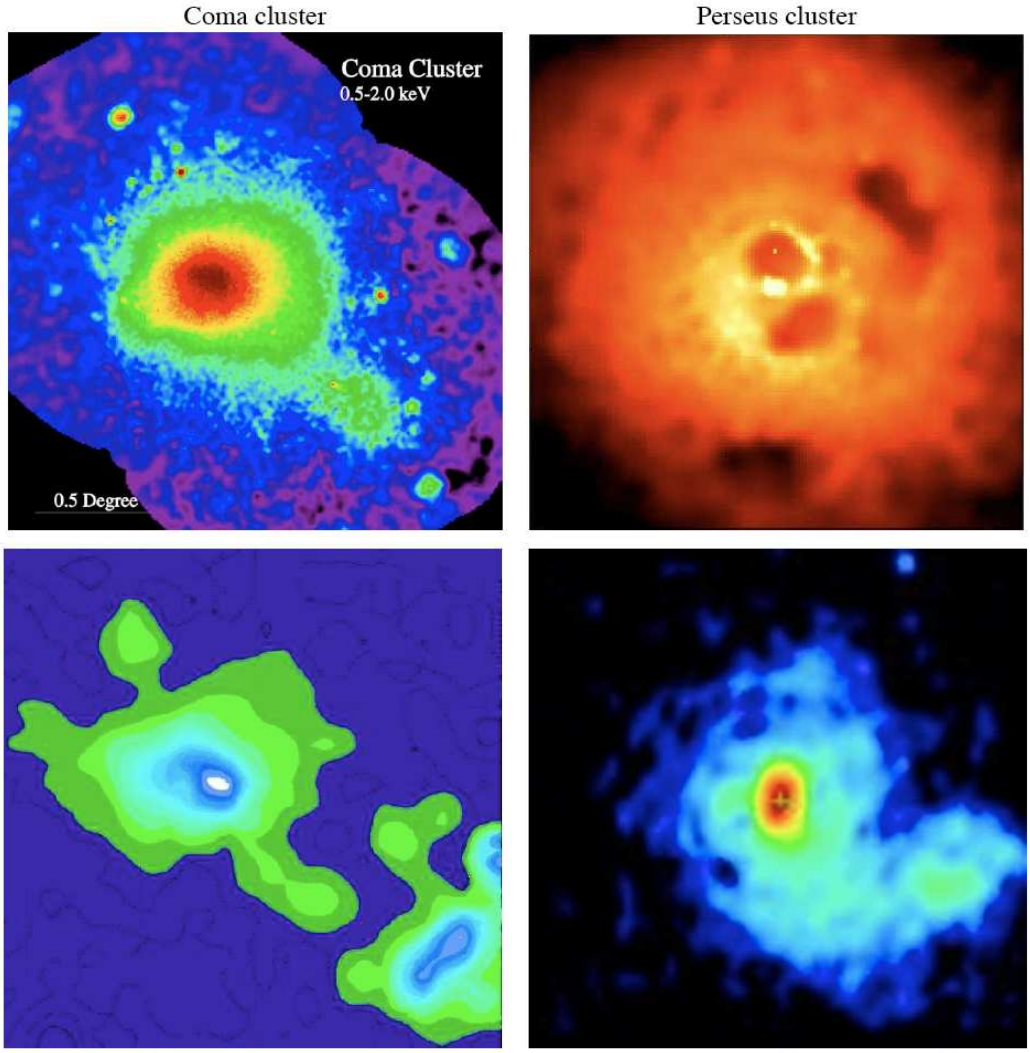

Figure 1.5: Comparison of thermal bremsstrahlung X-ray emission (top) and radio synchrotron emission (bottom) of the Coma (left) and Perseus (right) galaxy clusters. Coma is characterized by the merging of a large bright central cluster and a fainter group of galaxies to the lower right (the field is 2.5×2.5 deg in both images). The Perseus images show the cluster core region (6×6 arcmin^2 for the X-ray map, 9×9 arcmin^2 for the radio map). The bright yellow spot in the center of the X-ray map is due to accreting plasma onto a giant black hole in the nucleus of the central galaxy NGC 1275. The twin dark cavities are thought to be buoyant magnetized bubbles of relativistic particles produced by energy released from the vicinity of the black hole (Fabian et al., 2003). (Credits: Coma/X-ray: ROSAT/MPE/Snowden, Perseus/X-ray: NASA/IoA/Fabian et al., Coma/radio: Deiss/Effelsberg, Perseus/radio: Pedlar/VLA).

observed in clusters, as the total spectral curvature claimed in the Coma cluster radio halo or the spectral steepening observed at some RH edges. In a recent work, Enßlin et al. (2011) asses these problems by analyzing how the CR distribution is shaped within a cluster. While CR advection

tends to result in centrally enhanced CR profiles, the propagation in form of CR streaming and diffusion tends to produce flat CR profiles. The different effects of such CR transport phenomena may account, in the hadronic model, for the observed radio-to-X-ray bimodality, as shown by Enßlin and collaborators and in this thesis (see chapter 6), and can have an important impact in clusters in general. These phenomena were not considered in earlier analytical works (see e.g. Pfrommer & Enßlin, 2004a,b) as well as in hydrodynamic simulations (see e.g. Pfrommer et al., 2008; Pinzke & Pfrommer, 2010) for seek of simplicity, but can have a dramatic impact. Note that the effect of CR transport processes could also explain the spectral features observed in some clusters (see Enßlin et al., 2011 for details).

More recently, Basu (2012) has presented the first scaling relations between RH luminosity and integrated Sunyaev-Zel'dovich (SZ) effect measurements, using the *Planck* all-sky cluster catalogue and published radio data. While the correlation agrees well with previous scaling measurements based on X-ray data, Basu has found no strong indication for a bimodal cluster population split between radio-loud and radio-quiet objects. This issue is further investigated in chapter 6 of this thesis.

A clear way out to disentangle between the hadronic and the re-acceleration models is to search for the gamma-ray emission resulting from the neutral pion decays, secondary product of the hadronic CR interaction with the ICM, which is not predicted to be present by the re-acceleration model. Such observational effort has been undertaken in the last few years without being able to detect cluster gamma-ray emission. For space-based cluster observations in the GeV-band, see Reimer et al. (2003), for the results of the EGRET satellite, and Ackermann et al. (2010a), Ackermann et al. (2010b), Zimmer et al. (2012) and Han et al. (2012) for recent results from the *Fermi* satellite. In particular, very recently, Han et al. (2012) have claimed an evidence for diffuse gamma-ray emission in the *Fermi* satellite data of the Virgo cluster which however needs to be carefully scrutinized by varying the uncertain foreground modeling. However, this detection has been not confirmed by a dedicated analysis from the *Fermi* collaboration itself.[1] For ground-based observations at energies above approximately 100 GeV, see Perkins et al. (2006), Perkins (2008), Aharonian et al. (2009a), Aharonian et al. (2009b), Domainko et al. (2009), Galante et al. (2009), Kiuchi et al. (2009), Acciari et al. (2009a), Aleksić et al. (2010a) and Aleksić et al. (2012a). Despite the negative detections, significant constraints on the gamma-ray predictions have been obtained both from *Fermi* and Cherenkov telescopes. Indeed, a very important step forward in this direction has been the work presented in this thesis. I am in fact the P.I. of a long-term gamma-ray observation campaign of the Perseus cluster with the MAGIC gamma-ray telescopes. The results of this three-years effort are presented in chapters 3 and 4.

Another important step forward in this scenario would come from detailed RHs population analyses. Actually, only about 30 clusters harboring RHs are known (see Enßlin et al., 2011 for an almost up-to-date list). Only two X-ray flux-limited studies, relevant for the universality of the conclusions, have been performed and only few of the considered clusters resulted to host a RH (Giovannini et al., 1999; Venturi et al., 2008). With such small samples, the conclusions that can be drawn on the underlying mechanisms acting in the RHs generation are not very robust. Fortunately, this is going to change thanks to the next-generation radio observatory Low

[1] See Elliot Bloom talk at the UCLA Dark Matter 2012 conference (https://hepconf.physics.ucla.edu/dm12/).

Frequency Array (LOFAR) which officially started operations in 2010.[2] In fact, a deep cluster survey is part of the LOFAR science key projects. This will soon provide us with a large number of radio-observed galaxy clusters up to redshift $z \approx 1$ (see e.g. Cassano et al., 2010; Röttgering et al., 2012 and chapter 6). This would hopefully permit to clearly determine the RH characteristics against the galaxy cluster properties investigating the relations between radio-loud/quiet, non cool-core/cool-core and non-merging/merging clusters, and exploring the role of different parameters like the magnetic field, the CR-to-thermal pressure, and the CR transport properties. The chapter 6 of this thesis is dedicated to this topic, presenting predictions for the LOFAR survey in the case of the hadronic model.

1.2.2 Dark Matter

As anticipated above, a large amount of astrophysical evidences suggests that most of the Universe matter content is in the form of CDM. The precise nature of DM is however still one of the most important open questions in modern physics. Many different candidates have been proposed as DM constituents, yet for the time being there is no evidence in favour of any model. One of the most studied scenarios is that of weakly interacting massive particles (WIMPs) for which the most representative candidate is the supersymmetric lightest particle, namely the neutralino. See for example Bertone et al. (2005) and Bertone (2010) for a review on the topics introduced in this section.

What is supersymmetry? In the standard model of particle physics there is a fundamental distinction between bosons and fermions: while bosons are the interaction mediators, fermions are the matter constituents. Therefore, it is natural to ask if there exists a symmetry relating them in such a way to give a unified description of matter and interactions. There are other major reasons to be interested in supersymmetry, e.g. the hierarchic problem and the unification of coupling constants. The most studied supersymmetric model is the the minimal supersymmetric extension of the standard model (MSSM); it is minimal in the sense that it contains the smallest possible field content necessary to give rise to all the standard model fields. A fundamental ingredient of the MSSM is th R-parity conservation.[3] The consequence of the R-parity conservation is that superpartners can only decay into an odd number of superpartners plus standard model particles. The lightest superpartner, i.e. the lightest supersymmetric particle (LSP), is stable and can only be destroyed via pair annihilations, making it an excellent DM candidate. In order to determine the LSP in a given supersymmetric scenario, it is necessary to specify how supersymmetry is broken. In fact, if supersymmetry is not broken, each superpartner would have a mass identical to its standard model counterpart, which is clearly not the case. In the MSSM framework, the superpartners of the B, W_3 gauge bosons (or the photon and Z, equivalently) and the neutral Higgs bosons, H_1^0 and H_2^0, are called *binos*, *winos*, and *higgsinos*, respectively. These states mix into four Majorana fermionic mass eigenstates called *neutralinos*. The lightest of the four neutralinos is also called *the* neutralino and it is denoted simply as χ. The neutralino, being of course not the

[2] www.lofar.org

[3] The R-parity is a multiplicative quantum number defined as $R = (-1)^{3B+L+2s}$ where B is the barion number, L is the lepton number and s is the spin.

only option, is however up to date the most studied DM candidate.
In general, WIMPs can self-annihilate or decay. In the context of annihilating DM, WIMPs are favored by the fact that they naturally have a relic density that matches the observed DM abundance (see e.g. Bertone et al., 2005), while for decaying DM, it has been shown that WIMPs can have decay lifetimes larger than the age of the Universe, and are therefore viable DM candidates (see e.g. Arvanitaki et al., 2009). The secondary products of the DM decay or annihilation can generate non-thermal emission from radio to gamma-ray frequencies (Colafrancesco et al., 2006; Pinzke et al., 2009; Jeltema et al., 2009; Cuesta et al., 2011; Dugger et al., 2010; Pinzke et al., 2011; Sánchez-Conde et al., 2011; Gao et al., 2012). In particular, being the gamma-ray range not as crowded as other frequencies, is a powerful tool to study the DM nature as a complementary approach to direct searches. The classical DM gamma-ray candidates are the Galactic Center and dwarf spheroidal galaxies, satellites of the Milky Way. The Galactic Center, being so close, would be the most promising target for DM searches. However, it is an extremely crowded region and it is very difficult to understand the corresponding gamma-ray emission (e.g. Aharonian et al., 2006a). Dwarf spheroidal galaxies are the objects with the higher mass-to-light ratio in the Universe and they are not expected to contain any type of background emission which could render the DM searches more challenging. Indeed, they are considered the best targets for DM searches (e.g. Aliu et al., 2009a; Aleksić et al., 2011; Sánchez-Conde et al., 2011).
As explained above, about 80% of galaxy cluster mass is in form of DM. So even if the cluster mass-to-light ratios are not as high as the dwarf ones, the huge amount of DM content make them very good candidates for DM searches. There are two main advantages of clusters over dwarf galaxies. The first is that clusters are known to exist. The dwarf galaxies detection and study is often based on the dynamics of a handful of stars which sometimes renders difficult their precise determination; this is particularly true for the best candidates, the ones with the higher mass-to-light ratios (see e.g. Willman et al., 2011). The second advantage is the DM substructures effect. In the ΛCDM paradigm, the smallest dense halos form first and later merge to originate larger structures. This hierarchical scenario has as direct consequence the presence of a large amount of substructure in CDM halos. As the DM annihilation signal is proportional to the DM density squared, this clumpy distribution of sub-halos inside larger halos may boost the DM annihilation flux considerably. This would impact also a DM decay signal but in a fainter way being it directly proportional to DM density. In clusters, substructures can significantly enhance the DM signal over the smooth halo (Pinzke et al., 2011; Sánchez-Conde et al., 2011; Gao et al., 2012), while this effect is less important for dwarf spheroidal galaxies.
The left plot in figure 1.6 shows the comparison between the spatial distribution of the DM annihilation signal of few promising dwarfs and clusters from Sánchez-Conde et al. (2011) (work of which I am third author), where the substructure effect is included. Note particularly that the cluster signal is very flat out to the outskirts, and this is due to the substructure effect. The central part of dwarfs has still a higher DM signal, but integrating over the whole cluster extension results in a comparable or even higher DM annihilation signal with respect to Milky Way satellites. The right plot in figure 1.6 shows the cumulative DM annihilation luminosity and substructure boost in dwarfs, galaxy-size objects and clusters form Pinzke et al. (2011). The substructure boost in clusters is about two orders of magnitude higher than in dwarfs. Despite Sánchez-Conde et al. (2011) and Pinzke et al. (2011) use two different substructure treatments, their absolute

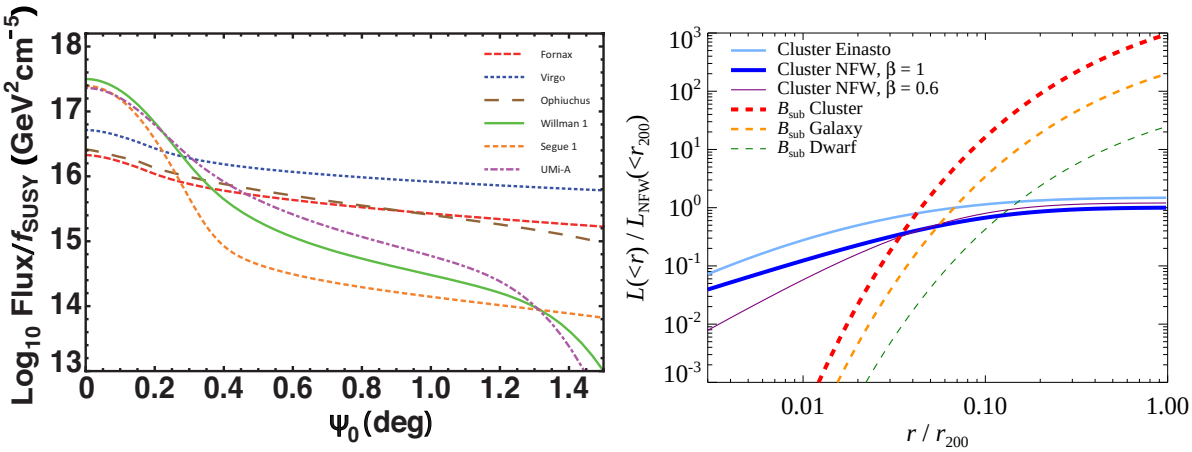

Figure 1.6: DM substructures effect in galaxy clusters. The left plot shows the DM annihilation signal spatial distribution (normalized such that it is independent from the chosen particle physics model f_{SUSY}) of few dwarf and cluster good DM candidates (figure from Sánchez-Conde et al., 2011). Substructures render the cluster DM signal very flat up to their outskirts. The right plot shows the cumulative DM annihilation luminosity and substructure boost for dwarfs, galaxy-like objects and clusters (figure from Pinzke et al., 2011). The substructure boost in clusters is around two orders of magnitude higher than in Milky Way satellites.

conclusions on the signal boost and comparison between dwarfs and clusters are consistent. Concluding, galaxy clusters can be considered DM candidates as good as dwarfs are, or even better, but when there is the possibility to integrate up to their viral radii. This is of course an important aspect to consider when planning observations. In fact, existing Cherenkov telescopes (see next section) have field of views which are comparable with cluster extensions (about few degrees) making DM cluster studies very challenging. On the other hand, the *Fermi* gamma-ray satellite, constantly surveying all the sky, can more easily deal with very extended sources. *Fermi*-LAT data have been already used to search for DM induced emission in clusters (Ackermann et al., 2010b), even producing a claim of detection in the Virgo cluster (Han et al., 2012) which however has been not confirmed by the *Fermi* collaboration itself. In chapter 3 of this thesis we investigate the DM content of the Perseus galaxy clusters using the MAGIC telescope observations, while in chapter 5 a cosmological simulation of the local Universe is used to investigate the possibilities for the *Fermi* satellite to detect DM in extragalactic structures, mainly clusters.

1.3 The Gamma-ray Astronomy

A considerable part of the work of this thesis has been done using the MAGIC telescopes. Therefore this section is meant to be an introduction to gamma-ray astronomy and in particular to Cherenkov telescopes.

1.3.1 A Brief Introduction

The CR discovery came from the Italian physicist Domenico Pacini and the Austrian physicist Viktor Hess. Hess announced the experimental evidence of a ionized radiation that constantly impinges the Earth atmosphere in 1912. For this discovery, Hess was awarded with the Nobel prize for Physics in 1936.
Excluding neutrinos, which are weakly interacting particles, CR radiation mainly consist of charged particles, such as protons (90%), α-particles, ionized heavier elements nuclei, and electrons, while only about 0.1% of the total radiation consist of photons with an energy higher than 1 MeV, the so-called *gamma-rays*.
As the main part of CRs are charged, they interact with magnetic fields. This implies that these particles arrive isotropically to the Earth, making impossible the reconstruction of both the emitter original direction or of an eventual signal time structure. This is the reason of the CR origin being still a challenge after one century from the discovery. The particles keeping directional information about their origin are the neutral ones because not affected by magnetic fields. Neutrons, neutrinos and photons are in this category. Here we are mainly interested in photons. Indeed, gamma-rays *trace back to the origin of their generator*, *carry energy information about their generator* and *preserve the time structure of the emission signal*. It is commonly believed that very high energy gamma-rays are destined to play a crucial role in the exploration of non-thermal phenomena in the Universe in their most extreme and violent forms.

1.3.2 The Detection of Gamma-rays

Gamma-rays can be detected by ground-based instruments or by satellites. In these two categories, here we are mainly interested in the so-called Imaging Atmospheric Cherenkov Telescopes (IACTs) and in the NASA satellite *Fermi* (see next section). The detection from space is "easy" to achieve through pair-production tracking, with the main limitation being the needed detection area of satellites. On the contrary, CRs cannot be directly detected by the ground-based telescopes because they hardly reach the Earth.
CRs from space collide with the nucleons, mainly nitrogen, present in the Earth atmosphere. In such collisions, new particles are created which themselves interact with the atmospheric atoms, leading to the creation of an atmospheric shower. Depending on whether the incident particle is a hadron (nucleus) or an electromagnetic particle (electron or photon), the distinction between electromagnetic and hadronic showers is made as shown in figure 1.7.
The observations of gamma-rays using atmospheric showers is possible by detecting the electromagnetic radiation of the secondary shower particles. The imaging technique employed by the IACT instruments is based on the detection of the Cherenkov light emitted by these secondaries. This effect was discovered from the Russian physicists Pavel Cherenkov and Sergey Vavilov in 1934. The Cherenkov effect occurs when a charged particle travels in a dielectric medium, of reflective index n, with a speed exceeding the light speed in the medium c/n. When a charge moves in a dielectric medium, a polarization occurs. When the charged particle velocity is superluminal, $v > c/n$, the particle is moving faster than the electromagnetic information inducing the polarization. As a consequence, a coherent wave front appears, and the emitted radiation is

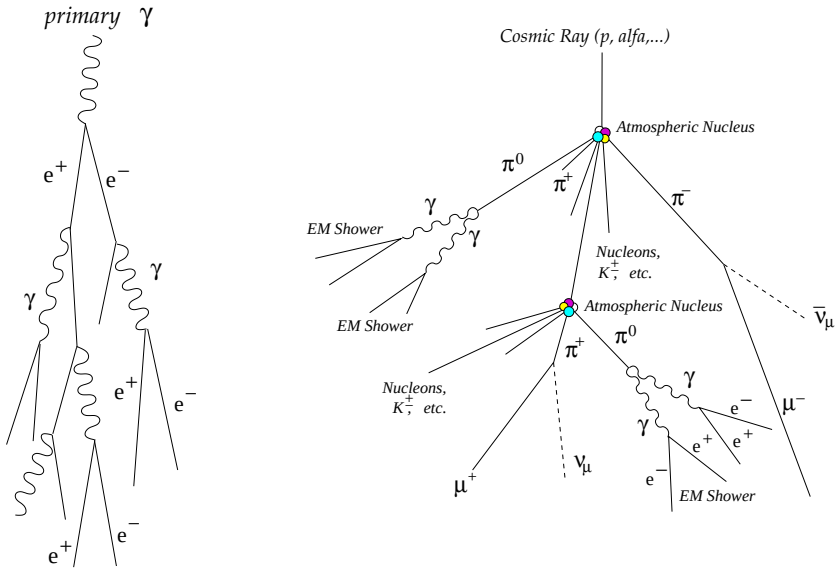

Figure 1.7: Schematic development of atmospheric showers. An electromagnetic shower on the left and a hadronic shower on the right.

called *Cherenkov light*. The Cherenkov radiation emitted by a shower has a typical spectrum that spans from 300 to 600 nm, where the lower limit is mainly due to the ozone absorption and the upper one principally to the Rayleigh and Mie scattering.

The primary target for the ground-based gamma-ray instruments is obviously the identification of the differences between electromagnetic and hadronic cascades. Since the gamma-ray-to-charged CRs ratio is very small, (about 10^{-4}), a very powerful technique is needed to separate the gamma events from the dominating hadronic ones. A successful method is the *imaging technique*. Basically, it consists in studying the atmospheric showers by analyzing the images produced by the Cherenkov photons when they are focused on a plane. The IACT instruments can be considered as operators transforming the arrival directions of the detected photons into points of a *shower image*: a parabolic mirror surface reflects the incoming light and concentrates it into a pixelled camera which converts the electromagnetic radiation into electric signal. In figure 1.8, left image, a schematic view is presented.

The images formed on the camera have an *elliptical shape* whose edges represent the head an the tail of the shower, while the inner pixels correspond to its core. The shape, orientation and light content of an image can be used to infer physical information about the particle producing the atmospheric shower, such as energy, incident direction and, eventually, the particle type. The elliptical image can be parameterized by a set of parameters, the so-called *image parameters*, that permit to extract all the physical information described above. These parameters were introduced by A. M. Hillas in 1985 (Hillas, 1985) allowing a ground-based telescope to achieve a clear detection of a source for the first time in history, the Crab Nebula detection from the Whipple collaboration in 1989 (Weekes et al., 1989). In fact, the image parameters are also called *Hillas parameters*. The extraction of the Hillas parameters is based on the computation of the image

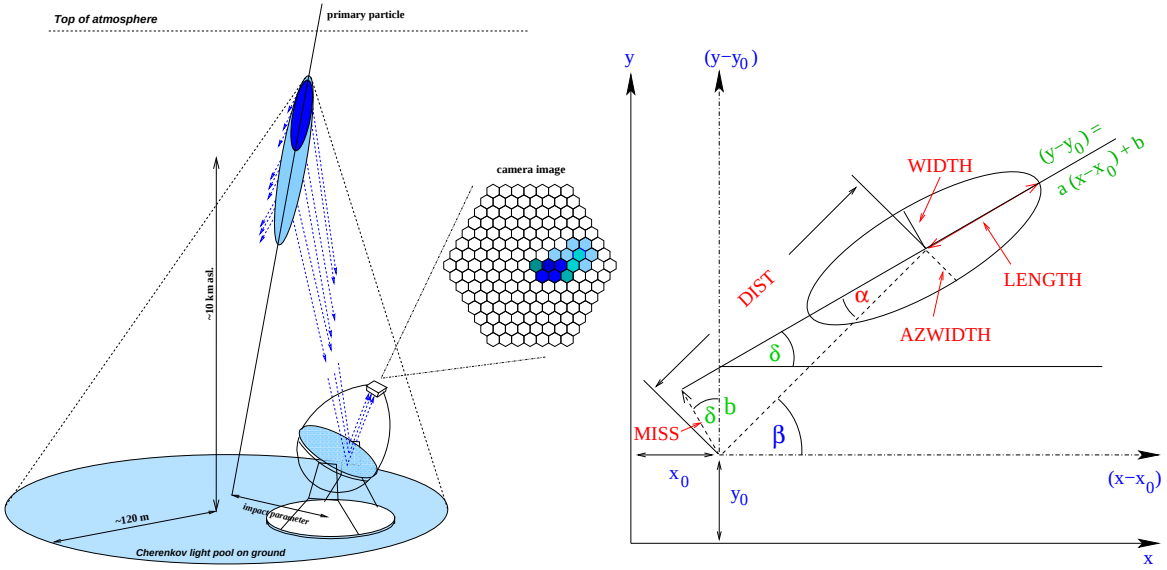

Figure 1.8: On the left, the schematic view of the IACT detection of an atmospheric shower is shown. When the primary particle interacts with the atmosphere, an atmospheric shower is generated, characterized by a head (dark blue) and a tail (light blue). The Cherenkov light (blue lines) propagates to the ground at increasing angle with increasing shower development and atmospheric depth. Photons are reflected onto the focal plane at a distance from the center of the camera which reflects the shower impact parameter, i.e. the distance from the telescope axis. Figure from Prandini (2011), adapted from Lopez Moya (2007). On the right, the schematic view of the Hillas parameters calculated according to the imaging technique is shown.

moments. Figure 1.8, right scheme, shows the parameterization of an elliptic image. The main Hillas parameters are:

- *Size*: the total number of photo-electrons collected in a shower image. In first approximation, the size is proportional to the primary particle energy.

- *Width*: the half width of a shower ellipse minor axis. It is correlated to the transversal development of a shower and since an hadronic shower has a larger transversal momentum with respect to a gamma one, the Width parameter is important for the signal-to-background discrimination.

- *Length*: the half length of the major axis of a shower ellipse. It is correlated to the longitudinal development of a shower.

- *Alpha*: the angle between the major axis of an ellipse and the direction from the image center of gravity (i.e. the center of the ellipse) to the reference point. Since the reference point should be the source position in the camera, images induced by primary gamma-rays have Alpha close to zero. Instead, images produced by primary charged CRs have a

random Alpha distribution because the hadron directions are nearly isotropic. For these reasons, the Alpha parameter is very powerful for the signal-to-background separation.

- *Dist*: the distance of an ellipse center of gravity from the camera center. It provides information about the distance of the shower maximum from the telescope axis and about the impact parameter. The Dist is very important for the energy estimation of a shower primary particle.

When an image is parameterized, it can be tagged as background, i.e. with a good approximation *hadron-like*, or as *gamma-like*, depending on the values of its Hillas parameters. This procedure is called *gamma-hadron separation* and it is based on the fact that gammas and hadrons are characterized by different parameter values. A detailed description of this procedure will be done in the next chapter. However, the basic idea is that different primary particles induce different image topologies. For example, during the data taking the telescope points directly to a source, thus it is expected that images induced by gamma-rays have the major axis pointing toward the camera center. Instead, images induced by charged CRs have a randomly distributed arrival directions. In light of this, the Alpha distribution for hadrons should be uniform, while that for gammas should be peaked at low angles.

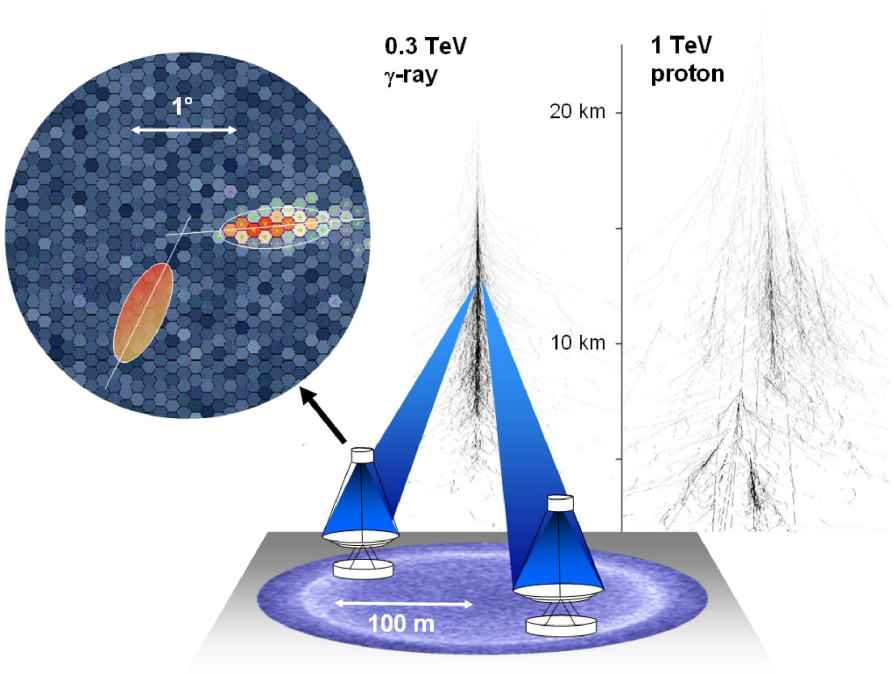

Figure 1.9: Schematic view of a shower image formation for a sterescopic IACT. Figure form Prandini (2011), adapted from Hinton & Hofmann (2009).

In case of having a multiple telescope systems, each detector is synchronized and operated together with the others in the so-called *stereoscopic* mode. The showers are seen under different angles by each telescope, and the process of characterization of the primary particle is largely

simplified. Indeed, when two or more telescopes register the same shower, the determination of the incoming direction of the primary particle becomes straightforward as can be seen in figure 1.9. Additionally, also the background suppression is much more efficient.

1.3.3 Existing Instruments

The imaging technique was pioneered by the Whipple collaboration whom 10 m telescope was located at Mount Hopkins in Arizona (United States), and led to the discovery of TeV emission from the Crab Nebula in 1989. The High Energy Gamma Ray Astronomy (HEGRA) telescope array at the Roque de Los Muchachos observatory on the Canary Island of La Palma (Spain) was the first system to use multiple telescopes and therefore the stereoscopic technique.

Figure 1.10: View of the four existing IACTs. From top to bottom and left to right, MAGIC, HESS, VERITAS and CANGAROO-III are shown, respectively.

Nowadays, the largest IACT system is represented by the two 17 m MAGIC telescopes located at the Roque de los Muchachos Observatory in La Palma, which will be presented in detail in the next chapter. MAGIC is larger in the sense of the telescopes diameter, not of the number of telescopes. There are other three IACTs which, together with MAGIC, lead the field at present: CANGAROO-III (see e.g. Mori & Cangaroo Collaboration, 2001), the High Energy Stereoscopic

System (HESS; see e.g. de Oña Wilhelmi, 2009) and the Very Energetic Radiation Imaging Telescope Array System (VERITAS; see e.g. Otte et al., 2009). These last experiments are all composed by four telescopes, but of smaller diameter with respect to MAGIC. HESS and VERITAS are made of 12 m telescopes, while CANGAROO-III is made of 10 m telescopes. These IACTs are shown in figure 1.10. While MAGIC and VERITAS are located in the northern hemisphere, being VERITAS on Mount Hopkins. HESS and CANGAROO-III are located in the southern hemisphere, on the Khomas Highland (Namibia) and Woomera (Australia), respectively.
There already exists a plan for the development of next generation IACTs. The current idea is to construct a giant array of Cherenkov telescopes of different sizes, called Cherenkov Telescope Array (CTA). The main purposes of the project include the attainment of a low energy threshold and a high sensitivity, one order of magnitude better than the current generation of IACTs (Actis et al., 2011).
Orbiting in space around the Earth, we currently have two instruments: the small Italian satellite Astro-rivelatore Gamma a Immagini Leggero (AGILE; see e.g. Tavani & AGILE Team, 2011) which, despite the performances not comparable with *Fermi*, has been and is very successful, and the NASA *Fermi* Gamma-ray Space Telescope satellite (see e.g. Atwood et al., 2009). *Fermi* is a new generation of high-energy gamma-ray observatory designed for making observations in the energy band from 10 MeV to about 300 GeV. It follows in the footsteps of the CGRO-EGRET experiment, which was operational between 1991 and 1999. Effectively, the *Fermi* Large Area Telescope (LAT), one of the two instruments on board in the satellite (the other being the Gamma Burst Monitor), is the successor of EGRET (Hartman et al., 1999), with greatly improved sensitivity, resolution and energy range.

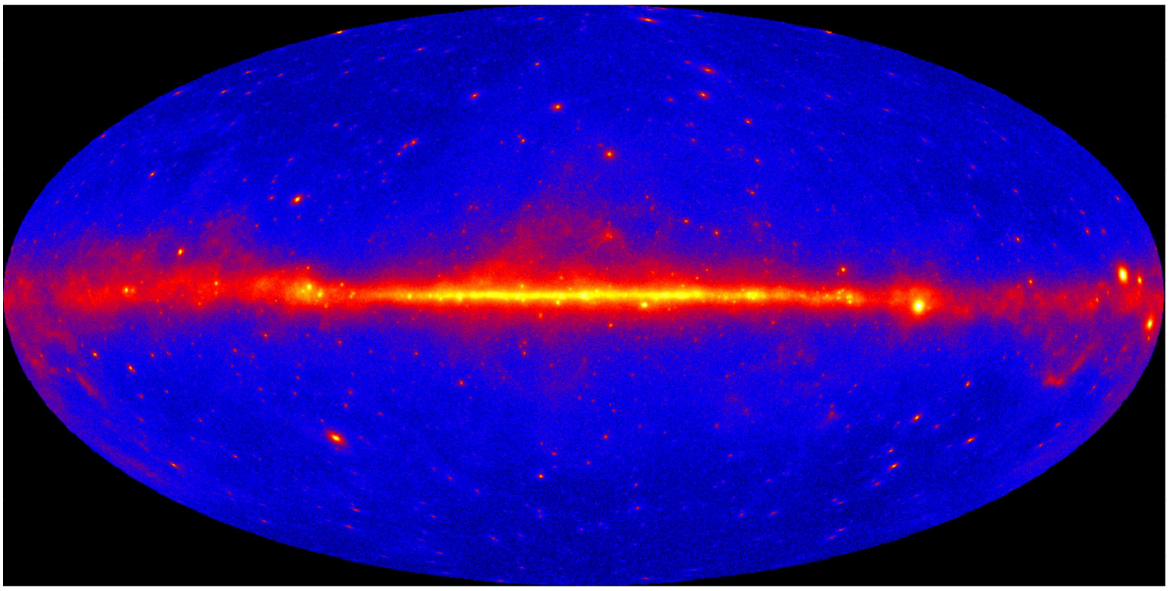

Figure 1.11: *Fermi* satellite 2-years all-skymap from Nolan et al. (2012).

In particular, the LAT is a pair-conversion telescope. The LAT improved sensitivity with respect to EGRET stems from a large peak effective area (~8000 cm^2, about 6 times greater than

EGRET), large field of view (~2.4 sr, nearly 5 times greater than EGRET), good background rejection, superior angular resolution (68% containment angle ~ 0.6 deg at 1 GeV) and improved observing efficiency (it is constantly surveying all the sky, making a full exposure of it in about 3 hours). The sensitivity is about 50 times better than that of EGRET at 100 MeV and even more at higher energies. It can locate sources to positional accuracies of 30 arcsec to 5 arcmin, depending on energy.
The *Fermi* satellite was successfully launched in June 2008, and began a sky survey in August 2008. The *Fermi*-LAT instrument in 3 months produced a deeper and better-resolved map of the gamma-ray sky than any previous space mission, revolutionizing our view of the very-high energy Universe. In figure 1.11, the 2-years all-skymap of *Fermi* is shown. It is particularly impressive to think that the 2-years *Fermi* catalog contains 1873 sources (Nolan et al., 2012), while EGRET could detect only 271 sources in nearly ten years of operation (Hartman et al., 1999).
IACTs and space-born instruments, working in different energy bands and with different philosophies, are complementary tools for the study of the high-energy phenomena in the Universe.

1.4 Outline

As explained in the previous sections, the main research activities of this PhD thesis are focused on the study of non-thermal emission coming from CR and DM in clusters of galaxies, with the ultimate purpose of a better understanding of the cluster evolution and therefore of the Universe formation history. This work combines both observational and theoretical approaches, the former thanks to my participation in the MAGIC experiment.
This *first chapter* serves to define the thesis scientific case and to make a short introduction on gamma-ray astronomy, which is the dominant part of this work. The thesis in then divided in three parts.
The *first part* is dedicated to the gamma-ray observations of the Perseus galaxy cluster with the MAGIC telescopes. In *chapter 2*, the MAGIC instruments are described and the analysis chain is explained in detail. In *chapter 3*, the MAGIC-I (single telescope) observation of the Perseus cluster performed in 2008 is presented. Constraints on both the possible CR and DM-induced emissions are derived. Subsequently, in *chapter 4*, the stereoscopic observation campaign of the Perseus cluster performed from 2009 to 2011, for which I was the P.I., is presented. This campaign resulted in the detections of the head-tail galaxy IC 310 and of the central cluster radio galaxy NGC 1275. The resulting 85 hours of stereoscopic data represent the deepest galaxy cluster observation ever made at very high energy. Indeed, this permits to put the most stringent constraints on the CR induced emission in clusters to date.
The *second part* is dedicated to theoretical predictions. In *chapter 5*, a constrained N-body simulation of the local Universe from the CLUES project is used to produce all-sky maps of the extragalactic DM annihilation and decay signals. It is shown that the *Fermi* satellite might detect DM induced gamma-ray emission from nearby galaxy clusters as well as from filaments of the cosmic web, particularly for some DM decay models. In *chapter 6*, the MultiDark N-body simulation is used to create a complete cluster mock catalog which well reproduces the

observed X-ray cluster properties and statistics through a phenomenological model in which a gas density is assigned to each DM-only simulated MultiDark halo using only its total mass. A new hybrid hadronic model is then constructed merging previous simulation and analytical results. This permits to compute the diffuse radio and gamma-ray emission due to hadronic CR interactions with the ICM. In particular, predictions for the LOFAR cluster survey are presented, investigating how this can constrain the physical mechanism generating RHs

The *third* and last *part* is dedicated to present the conclusions and future prospects of the work done in this thesis.

Part I

GAMMA-RAY OBSERVATIONS OF GALAXY CLUSTERS

Chapter 2

The MAGIC Telescopes

A perfection of means, and confusion of aims,
seems to be our main problem.
Albert Einstein

Since fall 2009, MAGIC (Major Atmospheric Gamma-ray Imaging Cherenkov) is a stereoscopic system of two IACTs observing the sky at energies above approximately 50 GeV. It is located at the Roque de los Muchachos observatory on the Canary Island of La Palma at 2200 m above the sea level. The telescopes have been recently renamed *MAGIC Florian Goebel Telescopes* in memory of our colleague who accidentally died in 2008.
This chapter describes in detail the MAGIC instruments and the corresponding data analysis chain which is then applied to obtain the results presented in the next two chapters. This chapter is partially inspired to Zandanel (2007) and Prandini (2011).

2.1 The Instrument

The second telescope, MAGIC-II, is basically an improved version of the first telescope, MAGIC-I, which has been operating alone from August 2004 to November 2009. Thanks to its unique characteristics such as the low energy threshold, the light structure and fast electronics, MAGIC-I has been the suitable instrument for the observation of a wide range of objects. However, the improvement obtained passing form *mono* to *stereoscopic* observations has been dramatic as demonstrated by the growing number of new detections MAGIC achieved since fall 2009. As a matter of fact, the Perseus cluster head-tail galaxy IC 310, presented in chapter 4, has been the first source detected by the MAGIC stereoscopic system. The detection of the radio galaxy NGC 1275, at the center of the Perseus cluster, also presented in chapter 4, is another great success of the new MAGIC system. In figure 2.1, the two telescopes are shown.
In the following sub-sections, the main hardware characteristics of the MAGIC telescopes are described. As MAGIC-II is an improved clone of MAGIC-I, different technical solutions were adopted at the the time of its construction. In particular, the camera and readout system were substantially different in the two telescopes. However, during summer 2011 an upgrade of MAGIC-I has started which will hopefully finish in summer 2012. At the time of writing this thesis, the

Figure 2.1: Picture of the two MAGIC telescopes while pointing at the sky.

readout of the two telescopes are identical while the camera of MAGIC-I is still waiting to be replaced by a clone of the MAGIC-II one. After this upgrade, the two instruments will be almost identical, with great advantage for the data analysis and simplicity of maintenance. In the following, when not explicitly mentioned, the presented details should be considered valid for both instruments.

2.1.1 Structure and Drive System

MAGIC was conceived as a fast pointing system so lightness was one of the main goals; indeed, the structure holding the mirrors is a very lightweight carbon fiber frame. The carbon fiber also guarantees a good resistance to atmospheric agents, particularly aggressive in the island. The rest of the support is made of aluminum. The total weight of the frame is of 5.5 tons.

MAGIC is a system made of two *alt-azimuth mount* telescopes. In figure 2.2, the structure of one of the two telescopes, MAGIC-I, can be appreciated in detail. The whole structure is mounted on a circular rail with a diameter of 19 m. There is a tower which permits the access to the camera. This latter is located at a distance of around 17 m from the reflector and is carried by a single aluminum tubular arc supported by narrow steel cables connected to the main structure. The weight of the camera is around half a ton, and the small bending, unavoidable during the telescope tracking, is corrected via re-orientation of the mirrors. The azimuth motion is controlled by two motors while the zenith motion by one. A starguider camera, mounted at the center of the reflector system, monitors the positioning of the telescope by viewing both the camera of the telescope and the corresponding section of the sky starfield. The lightweight structure permits very fast repositioning of the telescopes to any position in the sky within about 30 s. This feature was designed to instantly react to Gamma-Ray Burst (GRB) alerts from dedicated satellites in the KeV/MeV domain.

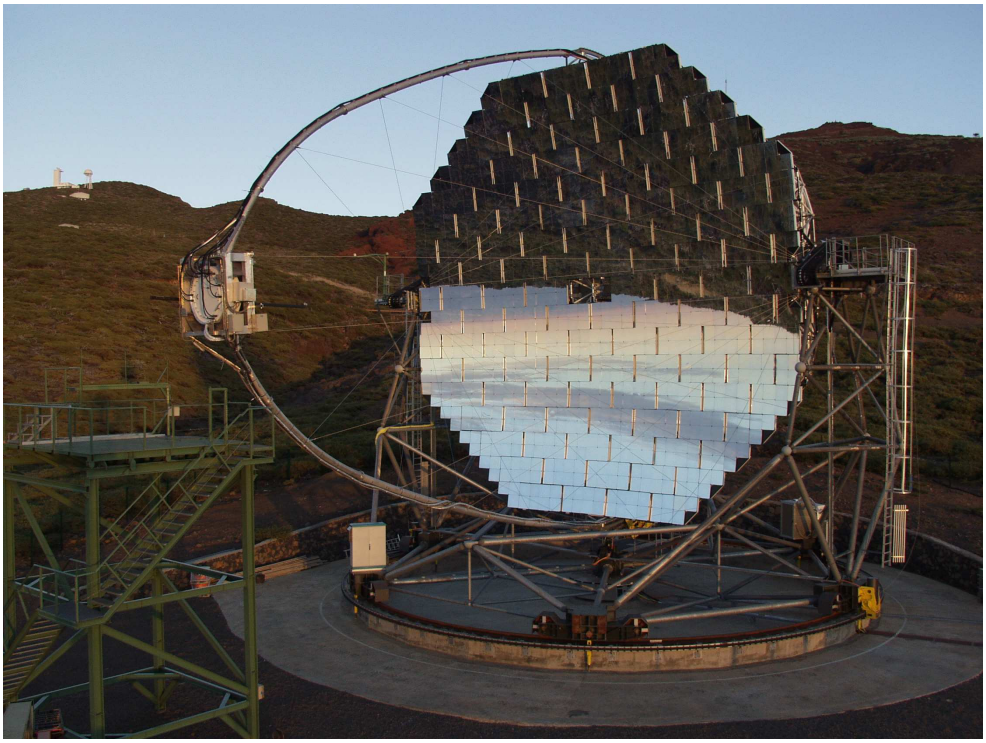

Figure 2.2: Picture of the MAGIC-I telescope. The structure is well visible, particularly the reflecting surface, the camera and the access tower.

2.1.2 Reflector

The reflector surface is parabolic in order to minimize the time spread of the Cherenkov light flashes on the camera plane ($\leq$ 1 ns instead of 6 ns in the spherical surface case, where the typical duration of a Cherenkov flash is less than 5 ns). The time structure preservation is important to minimize the trigger integration window, reducing the number of random coincidence trigger due to the night sky background (NSB) which does not have any coherent time structure, and also to increase the signal-to-noise ratio.
The parabolic reflector has a diameter of 17 m and is composed by 1 m^2 movable panels. These are adjusted by the Active Mirror Control (AMC) during the data taking depending on the telescope position. The total reflecting area is of about 240 m^2.
Three different types of mirrors are installed:

- 1 m^2 *Aluminum Mirrors.* These are composed of an aluminum box open on the upper side where an honeycomb aluminum structure is inserted in order to guarantee the necessary rigidity of the mirror. A thin aluminum plate is located on the top and glued to the honeycomb. The upper side of the plate is finally polished using a special diamond milling machine which makes the surface reflective. The reflecting surface, spherically shaped, is protected by a final layer of quartz-based material which coats the mirror and protects the

surface from scratches and the aluminum from oxidation. The mirror surface has a high reflectivity of about 90% in the wavelengths range 300 – 600 nm. This innovative technology was indeed motivated by the demand of keeping the weight of the telescope as small as possible. MAGIC-II has 143 of such mirrors out of 247.

- 0.25 m^2 *Aluminum Mirrors.* The same as before but for the dimension. The MAGIC-I reflective surface is made of such mirrors, in number of four per moving panel. The change to 1 m^2 mirrors in MAGIC-II reduced costs and manpower.

- 1 m^2 *Glass Mirrors.* The remaining 104 mirrors of MAGIC-II are produced as a sandwich of 2 mm glass plates around a aluminum honeycomb layer. The frontal glass surface is coated with a reflecting aluminum layer and a protecting quartz coating. These mirrors have a PSF which almost doubles that of the aluminum mirrors but the light spot is still well inside the size of a camera pixel.

Starguider

In order to monitoring the tracking system on-line, a sensitive CCD-camera has been installed in the center of each mirror dish. It has a 4.6 deg ×4.6 deg field of view and images the sky in the telescope pointing direction as well as part of the camera. Six reference points (LEDs) on the camera frame indicate its position, while individual stars get recognized by a dedicated software and compared to starfield catalogs. With this information, the real pointing position of each telescope can be retrieved.

2.1.3 Camera

The MAGIC-I camera has a diameter of 1.5 m, 450 kg weight and covers 3.5 deg of field of view (FOV). It is composed of 577 pixels, positioned in a hexagonal structure, collecting the incoming light by high Quantum Efficiency (QE) PhotoMulTipliers (PMTs). The PMTs are hemispherical tubes, out of which 397 have 0.1 deg FOV 1″ diameter surrounded by 180 of 0.2 deg FOV 1.5″. The smaller pixels are also called *inner pixels* because they occupy the inner region of the hexagon, while the bigger ones are called *outer pixels*. The motivation to use two different PMT sizes is due mainly to a compromise between performances and costs. The typical time response of each PMT is below 1 ns full-width half-maximum (FWHM). The photo-catode QE is enhanced up to a 25% peak value and extended to the UV by a special coating on the PMT surface acting as a wavelength shifter. In front of each pixel there is a light guide consisting of a thin aluminum tube, in the approximate form of a Winston cone, which guides the light inside the PMTs with an incident angle of about 40 deg. Each cone is put directly into the PMT tube and is 5 cm long with an hexagonal shape at the end. In this way, there are no dead regions between the pixels. The left scheme in figure 2.3 shows the MAGIC-I camera design.
The camera is protected by a transparent plexiglass window with an uniform transmission over all wavelengths down to 300 nm and a low absorption. The camera has two lids which are opened during the data taking and protect the camera from the light during the day. Additionally, there are a water and air cooling and heating system. The whole camera structure can be moved

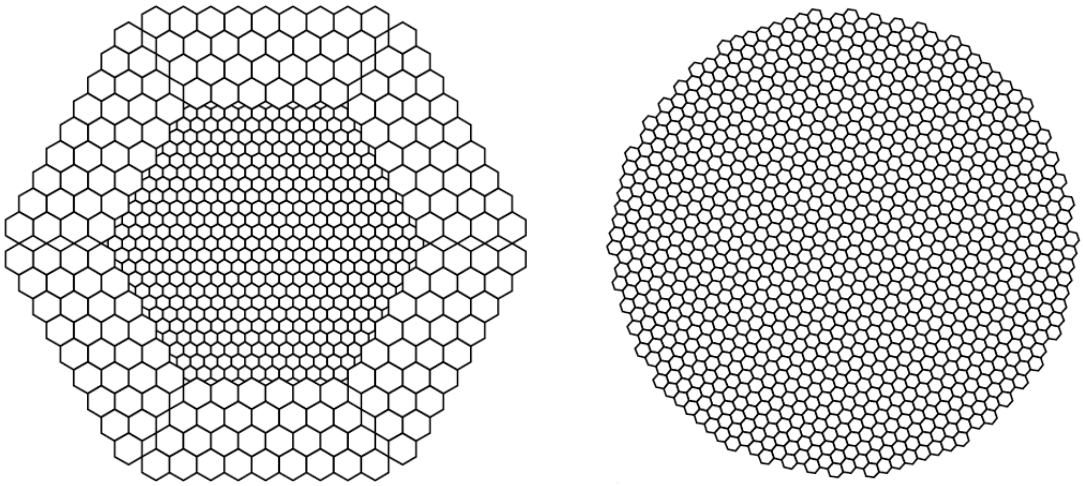

Figure 2.3: On the left, the scheme of the MAGIC-I camera. The 397 inner pixels and the 180 outer pixels are clearly recognizable. On the right, the scheme of the improved MAGIC-II camera.

forward and backward with respect to the mirror dish to get different focuses, ranging from 1 km to infinity.
The MAGIC-II camera, which design is shown in the right scheme of figure 2.3, has a circular shape and the same FOV of the camera of MAGIC-I. It is equipped uniformly with 1039 pixels of 0.1 deg, grouped in clusters. Each cluster comprises seven pixels in a hexagonal configuration. The modular design allows an easier control and maintenance of the camera. Besides the larger number of pixels, the real improvement of the MAGIC-II camera is the installation of increased QE PMTs which reach a peak QE of 34%.

2.1.4 Readout and Trigger System

The PMT signals are amplified by ultrafast and low-noise transimpedance pre-amplifiers in the camera housing. The amplified analog signals are transmitted over optical fibers using Vertical Cavity Surface Emitting Laser Drivers (VCSELs, with a wavelength of 850 nm). Such a type of transmission over optical links drastically reduces the weight and size of the cables, protects the transmitted signal from ambient electromagnetic noise in the line and gets a large band width.
Since gamma-ray signals are very short in time, a very fast readout electronics is needed. The pulses have to be first processed to generate the trigger signal and then digitized at ultra-fast speed. Afterwards they have to be stored for the subsequent analysis. In the receiver board the signal is converted back to electric and, if passing the trigger requirements, digitized. The digitization system is also referred as the Flash Analog to Digital Converters (FADCs), in virtue of the high speed of digitization where pulses are sampled at the speed of 2 GSample/s.
The 2 GSample/s digitization and acquisition system is based upon a low power analog sampler chip called Domino Ring Sampler. The analog signals are stored in a multi-capacitor bank that

is organized as a ring buffer, in which the single capacitors are sequentially enabled by a shift register driven by an internally generated 2 GHz clock locked by a phase lock loop (PLL) to a common synchronization signal. Once an external trigger has been received, the sampled signals in the ring buffer are readout at the lower frequency of 40 MHz and digitized with a 12 bits resolution.
The MAGIC trigger is a multi-level decisional system with programmable logic. Its purpose is to set out the beginning of the image acquisition process simultaneously with the shower detection. The trigger system should discriminate the Cherenkov flash induced signals from the background. Therefore, it selects very fast events happening in compact regions of the camera. In MAGIC-I, the trigger area covers 1.9 deg diameter FOV, while the uniform camera design of the MAGIC-II camera permits an increased trigger area of 2.5 deg diameter FOV. This increases the potentiality to study extended sources and to perform sky scans. Moreover, it enhances the efficiency of point-like sources observation of about 15%.
The trigger system is composed of three decisional level:

- *Level Zero Trigger* (L0T): this is the first decisional level. Its task is to check if the signal from each PMT is greater than a fixed threshold (*discriminator threshold*) set via software (see figure 2.4 left scheme). If this happens, a fast signal, of the order of a Cherenkov flash duration, is generated. A pixel is considered lighted when its signal passes the level zero trigger.

- *Level One Trigger* (L1T): to get advantages from the spatial compactness of the desired signals, this level requires a temporal coincidence (multiplicity) of the signal selected by L0T and then introduces a *topology* in order to combine temporal and spatial information (see figure 2.4 right scheme). The requirement is to accept only those signals having a certain amount of adjacent lighted pixels with a compact configuration (i.e. if a pixel is taken away, the others must remain still connected). This topology is called Close Compact Next Neighbors (CCNN).

- *Level Two Trigger* (L2T): this level can be used to perform a rough analysis and to apply topological constraints on the images. It consists of a set of look-up tables (LUTs) enabled from L1T and acting on the trigger cells with a tree-structured set of programmable fast memories. Using some topological constraints, such as a fast evaluation of the image size by L2T, it is possible to significantly reduce the NSB rate, permitting a reduction of the discriminators and thus of the energy threshold. However, up to now the L2T has been used just in flag-mode, i.e. the events are tagged with L2T but not rejected yet.

- *Level Three Trigger* (L3T): this is used when the two telescopes are operated in stereoscopic mode. Practically, it is a coincidence trigger rejecting events triggered by only one telescope. In order to minimize the L3T coincidence window, the triggers produced by the individual telescopes are delayed by a time depending on the pointing direction. This reduces the overall trigger rate to a value which is manageable by the data acquisition system.

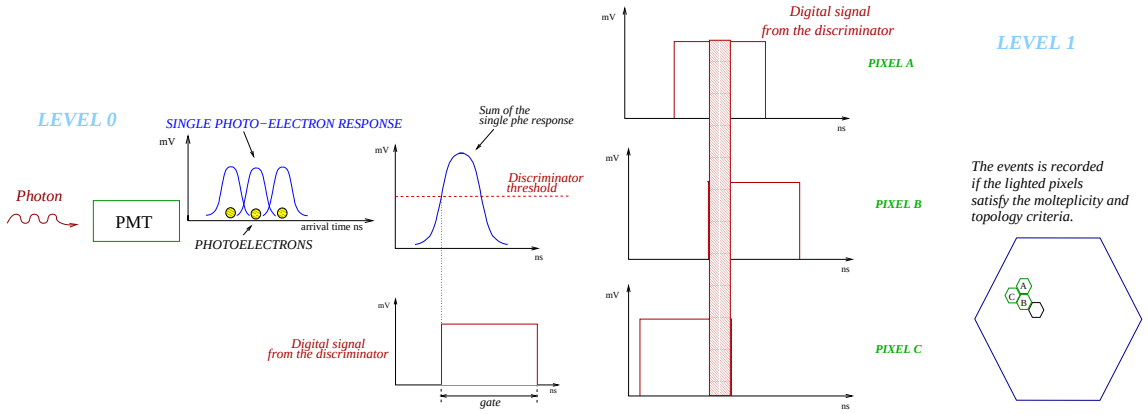

Figure 2.4: Left: schematic view of the level zero trigger (L0T). Right: schematic view of the level one trigger (L1T).

Eventually, after passing the trigger conditions, events are digitalized by the FADCs and stored. Time and trigger information for each event are also recorded by dedicated digital modules which are read-out together with the FADC modules.

2.2 Data Taking and Analysis Chain

As explained in chapter 1, IACTs detect the Cherenkov light produced by atmospheric showers which appears in the form of fast light pulses of a few nanoseconds duration. The steps leading from the Cherenkov pulses reflection to the data storage can be resumed in the following main points:

- The Cherenkov light that reaches the mirror surface is focused in the focal plane onto the camera.
- PMTs convert the photon signal to a current signal which is amplified inside the camera.
- The resulting amplified electric pulses are re-converted into light pulses and sent to the data acquisition system through optical fibers.
- The signal is converted once more into electric pulses, triggered and the final signal is digitized by the FADC system.

The collected digital signals, called *raw data*, are stored to disk and analyzed offline. The data analysis is performed with the standard MAGIC collaboration software called Magic Analysis and Reconstruction Software (MARS) working in the ROOT framework, both on C++ platform.

2.2.1 Data Taking

IACTs collect the data during night. The sunlight is a dominating background that makes it impossible to register the faint Cherenkov flashes. The weather conditions are an essential factor influencing data quality. Main causes of bad quality data are the presence of clouds in the sky, high humidity and *calima* (desert sand coming from Africa typical of Canary Islands).
Since MAGIC is a stereoscopic system, the standard data taking procedure is the so-called stereo observation mode in which the two telescopes observe at the same time and only events seen by both telescopes are recorded. However, each telescope can take data individually, in the so-called mono observation mode.

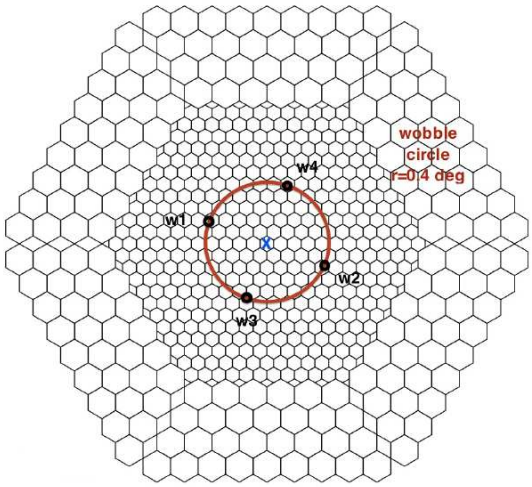

Figure 2.5: Geometry of the wobble data taking mode on the MAGIC-I camera. The W1, W2, W3 and W4 positions are indicated as black circles and the wobble circle itself is indicated in red. The camera center is the blue cross.

MAGIC can adopt two different data taking modes; the On/Off mode, in which the signal and background events are collected separately pointing to different sky regions, and the wobble mode (Fomin et al., 1994), in which each telescope is alternated every 20 minutes between four sky positions at 0.4 deg offset from the source position. This technique permits On and Off to be collected simultaneously thus halving the observation time. In figure 2.5, the geometry of the MAGIC wobble data taking mode is shown. There are four positions (W1, W2, W3 and W4) located at 0.4 deg from the camera center. When tracking in wobble mode, the telescopes point alternatively to these positions, switching each 20 minutes. In camera coordinates, the source is therefore located in one of these positions (while it is the camera center in case of On/Off mode). In this way, when the source is e.g. in W1, the background can be extracted from the other three positions. There also exists the possibility of using only two of the four wobble positions. Lately, the four wobble positions have become standard as they permit a more accurate background estimation.

2.2.2 Data Reduction

The main steps of the data reduction are the following:

- *Signal Extraction and Calibration.* The executable MARS program CALibrate LIght Signals and Time Offsets (CALLISTO) performs the signal extraction from the FADC slices recorded in the raw data. The charge of each triggered event is then calibrated and converted into number of photo-electrons (phes).

- *Image Cleaning.* The background surrounding each shower image is rejected so that all the information regarding the pixels not involved in the shower image is discarded, resulting in greatly reduced data file dimension. The Hillas parameters are then calculated for each cleaned image (see section 1.3.2). This is done by a MARS program called STandard Analysis and Reconstruction (STAR). Figure 2.6 illustrates this step.

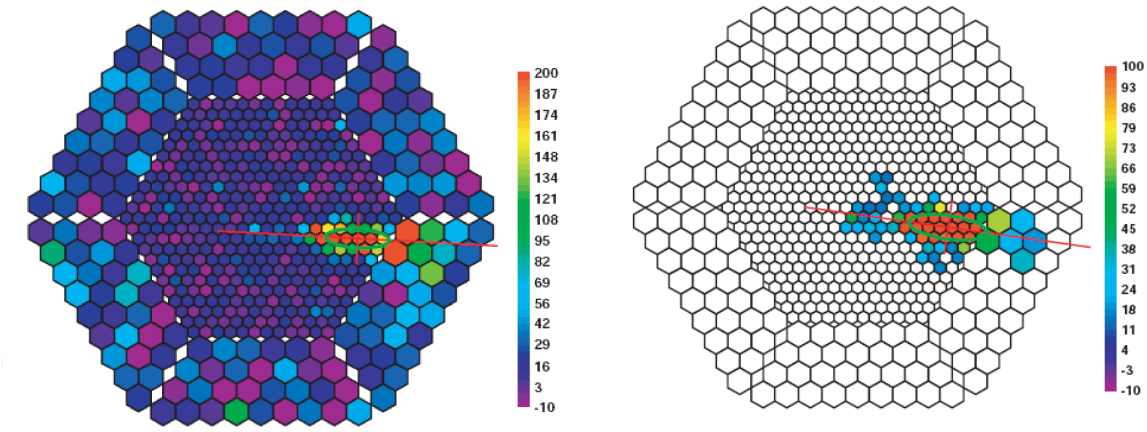

Figure 2.6: Example of a shower induced image before (left panel) and after (right panel) the image cleaning. The superimposed ellipse shows the Hillas parametrization.

- *Data Quality Selection.* After the image cleaning, data of bad quality are rejected mainly due to bad weather or hardware problems. In particular, bad weather conditions affect the data in a non-predictable way, since a model for showers development in every atmospheric condition does not exist. Therefore, data affected by the presence of clouds, high humidity or calima are discarded. The MAGIC analysis is not provided with a standardized data quality selection because Hillas parameters are largely variable from event to event and depending on the precise atmospheric conditions and telescopes setting. Generally, at this level, the *rate* after the image cleaning is the main parameter to perform a quality selection on single file basis.

- *Stereoscopic Image Reconstruction.* The analysis chain described up to here is applied to the data collected by both telescopes separately, independently if taken in mono or

stereo observation mode. Therefore, in case of stereoscopic observations, two sets of files containing two different views of the same cleaned showers are available. The MARS program called SuperSTAR reduces the two sets of files in a single one, containing all the necessary information. In this step, additional image parameters, referring to stereoscopic view of a shower, are also calculated (such as e.g. the primary particle incoming direction).

- *Gamma-Hadron Separation and Energy Reconstruction.* These tasks are performed via the Random Forest (RF) method (Albert et al., 2008b) in two subsequent steps: the *training* and *test* phases. In the training phase, two specific matrices, one for the gamma-hadron separation and one for the energy reconstruction, are created using Monte Carlo (MC) simulations and real data. These matrices are applied to both real and MC data in the test phase where two new parameters are assigned to each event: its *hadronness* and reconstructed energy. The hadronness is a real number, ranging from 0 to 1, related to the probability of a event to be hadron-like (≈ 1) or gamma-like (≈ 0). Therefore, while gamma-like events are peaked at 0, hadron-like events are peaked at 1. As explained above and in the previous chapter, hadronic showers represent the large majority of the collected events, hence, the hadronness parameter is used to reject the hadron-like showers and select the events most likely produced by gamma-rays. Actually, the energy reconstruction of stereo events can also be performed using look-up tables based on the values of some selected image parameters. Although this method is simpler than the RF method, it provides a better energy resolution, especially at low energies, thanks to the shower 3D parameters which are well reconstructed in stereo observations. The matrices are calculated by the MARS program Optimize STandard Energy Reconstruction and Image Analysis (OSTERIA) for mono data, and by Compressed Osteria Alias Computation of the Hadronness parameter (COACH) for stereo data. Finally, the MErge and Link Image parameters Before Energy Analysis (MELIBEA) program applies them to the real and MC data.

2.2.3 Signal Search

There are two approaches for the detection of a signal: the *Alpha* and *Theta* techniques.
The standard approach for mono observations consists in using the so-called *Alpha plot*, which is the distribution of the absolute value of the α parameter. This parameter, already introduced in section 1.3.2, is the angle between the major axis of an ellipse and the direction from the image center of gravity (i.e. the center of the ellipse) to the reference point (i.e. camera center or wobble positions in On/Off or wobble observation mode, respectively) as shown in figure 2.7 left scheme. This parameter has a high gamma-hadron discriminating power, allowing the extraction of gamma events over the background: while gamma events have small Alpha values, the hadronic events are uniformly distributed in an Alpha plot.
An alternative is to use the Disp parameter which is characterized by the fact that no a priori assumption on the source position is made. The *Disp* is defined as the distance between the image center of gravity and the unknown source position, which is assumed to lie on the ellipse major axis as shown in figure 2.7 right scheme. The Disp can be estimated by using the *elongation* of the image, defined as the ratio of the Width and Length parameters (see section 1.3.2). The basic

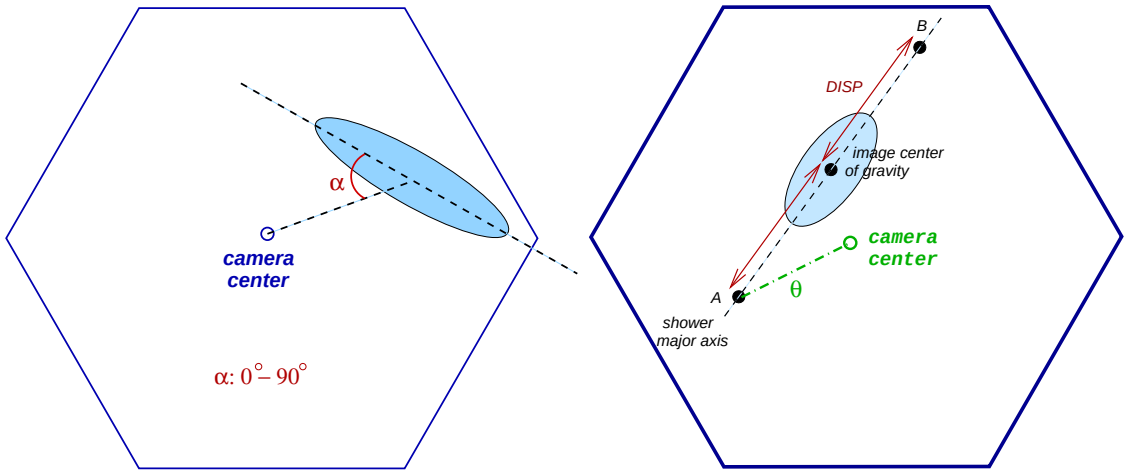

Figure 2.7: On the left: schematic view of the Alpha parameter. On the right: schematic view of the Theta parameter. The Disp parameter provides two possible solutions and the correct one is established by using a head-tail discriminator.

idea is that shower images which are closer to the source position are most roundish, i.e. their elongation is close to 1, while shower images which are further away from the source position are more elliptical. As shown in figure 2.7, the Disp calculation provides two possible source positions that lie on the shower image major axis and therefore a *head-tail discriminator* is used to disentangle between them. The Theta θ parameter is the angular distance between the nominal and the reconstructed source position, i.e. the distance between the camera center (in the case of On/Off observation mode) and the source position found with the Disp method. The number of background events is independent from the arrival direction, thus, for geometrical reasons, it is proportional to θ^2 ($N_{bk} \propto 2\,\pi\,\theta\,d\theta \propto d\theta^2$). Since the hadronic events are uniformly distributed and the gamma ones are peaked at values close to 0 deg, a θ^2 plot gives an equivalent alternative to the classical Alpha plot. In particular, this is the method used in case of stereoscopic observations.
As a convention in the IACT world, a source is considered detected if significance of the excess events is above 5 σ, where the significance σ is defined according to the formula 17 of Li & Ma (1983). The number of excess events is calculated by subtracting the background events from the number of signal events. This is done in the so-called *signal region* $\alpha < \alpha_{cut}$ or $\theta^2 < \theta^2_{cut}$ for an Alpha or Theta plot, respectively, as shown in figure 2.8.
Details on the Disp RF calculation as performed by the MAGIC collaboration, as well as on the other steps of the stereo analysis, can be found in Aleksić et al. (2012c). Details on the origial mono analysis can be found in Albert et al. (2008c) and Aliu et al. (2009b).

2.2.4 Flux Estimation

In case of detection, the final goal of the data analysis is the calculation of the observed source flux. The *differential flux* of a source is the number of photons of a given energy E observed by the telescope per unit surface and time $f(E) = dN(E)/dA\,dt$, where t is the *effective time*

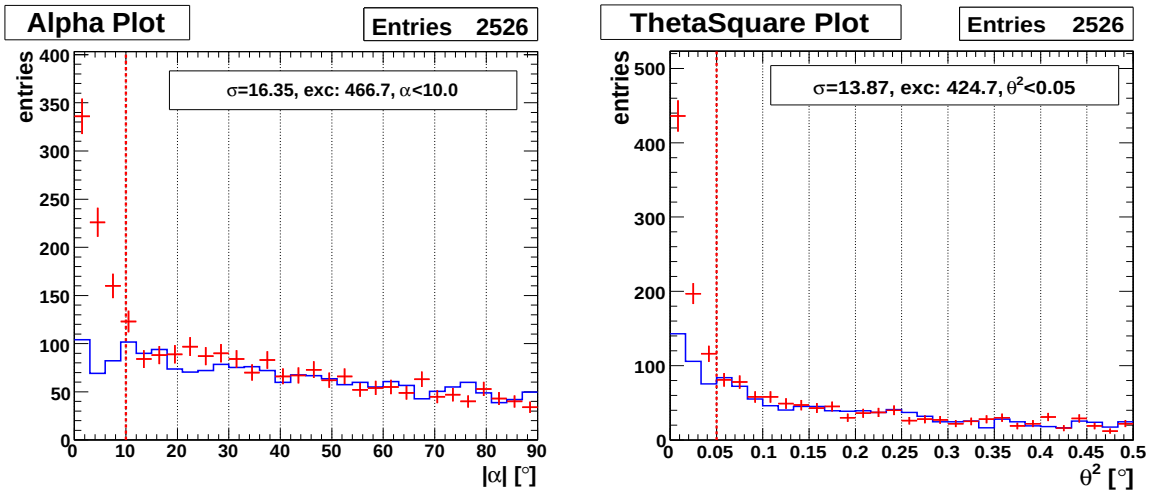

Figure 2.8: Alpha (left) and Theta (right) plot, in the energy range 300 – 700 GeV, for about 2 hours of Crab Nebula data taken with the MAGIC-I telescope in 2007. Signal regions are $\alpha_{cut} = 10$ deg and $\theta^2_{cut} = 0.05$ deg. Red crosses represent the signal while the blue line is the background.

and A is the effective collection area. The IACT *effective area* is the area in which atmospheric showers can be potentially observed by the telescopes, folded by the detection efficiency, after all analysis cuts. It depends principally on the incident gamma-ray energy E and on the zenith angle of observation Θ; it increases with energy and with zenith angle. The effective area is defined as:

$$A_{eff}(E,\Theta) = A_{sim}\,\frac{N_{analysis}(E,\Theta)}{N_{sim}(E)} \tag{2.1}$$

where $N_{sim}(E,\Theta)$ is the number of simulated gamma events, A_{sim} is the simulated incident area and $N_{analysis}(E,\Theta)$ is the number of simulated gamma events after all the analysis steps and the chosen cuts. Eventually, the differential flux is obtained as:

$$f(E) = \frac{N_\gamma(E)}{A_{eff}\,t_{eff}} \tag{2.2}$$

where $N_\gamma(E)$ is the excess number obtained from an Alpha or Theta plot in the adopted (reconstructed) energy bin.
The calculation of the source flux or of a flux upper limit in case of non-detection (see below), is done with the MARS executable fluxlc. Effects on the spectrum determination introduced by the limited energy resolution are usually corrected by *unfolding* the final spectrum.

Flux Upper Limits

In case of a non-detection, flux upper limits are calculated. Supposing the source gamma-ray flux $dN/dE\,dA\,dt$ is known, the number of events collected by the telescopes can be predicted as:

$$N_{obs} = \int \int \frac{dN}{dE\, dA\, dt} A_{eff}(E)\, dt\, dE \tag{2.3}$$

which, dividing the observed excess number in bins of reconstructed energy E, becomes:

$$N_{obs}(E_{min}, E_{max}) = \int \int \frac{dN}{dE\, dA\, dt} A_{eff}(E, E_{min}, E_{max})\, dt\, dE \tag{2.4}$$

where E_{min} and E_{max} are the bin limits. When no signal is detected, the number of observed excess events fluctuates statistically around an average value of 0. From the number of observed events, it is possible to derive an upper limit on the number of observable events, typically giving a confidence level[1] of 95%:

$$N_{>95\%}(E_{min}, E_{max}) > \int \int \frac{dN}{dE\, dA\, dt} A_{eff}(E, E_{min}, E_{max})\, dt\, dE\,. \tag{2.5}$$

$N_{>95\%}$ has to be transformed into a flux upper limit.
The informations known at this stage of the analysis are: the number of signal N_{sign}^{obs} and background N_{back}^{obs} events observed within the signal region, the statistical uncertainty on the background events and the global systematic uncertainty on the detector efficiency. Starting from the observed excess number $N_{EX}^{obs} = N_{sign}^{obs} - N_{back}^{obs}$, an upper limit can be obtained constructing a probability density function (PDF) for N_{sign}, given a hypothesis on the excess and background event numbers and inverting the original PDF to get the PDF for the number of the excess events. In order to invert the PDF, two statistical approaches exist: a Bayesian and a frequentist approach. The MAGIC collaboration publishes upper limits using this last method, precisely the Rolke et al. (2005) method, assuming N_{sign} is Poissonian distributed and N_{back} is Gaussian distributed. The considered systematic uncertainty is about 30% and is obtained by adding up the individual contributions in quadrature. The different sources of systematic uncertainties are mainly related to the differences between the real experimental conditions and the simulated ones (see Albert et al., 2008c for a detailed discussion on the systematic errors).
In the case of no detection, neither the source energy spectrum dN/dE nor the time evolution dN/dt are known. Hence, some assumptions need to be made. Typically, a power-law spectrum is assumed:

$$\frac{dN}{dE\, dA\, dt} = f_0 \left(\frac{E}{E_0}\right)^{-\alpha} \tag{2.6}$$

where E_0 is the mean energy at which the limit is calculated (estimated from MC data) and α is the hypothetic spectral index. Here, the light curve dN/dt has to be assumed approximately constant. If this is not possible, the observation time window is splitted into small intervals where the approximation can be considered valid. The *differential* flux upper limit in the energy bin $[E_{min}, E_{max}]$ is therefore obtained as:

[1] A *confidence interval* is an interval $[N_{low}, N_{up}]$ out of which only a percent of ξ events can be found. The corresponding *confidence level* (CL) for the interval is $CL = 100\,(1-\xi)$ [%]. Therefore, an upper limit of confidence level CL is defined by a confidence interval $[0, N_{up}]$ and coincides with the number N_{up} above which only a percent of ξ events can be found: $P(N > N^{up}) = \xi$.

$$f_0^{ul} < \frac{N_{>95\%}(E_{min}, E_{max})}{t_{eff} \int \left(\frac{E}{E_0}\right)^{-\alpha} A_{eff}(E, E_{min}, E_{max})\, dE}\,, \tag{2.7}$$

while the *integral* flux upper limit above a certain energy threshold E_{th} is:

$$\phi^{ul}(E_{th}) = f_0^{ul} \int_{E_{th}}^{\infty} \left(\frac{E}{E_0}\right)^{-\alpha} dE\,. \tag{2.8}$$

2.3 Performances

The improvement obtained upgrading to stereo observations has been impressive (Aleksić et al., 2012c). This can be appreciated in figure 2.9 left panel, where the integral sensitivity achieved by MAGIC-I and by the stereoscopic system is shown and compared to the integral flux of the Crab Nebula, the standard candle of gamma-ray astronomy. The integral sensitivity has improved from a factor of 2 to a factor of 3, depending on the energies. The angular resolution achieved by the MAGIC stereoscopic system is also shown in the right panel of figure 2.9, going from about 0.1 deg at 100 GeV to about 0.04 deg at energies above 1 TeV, thus improving up to a factor of 2 the MAGIC-I angular resolution (Colin et al., 2009).

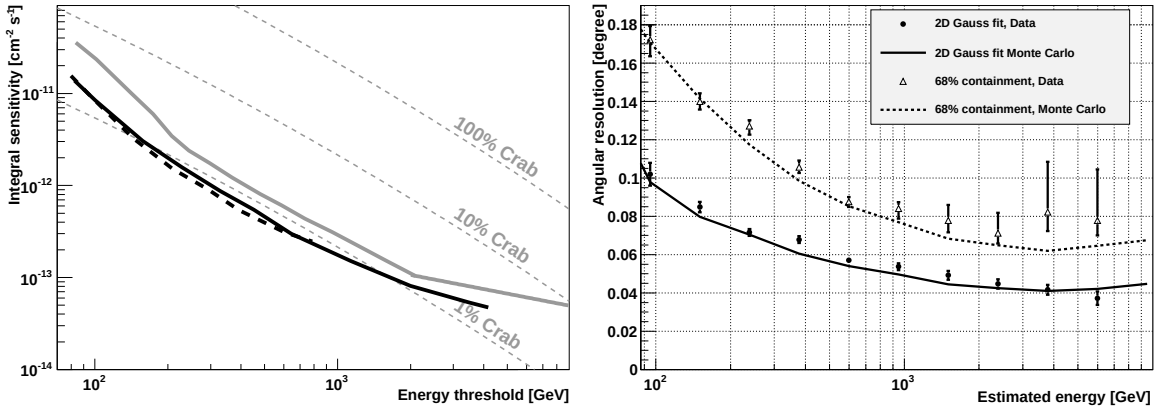

Figure 2.9: On the left, the MAGIC-I and MAGIC stereoscopic integral sensitivity, i.e. the flux of a source above a certain energy for which $N_{excess}/N_{background} = 5$ after 50 hours of effective observation time achieved by MAGIC-I (solid gray line) and by the MAGIC stereoscopic system (black line, where solid is from data and dashed from MC simulations). On the right, the stereoscopic system angular resolution as a function of the estimated energy obtained with a Crab Nebula data sample (points) and compared with the MC simulations (lines). Figures taken from Aleksić et al. (2012c).

The energy threshold of the stereoscopic system is approximately of 50 GeV (Aleksić et al., 2012c) while the MAGIC-I threshold was around 60 – 70 GeV (Albert et al., 2008c). The energy resolution finally achieved by the stereoscopic system is of about 20% at 100 GeV and 15% around 1 TeV, while for MAGIC-I it was of about 26% and 19%, respectively (Albert et al., 2008b).

In the next chapter 3, the observations of the Perseus galaxy clusters performed in 2008 only with the MAGIC-I telescope will be presented, while chapter 4 is dedicated to the cluster large observation campaign performed form 2009 to 2011 with the stereoscopic system. Note that the serendipitous detection of the cluster head-tail galaxy IC 310 was the first detection of the newly inaugurated MAGIC stereoscopic system. The subsequent detection of the cluster central radio galaxy NGC 1275 has also represented a big success of the stereoscopic system given the extreme spectral characteristics of this source.

Chapter 3

The MAGIC-I Observation of the Perseus Galaxy Cluster

The beginning is the most important part of the work.
Plato

As anticipated in the Introduction, gamma-ray observations of galaxy clusters are very important in order to shed light on the RH generation mechanism and for DM searches. This chapter is dedicated to the results of the Perseus cluster *mono* observation performed by the MAGIC-I telescope during November-December 2008 for a total effective time of 24.4 hours. The physical motivations for which Perseus was chosen over other galaxy clusters, together with its main characteristics, are presented. After describing the data sample, the analysis and the obtained flux upper limits, the implications for the CR pressure and the possible DM annihilation induced gamma-ray emission are discussed.
The work presented in this chapter has been published with the title *MAGIC Gamma-Ray Telescope Observation of the Perseus Cluster of Galaxies: Implications for Cosmic Rays, Dark Matter and NGC1275* in the Astrophysical Journal in 2010 (APJ 710, 634, 2010; Aleksić et al., 2010a). I am the corresponding author of this publication together with Christoph Pfrommer. My main contributions are the MAGIC data analysis and the paper writing. I also substantially contributed to the theoretical interpretation of the obtained results.

3.1 Target Selection and Preliminaries

The Perseus cluster, also called A426, is at a distance of 77.7 Mpc ($z = 0.018$). It is the brightest X-ray cluster (Edge et al., 1992) and hosts a massive cooling flow with high central gas densities of $0.05\ \mathrm{cm}^{-3}$ (see table 3.1). Perseus furthermore hosts a luminous radio mini-halo – diffuse synchrotron emission that fills a large fraction of the cluster core region – and shows a source extension of ~ 200 kpc (Pedlar et al., 1990). This radio mini-halo is well modeled by the hadronic scenario where the radio emitting electrons are produced in hadronic CR proton interactions with ambient gas protons requiring only a very modest fraction of a few percent CR pressure relative

to thermal pressure (Pfrommer & Enßlin, 2004a). In particular, the similarity of the thermal X-ray emission and that of the radio mini-halo comes about naturally as both processes scale with the number density squared. An alternative model for the radio emission has been proposed by Gitti et al. (2002) which explains the radio mini-halo by re-acceleration of relativistic electrons through second order interactions with magneto-hydrodynamic (MHD) turbulence. However, it remains to be shown whether the necessary turbulent energy density can be provided throughout the entire cooling flow region of Perseus. These conditions provide high target densities for hadronic CR interactions and enhance the resulting gamma-ray flux.
The Perseus galaxy cluster was carefully chosen over other nearby clusters after considering the expected gamma-ray emission from the pion-decay and DM annihilation as explained in the following subsections.

z	$D_{\rm lum}$ [Mpc]	R_{200} [Mpc]	M_{200} [$M_\odot$]	$L_{\rm X,0.1-2.4\ keV}$ [erg s^{-1}]	T_X [keV]	$L_{\rm 1.4\ GHz}$ [erg s^{-1} Hz^{-1}]
0.0183	77.7	1.9	7.71×10^{14}	8.31×10^{44}	6.8	3.38×10^{31}

Table 3.1: Properties of the Perseus galaxy cluster. The data is taken from Reiprich & Böhringer (2002), Pedlar et al. (1990) and Churazov et al. (2003).

3.1.1 Cosmic Ray Induced Emission

In the course of this work, cosmological simulations of the formation of galaxy clusters are used to inform about the expected spatial and spectral characteristics of the CR induced gamma-ray emission. A clear detection of the IC emission from shock-accelerated CR electrons will be challenging for IACTs due to the large angular extent of these accretion shocks that subtend solid angles up to six virial radii. For these instruments, the spatially concentrated pion-decay gamma-ray emission resulting from hadronic CR interactions that dominates the total gamma-ray luminosity (Pfrommer et al., 2008; Pfrommer, 2008) should be more readily detectable than the emission from the outer region.
To address the question of universality and predictability of the expected gamma-ray emission, the work of Pinzke & Pfrommer (2010) has been taken as reference. They have simulated a sample of 14 galaxy clusters that span one and a half decades in mass and show a variety of dynamical states ranging from relaxed cool-core clusters to violent merging clusters (details are given in Sect. 3.3.1). In order to find the most promising target cluster in the local Universe for detecting the pion decay emission, they computed the scaling relations between gamma-ray luminosity and cluster mass of the sample (Pfrommer, 2008) and used these to normalize the CR induced emission of all clusters in a complete sample of the X-ray brightest clusters (the extended HIFLUGCS catalogue of Reiprich & Böhringer, 2002). This favors high-mass, nearby galaxy cluster with a scaling $M_{200}^{\beta}/D_{\rm lum}^2$, where M_{200} is the virial mass[1], $D_{\rm lum}$ the luminosity

[1]The virial mass M_Δ and the virial radius R_Δ are defined as the mass and radius of a sphere enclosing a mean

distance, and $\beta \simeq 1.32$ a weakly model dependent scaling parameter that provides the rank ordering according to the brightness of each individual cluster (Pfrommer, 2008). As a second criterion, low zenith angle observations, i.e below 35 deg, are required. This ensures the lowest possible energy threshold and the maximum sensitivity for the detector. The most promising targets were carefully modeled, accounting for the measured gas density and temperatures from thermal X-ray measurements while assuming a constant CR-to-thermal gas ratio (Pfrommer & Enßlin, 2004a). Cluster-wide extended radio synchrotron emission that informs about present high-energy processes were additionally taken into account before the selection of the Perseus cluster as the most promising source. Although other clusters showed a somewhat higher gamma-ray flux in the Pinzke & Pfrommer (2010) simulations (e.g. Ophiuchus), the facts that Perseus is observable at low zenith angles and that the expected emission is more spatially concentrated make it the best suited target for this observation.

3.1.2 Dark Matter Content

Typically up to 80% of the total mass of a galaxy cluster is in the form of non-baryonic DM. Since the DM annihilation gamma-ray signal is expected to be proportional to the integrated squared DM density along the line of sight (Evans et al., 2004; Bergström & Hooper, 2006), it is obvious that galaxy clusters could be good candidates to look for DM as well (Sánchez-Conde et al., 2011; Pinzke et al., 2011). This is true despite the fact that they are located at much larger distances than other potential DM candidates, such as dwarf spheroidal galaxies satellites of the Milky Way or the Galactic Center. One obvious reason is the huge amount of DM hosted by clusters compared with the rest of candidates. Perseus, for example, is located ~1000 times farther than Milky Way dwarfs, but it contains roughly six orders of magnitude more DM than the Willman 1 dwarf galaxy, one of the most promising DM candidates according to recent works (Strigari et al., 2007; Aliu et al., 2009a). Additionally, the presence of substructures could be of crucial importance. Substructures in clusters may significantly enhance the DM signal over the smooth halo, while we do not expect this to be of special relevance for dwarf galaxies since their outer regions are severely affected by tidal stripping (Sánchez-Conde et al., 2011; Pinzke et al., 2011).

Essentially, the annihilation flux is proportional to the product of two parameters (see e.g. Evans et al., 2004 for details): a first one that captures all the particle physics (DM particle mass, cross section, etc), f_{SUSY}, and a second one, J_{astro}, that accounts for all the astrophysical considerations (DM distribution, telescope PSF, etc). The particle physics factor just acts as a normalization in the expected annihilation flux, so it can be neglected when performing a comparative study – as in this section. Concerning the astrophysical factor, the DM distribution is commonly modeled with radial density profiles of the form $\rho(r) = \rho_s/[(r/r_s)^{\gamma}\ (1 + (r/r_s)^{\alpha})^{(\beta-\gamma)/\alpha}]$, where ρ_s and r_s represent a characteristic density and a scale radius respectively (Kravtsov et al., 1998). These density profiles are well motivated by high-resolution N-body cosmological simulations. Here the Navarro-Frenk-White (Navarro et al., 1997; hereafter NFW) DM density profile, with (α,β,γ) = (1,3,1), is adopted. For a NFW profile, 90% of the DM annihilation flux comes from the

density that is $\Delta = 200$ times the critical density of the Universe.

region within r_s, so that the corresponding integrated luminosity is proportional to $r_s^3 \rho_s^2$. One can derive r_s and ρ_s for Perseus, assuming $M_{200} = 7.7 \times 10^{14}\ M_\odot$ (as given in table 3.1) and a concentration of ∼6 (as given by the Bullock et al., 2001 virial mass-concentration scaling relation). The result is $r_s = 0.384$ Mpc and $\rho_s = 1.06 \times 10^{15}\ \mathrm{M}_\odot\ \mathrm{Mpc}^{-3}$, which translates into a *total* value of $J_{\mathrm{astro}} \sim 1.4 \times 10^{16}\ \mathrm{GeV}^2\ \mathrm{cm}^{-5}$ for the scale radius region.
In the case of Coma, although slightly (∼15%) more massive than Perseus, the fact that it is located significantly farther (101 Mpc) translates into a slightly lower annihilation flux. Virgo, only 17 Mpc away from us, gives a larger DM annihilation flux, but here the large extension of the region from which most of the annihilation flux is expected to come compared with Perseus ($r_s \sim 1.2$ deg and $r_s \sim 0.3$ deg, respectively) could represent an obstacle from the observational point of view. Source extension is of special relevance for single telescope IACTs, for which point-like sources (sources with an angular extension smaller or similar to the telescope PSF) are more readily observable.

3.2 MAGIC Observation and Results

MAGIC-I observed the Perseus cluster for 33.4 hours during November and December 2008, at zenith angles between 12 deg and 32 deg, which guarantees the lowest energy threshold. The observation was performed in wobble mode pointing alternatively to two different sky directions, each at 0.4 deg distance from the nominal target position.
Part of the data have been rejected mainly due to the bad weather conditions during some observation days. The total data rejected amount to ∼ 27%, resulting in 24.4 hours effective observation time of very high data quality. Another independent analysis was performed on the data from Saverio Lombardi giving compatible results.

3.2.1 Results

Given the good data quality and the low zenith angles of observation, the analysis energy threshold results to be 80 GeV. Beyond this threshold, no significant excess of gamma-rays above the background was detected in 24.4 hours of observation. In figure 3.1, the α-plot for energies above 250 GeV, where the best integral sensitivity is obtained from a Crab Nebula data sample, is reported. A signal region $\alpha < 6$ deg and a hadronness cut of 0.05 are chosen by optimizing the analysis on a Crab Nebula data sample.
In figure 3.2, the significance map for events above 150 GeV in the observed sky region is shown. The source independent Disp method has been used. This implies the rise of the energy threshold from 80 GeV to around 150 GeV (see Domingo-Santamaria et al., 2005 for a detailed description). The significance distribution in the map is consistent with background fluctuations. In figure 3.2, X-ray contours from the *XMM-Newton* observations (Churazov et al., 2003) are also shown.
In sections 3.3 and 3.4, the implications of this observation for the CR and DM annihilation induced gamma-ray flux, respectively, will be discussed. Using the true density profile as obtained by X-ray measurements (Churazov et al., 2003), the spatial characteristics of the CR induced

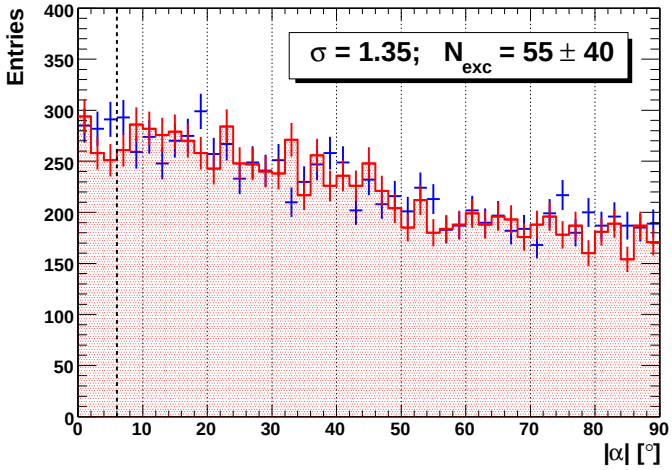

Figure 3.1: Perseus α-plot as seen by MAGIC in 24.4 hours above 250 GeV using a hadronness cut of < 0.05. The blue crosses represent the signal, the red shaded region is the background. The vertical black dotted line represents the signal region $\alpha < 6$ deg. Displayed are only events above 250 GeV since the best integral sensitivity, around 1.6% of Crab, is obtained from a Crab Nebula data sample in this energy range.

gamma-ray signal can be modeled. The Pinzke & Pfrommer (2010) simulations indicate that 60% of the total gamma-ray flux are contained within a circle of radius $r_{0.6} = 0.15$ deg (this angular scale corresponds to a physical radius of 200 kpc). The flux from within this region is compared to the upper limits. As the characteristics of the considered emission region are close to a point source, point-like upper limits are used. The same conclusion is valid also for the DM annihilation signal. In this case, as explained in section 3.1.2, the 90% of the expected emission is coming form the scale radius region. For Perseus, $r_s \sim 0.3$ deg, which is somewhat extended compared to the telescope angular resolution. However, the fact that the NFW profile is very steep implies that the main DM emission comes from the core of the source that can be considered approximately point-like compared to the MAGIC angular resolution.

To compute flux upper limits, specific spectral indices that have been motivated by an astrophysical scenario in mind (see the following sections) are assumed. This "scenario guided" approach permits to provide the tightest limits on physically motivated parameters and underlying astrophysical models. In the next sections, flux upper limits computed using a power-law gamma-ray spectrum $F \propto E^{\Gamma}$ with spectral indexes Γ of -1.5, -2.2 and -2.5 are used. In table 3.2, the corresponding integral flux upper limits for energies above 100 GeV are listed.

In section 3.3, an integral flux upper limit set above given energy thresholds are used in order to trace the energy range where models are better constrained. In table 3.3 the obtained integral flux upper limits for $\Gamma = -2.2$ are shown. Note that the integral upper limits above 80 GeV is not calculated (as a cumulative α-plot for energies above this value is not shown). This is because the gamma-hadron separation for events below 100 GeV works in a substantially different way with respect to the higher energy events. Therefore, events below 100 GeV and the events of higher energy are analyzed separately, with different sets of analysis cuts.

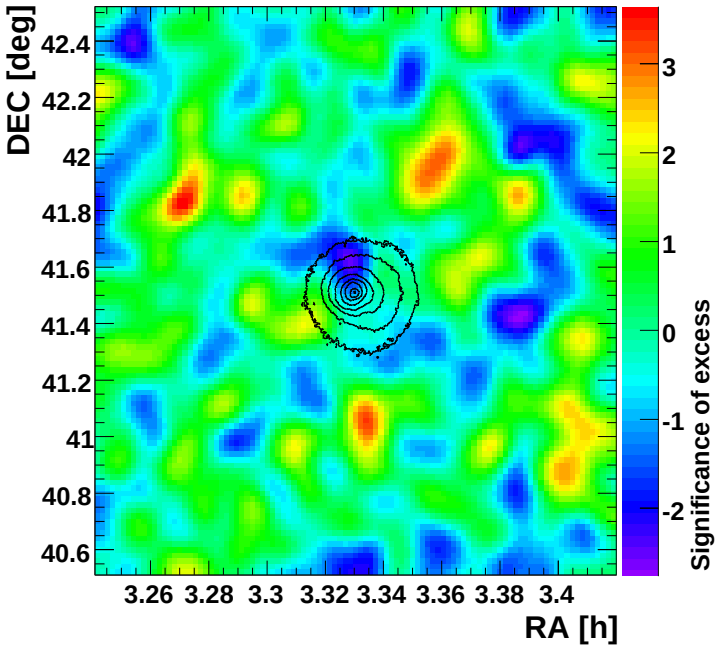

Figure 3.2: Significance map for events above 150 GeV in the observed Perseus cluster sky region. The significance distribution is consistent with background fluctuations. Black contours from *XMM-Newton* observations in the X-ray band (Churazov et al., 2003) are also shown. The angular extent of the outermost contours is approximately 0.45 deg, which corresponds to $\sim$ 610 kpc.

Finally, for completeness, in table 3.4 the differential flux upper limits for the assumed spectral indexes are shown in different energy intervals. Spectral energy density (SED) upper limits can also be obtained from those differential flux upper limits.

Γ	F_{UL} [$\times 10^{-12}$ cm^{-2} s^{-1}]
-1.5	4.63
-2.2	6.55
-2.5	7.52

Table 3.2: Integral flux upper limits for a power-law gamma-ray spectrum with spectral index Γ for energies above 100 GeV. The corresponding upper limit for the number of excess events is 186.

3.2.2 Comparison to Previous Observations

There are few existing IACT observations of galaxy clusters (Perkins et al., 2006; Perkins, 2008; Aharonian et al., 2009a,b; Domainko et al., 2009; Galante et al., 2009; Kiuchi et al., 2009; Acciari

E_{th}[GeV]	F_{UL} [$\times 10^{-12}$ cm^{-2} s^{-1}]
100	6.55
130	6.21
160	6.17
200	5.49
250	4.59
320	3.36
400	1.83
500	1.39
630	0.72
800	0.65
1000	0.47

Table 3.3: Integral flux upper limits for a power-law gamma-ray spectrum with spectral index $\Gamma = -2.2$ above a given energy threshold E_{th}.

Γ	[80-100]	[100-160]	[160-250]	[250-400]	[400-630]	[630-10^3]	[10^3-10^4]
-1.5	130.7	23.6	12.6	4.33	0.865	0.168	0.015
-2.2	144.8	25.3	13.2	4.53	0.897	0.174	0.018
-2.5	150.6	25.8	13.3	4.57	0.903	0.176	0.018

Table 3.4: Differential flux upper limits in units of 10^{-11} cm^{-2} s^{-1} TeV^{-1} for a power-law gamma-ray spectrum with spectral index Γ in energy ranges in units of GeV.

et al., 2009a). In section 3.3.3, the limits on the CR-to-thermal pressure obtained by other IACTs will be compared with those derived in this work. However, there are two observations of the Perseus galaxy cluster made by WHIPPLE (Perkins et al., 2006) and VERITAS (Acciari et al., 2009a) with which the obtained upper limits can be directly compared.
The WHIPPLE collaboration observed the Perseus galaxy cluster (Perkins et al., 2006) for $\sim$ 13 hours obtaining an integral upper limit above 400 GeV of 4.53×10^{-12} cm^{-2} s^{-1} assuming a spectral index $\Gamma = -2.1$. This value can be compared with the integral upper limit above 400 GeV of 1.83×10^{-12} cm^{-2} s^{-1} with $\Gamma = -2.2$ (see table 3.3). The MAGIC-I upper limit is significantly lower than the WHIPPLE one; clearly, this is not a surprise as the MAGIC telescope belongs to a new generation of IACTs. More recently, the VERITAS collaboration observed Perseus (Acciari et al., 2009a) for $\sim$ 8 hours and obtained an integral upper limit above 126 GeV of 1.27×10^{-11} cm^{-2} s^{-1} assuming $\Gamma = -2.5$. This value can be compared with the corresponding integral upper limit above 100 GeV of 7.52×10^{-12} cm^{-2} s^{-1} (see table 3.2). Despite the fact that the VERITAS sensitivity of about 1% of Crab Nebula (Otte et al., 2009) is better than the MAGIC-I one, the MAGIC-I upper limit is slightly better than that found by Acciari et al. (2009a) as expected from the significant difference in observation time.

3.3 Cosmic Ray Induced Emission

The upper limits on the integrated flux (table 3.3) are used to put constraints on the CR-to-thermal pressure distribution and pursue three different approaches. (1) The Pinzke & Pfrommer (2010) high-resolution hydrodynamical simulations of cluster formation and evolution are used to predict the gamma-ray emission and to obtain limits on the CR-to-thermal pressure. (2) Following Pfrommer & Enßlin (2004a), a simplified approach that assumes a constant CR-to-thermal energy density, a power-law spectrum in momentum, is used, and the resulting CR-to-thermal pressure limits are compared to those obtained by other IACT observations. (3) The observed luminosity of the radio mini-halo is used to place a lower limit on the expected gamma-ray flux in the hadronic model of the radio mini-halo. This translates into a minimum CR pressure that is crucial for disentangling the emission mechanism in the radio and provides a clear prediction for the expected gamma-ray flux.

3.3.1 Cosmological Simulations

The Pinzke & Pfrommer (2010) simulations are high-resolution cluster simulations that included radiative hydrodynamics, star formation, supernova feedback, and followed CR physics spectrally and spatially by tracing the most important injection and loss processes self-consistently while accounting for the CR pressure in the equation of motion (Pfrommer et al., 2006; Enßlin et al., 2007; Jubelgas et al., 2008). Note that the overall normalization of the CR distribution scales with the maximum acceleration efficiency at structure formation shock waves. Following recent observations at supernova remnants (Helder et al., 2009) as well as theoretical studies (Kang & Jones, 2005), they adopt a realistic value of this parameter and assume that 50% of the dissipated energy at strong shocks is injected into CRs while this efficiency rapidly decreases for weaker shocks (Enßlin et al., 2007).
Pinzke & Pfrommer (2010) computed the gamma-ray emission signal and found that it obeys a *universal spectrum and spatial distribution*. The CR distribution has a spectral index of $\Gamma \simeq -2.5$ at GeV energies and experiences a flattening towards higher energies resulting in $\Gamma \simeq -2.2$ at energies above a few TeV. Hence, the resulting gamma-ray spectrum from CR induced pion-decay shows a characteristic spectral index of $\Gamma \simeq -2.2$ in the energy regime ranging from 100 GeV to TeV. The *spatial distribution* of the CR number density is mainly governed by adiabatic transport processes (Pfrommer et al., 2007) and similarly attains an approximate universal shape relative to that of the gas density. These findings permit to reliably model the CR signal from nearby galaxy clusters using their true density profiles as obtained by X-ray measurements that are mapped onto the simulated density profiles.
In addition to CR protons, Pinzke & Pfrommer (2010) modeled relativistic electrons that have been accelerated at cosmological structure formation shocks (primary CR electrons) and those that have been produced in hadronic interactions of CRs with ambient gas protons (secondary CR electrons). Both populations of CR electrons contribute to the gamma-ray emission through Compton up-scattering photons from the CMB as well as the cumulative star light from galaxies. It turns out that the pion-decay emission of the cluster dominates over the IC contribution – in particular for relaxed systems (Pfrommer, 2008).

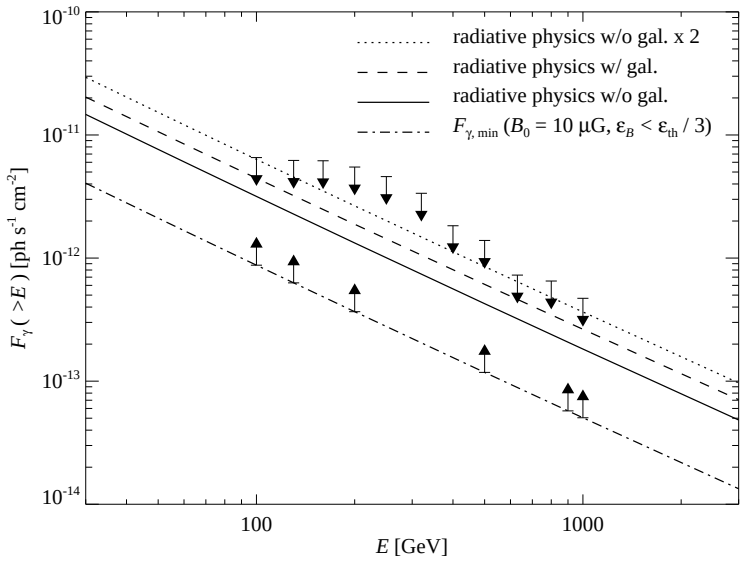

Figure 3.3: Integral flux upper limits (table 3.3) are compared with simulated integrated spectra of the gamma-ray emission from decaying neutral pions that result from hadronic CR interactions with the ambient gas in the Perseus cluster. Additionally shown are minimum gamma-ray flux estimates for the hadronic model of the radio mini-halo of the Perseus cluster (dash-dotted with minimum flux arrows, see main text for details).

In the optimistic CR model (*radiative physics with galaxies*), the cluster total gamma-ray flux within a given solid angle is calculated. In contrast, the emission from individual galaxies and compact galactic-sized objects are cut in the more conservative model (*radiative physics without galaxies*). These gas clumps dissociate incompletely in the ICM due to insufficient numerical resolution as well as so far incompletely understood physical properties of the cluster plasma. Everything contributes to the gamma-ray emission from a cluster. To assess the bias associated with this issue, the analysis is performed with both limiting cases bracketing the realistic case.
In figure 3.3, the integral flux upper limits obtained in this work (see table 3.3) are compared with the simulated flux that is emitted within a circle of radius $r_{0.6} = 0.15$ deg. The upper limits are a factor of two larger than the conservative model and a factor of 1.5 larger than the most optimistic model predictions implying consistency with the cosmological cluster simulations of Pinzke & Pfrommer (2010). Note however that the simulated flux represents a theoretical upper limit of the expected gamma-ray flux from structure formation CRs; lowering the maximum acceleration efficiency would decrease the CR number density as well as the resulting gamma-ray emission.

3.3.2 Constraints on the Cosmic Ray Pressure

In figure 3.4, the simulated gamma-ray surface brightness map of a cooling flow cluster of mass similar to Perseus is shown. As the CR induced gamma-ray flux is a radially declining function so is the CR pressure. A quantity that is of great theoretical interest is the CR pressure relative to

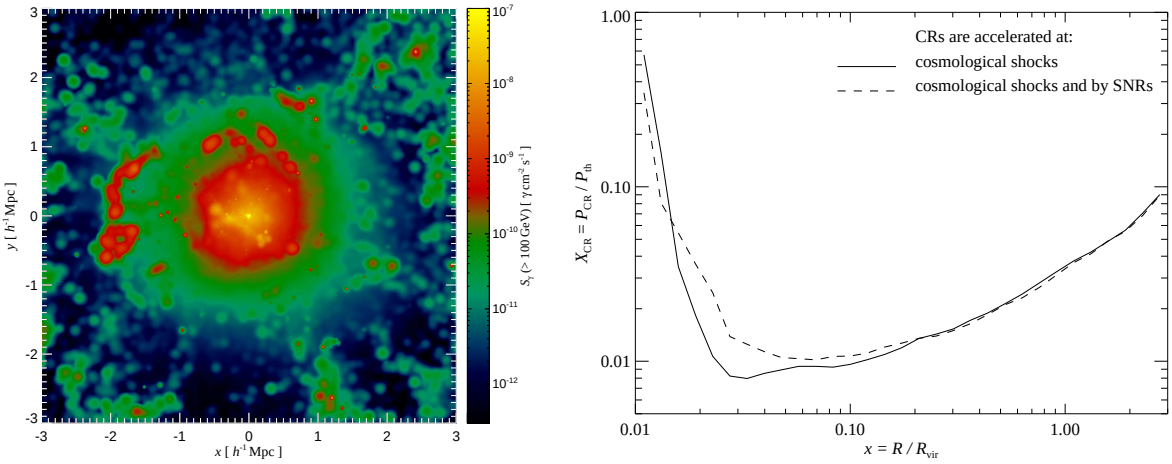

Figure 3.4: Left: simulated gamma-ray emission at energies $E > 100$ GeV from a cluster that has twice the mass as Perseus (using the simulation of the cooling flow cluster g51 from Pfrommer et al. 2008). The sum of pion-decay induced gamma-rays (which dominates the central and the total flux) and the IC emission of CR electrons accelerated at formation shocks and by hadronic CR interactions are shown. Right: profile of the CR-to-thermal pressure (volume-weighted) of this cluster (Pinzke & Pfrommer, 2010).

the thermal pressure $X_{\rm CR} = P_{\rm CR}/P_{\rm th}$ as it is a good measure of the dynamical effects of the CRs on the ICM and gives clues on the dynamical state of a cluster. On the right-hand side of figure 3.4, the profile of the CR-to-thermal pressure (volume-weighted) of this simulated cluster is shown. Moving from the periphery towards the center, this quantity is a steadily declining function until it approachs the cooling flow region around the cD galaxy of this cluster (similar to NGC 1275) where the CR pressure rises dramatically relative to that of the thermal gas which cools on a short time scale (Pfrommer et al., 2006). The volume average is $\langle X_{\rm CR}\rangle = \langle P_{\rm CR}\rangle/\langle P_{\rm th}\rangle = 0.02$, dominated by the region around the virial radius, while the ratio of CR-to-thermal energy is given by $E_{\rm CR}/E_{\rm th} = 0.032$[2]. Perseus has a smaller mass and a corresponding temperature that is only half of that of the simulated cooling flow cluster of Pinzke & Pfrommer (2010). Noting that $X_{\rm CR} \propto 1/P_{\rm th} \propto 1/kT$,[3] these values are expected to be a factor of about 2 larger in Perseus, yielding $\langle X_{\rm CR}\rangle \simeq 0.04$ for the entire cluster and $\langle X_{\rm CR}\rangle \simeq 0.02$ for the core region that is probed with the present observation.

The conservative model prediction is scaled by a factor of ~ 2 to reach the upper limits (see figure 3.3) which implies that this observation constrains the relative pressure contained in CRs to $< 8\%$ for the *entire cluster* and to $< 4\%$ for the *cluster core region*. The presence of dense

[2]Note that for a CR population in clusters that have been accelerated in structure formation shocks the relativistic limit $E_{\rm CR}/E_{\rm th} = 2\langle P_{\rm CR}\rangle/\langle P_{\rm th}\rangle$ is not applicable since the CR pressure is dominated by the trans-relativistic regime. This implies a somewhat harder equation of state for the CRs with a larger adiabatic index and yields the relation $E_{\rm CR}/E_{\rm th} = 1.6\langle P_{\rm CR}\rangle/\langle P_{\rm th}\rangle$.

[3]This relation only holds for regions with long thermal cooling times compared to the dynamical time scale. In particular it breaks down towards the center of a cooling flow cluster where the thermal gas cools on a shorter time scale such that the forming cooling flow causes adiabatic contraction of the CR population.

gas clumps potentially biases the simulated gamma-ray flux high and hence the inferred limits on $X_{\rm CR}$ low. Another source of bias could be unresolved point sources inside the cluster such as active galactic nuclei (AGN). In the presented simulation of the cool core cluster g51, the bias due to subclumps amounts to a factor of 1.5 but it could be as high as 2.4 which is the mean difference between the conservative and optimistic model across the Pinzke & Pfrommer (2010) scaling relations. Note however that the latter case is already excluded by the pesent upper limits provided the maximum shock acceleration efficiency is indeed as high as 50%. While there are indications from supernova remnant observations of one rim region (Helder et al., 2009) as well as theoretical studies (Kang & Jones, 2005) that support such high efficiencies, to date it is not clear whether these efficiencies apply in an average sense to strong collisionless shocks or whether they are realized for structure formation shocks at higher redshifts.
In figure 3.4, a simulation where CRs are acceleratesd only at structure formation shocks is compared with one where CRs are additionally injected through supernova feedback within the star forming regions of the Pinzke & Pfrommer (2010) simulations. Outside the cD galaxy, there is no significant visible difference which suggests that the CRs injected into the ICM by supernova driven winds are negligible compared with those accelerated by structure formation shocks. While this is partly an artifact of the simulations that neglect CR diffusion, this behavior is expected due to the adiabatic losses that CRs suffer as they expand from the compact galactic ISM into the dilute ICM.

3.3.3 Simplified Approach and Comparison to Previous Results

There are few existing IACT observations of galaxy clusters, some of which derived limits on the CR-to-thermal pressure contained in clusters, in particular the WHIPPLE observation of the Perseus cluster (Perkins et al., 2006) and the HESS observations of the Abell 85 (Aharonian et al., 2009a; Domainko et al., 2009) and Coma (Aharonian et al., 2009b) clusters. These work used simplifying assumptions about the spectral and spatial distribution of CRs. They typically assumed a single CR power-law distribution with a spectral index of $\Gamma = -2.1$ (that provides optimistic limits on the CR-to-thermal pressure) and assumed that the CR energy density is a constant fraction of the thermal energy density throughout the entire cluster. Based on these two assumptions, WHIPPLE and HESS found in Perseus and Abell 85 $E_{\rm CR}/E_{\rm th} < 0.08$, respectively, while HESS found $E_{\rm CR}/E_{\rm th} < 0.2$ in Coma.
To facilitate comparison with these earlier works, the data analysis is repeated with a spectral index $\Gamma = -2.1$ obtaining an integral upper limit of $\mathcal{F}_{\rm UL}(> 100\,{\rm GeV}) = 6.22 \times 10^{-12}\,{\rm cm}^{-2}\,{\rm s}^{-1}$. Following the formalism of Pfrommer & Enßlin (2004a), the gamma-ray flux of a CR population with $\Gamma = -2.1$ is computed within a circular region of radius $r_{0.6} = 0.15$ deg or equivalently 200 kpc. In the *isobaric model of CRs*, the CR pressure is assumed to scale exactly as the thermal pressure and constrain $E_{\rm CR}/E_{\rm th} < 0.053$ which corresponds to an averaged relative pressure of $\langle X_{\rm CR}\rangle = \langle P_{\rm CR}\rangle/\langle P_{\rm th}\rangle = 0.033$. In the *adiabatic model of CRs*, the centrally enhanced CR number density due to adiabatic contraction during the formation of the cooling flow (Pfrommer & Enßlin, 2004a) is taken into account. The CRp population is assumed to scale originally as the thermal population but was compressed adiabatically during the formation of the cooling flow without relaxing afterwards (temperature and density profiles are

taken from Churazov et al., 2003). In this model, an enhanced gamma-ray flux level for virtually the same volume averaged CR pressure (or vice versa) is obtained for a given flux limit, hence one can put a tighter constraint on the averaged CR pressure. Therefore, the present observation constrains $E_{\rm CR}/E_{\rm th} < 0.03$ which corresponds to an averaged relative pressure of $\langle X_{\rm CR}\rangle = \langle P_{\rm CR}\rangle/\langle P_{\rm th}\rangle = 0.019$.
How these tighter limits can be reconciled with the simulation based slightly weaker limit? The simulated CR profile has to be compared to a CR distribution that does not show any enhancement relative to the gas density. In the central region for $r < 200$ kpc, the adiabatic compression factor of 1.7 matches that in the simplified approach – suggesting that the simple adiabatic model captures the underlying physics quite realistically. Secondly, the pressure of a power-law spectrum with $\Gamma = 2.1$ has to be related to the simulated concave spectrum of Pinzke & Pfrommer (2010). Noting that the gamma-rays at 100 GeV are produced by CR protons at $\simeq 1$ TeV, both spectra are normalized at 1 TeV and one finds that the simulated spectrum contains a larger pressure by a factor of 1.8. This factor brings the limit of the simplified adiabatic model into agreement with the simulation-based limit of the relative CR pressure $\langle X_{\rm CR}\rangle < 4\%$ for the *cluster core region*. Finally, since gamma-ray observations are only sensitive to the cluster core regions (the emission is expected to peak in the center due to the high target gas densities), they cannot constrain the average CR-to-thermal pressure within the entire cluster. Hence cosmological cluster simulations are used to address how much CR-to-thermal pressure could be additionally hidden in the peripheral cluster regions.

3.3.4 Minimum gamma-ray Flux

For clusters that host radio (mini-)halos, a minimum gamma-ray flux in the hadronic model of CR interactions can be derived. The idea is based on the fact that a steady state distribution of CR electrons loses all its energy to synchrotron radiation for strong magnetic fields ($B \gg B_{\rm CMB} \simeq 3.2\mu$G) so that the ratio of gamma-ray to synchrotron flux becomes independent of the spatial distribution of CRs and thermal gas (Pfrommer, 2008). This can be easily seen by considering the pion decay induced gamma-ray luminosity L_γ and the synchrotron luminosity L_ν of a steady state distribution of CR electrons that has been generated by hadronic CR interactions:

$$L_\gamma = A_\gamma \int {\rm d}V\, n_{\rm CR} n_{\rm gas}, \tag{3.1}$$

$$L_\nu = A_\nu \int {\rm d}V\, n_{\rm CR} n_{\rm gas} \frac{\varepsilon_B^{(\alpha_\nu+1)/2}}{\varepsilon_{\rm CMB}+\varepsilon_B} \tag{3.2}$$

$$\simeq A_\nu \int {\rm d}V\, n_{\rm CR} n_{\rm gas} \quad \text{for } \varepsilon_B \gg \varepsilon_{\rm CMB}. \tag{3.3}$$

where A_γ and A_ν are dimensional constants that depend on the hadronic physics of the interaction (see chapter 6, Pfrommer et al., 2008 and Pfrommer, 2008) and $\alpha_\nu \simeq 1$ is the observed synchrotron spectral index. Hence a minimum gamma-ray flux in the hadronic model ca be derived as:

$$\mathcal{F}_{\gamma,\mathrm{min}} = \frac{A_\gamma}{A_\nu}\frac{L_\nu}{4\pi D_{\mathrm{lum}}^2} \tag{3.4}$$

where L_ν is the observed luminosity of the radio mini-halo and D_{lum} denotes the luminosity distance to the respective cluster. Lowering the magnetic field would require an increase in the energy density of CR electrons to reproduce the observed synchrotron luminosity and thus increase the associated gamma-ray flux.

Using the values of table 3.1, the minimum gamma-ray flux in the hadronic model of the radio mini-halo results to be $\mathcal{F}_{\gamma,\mathrm{min}}(> 100\,\mathrm{GeV}) = 6 \times 10^{-13}\mathrm{cm}^{-2}\,\mathrm{s}^{-1}$, assuming a power-law CR distribution with $\Gamma \gtrsim -2.3$. This lower limit is independent of the spatial distribution of CRs and magnetic fields. Note that the spectral index is consistent with the radio data. It turns out that the requirement of strong magnetic fields violates the energy conditions in clusters as it implies a magnetic energy density that is larger than the thermal energy density – in particular at the peripheral cluster regions. The minimum gamma-ray flux condition requires a constant (large) magnetic field strength throughout the cluster while the thermal energy density is decreasing by more than a factor of 100 from its central value. This would imply that the magnetic field eventually dominates the energy density at the virial regions. Such a configuration would be impossible to achieve in first place as the magnetic energy density typically saturates at a fixed fraction of the turbulent energy density which itself is only a small fraction of the thermal energy density in clusters (Schuecker et al., 2004). Hence these considerations call for lowering the assumed cluster magnetic fields which should strengthen the lower limits on the gamma-ray flux considerably – however at the expense that these limits inherit a weak dependence on the spatial distribution of magnetic fields and CRs.

Estimates of magnetic fields from Faraday rotation measures (RMs) have undergone a revision in the last few years with more recent estimates typically in the order of a few μG with slightly higher values up to 10 μG in cooling flow clusters (Clarke, 2004; Enßlin & Vogt, 2006). For the Perseus radio mini-halo, Faraday RMs are available only on very small scales (Taylor et al., 2006), i.e. few tens of pc. RM estimates are of the order of ~ 7000 rad m^2 leading to magnetic field values of $\sim 25\mu$G assuming the Faraday screen is localized in the ICM. This, however, appears to be unlikely as variations of 10% in the RM are observed on pc-scales (Taylor et al., 2002), while ICM magnetic fields are expected to be ordered on significantly larger scales of a few kpc (Taylor et al., 2006; Vogt & Enßlin, 2005; Enßlin & Vogt, 2006). Application of the classical minimum-energy argument to the Perseus radio mini-halo data leads to estimates for the central magnetic field strength of $B_0 \simeq 7\mu$G or even $B_0 \simeq 9\mu$G for the more appropriate hadronic minimum-energy argument (Pfrommer & Enßlin, 2004b).

The cooling flow cluster g51, morphologically similar to Perseus and with a mass $M_{200} \simeq 10^{15}\,\mathrm{M}_\odot$, is selected from the Pinzke & Pfrommer (2010) sample. The central magnetic field strength is conservatively taken as $\sim 10\mu$G and the magnetic energy density is parametrized in terms of the thermal energy density by $\varepsilon_B \propto \varepsilon_{\mathrm{th}}^{0.5}$ which ensures $\varepsilon_B < \varepsilon_{\mathrm{th}}/3$ in the entire cluster. This permits to strengthen the physically motivated lower limit to $\mathcal{F}_{\gamma,\mathrm{phys.\,min}}(> 100\,\mathrm{GeV}) = 8.5 \times 10^{-13}\,\mathrm{cm}^{-2}\,\mathrm{s}^{-1}$ as shown by the dash-dotted line in figure 3.3. In the hadronic model, this minimum gamma-ray flux implies a minimum CR pressure relative to the thermal pressure. Figure 3.3 shows that the minimum flux $\mathcal{F}_{\gamma,\mathrm{phys.\,min}}$ is a factor of 3.6 lower than the

simulated flux for Perseus in the conservative model. As seen in Sect. 3.3.2, this model corresponds to a relative CR pressure of $\langle X_{\rm CR}\rangle = \langle P_{\rm CR}\rangle/\langle P_{\rm th}\rangle = 0.04$ where the averages represent volume averages across the entire cluster. Hence a minimum relative CR pressure of $\langle X_{\rm CR,\,min}\rangle = \langle P_{\rm CR,\,min}\rangle/\langle P_{\rm th}\rangle/3.6 = 0.01$ is obtained. This minimum CR pressure corresponds to a minimum total CR energy of $E_{\rm CR\,min} = E_{\rm CR\,min}/E_{\rm th} \times E_{\rm th} = 1.6\,\langle X_{\rm CR,\,min}\rangle \times E_{\rm th} = 9 \times 10^{61}$ erg where the temperature and density profiles are integrated from X-ray observations (Churazov et al., 2003) to obtain the total thermal energy of $E_{\rm th} = 5.7 \times 10^{63}$ erg. These considerations show the huge potential of combining future TeV gamma-ray and radio observations in constraining physical models of the non-thermal cluster emission and to obtain important insights in the average distribution of cluster magnetic fields.

3.4 Dark Matter Annihilation

As discussed in section 3.1.2, the expected DM annihilation flux is proportional to the product of a factor that encloses all the particle physics and a second one that accounts for all the involved astrophysics. Therefore, in order to obtain an estimate of the annihilation flux, one needs to choose a particular particle physics model in addition to the modeling of the DM distribution. Although the uncertainties in the particle physics factor $f_{\rm SUSY}$ are very large and spread over some orders of magnitude (see e.g. Albert et al., 2008d), it is common to use the most optimistic value for a given energy threshold of the telescope. This factor just acts as a rescaling factor in the total flux, so one could change to another particle physics model simply by rescaling for its new value. Here it is assumed to be $f_{\rm SUSY} = 10^{-32}$ GeV^{-2} cm^3 s^{-1} above 100 GeV, which corresponds to one of the most optimistic allowed scenarios with the neutralino as DM particle (Sánchez-Conde et al., 2007). Taking than a value of 1.4×10^{16} GeV^2 cm^{-5} for the integrated astrophysical factor inside r_s, as given in section 3.1.2, the maximum DM annihilation flux for energies above 100 GeV is about 1.4×10^{-16} cm^{-2} s^{-1}. The comparison with the upper limits obtained by this observation is not very constraining. Assuming a generic DM annihilation spectrum without cutoff and spectral index -1.5 as a good approximation (e.g. Albert et al., 2008d; Aliu et al., 2009a), it can be seen from table 3.2 that a boost in flux of the order of 10^4 is needed to reach the predicted DM annihilation flux values, since $\mathcal{F}_{\rm UL}$ (>100 GeV) = 4.63×10^{-12} cm^{-2} s^{-1}.
This boost factor could come from different uncertainties that may enhance the annihilation gamma-ray flux notably and that were not taken into account in the above calculation. One of them, the presence of substructures, could play a crucial role for Perseus, as explained in section 3.1.2. As shown in Sánchez-Conde et al. (2011), its effect could enhance the expected annihilation flux by a factor of about 30 for Perseus-size halos. Pinzke et al. (2011), using a different formalism, found substructure boost factors as high as 10^3. However, with IACTs it is challenging to make use of these large boost factors as their contribution is spread on large angular scales up to the virial extend of the cluster. Finally, also recently proposed mechanisms in the particle physics side, such as the internal bremsstrahlung (Bringmann et al., 2008) and the Sommerfeld effect (Lattanzi & Silk, 2009; Pinzke et al., 2009), could enhance the DM annihilation flux by more than one order of magnitude for some particle physics models.
It is worth noting that the result obtained here for the boost factor needed in order to probe

the predicted DM annihilation flux is comparable with previous observations of the Milky Way satellite galaxies (Albert et al., 2008d; Aliu et al., 2009a).

3.5 Conclusions

The Perseus cluster was observed by MAGIC-I during November and December 2008 resulting in 24.4 hours effective observation time of very high data quality. No significant excess of gamma-ray was detected above the energy threshold of 80 GeV.
Using simplified assumptions (power-law CR spectra, constant ratio of CR-to-thermal energy density) that have been adopted in earlier work, a limit on the CR energy of $E_{\rm CR}/E_{\rm th} < 5\%$ is derived. This limit could be tightened furthermore by considering an adiabatically contracted CR population during the formation of the cooling flow yielding $E_{\rm CR}/E_{\rm th} < 3\%$. Using cosmological cluster simulations, it turns out that these assumptions are not fulfilled for CR populations that have been accelerated by structure formation shocks: while the adiabatic model seems to match the simulated CR profiles towards the center very well, the expected ratio of CR-to-thermal pressure is increasing towards the peripheral cluster regions causing the volume averaged pressure across the entire cluster to increase by a factor of two. In addition, the CR spectral distribution shows a concave curvature with a spectrum that flattens towards high energies with a spectral index of $\Gamma \simeq -2.2$ in the TeV regime. This implies that the CR pressure is enhanced by an additional factor of almost two. Using the prediction from Pinzke & Pfrommer (2010) simulations, the upper limit on the CR-to-thermal pressure averaged across the *entire cluster volume* is $\langle X_{\rm CR} \rangle < 8\%$ and it is $< 4\%$ for the *cluster core region*. This corresponds to an upper limit on the CR energy of $E_{\rm CR}/E_{\rm th} < 13\%$ and $< 6.5\%$, respectively. Note that this is the first work where results from cosmological simulations and observational data analysis were combined. This demonstrates the need for cosmological simulations in order to make more reliably predictions on CR spectra providing a safeguard against too simplified and optimistic models leading to limits that are too tight.
The upper limits resulting from the data analysis are a factor of $\simeq 2$ larger than the conservative model prediction for the CR induced gamma-ray emission and hence in agreement with the cosmological cluster simulations of Pinzke & Pfrommer (2010). Using minimum gamma-ray flux arguments show that improving the sensitivity of this observation by a factor of about seven would permit to critically test the hadronic model for the Perseus radio mini-halo. Note however that the new hadronic model developed in chapter 6 of this thesis is characterized by a wider parameter space with respect to previous models, as the one used here, and therefore even deeper observations may be needed to test it.
As DM dominates the cluster mass, significant gamma-ray emission resulting from its annihilation is also expected. With the assumed particle physics model, one of the most optimistic allowed scenarios (Sánchez-Conde et al., 2007) with the neutralino as DM particle, the boost factor for the typically expected DM annihilation induced emission is constrained to $< 10^4$. Note that possible contributions from internal bremsstrahlung, Sommerfeld enhancement as well as boost factors due to substructures are neglected in the presented calculation.

Chapter 4

The MAGIC Stereoscopic System Observation of the Perseus Galaxy Cluster

Would you believe it, Ariadne?
The Minotaur scarcely defended himself.
Jorge Luis Borges

This chapter is dedicated to the results of the Perseus cluster *stereo* observation campaign performed with the MAGIC telescopes from October 2009 to February 2011 for a total effective time of 84.5 hours. This chapter is divided in three parts. The first two parts describe the detections of the head-tail galaxy IC 310 and of the central radio galaxy NGC 1275, while the last part presents the implications of the whole observation campaign for the cluster CR induced emission.
The work presented in this chapter has been published in three separated articles. The IC 310 serendipitous detection has been published with the title *Detection of very high energy gamma-ray emisson from the Perseus cluster head-tail galaxy IC 310 by the MAGIC telescopes* in the Astrophysical Journal Letters in 2010 (APJ Letters, 723, L207, 2010; Aleksić et al., 2010b). I am the corresponding author of this publication together with Julian Sitarek and Saverio Lombardi. The NGC 1275 detection has been published with the title *Detection of very-high energy gamma-ray emission from NGC 1275 by the MAGIC telescopes* in the Astronomy & Astrophysics Letters in 2012 (A&A Letters, 539, L2, 2012; Aleksić et al., 2012b). I am the corresponding author of this publication together with Saverio Lombardi, Pierre Colin and Dorothee Hildebrand. Finally, the implications of the whole observation campaign for the cluster CR induced emission have been published with the title *Constraining Cosmic Rays and Magnetic Fields in the Perseus Galaxy Cluster with TeV observations by the MAGIC telescopes* in the Astronomy & Astrophysics Journal in 2012 (A&A, 541, A99, 2012; Aleksić et al., 2012a). I am the corresponding author of this publication together with Christoph Pfrommer, Pierre Colin, Anders Pinzke and Saverio Lombardi. I was the P.I. of the Perseus cluster campaign proposal and co-P.I. of the NGC 1275 proposal. My main contributions to these articles are the MAGIC data analysis and the paper writing. I also substantially contributed to the theoretical interpreation of the obtained results.

4.1 The Detection of the Head-Tail Galaxy IC 310

Most of the presently known extragalactic very high energy (VHE, > 100 GeV) gamma-ray emitters (~40) are blazars (Urry & Padovani, 1995). So far only two radio galaxies, M 87 (Aharonian et al., 2003) and Cen A (Aharonian et al., 2009c), and two starburst galaxies, NGC 253 (Acero et al., 2009) and M82 (Karlsson et al., 2009), have been clearly identified in this energy range.
IC 310 ($z = 0.019$) is a head-tail radio galaxy located in the Perseus cluster at 0.6 deg (corresponding to ~ 1Mpc) from the central galaxy NGC 1275. Head-tail radio galaxies display a radio morphology consisting of a bright head, close to the optical galaxy, and a fainter elongated tail. In the standard explanation, the jets are bent towards one direction creating the "head" structure. At larger distances they fan out in a characteristic tail that extends over many tens to hundreds of kpc. When the ICM flow impacting these galaxies (in their rest frame) is super-sonic (Mach number larger than 1), the ram pressure of the ICM causes the jets to bend (Begelman et al., 1979). If the flow is trans-sonic (Mach number ~ 1), the thermal pressure gradient of the interstellar medium of these galaxies, due to their motion through the ICM, determines the bending (Jones & Owen, 1979). In this last model, the inflow is decelerated and heated by a bow shock in front of the galaxy, which also generates a turbulent wake that re-accelerates the relativistic particle population in the tail and illuminates the tail.
The radio contours of IC 310 show an extended emission, pointing away from the direction of NGC 1275. The length of this tail measured in radio varies between 0.12 deg and 0.27 deg (Sijbring & de Bruyn, 1998; Lal & Rao, 2005). The X-ray image of IC 310 observed by *XMM-Newton* is compatible with a point-like emission from the core and with no X-ray emission from its extended radio structure (Sato et al., 2005). Interestingly, Sato et al. (2005) also showed that the X-ray emission may originate from the central AGN of the BL Lac-type object. Other observed characteristics of IC 310 (e.g. no strong emission lines, spectral indexes in radio and X-ray) suggest that it may also be a dim (weakly beamed) blazar (Rector et al., 1999).
The LAT instrument on board the *Fermi* satellite (Atwood et al., 2009) has recently detected IC 310 (Neronov et al., 2010) with 5 (3) photons above 30 GeV (above 100 GeV). At lower energy (i.e. from 100 MeV to 1 GeV), only the central galaxy NGC 1275 is visible (Abdo et al., 2009; Neronov et al., 2010). This triggered the interest of the MAGIC collaboration which resulted in the IC 310 serendipitous detection in the Perseus data collected from November 2008 to February 2010 presented here.

4.1.1 Observation and Analysis

The MAGIC-I telescope observed the Perseus cluster for a total of 94 hours between November 2008 and February 2010. The analysis of the 33.4 hours of data taken in 2008 is presented in the previous chapter (Aleksić et al., 2010a) and focused on the physics of the Perseus cluster. Note that the skymap presented in chapter 3, figure 3.2, does not show significant excesses from the IC 310 position. Since the end of October 2009 the second MAGIC telescope was also taking data, allowing the stereoscopic analysis.
Observations were performed in wobble mode with data equally split in two pointing positions offset by 0.4 deg from the direction of NGC 1275. IC 310 was in the field of view at the angular

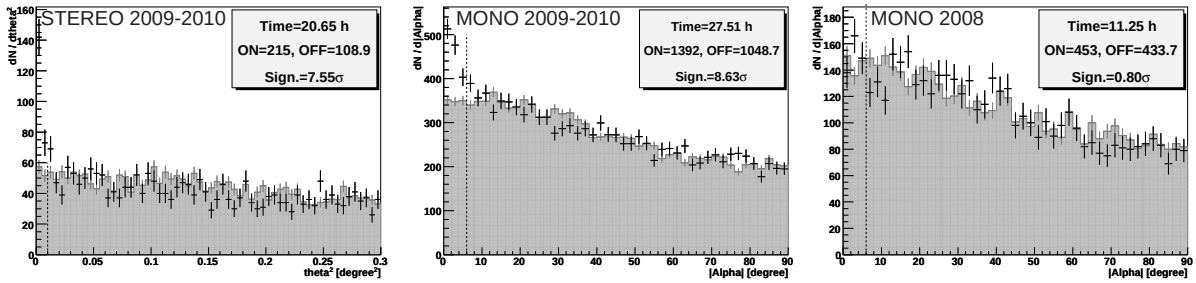

Figure 4.1: θ^2-distribution of the IC 310 signal and background estimate from stereo observations taken between October 2009 and February 2010 (left panel). α-distribution from mono observations taken between September 2009 and February 2010 (middle panel), and November-December 2008 (right panel). Only the pointing position 0.25 deg away from IC 310 is used. The cuts result in an energy threshold (defined as a peak of the differential MC energy distribution) of $\sim$ 260 GeV for both mono and stereo data (see the text for details).

distance of 0.25 deg and 1 deg for individual wobble positions. Since the gamma-ray collection area in the latter case is significantly lower (by a factor of $\sim$ 3), only data with 0.25 deg offset are used here for the signal search and for obtaining the spectrum and the light curve. The mono and stereo data are analyzed separately. The mono and stereo are only partially independent systems, differing in the analysis method, thus there can be some residual systematic error between them. Additionally, IC 310 was not observed in the standard wobble observation mode; this increases the systematic error from the background estimate. Independent analyses were performed on the data also from Julian Sitarek and Saverio Lombardi giving compatible results.
Finally, *Fermi* data taken during the period between 2008 August 4 and 2010 July 15 has also been analyzed in collaboration with the authors of Neronov et al. (2010).

4.1.2 Results

A final sample of 20.6 hours of stereo data, after the data quality check, is obtained for the period from October 2009 to February 2010. The θ^2-distribution of the signal coming from IC 310 and the background estimation are shown in figure 4.1 (left panel). The source is detected with 7.6 σ significance.
The source is also detected in the 27.5 hours of mono data (September 2009 – February 2010) with a significance of 8.6 σ. Note that since part of the MAGIC-I data set are also used in the stereo analysis, the two significances are not completely independent. The corresponding α-distribution is also shown figure 4.1 (middle panel). The different signal significance obtained in stereo (7.6σ) is similar to the one of mono scaled to the same observation time ($8.6\sigma \times \sqrt{20.6\,\mathrm{hr}/27.5\,\mathrm{hr}} = 7.5\sigma$). This is because the mono data have been taken over a longer time period, including a higher emission state in October 2009 (see below). Moreover, in the significance calculated according to Li & Ma (1983), for a high signal-to-background ratio (as in the case of excellent gamma-hadron separation obtained in stereo observations), the background is overestimated and this lowers the significance. A perfectly known background of N_{back} events

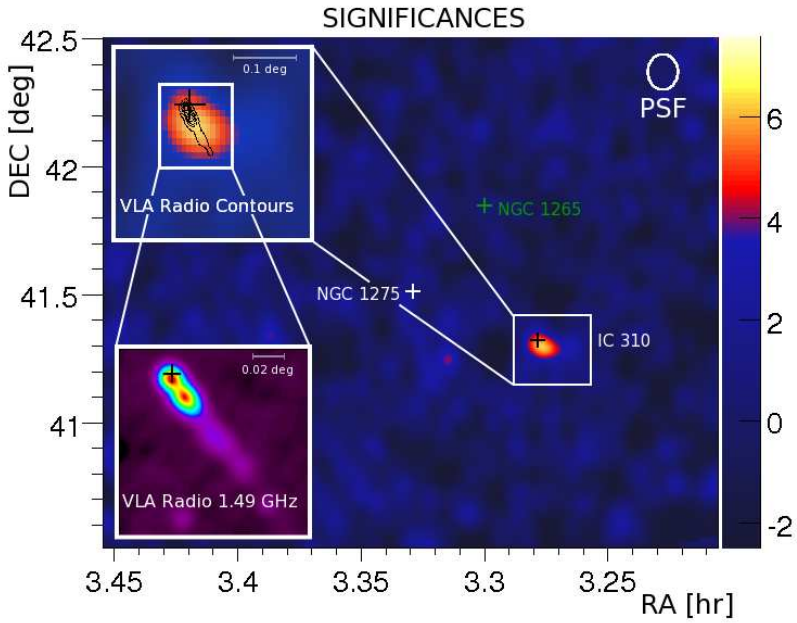

Figure 4.2: Significance skymap from the MAGIC stereo observation (42 hours; both pointing positions) for energies above 400 GeV. An enlargement of the IC 310 region overlaid with the NVSS (NRAO VLA Sky Survey at 1.49 GHz; Condon & Broderick, 1988) contours (top left inserted panel), and the corresponding image (bottom left inserted panel), are also shown. The NVSS data were obtained with *Aladin* (Bonnarel et al., 2000). Positions of IC 310, NGC 1275 and NGC 1265 are marked with black, white, and green crosses respectively.

will fluctuate with an RMS of $\sqrt{N_{back}}$, thus a significance of a weak signal of N_{EX} events can be approximated by $N_{EX}/\sqrt{N_{back}}$. This formula scaled to the same observation time gives a higher value for stereo, 10.2, than for mono, 9.2, observations.

It is interesting to note that the 11.2 hours of good quality, mono data taken at the end of 2008 do not show any significant excess at the position of IC 310 (see figure 4.1, right panel). These data yield an upper limit for the flux $F(> 300\text{GeV}) < 1.9\%$ CU.[1]

In figure 4.2, the significance skymap of the Perseus cluster region above 400 GeV is shown. The bright spot is consistent with the position of IC 310. In the panels inserted in figure 4.2, archival (non-simultaneous) IC 310 VLA radio data (Condon & Broderick, 1988) are also shown.

The MAGIC stereo observations reveal a flat SED between 150 GeV and 7 TeV without any visible curvature or cut-off as shown in figure 4.3. The differential flux dN/dE in units of $\text{cm}^{-2}\text{s}^{-1}\text{TeV}^{-1}$ is well described by a pure power law as $(1.1 \pm 0.2) \times 10^{-12}(E/\text{TeV})^{-2.00\pm0.14}$ ($\chi^2/n_{dof} = 2.3/4$). The mean gamma-ray flux above 300 GeV obtained from the stereo observations between October 2009 and February 2010 is $(3.1 \pm 0.5) \times 10^{-12}$ cm^{-2} s^{-1}, corresponding to $(2.5 \pm 0.4)\%$ CU. Comparing this with the upper limit from the 2008 data suggests variability of

[1] CU stands for Crab Units defined as the fraction of the Crab Nebula flux defined by eq. 2 of Albert et al. (2008c), that corresponds, e.g. for energies above 300 GeV, to 12.4×10^{-11} cm^{-2} s^{-1}.

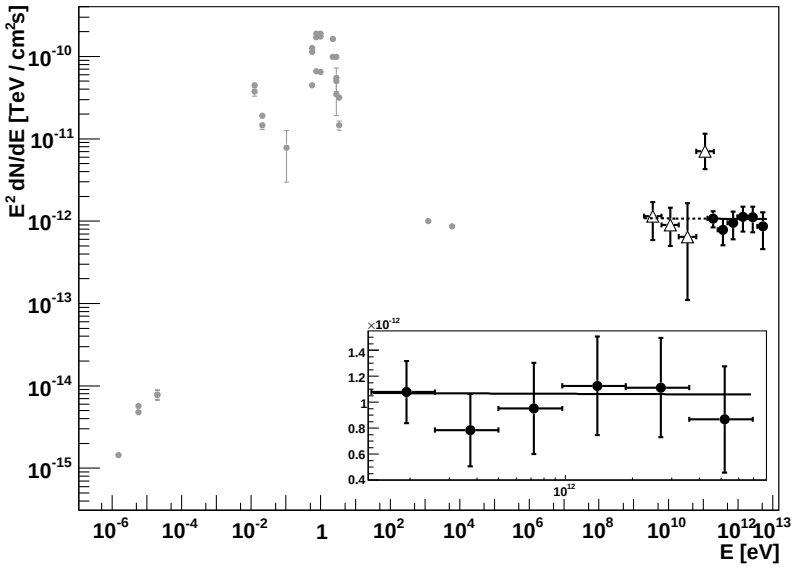

Figure 4.3: SED of IC 310 obtained with 20.6 hours of the MAGIC stereo data (full circles). Open triangles show the flux measurements from the *Fermi*-LAT from its first two years of operation. Archival X-ray (Sato et al., 2005), optical (Zwicky & Kowal, 1968), infrared (Knapp et al., 1989) and radio (Gregory & Condon, 1991; Becker et al., 1991; Condon et al., 2002; White & Becker, 1992; Douglas et al., 1996) data obtained from the NED database are shown with grey dots. The solid line shows a power law fit to the MAGIC data, and the dotted line is its extrapolation to GeV energies. A zoom-in of the MAGIC points is also shown.

IC 310 on a one-year time scale.

The light curves of the IC 310 gamma-ray emission above 300 GeV obtained both with the mono and stereo data are presented in figure 4.4. Hints of variability can be seen in the data. Fitting the individual light curves assuming constant flux yields $\chi^2/n_{dof} = 27.6/7$ (for mono, corresponding to 3.5σ) and $17.5/4$ (for stereo, corresponding to 3.0σ). The largest deviations from the mean value are for the intervals 13 – 14 October 2009 (3.1 σ in mono above the mean flux), and 9 – 16 November 2009 (3 σ in mono, 3.2 σ in stereo above the mean flux).

Until February 2010, the *Fermi*-LAT instrument observed only three photons with energies above 100 GeV from the direction of IC 310 (Neronov et al., 2010). It is interesting to note that one of those gamma-rays was observed on 15th of October, nearly coincident with the higher flux seen in mono. The standard *Fermi* likelihood analysis gave a "Test Statistics" value of 79 from IC 310 above 1 GeV (corresponding to a $\sim 9\ \sigma$ detection) [2]. Assuming a simple power law for the spectrum, a differential flux of $dN/dE = (9.5 \pm 2.9) \times 10^{-9}\,(E/10\mathrm{GeV})^{-1.58\pm0.25}\mathrm{cm}^{-2}\,\mathrm{s}^{-1}\,\mathrm{TeV}^{-1}$ is obtained. The *Fermi* spectral index is very hard, mostly due to the last point.

[2] Note that this significance is not calculated according to the Li & Ma (1983) method.

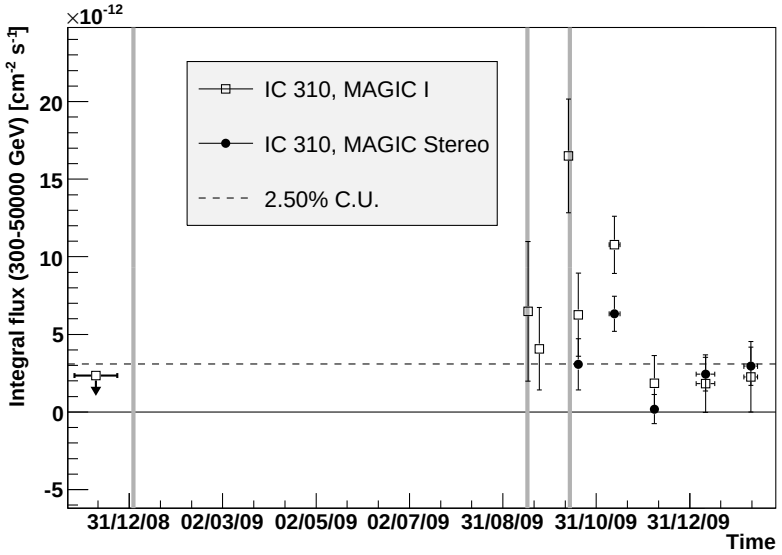

Figure 4.4: Light curve (in 10-day bins) of the gamma-ray emission above 300 GeV obtained with the mono (open squares) and the stereo (full circles) MAGIC data. The open square with an arrow is the upper limit on the emission in November-December 2008. Vertical grey lines show the arrival times of > 100 GeV photons from the *Fermi*-LAT instrument. The horizontal dashed line is a flux level of 2.5% CU.

4.1.3 Discussion

The MAGIC angular resolution is not sufficient to determine the location of the VHE emission region within the radio galaxy. Therefore, it is not clear whether the observed gamma-ray emission is connected with the tail of the source or if it is produced at the base of the jet, close to the central engine of the source (as in blazars). The strong indications of variability disfavor the gamma-ray production at the bow shock, discussed by Neronov et al. (2010), because in this case the emission should be steady on time scales of thousands of years. Variability with a time scale of a year (a week) constrains the size of emission region to be $\lesssim 10^{18}$ cm ($\lesssim 2 \times 10^{16}$ cm) across, assuming no Doppler boosting of the flux, which is much smaller than the total size of the tail ($\sim 10^{24}$ cm). Additionally, one can estimate the mass of the central black hole, $M_{\rm BH}$, of an active galaxy using the correlation between black hole mass and the central velocity dispersion of the host galaxy (Tremaine et al., 2002). The measured velocity dispersion in IC 310 (230 km/s, McElroy, 1995) yields $M_{BH} = 2.4 \times 10^8 M_\odot$, corresponding to a Schwarzschild radius of $R_{SH} = 7 \times 10^{13}$ cm. This indicates that the most probable location of the gamma-ray emission region is in the innermost part of the jet (as e.g. for M 87, see Acciari et al., 2009b).

The extrapolation of the IC 310 spectrum obtained with the MAGIC telescopes is in good agreement with the *Fermi* spectrum below 60 GeV. On the other hand, there is a large deviation in the highest energy bin measured by *Fermi* (see figure 4.3). The gamma-ray flux from MAGIC observations in this energy bin predicts 0.6 photons, while 4 photons were observed by *Fermi*-LAT. Assuming a Poisson distribution, the probability of obtaining ≥ 4 photons is 3.4×10^{-3}

(corresponding to 2.7 standard deviations) so the discrepancy may be a statistical fluctuation. However, *Fermi*-LAT, having an energy resolution of $\sim$ 10%, observed 3 of the 4 photons with nearly the same energies (98.5, 105, and 111 GeV). If confirmed by future observations, these events may indicate the presence of a peculiar peak or bump in the IC 310 spectrum given that the remaining *Fermi*-LAT data agree with the MAGIC measurement. The detection of such a relatively narrow feature in the spectrum of a radio galaxy may be a clue regarding the particle acceleration mechanism at the base of AGN jets (e.g. "direct" gamma-ray emission during acceleration of particles, Neronov & Aharonian, 2007). This remains a suggestion since the source seems to be variable, and the MAGIC and *Fermi* data used here were not taken simultaneously.
The combined MAGIC and *Fermi* spectrum (besides the above mentioned bump) is consistent with a flat E^{-2} spectrum stretching without a break over more than 3 orders of magnitude in energy (2 GeV – 7 TeV). This is similar to the flat VHE spectra of M 87, another radio galaxy detected at TeV energies (Aharonian et al., 2006b; Albert et al., 2008a; Acciari et al., 2008). Such an extended flat E^{-2} spectrum is hard to obtain in a simple one-zone synchrotron self-Compton (SSC) model (e.g. Maraschi et al., 1992). Instead, a viable model of emission might be IC scattering of external infrared background photons from accretion flow or from the inner jet (see e.g. Neronov & Aharonian, 2007). Alternatively, a flat spectrum can be produced in the hadronic models (e.g. Mannheim, 1993, Mücke et al., 2003). In more complicated, multi-zone leptonic models, the GeV-TeV emission of a few slightly shifted inverse Compton peaks can also emulate a flat spectrum (e.g. spine-sheath layer model, Tavecchio & Ghisellini, 2008). Finally, using the model by Domínguez et al. (2011), the change in the spectrum due to the absorption in the extragalactic background light radiation field is within the error of the spectral slope.
Note that this is the first source discovered above 300 GeV by the MAGIC telescopes working together in stereo mode.

4.2 The Detection of the Radio Galaxy NGC 1275

NGC 1275 ($z = 0.0179$), the central dominant galaxy of the Perseus cluster, harbors one of the closest AGN, already included in the original Seyfert list (Seyfert, 1943). The AGN is a very bright radio source showing an extended jet with Fanaroff-Riley I morphology (e.g. Vermeulen et al., 1994; Buttiglione et al., 2010). The optical emission of the nucleus is variable and strongly polarized from 3% to 6% (Maza, 1979; Martin et al., 1983), implying that the relativistic jet contributes significantly to the optical continuum (Angel & Stockman, 1980). The source has also been classified as a BL Lac object (Veron, 1978). The jet increases its inclination from 10 deg to 20 deg on milliarcsecond scales up to 40 deg to 60 deg at arcsecond scales (Krichbaum et al., 1992). Due to its brightness and proximity this source is ideally suited to study the physics of relativistic outflows and the "feedback" effects of the jet on the cluster environment (e.g. Fabian et al., 2008).
NGC 1275 is one of the closest gamma-ray emitting AGN. It was first unambiguously detected in the high-energy (HE, 100 MeV $< E <$ 100 GeV) gamma-ray range by *Fermi*, during the first four months of all-sky-survey observations, with an average flux above 100 MeV of $F_\gamma = (2.10 \pm 0.23) \times 10^{-7}$ cm^{-2} s^{-1} (Abdo et al., 2009). The differential energy spectrum between

100 MeV and 25 GeV was described by a power law with a spectral index of -2.17 ± 0.05. While no variability was observed during these four months of observations, subsequent results based on the first year *Fermi*-LAT observations (Kataoka et al., 2010) show evidence of flux variability on time scales of months. Furthermore, the average gamma-ray spectrum show a significant deviation from a simple power law, indicating an exponential cut-off at the break photon energy of $E_c = (42.2 \pm 19.6)$ GeV.
More recently, the results obtained from the first two years *Fermi*-LAT observations (Brown & Adams, 2011) have given clear evidence for variability on time scales of days above 800 MeV, revealing that several major flaring events occurred during the two-year observation period. A harder-when-brighter correlation between flux and spectral index was also found. Brighter and therefore harder > GeV states are then promising for triggering observations at VHE. Finally, present upper limits at VHE provided by MAGIC-I (previous chapter; Aleksić et al., 2010a) and VERITAS (Acciari et al., 2009a) combined with the *Fermi*-LAT results mentioned above suggested that NGC 1275 may have a break or cut-off in the spectrum around tens of GeV.
This section is dedicated to the VHE detection of NGC 1275 in the Perseus cluster stereo data collected from August 2010 and February 2011 by the MAGIC telescopes. The same data also confirm the VHE variability of IC 310.

4.2.1 Observation and Analysis

The Perseus galaxy cluster region was observed in stereo mode by the MAGIC telescopes during two different periods. The first campaign was carried out between October 2009 and February 2010, for a total observation time of 45.3 hours. This resulted in the IC 310 detection(Aleksić et al., 2010b). The latest campaign was performed between August 2010 and February 2011, for a total observation time of 53.6 hours. This resulted in the detection of NGC 1275 at VHE presented in this section. During this last campaign, Perseus was observed in the wobble mode, with data equally split in four pointing positions located symmetrically at 0.4 deg from NGC 1275, in order to ensure optimum sky coverage and background estimation. The survey was carried out during dark time at low zenith angles (from 12 deg to 36 deg), which guaranteed the lowest energy threshold ($\sim$ 50 GeV).
After the application of standard quality checks, 7.9 hours of data were rejected mainly due to non-optimal atmospheric conditions. The final sample is therefore composed by 45.7 hours of good quality stereo data. Independent analyses were performed on the data also from Saverio Lombardi, Pierre Colin and Dorothee Hildebrand giving compatible results.

4.2.2 Results

The θ^2-distribution of the signal and background (estimated from 3 distinct regions), for energies above 100 GeV, are shown in figure 4.5. NGC 1275 is detected with a significance of 6.6 σ. It is worth noting that the background estimation is not affected by a possible IC 310 contribution, since the latter source is not detected in the present data.
The NGC 1275 differential energy spectrum between 70 GeV and 500 GeV can be described by a simple power law ($\chi^2/n_{dof} = 0.76/1$):

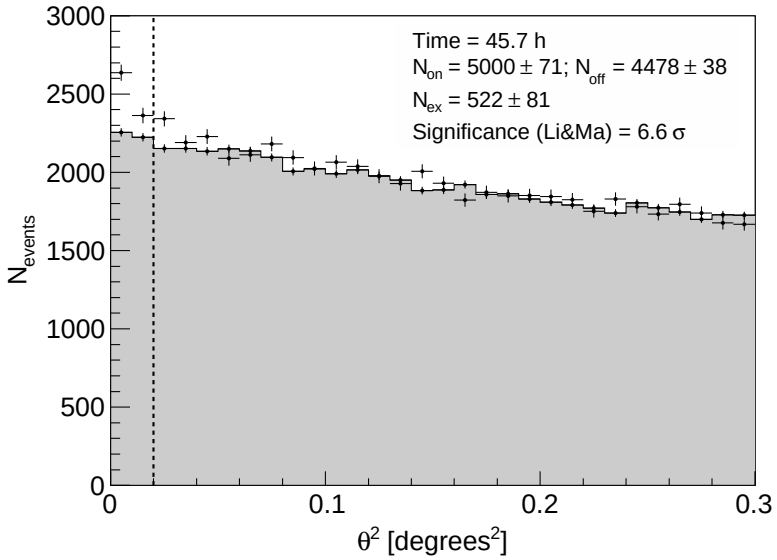

Figure 4.5: θ^2-distributions of the NGC 1275 signal and the background estimation from 45.7 hours of MAGIC stereo observations taken between August 2010 and February 2011, above an energy threshold of 100 GeV. The region between zero and the vertical dashed line (at 0.02 degrees^2) represents the signal region.

$$\frac{\mathrm{d}N}{\mathrm{d}E} = (3.1 \pm 1.0_{stat} \pm 0.7_{syst}) \times 10^{-10} \left(\frac{E}{100\ \mathrm{GeV}}\right)^{\Gamma}, \tag{4.1}$$

in units of cm^{-2} s^{-1} TeV^{-1}, with $\Gamma = -4.1 \pm 0.7_{stat} \pm 0.3_{syst}$.[3] The mean flux above 100 GeV is $F_\gamma = (1.3 \pm 0.2_{stat} \pm 0.3_{syst}) \times 10^{-11}$ cm^{-2} s^{-1}, corresponding to $(2.5 \pm 0.4_{stat} \pm 0.6_{syst})$% CU. The steepness of the spectral index measured by MAGIC strongly supports the presence of a break or cut-off in the NGC 1275 spectrum around tens of GeV, as already suggested by the *Fermi*-LAT results (Kataoka et al., 2010; Brown & Adams, 2011), and is consistent with the upper limits on the flux at VHE provided by MAGIC-I (Aleksić et al., 2010a) and VERITAS (Acciari et al., 2009a). The rapid decline in the spectrum, which causes the NGC 1275 signal to vanish above approximately 500 GeV, permits investigating the possible CR induced gamma-ray emission in the Perseus cluster environment above that energy (see next section; Aleksić et al., 2012a).
In figure 4.6, the SED is compared with the results in the 100 MeV – 100 GeV range provided by *Fermi*-LAT, averaging *Fermi* data over the first year (Kataoka et al., 2010) and the first two years (Brown & Adams, 2011). The comparison suggests that a significant spectral steepening occurs around $\sim$ 100 GeV. However, the present non-simultaneous data do not permit discussing whether the spectral change corresponds to a break between two power laws or an exponential cut-off.

[3]The systematic errors of the flux normalization and the energy spectral slope considered here have been estimated to be 23% and ±0.3, respectively, whereas the systematic error on the energy scale is 17%. These values are more conservative than those presented in Aleksić et al. (2012c), given the flux weakness and the spectral steepness of NGC 1275, as measured by MAGIC.

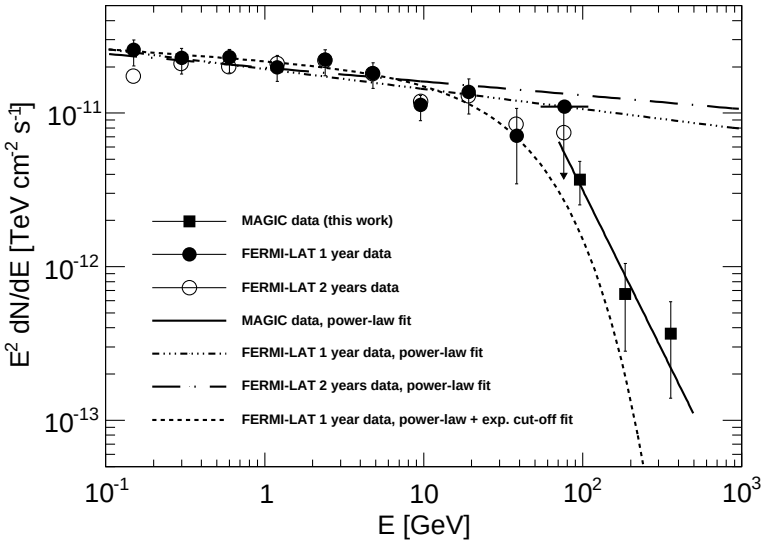

Figure 4.6: NGC 1275 SED measured by MAGIC between 70 GeV and 500 GeV (filled squares), together with the results above 100 MeV achieved from the first year (filled circles; Kataoka et al., 2010), and from the first two years (open circles; Brown & Adams, 2011) of *Fermi*-LAT observations. The power-law fits to the *Fermi*-LAT data (extrapolated up to 1 TeV) are also shown, together with the exponential power-law fit provided in Kataoka et al. (2010).

The August 2010 to February 2011 light curve of NGC 1275 computed for an energy threshold of 100 GeV and with a monthly binning is shown in figure 4.7. No evidence of variability can be derived from these measurements. In fact, fitting the light curve with a constant flux hypothesis yields a $\chi^2/n_{dof} = 7.4/6$, corresponding to a probability $P(\chi^2) = 0.29$.
No significant excess events coming from IC 310 have been found in the observations presented here. The corresponding integral flux upper limit above 300 GeV is $F_\gamma^{UL}(> 300\ \text{GeV}) = 1.2 \times 10^{-12}\ \text{cm}^{-2}\ \text{s}^{-1}$, for a spectral index of $\Gamma = -2.0$ (i.e. the spectral index of the source measured by MAGIC). This value is about a factor 3 lower than the average integral flux $F_\gamma(> 300\ \text{GeV}) = (3.1 \pm 0.5) \times 10^{-12}\ \text{cm}^{-2}\ \text{s}^{-1}$ measured by MAGIC from October 2009 to February 2010, thereby confirming the variability of the latter source on a year time scale.

4.3 Constraining Cosmic Rays and Magnetic Fields

Eventually, the MAGIC telescopes observed the Perseus cluster in stereoscopic mode from October 2009 to February 2011 for a total of ~ 85 hours of effective observation time. This section is dedicated to derive constraints on the possible CR induced gamma-ray emission in the Perseus cluster and, assuming the hadronic model is applicable to the radio mini-halo emission, on the ICM magnetic filed values.
Galaxy clusters are also very promising targets for constraining the DM annihilation cross section

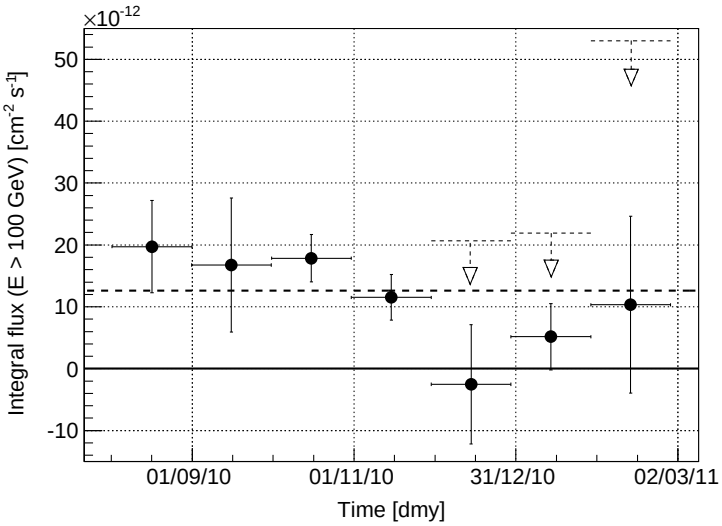

Figure 4.7: NGC 1275 light curve between August 2010 and February 2011 above an energy threshold of 100 GeV, and with a month time-scale binning. No hints of variability are seen in the data. The dashed horizontal line represents the constant function resulting from the fit to the data. For the December 2010, January 2011, and February 2011 data, the upper limits on the flux above 100 GeV for a spectral index of $\Gamma = -4.0$ are also shown (open dashed arrows).

or decay rate (Colafrancesco et al., 2006; Pinzke et al., 2009; Jeltema et al., 2009; Cuesta et al., 2011; Dugger et al., 2010; Sánchez-Conde et al., 2011; Pinzke et al., 2009; Gao et al., 2012). However, the presence of the NGC 1275 signal at energies < 600 GeV, combined with the expected flat DM annihilation emission profile out to the virial radius owing to the substructures that dominate the cluster emission (Sánchez-Conde et al., 2011; Pinzke et al., 2009; Gao et al., 2012), calls for novel analysis techniques. Therefore, such analysis is deferred to future work

4.3.1 Cool-core versus Merging Clusters

The Perseus cluster was selected for the MAGIC observations as it is the most promising target for the detection of gamma-rays coming from neutral pion decay resulting from hadronic CR interactions with the ICM (Aleksić et al., 2010a; Pinzke & Pfrommer, 2010; Pinzke et al., 2009). See the previous chapter 3 for details.

One of the most important questions in studies of non-thermal cluster emission is the origin of giant radio halos in merging clusters and radio mini-halos in CCCs and whether they have a common physical origin. Hence it is instructive to compare the prospects for detecting VHE gamma-ray emission from two representative clusters of each model class, namely Coma and Perseus. First, assuming universality of the gamma-ray spectrum, Coma is expected to be fainter than Perseus by approximately a factor of 3.4. This is mainly because of the lower central gas density in Coma (Pinzke et al., 2009). Second, the Coma X-ray emission is more extended than

in Perseus by the ratio of the half-flux radii of 0.18 deg/0.11 deg =1.6 (Pinzke & Pfrommer, 2010). Since the IACT sensitivity drops almost linearly with source extension for the angular scales considered here, this makes it even more challenging to detect the Coma cluster. Third, the CR spectral index is expected to steepen due to CR transport processes such as streaming and diffusion (Enßlin et al., 2011). The following line of arguments shows that this third point slightly favors Coma as a target source, but the sum of all points clearly favors Perseus:

- Coma should have a central magnetic field strength of $B_0 = 4.7^{+0.7}_{-0.8}\,\mu$G according to Faraday RM studies (e.g. Bonafede et al., 2010). While GHz-radio observations probe 2.5 GeV electrons that are produced in hadronic interactions of 40 GeV CR protons, gamma-rays at 200 GeV are from 1.6 TeV CRs: hence, for Coma, one has to extrapolate a factor of 50 in energy to connect the CRs probed by radio halo observations with those probed by IACTs and a weak bias due to possible CR spectral steepening is expected.

- For Perseus, a stronger $B_0 \sim 20\,\mu$G is expected from adiabatic magnetic field compression during the formation of the cool core (see also chapter 3). While GHz-radio observations probe 1.2 GeV electrons and the 20 GeV CR protons that generate those electrons hadronically, the MAGIC gamma-ray constraints at 1 TeV correspond to 8 TeV CR protons (since the detection of VHE gamma-ray emission from NGC 1275 renders it difficult to observe diffuse emission at lower energies). Hence the CRs probed by the radio observations and those probed by MAGIC are a factor of 400 different in energy. A possible CR spectral steepening, due to e.g. CR diffusion, would induce a larger bias in the CR pressure and magnetic field constraints. Assuming a change in the spectral index by 0.2 between 20 GeV and 8 TeV implies a decrease of the VHE gamma-ray flux by a factor of 3.3 – 1.6 times larger than the corresponding decrease of flux for Coma (over the eight times smaller energy range).

In summary, Perseus appears to be the most promising target for detecting CR-induced gamma-ray emission. Assuming that the energy dependence of the CR transport and the associated spectral steepening is representative for clusters, Coma would require ten times longer integrations to detect the corresponding gamma-ray in comparison to Perseus. However, CCCs and NCCCs are complementary and equally deep or deeper observations of merging clusters that host giant radio halos — such as Coma — are needed.

4.3.2 Observation, Analysis and Results

The Perseus cluster region was observed by the MAGIC telescopes from October 2009 to February 2011 for a total of about 99 hours. During the October 2009 - February 2010 campaign (45.3 hours), the data were taken in the so called soft-stereo trigger mode with the first telescope trigger working in single mode and the second telescope recording only events triggered by both telescopes. The soft-stereo trigger mode may result in slightly degraded performance at the lowest energies with respect to Aleksić et al. (2012c), but has a negligible impact at the energies of interest here. During the August 2010 - February 2011 campaign (53.6 hours), data

were taken in the standard full-stereo trigger mode where events are triggered simultaneously by both telescopes.
The final data sample consists of 84.5 hours of effective observation time. The data quality check resulted in the rejection of about 14.4 hours of data, mainly due to non-optimal atmospheric conditions. In order to combine data taken with different trigger modes, a high cut on the shower image Size has been applied . Only events with image Size above 150 photo-electrons in both telescopes were kept (the standard analysis uses 50 photo-electrons cuts). With this cut, the rate and image parameter distributions of the background events are compatible between the two samples.
The left panel of figure 4.8 shows the significance skymap obtained with this analysis with an energy threshold of 150 GeV. The two AGNs detected during the campaign can clearly be seen (NGC 1275 in the center and IC 310 in the lower-right part).

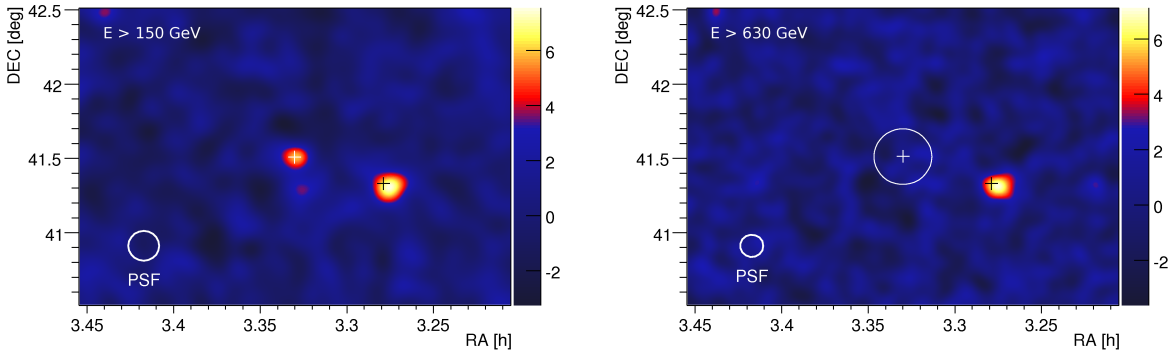

Figure 4.8: Left panel: significance skymap of the Perseus cluster above 150 GeV. The positions of NGC 1275 (white cross), which coincides with the cluster center, and the head-tail radio galaxy IC 310 (black cross) are marked. Right panel: significance skymap of the Perseus cluster region above 630 GeV. The central white circle marks the 0.15 deg region used to derive constraints (see main text for details). The quoted energy thresholds are obtained assuming a spectral index of -4 as observed in NGC 1275.

In this section, the attention is focused on the pion-decay gamma-ray emission resulting from hadronic CR interactions with thermal protons of the ICM. Cosmological simulations of Pinzke & Pfrommer (2010) suggest that the spectral energy distribution of gamma-rays follows a power-law, $F \propto E^{\Gamma}$, with a spectral index of $\Gamma = -2.2$ at the energies of interest here (Aleksić et al., 2010a). The simulated signal is extended with approximately 60% of the emission coming from a region centered on NGC 1275 with a radius of 0.15 deg (see figure 13 of Pinzke & Pfrommer, 2010). The emission from NGC 1275 is dominant below about 600 GeV and with a spectral index of about -4. Therefore, since the expected CR-induced signal is much harder than the measured NGC 1275 spectrum, it should appear at higher energies with no break or cut-off in the energy range covered by MAGIC. Hence, the data analysis is limited to energies > 630 GeV for which the NGC 1275 signal vanishes. The right panel of figure 4.8 shows the significance skymap above 630 GeV. In contrast to NGC 1275, the spectrum of IC 310 is very hard and remains detectable above 600 GeV. IC 310 is ~ 0.6 deg($\simeq 10$ PSF) away from the cluster center,

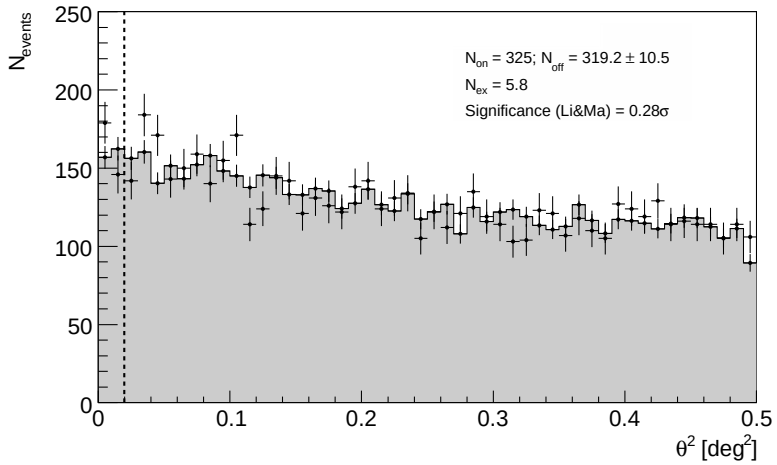

Figure 4.9: θ^2-distribution above 630 GeV of the signal (data points) and background (gray filled region) at the cluster center. The dashed line represents the signal region cut within which the excess event number is estimated. Here it corresponds to 0.02 deg^2. The quoted energy threshold is obtained assuming a spectral index of -4 as observed in NGC 1275.

far enough so that its emission does not leak into the signal region. However, if not explicitly accounted for, it could affect the estimated background. Here, the background is measured with three off-source positions at 0.4 deg from the the camera center and $>$ 0.28 deg away from IC 310. This distance guarantees that there is no contamination from IC 310.

In figure 4.9, the θ^2-distribution of the signal and background at the cluster center for energies above 630 GeV is shown. Since the emission is expected to be more extended than the MAGIC PSF, the cut in the θ^2 distribution which defines the signal region must be optimized. First, the θ^2-distribution of the expected signal is estimated considering the simulated surface brightness of the Perseus cluster emission smoothed with the MAGIC PSF. Second, the background level is estimated from the data. Finally, the significance for signal detection is calculated as a function of the θ^2 cut. The derived optimal θ^2 cut was close to 0.02 deg^2. As shown in figure 4.9, no significant excess is found within 0.02 deg^2.

Upper limits (ULs) are derived for several energy thresholds. The effective area of MAGIC is calculated using point-like source MC simulation and the ULs have to be corrected to take into account the expected source extension. To calculate this correction factor, the fraction of the total events inside the signal region for a point-like source is compared to the expected CR induced signal. Therefore, the presented ULs can be compared with the theoretical expectations for the region within a radius of 0.15 deg. In table 4.1, the integral flux ULs above specified energy thresholds calculated for a spectral index of -2.2 are presented. The point-like ULs, significance and ULs in number of events are also shown. The integral ULs for energies above E_{th} = 1 TeV corresponds to the best sensitivity for sources with spectral index -2.2 and it is the most constraining value; for this reason this UL is adopted for the following discussion. For purposes that will be clear in the following, the 0.15 deg integral flux UL above 1 TeV is recalculated for spectral indexes of -2.1, -2.3 and -2.5 resulting in 1.37, 1.38 and 1.39 $\times$

E_{th}[GeV]	σ^{PL}_{LiMa}	N^{PL}_{UL}	F^{PL}_{UL}	$F^{0.15^\circ}_{UL}$
630	0.59[a]	84.7	2.93	3.22
1000	0.15	41.4	1.25	1.38
1600	0.33	38.7	1.07	1.18
2500	0.38	28.8	0.79	0.87

Table 4.1: Integral flux ULs F_{UL} for a power-law gamma-ray spectrum with spectral index -2.2 above a given energy threshold E_{th}, both for a point-like source (PL) and for a 0.15 deg extended region, in units of 10^{-13} cm^{-2} s^{-1}. Additionally shown are the corresponding significance σ^{PL}_{LiMa} and ULs in number of events N^{PL}_{UL} (before applying the source extension correction). [a] Note that the significance reported for E_{th} = 630 GeV is slightly different than in figure 4.9 because different cuts were applied. In particular, computing the θ^2-distribution a hard gamma-ray selection cut, which is normally adopted for detection purpose, is adopted, while computing the flux ULs softer cuts are used in order to reduce the systematic errors.

10^{-13} cm^{-2} s^{-1}, respectively.

4.3.3 Implications for Cosmic Rays and Magnetic Fields

In this section, different approaches are adopted to constrain the CR pressure distribution in the Perseus cluster with the MAGIC ULs. This permits to explore the underlying plasma physics that produce the CR distribution. These approaches include (1) a simplified analytical approach that assumes a constant CR-to-thermal pressure and a momentum power-law spectrum, (2) an analytic model of CRs derived from cosmological hydrodynamical simulations of the formation of galaxy clusters, and (3) the use of the observed luminosity and surface brightness profile of the radio mini-halo in Perseus to place a lower limit on the expected gamma-ray flux in the hadronic model of radio mini-halos. This provides a minimum CR pressure which, using tight gamma-ray limits/detections, checks the hadronic model of the formation of radio mini-halos. (4) Alternatively, by constructing a CR distribution that is just allowed by the flux ULs, and requiring the model to match the observed radio mini-halo data, a lower limit on the magnetic field strength can be derived. Note, however, that this limit assumes that the observed synchrotron emission is produced by secondary electrons resulting from hadronic CR interactions.

1 - Simplified Analytical Cosmic Ray Model

A simplified analytical model is adopted assuming a power-law CR momentum spectrum, $f \propto p^{\Gamma}$, and a constant CR-to-thermal pressure ratio, i.e. the *isobaric model of CRs* following the approach of Pfrommer & Enßlin (2004a) (the low-momentum cutoff on the CR distribution function is assumed to be $q = 0$, this can be easily generalized to an arbitrary q using e.g. figure 1

Γ	$X_{\mathrm{CR,max}}$ [%]	$X_{\mathrm{CR,min}}$ [%]	$X_{\mathrm{CR,max}}/X_{\mathrm{CR,min}}$	$F^{a}_{\gamma,\mathrm{min}}$
-2.1	0.77	0.42	1.8	7.4
-2.2	1.12	0.35	3.2	4.3
-2.3	2.17	0.38	5.7	2.4
-2.5	11.6	0.67	17.3	0.8

Table 4.2: Constraints on CR-to-thermal pressure ratio in the Perseus cluster core, $X_{\mathrm{CR,max}}$, which is assumed to be constant in the simplified analytical model. Those constraints are compared to minimum CR-to-thermal pressure ratios, $X_{\mathrm{CR,min}}$, and minimum gamma-ray fluxes in the hadronic model of the Perseus radio mini-halo. [a] Minimum gamma-ray flux in the hadronic model of the Perseus radio mini-halo, $F_{\gamma,\mathrm{min}}(> 1\,\mathrm{TeV})$, in units of 10^{-14} cm^{-2} s^{-1}.

of Pfrommer & Enßlin 2004a). Since a priori the CR spectral index[4] Γ is unconstrained, it is assumed to vary within a plausible range of $-2.1 < \Gamma < -2.5$. The central value of this spectral range is compatible with the radio spectral index in the core of the Perseus radio mini-halo of $\alpha_\nu = -\Gamma/2 \sim 1.25$ (Sijbring, 1993). To model the thermal pressure, the measured electron temperature and density profiles for the Perseus cluster (Churazov et al., 2003) are adopted. The temperature profile has a dip in the central cool core region and otherwise a constant temperature of $kT = 7$ keV. The density profile is hybrid in the sense that it combines *Einstein* X-ray observations on large scales with high-resolution *XMM-Newton* observations of the cluster core (Churazov et al., 2003).
Table 4.2 shows the resulting constraints on the CR-to-thermal pressure ratio, $X_{\mathrm{CR}} = \langle P_{\mathrm{CR}} \rangle \,/\, \langle P_{\mathrm{th}} \rangle$, averaged within the virial radius, $R_{\mathrm{vir}} = 2$ Mpc, defined as the radius of a sphere enclosing a mean density that is 200 times the critical density of the Universe. The inferred constraints on X_{CR} strongly depend on Γ due to the comparably large lever arm from GeV-CR energies (that dominate the CR pressure) to CR energies at 8 TeV. Using the integral flux UL above 1 TeV, X_{CR} is constrained to be between 0.77% and 11.6% (for Γ varying between -2.1 and -2.5). For a spectral index of -2.2, favored by the simulation-based model of Pinzke & Pfrommer (2010) at energies > 1 TeV, $X_{\mathrm{CR}} < 1.1\%$.

2 - Simulation-inspired Cosmic Ray Model

For a more realistic approach, cosmological hydrodynamical simulations must be used. These have considerable predictive power, e.g. calculating the CR spectrum self-consistently rather than leaving it as a free parameter, and permit tests of various assumptions about the underlying CR physics. The universal spectral and spatial CR model developed by Pinzke & Pfrommer (2010) is used. This model uses only a density profile as input which can be inferred from cosmological

[4]The hadronic interaction physics guarantees that the CR spectral index coincides with that from pion-decay gamma-ray emission.

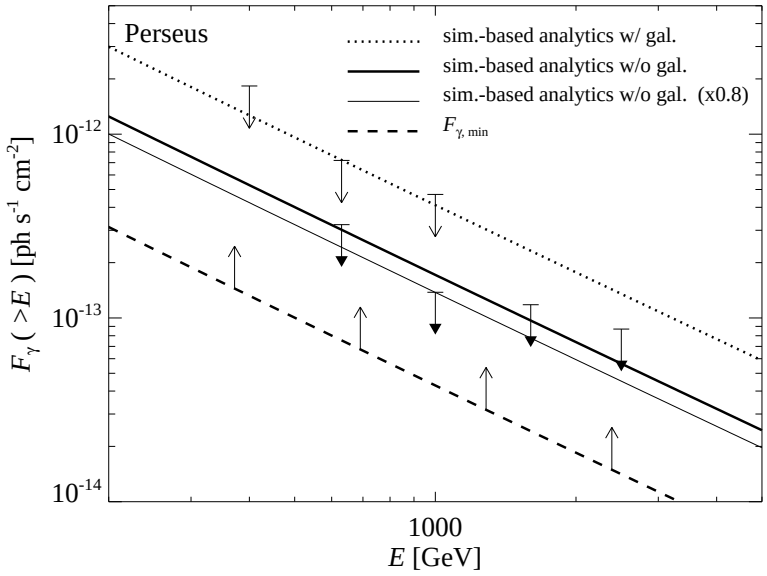

Figure 4.10: Integral flux ULs of mono (point-like ULs, upper arrows; see previous chapter; Aleksić et al., 2010a) and stereo (solid arrows; table 4.1) observations are shown. These are compared to the integrated spectra of the gamma-ray emission from decaying neutral pions that result from hadronic CR interactions with the ICM in the Perseus cluster coming from within a radius of 0.15 deg around the center. Also shown is the minimum gamma-ray flux estimates for the hadronic model of the Perseus radio mini-halo (dashed line with minimum flux arrows) using the universal gamma-ray spectrum resulting from pion decay (Pinzke & Pfrommer, 2010) and adopting the spectral index -2.2.

simulations or X-ray observations. This analytic approach models the CR distribution, and the associated radiative emission processes from hadronic interactions with gas protons, from radio to the gamma-ray band. See also chapter 6 where a new *hybrid* model is constructed by merging the simulation-driven approach of Pinzke & Pfrommer (2010) and the analytical results of Enßlin et al. (2011).

There are at least two major uncertainties in modeling the CR physics that significantly affect the resulting spatial and spectral CR distribution: the CR acceleration efficiency and the microscopic CR transport relative to the thermal plasma. The overall normalization of the CR and gamma-ray distribution scales with the maximum acceleration efficiency at structure formation shocks. Following recent observations (Helder et al., 2009) and theoretical studies (Kang & Jones, 2005) of supernova remnants, here a value of 50% for this parameter is adopted (see also the corresponding discussion in the previous chapter 3). The Pinzke & Pfrommer (2010) cosmological simulations only consider advective transport of CRs by turbulent gas motions which produces a centrally enhanced profile. However, active CR transport such as CR diffusion and streaming flattens the CR radial profile, producing a spatially constant CR number density in the limiting case. As a consequence, this produces a bimodality of the diffuse radio and gamma-ray emission of clusters, since more centrally concentrated CRs will find higher target densities for hadronic

CR proton interactions (see chapter 6; Enßlin et al., 2011).
As in chapter 3, an optimistic CR model (*simulation-based analytics with galaxies*) and a more conservative one (*simulation-based analytics without galaxies*) are used in order to bracket our ignorance. The hybrid electron density and temperature profile from X-ray observations of the Perseus cluster are adopted (Churazov et al., 2003). The temperature profile is here modified in the outer cluster regions (beyond $0.2R_{200} \simeq 400\,\mathrm{kpc}$) in order to reproduce the characteristic decline toward the cluster periphery as found in simulations (Pinzke & Pfrommer, 2010; Pfrommer et al., 2007) and in a nearby sample of deep *Chandra* cluster data (Vikhlinin et al., 2005). While this modification has little influence on the expected gamma-ray emission (in projection onto the core region) as the densities drop considerably in these regions, the resulting profiles for the CR-to-thermal pressure ratio are changed.
Figure 4.10 shows the expected spectrum of Perseus within an aperture of radius 0.15 deg as calculated using the semi-analytical model of Pinzke & Pfrommer (2010). The MAGIC limit for $E_\gamma > 1$ TeV falls below the flux level of the conservative model[5] by 20%; thereby constraining assumptions about the adopted CR physics in the simulations and the resulting CR pressure.
Figure 4.11 shows the CR-to-thermal pressure ratio $X_{\mathrm{CR}} = \langle P_{\mathrm{CR}} \rangle / \langle P_{\mathrm{th}} \rangle$ as a function of radial distance from the Perseus cluster center, in units of the virial radius, R_{vir} (to compute P_{CR}, a low-momentum cutoff of the CR distribution of $q = 0.8\, m_p c$ is adopted, as found in cosmological simulations by Pinzke & Pfrommer (2010). The ratio X_{CR} *rises toward the outer regions* because of the higher CR acceleration efficiency in the peripheral strong accretion shocks compared to the weak central flow shocks. Adiabatic compression of a mixture of CRs and thermal gas reduces the CR pressure relative to the thermal pressure due to the softer CR equation of state. *The strong increase of* X_{CR} *toward the core* is a remnant of the formation of the cool core in Perseus. During this transition, the mixed gas of CRs and thermal particles has been adiabatically compressed. While the thermal gas radiates on a comparatively fast thermal bremsstrahlung timescale, the long hadronic interaction time scale for energetic CRs ensures an accumulation of this population, thus diminishing the thermal pressure support relative to that in CRs.
The MAGIC flux limits constrain X_{CR} of the simulation-based analytical model to be less than 1.6% within 0.15 deg (200 kpc). Assuming this spatial CR profile yields a CR-to-thermal pressure ratio $< 1.7\%$ within $R_{\mathrm{vir}} \simeq 2$ Mpc and $< 5\%$ within 20 kpc (adopting the conservative model). The X_{CR}-limit within the virial radius is larger by a factor of 1.5 than that of the simplified approach because the concave curvature of the simulated spectrum accumulates additional pressure toward GeV energies relative to a pure power-law.
With these gamma-ray flux ULs, the CR physics in galaxy clusters is constrained: this either limits the maximum acceleration efficiency of CRs at strong structure formation shocks to $< 50\%$ or indicates possible CR streaming and diffusion out of the cluster core region. The latter would populate the peripheral cluster regions and X_{CR} would increase toward the cluster periphery at

[5]Note that the models "with galaxies" and "without galaxies" differ from those used in the previous chapter where they were based on the simulated Pinzke & Pfrommer (2010) cluster g51 (which is similar in morphology to Perseus). On the contrary, here the universal CR model, obtained by Pinzke & Pfrommer (2010) from 14 galaxy clusters that span almost two decades in mass, is used. The spectral normalization (between the two models) therefore increased from 1.5 to 2.4 and the gamma-ray flux in the model "without galaxies" used here differs by 10%.

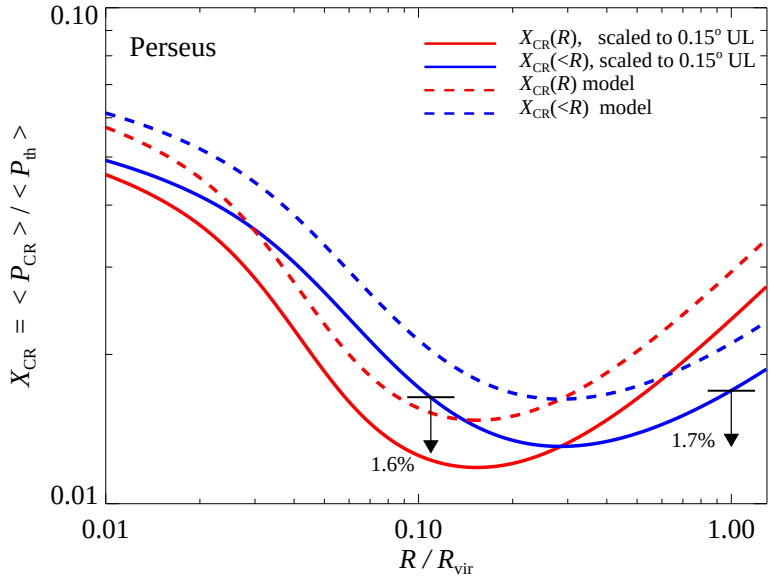

Figure 4.11: CR-to-thermal pressure ratio $X_{\rm CR} = \langle P_{\rm CR} \rangle / \langle P_{\rm th} \rangle$ at the radial distance from the Perseus cluster center, $R/R_{\rm vir}$ (red lines), and integrated up to $R/R_{\rm vir}$ (blue lines), using the simulation-based analytical model of CRs (Pinzke & Pfrommer, 2010). The simulation model (dashed) is contrasted to a model that has been scaled by the MAGIC constraints obtained here (solid).

the expense of a decrease of the central $X_{\rm CR}$ (Enßlin et al., 2011) compared to the simulation model. The X-ray morphology of the central region in Perseus shows spiral structure in the density and temperature maps with an anti-correlation of both quantities (Fabian et al., 2011a). This resembles sloshing motions after a past merger event, suggesting that Perseus is currently relaxing. If CR streaming and diffusion out of the central core region is indeed correlated with a dynamical relaxation of a cluster after a merger event as suggested by Enßlin et al. (2011), this would render CR transport more plausible for explaining the smaller gamma-ray flux relative to the simulation model. By the same token, it may argue for a more extended gamma-ray emission signature than that seen in the radio, further justifying the larger source extension of 0.15 deg adopted here (which is twice that of the largest radial extend of the mini-halo of 0.075 deg).

3 - Minimum Gamma-ray Flux

As explained in the previous chapter (section 2.3.4), for clusters with radio (mini-)halos, a minimum gamma-ray flux in the hadronic model of radio (mini-)halos can be derived. The point is that lowering the magnetic field strength would require increasing the CR electron energy density to reproduce the observed synchrotron luminosity and thus increases the associated gamma-ray flux. The maximum emission radius of the Perseus radio mini-halo of 100 kpc corresponds to an angular size of 0.075 deg, well within the MAGIC PSF; hence L_ν does not need to be cut to match the angular region tested here. The magnetic files is assumed to be $B \gg B_{\rm CMB}$ everywhere in the

radio-emitting region, and (in order to obtain this minimum gamma-ray flux) it is required a considerable drop in the CR distribution outside the radio mini-halo. The large magnetic field can be realized by adiabatically compressing the magnetic field during the formation of the cool core and the edge of the radio emitting region can be caused by a region of predominantly toroidal magnetic field which efficiently confines CRs to the central region (see e.g. Lyutikov, 2006; Dursi & Pfrommer, 2008; Quataert, 2008; Parrish & Quataert, 2008; Pfrommer & Dursi, 2010; Enßlin et al., 2011).
In contrast to what done in the previous chapter (Aleksić et al., 2010a), here the *absolute* minimum gamma-ray flux is derived rather than the "physical" minimum gamma-ray flux that depends on the assumed magnetic field distribution. The results for the minimum gamma-ray flux $F_{\gamma,\mathrm{min}}(> 1\ \mathrm{TeV})$ and the minimum CR-to-thermal pressure ratio, $X_{\mathrm{CR,\,min}} = X_{\mathrm{CR}} F_{\gamma,\mathrm{min}}/F_{\gamma,\mathrm{iso}}$ are presented in table 4.2 and figure 4.10 (assuming $\Gamma = -2.2$). Here, $F_{\gamma,\mathrm{iso}}$ is the gamma-ray flux in the *isobaric model of CRs*. The ratio of the maximum to minimum CR pressures $X_{\mathrm{CR,max}}/X_{\mathrm{CR,min}}$ varies between 1.8 and 17.3 for a spectral index between $-2.1 \leq \Gamma \leq -2.5$. For the spectral index $\Gamma = -2.2$ of the universal gamma-ray spectrum around TeV energies, the ratio is $X_{\mathrm{CR,max}}/X_{\mathrm{CR,min}} = 3.2$. This puts the long-sought gamma-ray detection of clusters, in particular for Perseus, within the reach of deeper campaigns with the possibility of scrutinizing the hadronic emission model of radio (mini-)halos.

4 - Implications for the Cluster Magnetic Field

An absolute lower limit on the hadronic model gamma-ray emission comes from assuming high magnetic field strengths ($B \gg B_{\mathrm{CMB}}$) everywhere in the radio-emitting region. Using the MAGIC ULs, this argument can be turn around to derive a lower limit on the magnetic field strength needed to explain the observed diffuse radio emission within the hadronic model (Pfrommer & Enßlin, 2004b). Lowering the gamma-ray limit will tighten (increase) the magnetic field limit. If this conflicts with magnetic field measurements by means of other methods, e.g. Faraday RM, this would challenge the hadronic model of radio (mini-)halos. This depends on the assumed spatial structure of B that here is parametrize as:

$$B(r) = B_0 \left(\frac{n_{\mathrm{e}}(r)}{n_{\mathrm{e}}(0)} \right)^{\alpha_B}, \tag{4.2}$$

as suggested by the CCC cosmological MHD simulation of Dubois & Teyssier (2008). This last work demonstrates a tight correlation of the magnetic field with the ICM gas density and highlights the importance of cooling processes in amplifying the magnetic field in the core of galaxy clusters up to one order of magnitude above the typical amplification obtained for a purely adiabatic evolution. Moreover, such a parametrization is favored by Faraday RM studies (Bonafede et al., 2010; Kuchar & Enßlin, 2011, and references therein). Recent Faraday RM studies yield estimates for the central magnetic field of typically 5 μG for merging clusters (Bonafede et al., 2010, for Coma) and significantly higher values in CCCs of around 16 μG (Kuchar & Enßlin, 2011, for Hydra A). For the Perseus cluster, as discussed in the previous chapter, Faraday RMs are available only on very small (Taylor et al., 2006), and implies magnetic field strengths of $\sim 25\ \mu$G.

The point-source subtracted azimuthally averaged surface brightness profile at 1.38 GHz (Pedlar et al., 1990) of the Perseus radio mini-halo is fitted with a β-model as:

$$S_\nu(r_\perp) = S_0 \left[1 + \left(\frac{r_\perp}{r_c}\right)^2\right]^{-3\beta+1/2}, \tag{4.3}$$

where $S_0 = 2.3 \times 10^{-1}\,\mathrm{Jy\,arcmin^{-2}}$, $r_c = 30$ kpc, and $\beta = 0.55$. This profile is valid within a maximum emission radius of 100 kpc. An Abel integral deprojection then provides the radio emissivity distribution (see Appendix of Pfrommer & Enßlin 2004a). To constrain the magnetic field, the following steps are done:

1. Given a model for the magnetic field characterized by α_B and an initial guess for B_0, the $X_{\rm CR}(r)$ profile is derived such that the hadronically produced synchrotron emission matches the observed Perseus radio mini-halo emission.

2. Using this $X_{\rm CR}(r)$ profile, the pion-decay gamma-ray surface brightness profile is calculated. $X_{\rm CR}(r)$ is then scaled such as the flux coming within a radius of 0.15 deg match the corresponding MAGIC UL. This scaling factor depends on the CR spectral index Γ, the radial decline of the magnetic field α_B and the initial guess for B_0.

3. The $X_{\rm CR}(r)$ determined in the previous two steps is used to re-calculate the radio emission and find the B_0 value that matches the observed synchrotron (note that for $B_0 \gg B_{\rm CMB}$ and a radio spectral index of $\alpha_\nu = 1$, the solution is degenerate, as can be seen from equation 3.1).

Table 4.3 gives the resulting lower limits for B_0. These depend sensitively on the assumptions of Γ and α_B. The hardest CR spectral indices correspond to the tightest limits on B_0. This is because for an UL for CR energies of around 8 TeV (as probed by 1 TeV gamma-rays) and a CR population with a softer spectral index there is a comparably larger fraction of CRs at 25 GeV available which produce more radio-emitting electrons. Therefore, lower magnetic field strengths can be accommodated while still matching the observed synchrotron flux. On the other hand, for a steeper magnetic decline (larger α_B), the CR number density must be higher to match the observed radio emission profiles. This would yield a higher gamma-ray flux, so the ULs are more constraining, and implies tighter lower limits for B_0.
The inferred values for the minimum magnetic field strengths in table 4.3 range from 2 to 13 μG for the values of Γ and α_B used here and suggested by radio observations. These are much lower than the thermal equipartition value in the center of Perseus, $B_{\rm eq,0} \simeq 80\,\mu$G, or magnetic field estimates from the Faraday RM (Taylor et al., 2006). In table 4.3, the corresponding values for the CR-to-thermal pressure ratio (at the largest emission radius at 100 kpc), such that the model reproduces the observed radio surface brightness profile, are additionally shown.[6] Since they are

[6]Note that here $X_{\rm CR}$ is uniquely determined by the adopted model for the magnetic field and the observed synchrotron surface brightness profile. This differs from the simplified analytical CR model where $X_{\rm CR}$ = const. and contrasts with the simulation-based model where $X_{\rm CR}(r)$ is derived from cosmological cluster simulations of Pinzke & Pfrommer (2010).

	Minimum magnetic field, $B_{0,\mathrm{min}}$ [μG]:			
α_B	Γ			
	-2.1	-2.2	-2.3	-2.5
0.3	5.86	4.09	3.15	2.06
0.5	8.62	6.02	4.63	3.05
0.7	13.1	9.16	7.08	4.68
	Corresponding X_{CR} (100 kpc) [%]:			
0.3	1.7	2.5	4.9	26.7
0.5	1.7	2.5	4.8	26.1
0.7	1.6	2.3	4.5	23.6

Table 4.3: Constraints on magnetic fields in the hadronic model of the Perseus radio mini-halo and the corresponding CR-to-thermal pressure ratio (at the largest emission radius of 100 kpc) such that the model reproduces the observed radio surface brightness profile.

derived from flux ULs they are also ULs on the CR-to-thermal pressure ratio. The corresponding values for X_{CR} in the cluster center are lower than 5% for the entire parameter space probed here. Concluding, there is still considerable leeway for the hadronic model as an explanation of the radio mini-halo emission.

4.4 Conclusions

MAGIC observed the Perseus cluster for a total of about 85 hours of high quality data between October 2009 and February 2011. This campaign resulted in the serendipitous detection of the head-tail radio galaxy IC 310 (Aleksić et al., 2010b) and the detection of the central radio galaxy NGC 1275 (Aleksić et al., 2012b).

The IC 310 observed SED is flat with a differential spectral index of -2.00 ± 0.14. The source mean flux above 300 GeV between October 2009 and February 2010 is $(3.1\pm0.5)\times10^{-12}$ cm^{-2} s^{-1}, corresponding to (2.5 ± 0.4)% CU. Only an upper limit, of 1.9% CU of above 300 GeV, was obtained with the 2008 data. IC 310 is not detected in the August 2010 - February 2011 data, resulting in an UL of $F_\gamma^{UL}(> 300\ \mathrm{GeV}) = 1.2 \times 10^{-12}$ cm^{-2} s^{-1} which is a factor ~ 3 lower than the mean flux measured between October 2009 and February 2010, confirming the year time-scale variability of the source at VHE. Strong hints ($> 3\sigma$) of flares are also identified in the middle of October and November 2009. The MAGIC results favour a scenario with the IC 310 VHE emission originating from the inner jet close to the central engine. More complicated models than a simple one-zone SSC scenario, e.g. multi-zone SSC, external Compton or hadronic, may be required to explain the very flat spectrum and its extension over more than three orders of magnitude in energy.

The NGC 1275 differential energy spectrum between 70 GeV and 500 GeV can be described by a power law with a steep spectral index of $\Gamma = -4.1 \pm 0.7_{stat} \pm 0.3_{syst}$, and the average flux above 100 GeV is $F_\gamma = (1.3 \pm 0.2_{stat} \pm 0.3_{syst}) \times 10^{-11}$ cm^{-2} s^{-1}. These results, combined with the power-law spectrum measured in the first two years of observations by *Fermi*-LAT above 100 MeV, with a spectral index of $\Gamma \simeq -2.1$, strongly suggest the presence of a break or cut-off around tens of GeV in the NGC 1275 spectrum. The source light curve above 100 GeV does not show hints of variability on a month time scale.

No significant excess of gamma-rays was detected from the Perseus cluster central region at energies above 630 GeV where the NGC 1275 emission vanishes. The flux UL for the CR-induced emission above 1 TeV, for a region of radius of 0.15 deg around the cluster center, corresponds to 1.38×10^{-13} cm^{-2} s^{-1}.

Using a simplified analytical approach, the CR-to-thermal pressure can be constrained to $X_{\rm CR} <$ 0.8% and 12% (for a CR or gamma-ray spectral index, Γ, varying between -2.1 and -2.5). For the spectral index at TeV energies of $\Gamma = -2.2$, favored by simulations, $X_{\rm CR} < 1.1\%$. The simulation-based approach gives $X_{\rm CR} < 1.7\%$. This latter value is a factor of 1.5 less constraining because of the concave curvature of the simulated spectrum that has higher partial pressure toward GeV energies relative to a pure power-law spectrum.

The MAGIC UL is a factor of 1.25 below the simulation model and – for the first time – limits the underlying physics of the simulation. This could either indicate that the maximum acceleration efficiency of CRs relative to the total dissipated energy at strong structure formation shocks is $< 50\%$ (i.e. smaller than the value assumed in the simulations) or may point to CR streaming and diffusion out of the cluster core region that lowers the central $X_{\rm CR}$ values (see chapter 6 and Enßlin et al., 2011). The observed spiral X-ray structure in the central cluster region suggests that Perseus is currently in a relaxation state following a past merging event. If a net outward CR transport is indeed correlated with a dynamical relaxation state of a cluster, this would render CR transport a plausible agent that lowers the gamma-ray flux in comparison to the simulation model that neglects this mechanism.

Adopting a strong magnetic field everywhere in the radio-emitting region ($B \gg B_{\rm CMB}$) yields the minimum gamma-ray flux in the hadronic model of radio mini-halos. This is a factor of 2 to 18 below the MAGIC ULs for spectral indices varying between -2.1 and -2.5. For $\Gamma = -2.2$, following the universal CR model, the minimum gamma-ray flux is a factor of 3.2 lower than the MAGIC ULs.

Matching the radio emission profile (i.e. fixing the radial CR profile for a given magnetic field model) and by requiring the pion-decay gamma-ray flux to match the MAGIC flux ULs (i.e. fixing the normalization of the CR distribution), lower limits on the magnetic field distribution can be derived. The inferred values are $2\ \mu{\rm G} \leq B_{0,\rm min} \leq 13\ \mu{\rm G}$ for the parameter space spanned by the magnetic field strength radial index α_B and the CR spectral index Γ used here. Since $B_{0,\rm min}$ is smaller than recent field strengths estimates through Faraday RM studies in cool core clusters (e.g. Kuchar & Enßlin, 2011), this argues that the hadronic model is an interesting possibility in explaining the radio mini-halo emission.

This displays the potential of future gamma-ray observations of Perseus to further refine the parameters of the hadronic model and for eventually assess its validity in explaining RHs. This is true for the currently operating Cherenkov telescopes and for the future planned CTA whose

sensitivity is meant to be about an order of magnitude higher than current instruments.

Part II

MULTI-WAVELENGTH PREDICTIONS OF THE COSMIC RAY AND DARK MATTER INDUCED EMISSION

Chapter 5

Dark Matter Decay and Annihilation in Extragalactic Structures

Water, water, every where,
And all the boards did shrink.
Water, water, every where,
Nor any drop to drink.

Samuel T. Coleridge

This chapter is dedicated to study the DM induced gamma-ray emission of the extragalactic structures, particularly galaxy clusters, as would be observed by the *Fermi* satellite. A *constrained* cosmological simulation of the local Universe is used to construct all-skymaps of the DM annihilation and decay emissions. These are then analyzed simulating *Fermi* 5-years observations, adopting some representative DM annihilation and decay models, and calculating signal-to-noise ratios.
This work has been published with the title *Dark Matter Decay and Annihilation in the local Universe: CLUES from Fermi* in the Astrophysical Journal Letters in 2011 (APJ Letters 726, L6, 2011; Cuesta et al., 2011) and in a subsequent *erratum* in 2012, where an error on the pixel area computation has been corrected. I am the third author of this paper. My main contribution consisted in development of the code with which the DM annihilation and decay all-skymaps are obtained from the simulation, together with Antonio J. Cuesta. The *Fermi* observation simulations and choice of the DM models have been done by Tesla Jeltema and Stefano Profumo. The DM annihilation and decay all-skymaps obtained from the used Constrained local UniversE Simulations (CLUES; www.clues-project.org) box are made available on-line in a website made my myself (side.iaa.es/darkmattermaps/). I also contributed significantly in the paper writing and in the final analysis.

5.1 Constrained Simulations of the local Universe

In order to get a detailed description of the DM density distribution in the local Universe, a high-resolution cosmological simulation box from the CLUES project is used. This simulation

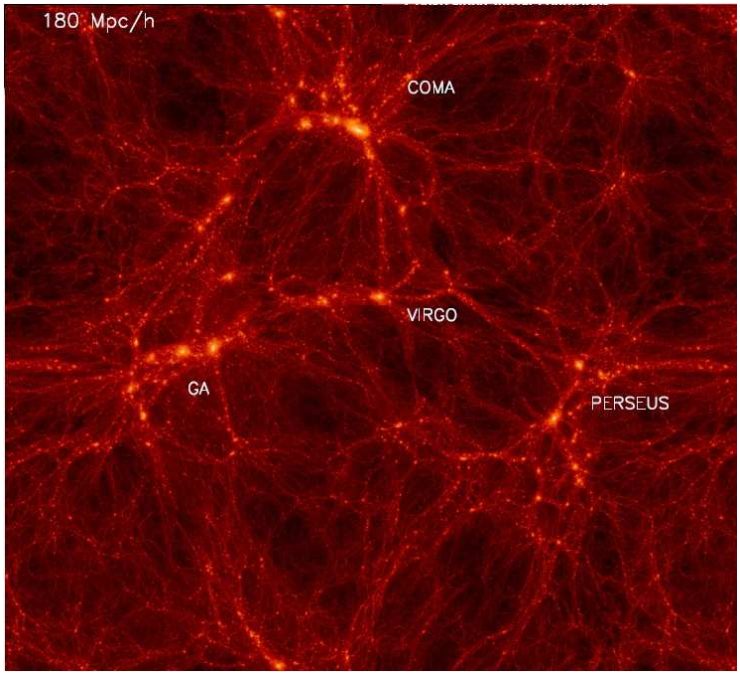

Figure 5.1: Large scale DM density distribution of the local Universe in the Box160CR constrained simulation of the CLUES project. The image shows a slice through the center of the box and its boundary is periodically wrapped to get a side length of 180 h^{-1} Mpc. Figure from www.clues-project.org.

set provides a realistic local density field which is consistent with the ΛCDM cosmology (see Yepes et al. 2009 and Gottloeber et al. 2010 for more details). Here the focus is on gamma-rays from large structures in the local Universe such as nearby galaxy clusters, therefore we choose the Box160CR simulation (see figure 5.1) which is a constrained realization of 1024^3 particles in a cube of 160 h^{-1} Mpc[1] on a side ran using the ART cosmological code (Kravtsov et al. 1997, Gottloeber & Klypin 2008). The initial conditions are set assuming WMAP3 cosmology and implements the constraints from the observed density field so that the simulation reproduces the observed matter distribution in the local Universe on large scales at redshift $z = 0$ (Hoffman & Ribak 1991, Klypin et al. 2003). The massive clusters such as Virgo, Coma and Perseus, together with the Great Attractor, are well reproduced. However, the final positions of these objects are not exactly at their observed positions, with a typical error around 5 h^{-1} Mpc.

This cosmological simulation permits to produce all-skymaps of the local DM density and density squared, which are proportional to gamma-ray emission due to particle DM decay and annihilation, respectively (to include more distant structures, one could use a box replication technique as in Zavala et al. 2010). Luminosities are computed following the method described in Kuhlen et al. (2008). The flux is proportional to $\sum_i m_p/4\pi d_i^2$ for decay and $\sum_i m_p \rho_i/4\pi d_i^2$ for

[1]Here h^{-1} indicates that the quantities quoted in this chapter are normalized to a value of $H_0 = 100$ km s^{-1} Mpc^{-1}, as typically done with cosmological simulations.

annihilation, where i runs from 1 to the number of particles in each pixel, m_p is the mass of the simulation particle, ρ_i is the density associated to the i-th particle, computed using the sphere which contains its 32 nearest neighbors (no smoothing kernel was used), and d_i is the distance to the observer. Only particles between 5 h^{-1} Mpc and 80 h^{-1} Mpc from the observer, placed at the right distance from the Virgo cluster which is the most constrained object in the simulation, are taken into account. A proper description of the density field in the innermost 5 h^{-1} Mpc would require a higher resolution simulation (as in Libeskind et al. 2010). This region, being empty of massive large structures, is not considered here. Fluxes are binned in a Cartesian grid of 3600 and 1800 pixels in galactic longitude and latitude, respectively. This corresponds to an angular resolution of roughly 0.1 deg per pixel, reproducing the best angular resolution of *Fermi*.
Due to the finite resolution of the simulation, the very inner center of DM halos cannot be resolved. For this reason, the flux is corrected in every pixel where the centers of DM halos lie (see Kuhlen et al. 2008). For each halo, a NFW profile (Navarro et al., 1996) is adopted and extrapolated up to the halo center. The scale radius r_s of these halos is calculated from the virial mass-concentration relation of Macciò et al. (2008). Typical corrections do not exceed ∼25% and ∼250% of their original value for decay and annihilation, respectively. Note that no boost factor due to DM substructures, or any other effect (such as adiabatic contraction from baryons or Sommerfeld enhancement), is included here.
The resulting all-skymaps are shown in figure 5.2, where known objects are highlighted. These maps are used as input for the *Fermi*-LAT observation simulations as described in the next section.

5.2 *Fermi* Satellite Observation Simulations

Using the full DM density and density squared skymaps, the simulated *Fermi*-LAT observations are produced using the `gtobssim` routine, part of the *Fermi* Science Tools package (v9r15p2), which incorporates the *Fermi*-LAT effective area and point spread function and their energy dependence. All simulations are run to generate a 5-year observation in the default scanning mode and using the P6_V3_DIFFUSE release of the LAT instrument response functions.
In the present study, two examples for the gamma-ray spectrum from decay or annihilation of the DM particle are adopted as representative of more general classes of DM models. The first model features a DM particle with a mass of 1.6 TeV yielding a pair of $\mu^+\mu^-$ (Bergström et al., 2009), which was shown to fit accurately the PAMELA data in Papucci & Strumia (2010). In this case, gamma-ray emission is produced directly in the final state radiation (FSR) as well as through inverse IC of the high energy e^+ and e^- produced off of CMB photons. The expected contributions from both FSR and IC are included (see Ackermann et al. 2010b for details). Given that the energy loss time scales for high-energy electrons and positrons produced by muon decays are much shorter than the diffusion time scales in the structures considered here, diffusion is neglected, and the emission of said electrons and positrons via IC up-scattering of CMB photons is calculated. This yields a significant low-energy component, extending all the way up to energies relevant for *Fermi* (Profumo & Jeltema, 2009). A second, more conventional, model is also adopted and it inspired by what expected in e.g. supersymmetric models with a bino-like lightest

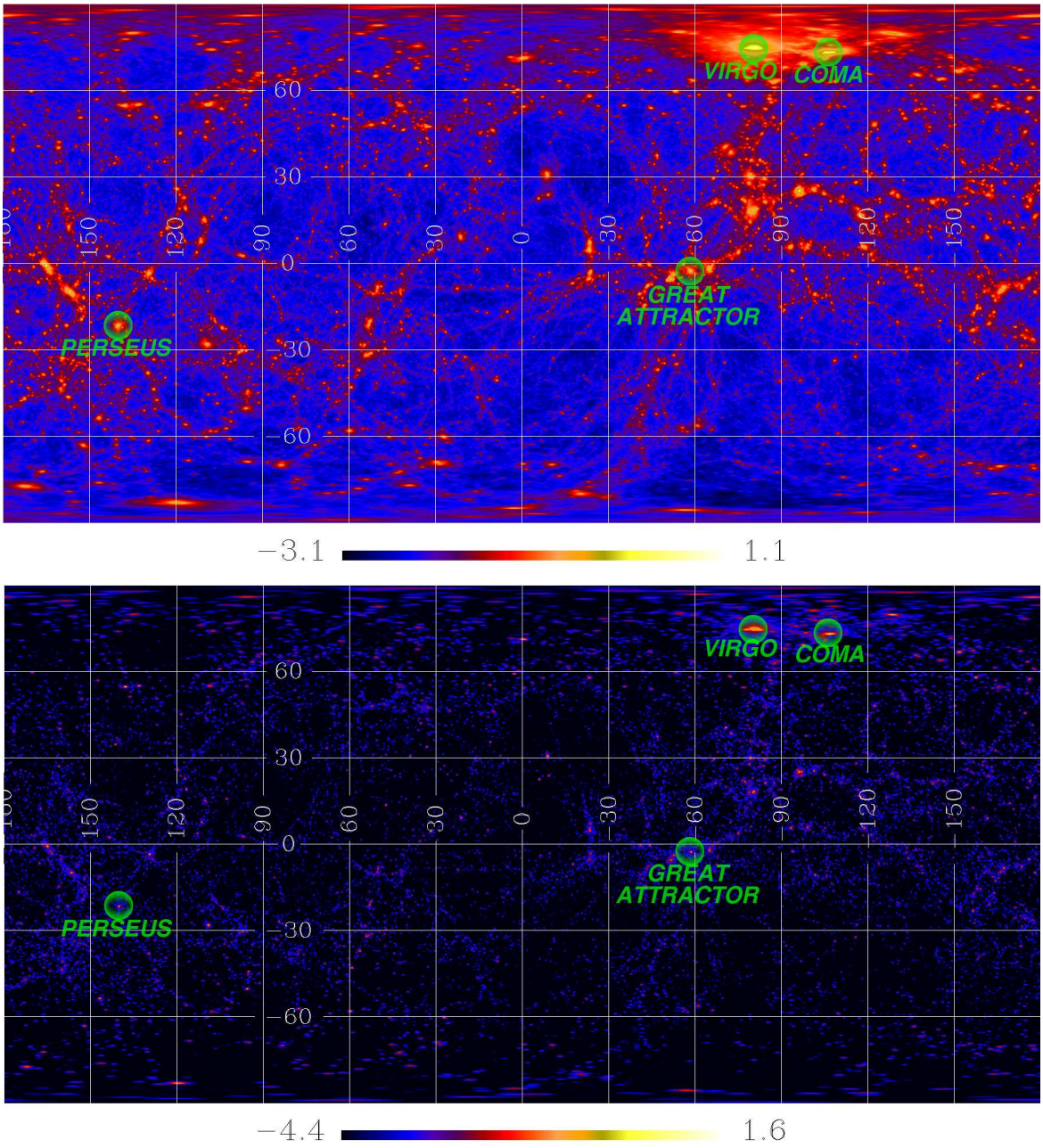

Figure 5.2: DM distribution in the local Universe constrained cosmological simulation Box160CR. These all-skymaps are Cartesian (equirectangular plate carrée) projections in Galactic coordinates. Top panel shows the density distribution, whereas the bottom panel displays the distribution of density-squared. The maps are color-coded according to the $\log_{10}$ of the DM flux, and units are GeV/c^2 cm^{-3} kpc sr^{-1} for decay map and GeV^2/c^4 cm^{-6} kpc sr^{-1} for the annihilation map. Large structures reproduced by the simulation such as Virgo, Coma, and Perseus clusters, together with the Great Attractor, are labeled. Images are done with HEALPix (healpix.jpl.nasa.gov).

supersymmetric particle: a 100 GeV neutralino yielding a quark-antiquark pair (of *b* flavor, for definiteness). The primary source of gamma-rays here is the decay of neutral pions produced in the $b\bar{b}$ hadronization chains.
The *Fermi* simulations of the gamma-ray signal from DM annihilation (both to $b\bar{b}$ and $\mu^+\mu^-$) are normalized to a DM flux in the *Fermi* energy range of 9×10^{-8} cm^{-2} s^{-1} integrated over the full sky. This is chosen in order to obtain good statistics to compare between different extragalactic structures. For $b\bar{b}$, this flux corresponds to a cross-section of 10^{-23}cm^{3}s^{-1}. This cross-section value has already been excluded by current indirect searches with *Fermi*, PAMELA and HESS (see e.g. Cirelli et al. 2010 and Papucci & Strumia 2010). Yet this extreme case is maintained for comparison purposes. For $\mu^+\mu^-$, the same total flux corresponds to an annihilation cross-section of 5.8×10^{-23}cm^{3}s^{-1}, which gives a good fit to the PAMELA positron excess. This value is only marginally excluded in Ackermann et al. (2010b) if cluster substructures are considered, and also in Papucci & Strumia (2010) if the Milky Way DM halo follows a NFW profile.
In the case of DM decay as e.g. in supersymmetry with very weak R-parity violation, a total *Fermi* flux over the full sky of 1.5×10^{-6} cm^{-2} s^{-1} is simulated. This corresponds to a decay lifetime of $\tau \simeq 10^{26}$ s for $b\bar{b}$ and $\tau \simeq 3 \times 10^{26}$ s for $\mu^+\mu^-$. These lifetimes are not currently excluded by other gamma-ray constraints and the latter case gives a good fit to the PAMELA measured positron fraction excess (e.g. Papucci & Strumia 2010; Cirelli et al. 2010; Chen et al. 2010; Meade et al. 2010; Zhang et al. 2010).
The observation simulations also include realistic treatments of both Galactic and isotropic diffuse backgrounds. In particular, the gamma-ray emission from the Galaxy is quite variable across the sky, an important consideration when comparing the expected signals from known objects. For example, structures lying at low Galactic latitudes like the Great Attractor will have much higher gamma-ray backgrounds than high latitude objects like the Virgo cluster. Therefore, 5-year *Fermi* observations of the Galactic and isotropic diffuse backgrounds are simulated using the `gll_iem_v02.fit` and `isotropic_iem_v02.txt` background models, respectively, released by the *Fermi* collaboration. The output background maps are then used to compute signal-to-noise (S/N) all-skymaps as shown in figure 5.3 and detailed in the next section.

5.3 Results and Discussion

The main result of this chapter is shown in figure 5.3 and table 5.1: the S/N prediction for the extragalactic gamma-ray emission in the 100 MeV–10 GeV energy range from DM annihilation and decay in the local Universe as it would be seen by the *Fermi* satellite after 5-years of observations. This is the first time that a constrained cosmological simulation is used to generate maps that are consistent with both the currently accepted cosmology and the observed local Universe. These maps assume a particle mass of 100 GeV which annihilates or decays through the $b\bar{b}$ channel. Maps for the DM model yielding $\mu^+\mu^-$ are similar but present lower S/N. Pixels are binned in squares of 1 deg which matches the *Fermi*-LAT PSF at around 1 GeV as well as the typical angular size in the sky of nearby clusters. In order to make a quantitative analysis of DM detectability in some large nearby structures, including cluster and filamentary regions, in table 5.1 the photon number counts and S/N from annihilation and decay in the 1 GeV–10 GeV

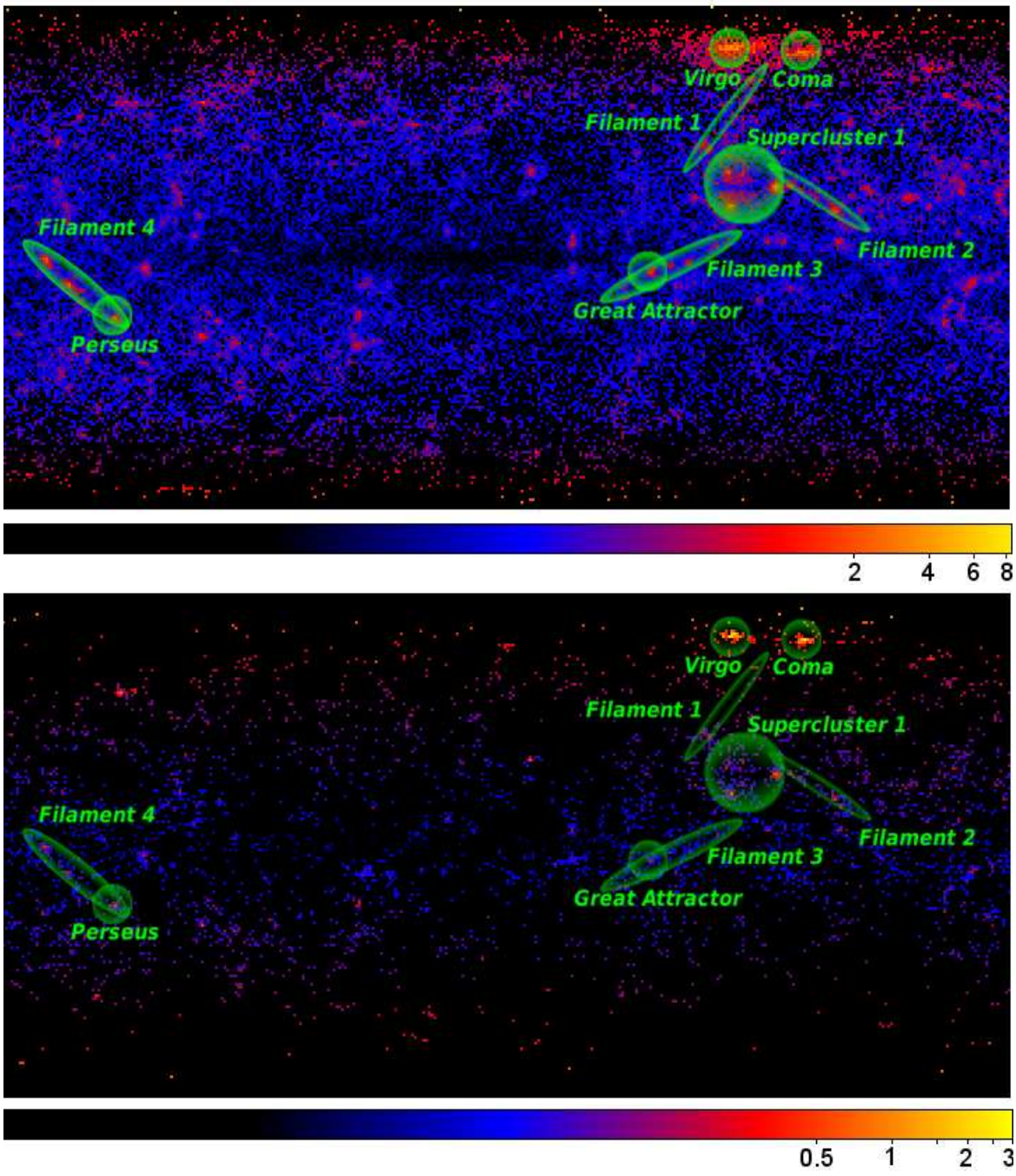

Figure 5.3: S/N all-skymaps from 5-year *Fermi* simulations for DM gamma-rays in the energy range 100 MeV–10 GeV built from the Box160CR constrained simulation of the local Universe. Results for DM decay (top) and annihilation (bottom) are shown for the $b\bar{b}$ channel model.

energy range are computed, for both the $b\bar{b}$ and $\mu^+\mu^-$ channels. Here, the S/N is defined as the signal over the square root of the signal plus the background gamma-ray emission. This choice of energy range maximizes the S/N ratio as compared to the 100 MeV–10 GeV range, as the *Fermi*-LAT sensitivity is significantly worse at lower energies.

In the case of DM decay, nearby clusters and filamentary regions could be detected for decay lifetimes longer than those currently ruled out by other gamma-ray constraints. This shows that extragalactic structures are excellent targets to search for a signal or to place constraints on DM decay models, including those fitting the PAMELA positron data. It is important to note that according to table 5.1 the most promising clusters for DM studies are high galactic latitude objects, like Virgo and Coma, which comes as no surprise given that they are less affected by the Galactic background. Moreover, the S/N is not very sensitive to the area of the region under analysis, provided that the aperture radius is no more than few degrees, where the signal saturates and therefore the background noise makes the S/N decrease. Note that, in the case of DM decay, the filamentary structure of the cosmic web constitutes an interesting target for DM searches. This is the first time that filaments have been considered as targets for DM searches. In this case the gamma-ray luminosity is just proportional to the enclosed mass, whereas this is only approximately true for annihilation (Pinzke et al., 2009). This means that massive extragalactic objects offer the best chance for detection (see table 5.1). Large filaments of DM match and even exceed the values of S/N as compared to those in large clusters, although caution should be taken regarding the exact orientation in the sky of these filaments as some variation in smaller volume constrained simulations is found. Superclusters such as the region marked in figure 5.3 show even more significant values. Hence, these features of the large scale structure of the Universe may prove to be a very promising novel way to detect decaying DM with *Fermi*. This is an important result as the *Fermi* collaboration and other authors have started to severely constrain models of annihilating DM (Ackermann et al. 2010b, Abdo et al. 2010c, Abdo et al. 2010a, Abdo et al. 2010b) while decaying DM has comparatively received considerably smaller attention (see e.g. Dugger et al. 2010). Currently available gamma-ray observations provide less stringent constraints in this case, and from a theoretical standpoint, decaying DM is a generic prediction of many theories beyond the Standard Model of particle physics, for both neutralino DM and models that explain the PAMELA positron excess.

The results obtained here do not show any strong hint in favor of a possible *Fermi* detection of extragalactic gamma-rays induced by DM annihilation. However, this cannot be excluded completely as boost factors from DM substructures (see e.g. Sánchez-Conde et al., 2011 and Pinzke et al., 2011), adiabatic compression and Sommerfeld effect that may significantly enhance the final gamma-ray emission are not considered. Besides, the predicted signals will be enhanced due to recent determinations of the cosmological parameter σ_8 suggesting a higher value than the one assumed here, which is consistent with WMAP3 cosmology.

These conclusions should be complemented by an analysis of the galactic components, mainly from DM subhalos like those hosting the DM-rich dwarf spheroidal galaxies around the Milky Way. This has been recently addressed in Anderson et al. (2010) based on the analysis of a high-resolution simulation of a galactic DM halo, as in previous papers by Kuhlen et al. (2008) and Springel et al. (2008). Note that the presence of any galactic foregrounds has a potential effect on the significance of the predictions presented here, although only the Galactic Center and massive

subhalos have been shown in these papers to be relevant. Moreover, the annihilation or decay of DM in Galactic subhalos will produce gamma-ray photons similar to those from DM in local extragalactic structures and thus if these happened to be coincident in the sky it would only enhance the signal. Nevertheless, a spectral confirmation of the potential DM signal is necessary to validate any claim of detection. On the other hand, these results on DM search will benefit from additional hints from the study of the angular power spectrum of the gamma-ray flux (e.g. Fornasa et al. 2009, Hensley et al. 2010, see also Zavala et al. 2010 for a similar approach to that presented here, extended to more distant contributions).

Concluding, *Fermi* will be able to place strong constraints on the DM nature by studying extragalactic objects, in particular for decay. The theoretical predictions from constrained simulations presented here provide the astroparticle community with the most interesting prospects for the detection of the elusive DM particle. In fact, the density all-skymaps produced here, and freely available on-line (side.iaa.es/darkmattermaps/), have also been used in Gómez-Vargas et al. (2012) (work of which I am third author) to study the *Fermi* prospects for the extragalactic detection of $\mu\nu$SSM gravitino DM.

Object	$b\bar{b}$ channel				$\mu^+\mu^-$ channel				background
	ann		dec		ann		dec		
Coma 1 deg	5.297	(44)	5.297	(44)	1.237	(7)	2.109	(13)	25
Coma 2 deg	5.068	(68)	7.583	(114)	0.818	(9)	2.741	(33)	112
Coma 5 deg	3.245	(85)	10.078	(303)	0.445	(11)	3.245	(85)	601
Virgo 1 deg	5.041	(36)	5.646	(43)	0.000	(0)	1.118	(5)	15
Virgo 2 deg	5.831	(68)	10.025	(147)	1.132	(10)	3.116	(31)	68
Virgo 5 deg	4.185	(102)	15.588	(488)	0.666	(15)	5.068	(126)	492
Perseus 1 deg	0.777	(8)	4.178	(51)	0.298	(3)	1.323	(14)	98
Perseus 2 deg	0.503	(10)	4.042	(88)	0.152	(3)	1.041	(21)	386
Perseus 5 deg	0.271	(14)	3.156	(168)	0.077	(4)	0.807	(42)	2665
GAttractor 1 deg	0.175	(5)	1.741	(51)	0.070	(2)	0.592	(17)	807
GAttractor 2 deg	0.130	(8)	1.654	(103)	0.033	(2)	0.438	(27)	3777
GAttractor 5 deg	0.089	(15)	1.379	(234)	0.024	(4)	0.343	(58)	28572
Filament1, $d = 65$Mpc/h	0.224	(14)	4.485	(290)	0.112	(7)	1.379	(87)	3891
Filament2, $d = 40$Mpc/h	0.517	(46)	6.541	(602)	0.135	(12)	1.797	(161)	7869
Filament3, $d = 65$Mpc/h	0.226	(54)	3.117	(750)	0.079	(19)	0.756	(181)	57127
Filament4, $d = 55$Mpc/h	0.380	(60)	5.486	(881)	0.120	(19)	1.338	(212)	24904
Supercluster1, $d = 45$Mpc/h	0.640	(101)	8.915	(1445)	0.177	(28)	2.343	(372)	24829

Table 5.1: S/N ratio and number of photon counts (in brackets) in the 1 GeV–10 GeV energy range for the different DM models. For cluster regions, three different radii are considered (1, 2, and 5 degrees). Filaments 1 to 4 represent elongated regions connected to these clusters which are potentially interesting due to their high S/N. Median distance of halos belonging to these filaments is indicated. Supercluster 1 is a collection of massive halos which accidentally lie along the line-of-sight. Background counts from the Galactic plus extragalactic diffuse in the same regions are also listed. The annihilation to $b\bar{b}$ case is shown for comparison purposes only as the corresponding cross-section is already excluded by current observational constraints. Note however that we are not considering any signal boost factor.

Chapter 6

On the Physics of Radio Halos: Scaling Relations and Luminosity Function

There are many aspects of the Universe
that still cannot be explained satisfactorily by science;
but ignorance only implies ignorance that may someday be conquered.

Isaac Asimov

This chapter is dedicated to make predictions for the RH population of a complete cosmological sample of galaxy clusters up to redshift $z = 1$ obtained from the MultiDark N-body cosmological simulation. A *phenomenological* model is constructed in order to assign to each DM-only simulated halo a gas density profile as to reproduce the basic observed X-ray cluster properties. Assuming then that RHs are generated by secondaries of the hadronic CR interactions with the ICM, a new *hybrid* hadronic model is constructed merging the result of previous hydrodynamic simulations and analytical works. In particular, the CR transport phenomena modeling is included in the approach presented here. The radio-to-X-ray and radio-to-SZ observed scaling relations are reproduced. It is shown that the *hybrid* hadronic model constructed here is a perfectly viable explanation for RHs and it is not in tension with any current observational constraint. The radio luminosity function at 1.4 GHz is calculated and compared to existing observations. Finally, predictions for the LOFAR survey at 120 MHz are presented.
At the time of writing this thesis, the work presented in this chapter is going to be submitted for publication in few weeks. I will be the first author of this paper having done all the work in collaboration with Christoph Pfrommer and my thesis supervisor Franciso Prada.
Note that in this chapter the cluster mass M_Δ and radius R_Δ are defined with respect to $\Delta = 200$ or $\Delta = 500$ times the Universe *critical* density. Additionally, $\Omega_\mathrm{m} = 0.3$, $\Omega_\Delta = 0.7$ and $H_0 = 100 \times h_{70}$ km s^{-1} Mpc^{-1} where $h_{70} = 0.7$.

6.1 Methodology

The two fundamental ingredients of this work are the cosmological simulation of the Universe from which the complete cluster sample is constructed, and the emission model. Here, the Multi-

Dark simulation is used and will be described in section 6.1.1, along with the final cluster sample. As it will be shown, for any given cluster, the necessary ingredients for the emission model are mass, temperature, and gas density distribution. The complete cluster sample is constructed from an N-body cosmological simulation, i.e. a *DM-only* simulation, where a gas density profile, phenomenologically constructed from state-of-art X-ray observations, is assigned to each object as shown in section 6.1.2. In doing this, it is shown that the approach can reproduce the known X-ray cluster characteristics, such as the X-ray luminosity function (XLF), the luminosity-mass relation, $L_X - M$, and the $Y_X - M$ relation, where $Y_X = M_{gas} k_B T_X$ with an X-ray-derived gas mass M_{gas} and the temperature T_X (Kravtsov et al., 2006). Moreover the $Y_{SZ} - M$ relation is compared to SZ-derived measurements. Only if the model matches available cluster data on the gas properties, it can be used to explore different parametrizations of CR physics and its implications for the radio and gamma-ray emission, explained in section 6.1.5.

6.1.1 MultiDark Simulation and Final Cluster Sample

The MultiDark simulation[1] used in this work is described in detail in Prada et al. (2011) and Riebe et al. (2011) (see also figure 1.3). It is a N-body cosmological simulation done with the the Adaptive Refinement Tree (ART) code (Kravtsov et al., 1997) of 2048^3 particles within a (1000 Mpc h^{-1})^3 cube. The latest WMAP5 and WMAP7 cosmological parameters were used. This simulation is particularly well suited for the purpose of this work because of its large number clusters.

The technique described in Hu & Kravtsov (2003) is used to convert M_{200} and R_{200} provided by the MultiDark halo catalog to M_{500} and R_{500}. In creating the cluster sample, only distinct halos are selected, i.e. those halos that are not sub-halos of any other halo, which by definition are not galaxy clusters.

Additionally, the main emission mechanism in the ICM is assumed to be the thermal bremsstrahlung, which is true only above approximately 3×10^7 K ≈ 2.6 keV (Sarazin, 1988). Below this temperature, there could be other important contributions to the emission, e.g. from atomic lines. Therefore, a mass cut of $M_{200} \geq 1 \times 10^{14}\ h^{-1}\ \mathrm{M}_\odot \approx 1.4 \times 10^{14}\ h_{70}^{-1}\ \mathrm{M}_\odot$ is imposed such as it ensures $kT \gtrsim 2.6$ keV, assuming the $M_{500} - T_{ci}$ relation of Mantz et al. (2010).

The LOFAR radio observatory is expected to detect RHs up to redshift $z \approx 1$. Thus, different simulation snapshots up to $z = 1$ are used. In table 6.1, the total cluster number in the final cluster sample of this work at different redshifts is shown.

6.1.2 Gas Density Modeling

A *phenomenological* approach is adopted to construct the gas density profiles directly from X-ray observations. A suitable X-ray sample that provides the needed information is the Representative *XMM-Newton* Cluster Structure Survey (REXCESS) sample (Croston et al., 2008; Pratt et al., 2009). It is a sample of 31 galaxy clusters of different dynamical states at redshift $0.06 < z < 0.18$ with detailed information of the de-projected electron density profiles (Croston et al., 2008). In

[1] www.multidark.org

Redshift z	Number of Halos
0	13763
0.2	12398
0.3	10783
0.4	7789
0.61	5187
0.78	3372
1	1803

Table 6.1: Number of halos in the MultiDark snapshots at redshift z for $M_{200} \geq 1 \times 10^{14}\ h^{-1}\ \mathrm{M}_{\odot} \approx 1.4 \times 10^{14}\ h_{70}^{-1}\ \mathrm{M}_{\odot}$.

figure 6.1, the 31 electron density profiles of the REXCESS sample color-coded by CCCs and NCCCs are shown.

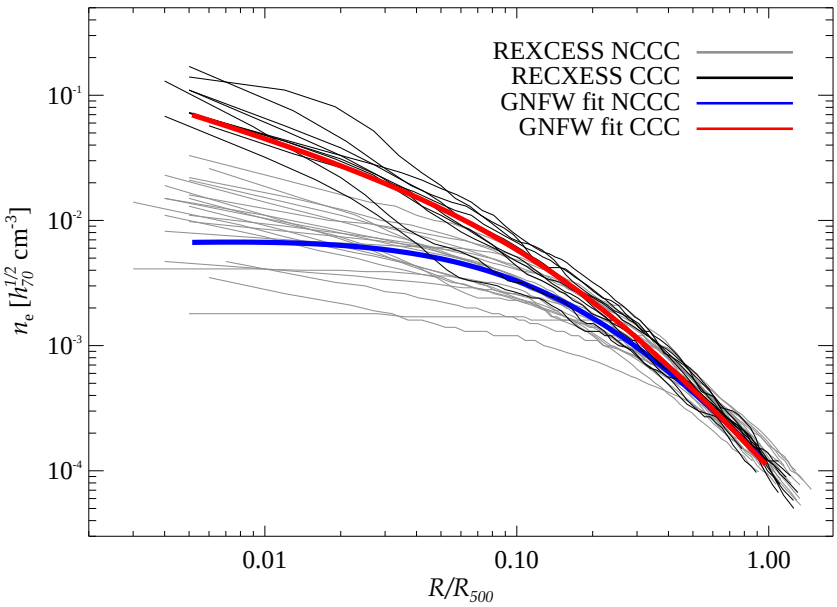

Figure 6.1: Electron density profiles of the 31 clusters in the REXCESS sample. Grey and black lines represent NCCCs and CCCs, respectively. The blue and red lines represent the GNFW mean profile for NCCCs and CCCs, respectively.

In order to obtain a general electron density profile that will be attached to the simulated clusters,

the REXCESS data are fitted with a generalized Navarro-Frank-White (GNFW) profile,

$$n_{\rm e}(x) = \frac{n_0}{x^{\beta}\,[1+x^{\alpha}]^{\frac{\delta-\beta}{\alpha}}}\,, \tag{6.1}$$

where $x = R/R_{\rm c}$ and $R_{\rm c}$ is the cluster core radius. To reduce the dimensionality of the fit, the representative values of $R_{\rm c} = 0.2\,R_{500}$, $\alpha = 1$ and $\delta = 2.5$ are fixed. The REXCESS profiles are fitted in log-log space, separating them in the two categories of NCCCs and CCCs as shown in figure 6.1. The resulting fits are shown in blue and red for the NCCC and CCC population, respectively. The results are $n_{0,\rm NCCC} = 1.02 \times 10^{-2}\ h_{70}^{1/2}$ cm^{-3}, $n_{0,\rm CCC} = 8.32 \times 10^{-3}\ h_{70}^{1/2}$ cm^{-3}, $\beta_{\rm NCCC} = -0.093$ and $\beta_{\rm CCC} = 0.592$.

The next step is to introduce a mass-scaling in order to apply the GNFW profiles to all simulated clusters. The gas mass fraction-mass scaling $f_{gas,500} - M_{500}$ of Sun et al. (2009) is used (their equation 8). $f_{\rm gas,500}$ can be expressed in the following way:

$$f_{\rm gas,500} = \frac{M_{\rm gas,500}}{M_{500}} = \frac{\int_0^{R_{500}} \rho_{\rm gas}{\rm d}V}{M_{500}} \tag{6.2}$$

with $\rho_{\rm gas} = n_{\rm e} m_{\rm p}/(X_{\rm H} X_{\rm e})$ where $m_{\rm p}$ is the proton mass, $X_{\rm H} = 0.76$ is the primordial hydrogen mass fraction and $X_{\rm e} = 1.157$ the ratio of electron-hydrogen number densities in the fully ionized ICM (Sarazin, 1988). For each cluster i, a *mass-scaled* gas profile is then defined as $\rho_{\rm gas,i} = C_i\,\rho_{\rm gas}$ with:

$$\begin{aligned} C_i &= (0.0656 \pm (0.0064 g_1)) h_{70}^{-1.5} \\ &\times \left(\frac{M_{500,i}}{1.04\times10^{13} h_{70}^{-1} {\rm M}_{\odot}}\right)^{0.135\pm(0.030 g_2)} \frac{M_{500,i}}{\int_0^{R_{500,i}} \rho_{\rm gas}{\rm d}V} \end{aligned} \tag{6.3}$$

where g_1 and g_2 are random Gaussian number which are used in order to simulate the natural scatter of the gas profiles.[2]

Hence, each cluster in the final sample has assigned a gas density profile $\rho_{\rm gas,i}$ that obeys the observed $f_{gas,500} - M_{500}$ relation and is uniquely determined by the object DM mass $M_{500,i}$ and by its property of being a NCCC or CCC. The latter property is assigned to each halo depending on its merging history. In particular, the offset parameter $X_{\rm off}$ computed for the MultiDark catalog is used. This is defined as the ratio between the distance from the halo center to the center of mass and the virial radius. The parameter assesses the dynamical state of the cluster and whether the halo experienced a recent merger or not. Current observations reveal a ratio of NCCCs and CCCs of about 50% (see, e.g. Chen et al., 2007; Sanderson et al., 2009). Since there is a correlation between merging clusters and NCCCs, the median of the $X_{\rm off}$ distribution is used to separate the sample into CCCs and NCCCs (with NCCCs as those halos with the larger dynamical offsets). Clearly, this is an over-simplification, and future X-ray surveys will have to determine this property also as a function of redshift.

[2]The values 0.0064 and 0.03 quoted in equation 6.3 do not represent the proper scatter of the $f_{\rm gas,500} - M_{500}$ relation but reflect the parameter errors. The parameter values are rescaled to a Hubble constant of h_{70} used in this work.

The redshift evolution of the gas profiles is also accounted for. While the NCCC and CCC gas profiles as derived from the REXCESS cluster sample are merely used to define a profile shape, the normalization of the gas profiles is set by the observational $f_{\rm gas,500} - M_{500}$ relation (Sun et al., 2009). The 43 clusters used in Sun et al. (2009) have redshifts $0.012 < z < 0.12$ with a *median* of $z \approx 0.04$. Thus, the phenomenological gas profile is representative of the cluster population at $z = 0$. To extend this profile to high-z, a *self-similar* scaling of the gas density as $\rho_{\rm gas}(z) = E(z)^2 \rho_{\rm gas}(z = 0)$ is included, where $E(z)^2 = \Omega_{\rm m}(1 + z)^3 + \Omega_\Lambda$.

6.1.3 X-ray and SZ Scaling Relations

In order to check whether the phenomenologically derived gas profiles are reproducing observations, the bolometric X-ray thermal bremsstrahlung luminosity $L_{\rm bol}$ of the MultiDark clusters is calculated as in Sarazin (1988)[3] and compared with the observed $L_{\rm bol} - M_{500}$ relation and XLF.[4] To assign a temperature to the MultiDark clusters (that is needed for calculating $L_{\rm bol}$ and $Y_{\rm X}$), the $T_{\rm ci} - M_{500}$ relation by Mantz et al. (2010) is used,

$$\log_{10}\left(\frac{k_{\rm B} T_{\rm ci}}{\rm keV}\right) = A + B\ \log_{10}\left(\frac{E(z) M_{500}}{10^{15} h_{70}^{-1} {\rm M}_\odot}\right) \tag{6.4}$$

where $A = 0.91$, $B = 0.46$, $T_{\rm ci}$ is the cluster temperature *not* centrally excised (see Mantz et al., 2010) and $k_{\rm B}$ is the Boltzmann constant. Mantz et al. (2010) report a scatter of $\sigma_{\rm yx} = 0.06$,[5] which is applied to the MultiDark clusters using Gaussian deviates.

In the top left panel of figure 6.2, the comparison between the $L_{\rm bol} - M_{500}$ relation obtained here and observations by Mantz et al. (2010) (*all* data, see their table 7) is shown. Their sample is composed of 238 clusters at $0.02 < z < 0.46$ with a median of $z \approx 0.2$ and self-consistently takes into account all selection effects, covariances, systematic uncertainties and the cluster mass function. For this reason, the Mantz et al. (2010) data is compared to the result obtained with the MultiDark snapshot at $z = 0.2$, where the comparison is limited to the mass range covered by the observations. Overall, there is reassuring agreement between the phenomenological model constructed here and the data, which probe the model most closely on scales around the cluster core radii (where the contribution to $L_{\rm X}$ per logarithmic interval in radius, $\mathrm{d}L_{\rm X}/\mathrm{d}\ln r \propto r^3 n^2(r) \sqrt{k_{\rm B} T}$ attain its maximum). In table 6.2, the $L_{\rm bol} - M_{500}$ scaling relation and its scatter for different redshifts are shown. The scatter of the MultiDark sample at all redshifts is Gaussian distributed

[3]The procedure is checked by fitting each of the 31 REXCESS clusters with equation 6.1 and calculating $L_{\rm bol}$ with the measured gas temperature of each cluster. As a result, we fall short to the observed luminosity by a mean (median) of about 21% (20%). This is reasonable considering that the parameters $R_{\rm c}$, α and γ are not allowed to vary between different objects. Additionally, atomic line emission, which may give a noticeable contribution, in particularly for low-mass clusters and in the cluster outskirts of larger systems, is neglected.

[4]The mean (median) difference at $z = 0$ between $L_{\rm bol}$ within R_{200} or within R_{500} is $\approx 5\%$ ($\approx 7\%$). While $L_{\rm bol}$ refers to the quantity calculated within R_{500}, note that the XLF for luminosities calculated within R_{200} will be barely changed.

[5]Scatter is calculated as $\sigma_{\rm yx} = \sqrt{\left\{\Sigma_{i=1}^{N} [Y_i - (A + B\, X_i)]^2\right\}/N - 1}$ where the sum extends over the data points X_i, Y_i, and A and B are the fit parameters.

with a standard deviation of $\sigma_{yx} \approx 0.18$ matching the observational result of Mantz et al. (2010), which report a scatter of $\sigma_{yx} = 0.185$.

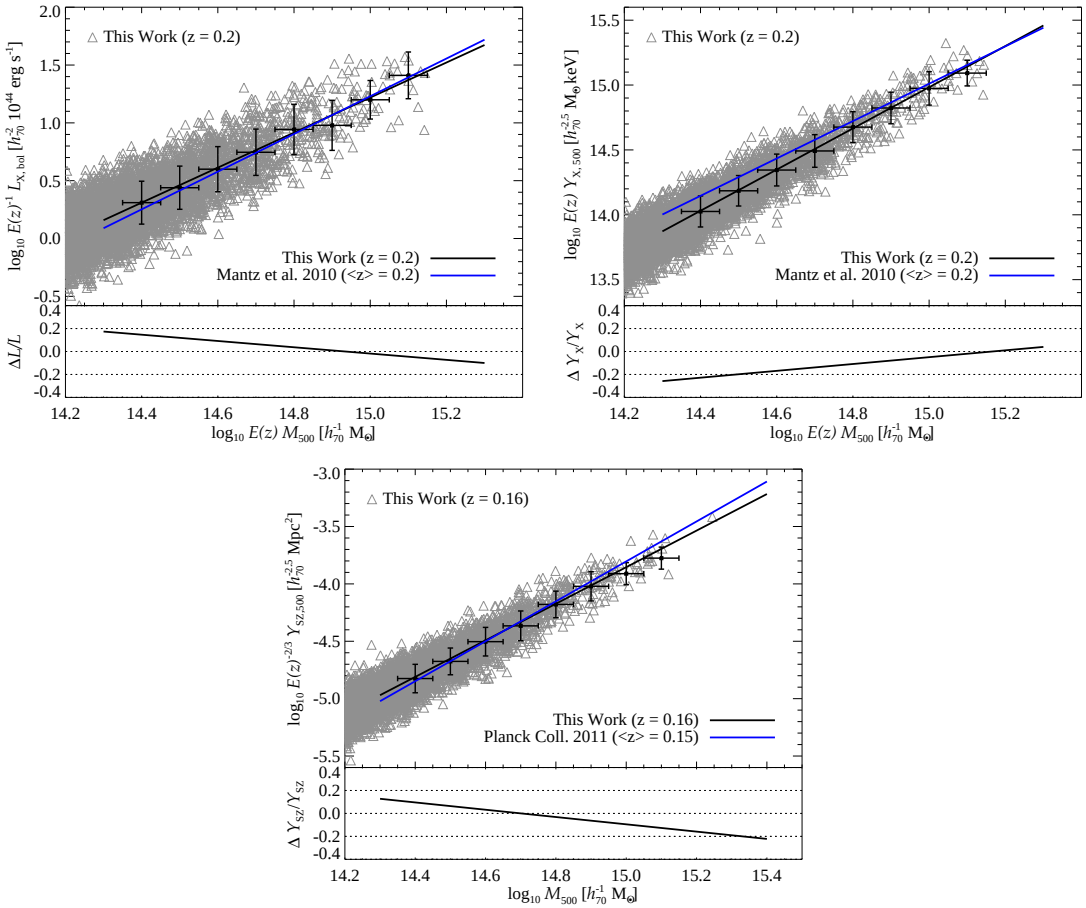

Figure 6.2: X-ray and SZ scaling relations. Grey triangles show the MultiDark sample (limited to the mass range covered by observations), the black line is the corresponding scaling relation, and the blue line is the observational result. The black crosses represent the median values of the quantity in question for a given mass bin (indicated by horizontal error bars), and the vertical error bars represent the standard deviation within a bin. *Top Left.* Bolometric X-ray luminosity-to-mass relation, $L_{\rm bol} - M_{500}$, at $z = 0.2$ compared to the observational sample by Mantz et al. (2010) with a median of $z \approx 0.2$. *Top Right.* $Y_{\rm X} - M_{500}$ scaling relation in comparison to the observational sample by Mantz et al. (2010). *Bottom.* $Y_{\rm SZ} - M_{500}$ scaling relation at $z = 0.16$ in comparison to the observational sample by Planck Collaboration et al. (2011) with a median redshift of about 0.15. The bottom panels show the relative difference to the observational scaling relations.

In the top right panel of figure 6.2, the $Y_{\rm X} - M_{500}$ relation obtained here is compared to observational data (Mantz et al., 2010). The phenomenological model agrees nicely at high-mass end, but under-predicts the observed scaling at low masses by about 20% (at the 1-σ level). This is the same level of deviations from the data as in the case of $L_{\rm X}$, which is more significant due to

Redshift z	A	B	σ_{yx}
0	-21.41 ± 0.11	1.50 ± 0.01	0.179
0.1	-21.30 ± 0.12	1.50 ± 0.01	0.179
0.2	-21.50 ± 0.13	1.51 ± 0.01	0.178
0.4	-21.13 ± 0.17	1.49 ± 0.01	0.178
0.61	-21.59 ± 0.22	1.53 ± 0.01	0.177
0.78	-20.73 ± 0.29	1.48 ± 0.02	0.177
1	-20.45 ± 0.42	1.46 ± 0.03	0.177

Table 6.2: $L_{\rm bol} - M_{500}$ scaling relations in the form of $\log_{10}\ (L_{\rm bol}\ /\ E(z)\ h_{70}^{-2}\ 10^{44}\ {\rm erg\ s^{-1}}) = A + B\ \log_{10}\ (E(z)\ M_{500}\ /\ h_{70}^{-1}\ {\rm M_\odot})$. The relation scatter σ_{yx} is also shown.

the smaller scatter in the $Y_{\rm X}$ relation. The differential contribution to the thermal energy per logarithmic interval in radius (and hence to the integrated Compton-y parameter), $\mathrm{d}Y/\mathrm{d}\ln r \propto r^3 P(r)$, peaks at scales slightly smaller than R_{500} with 1-σ contributions extending out to $3\,R_{500}$ (Battaglia et al., 2010). Hence, the observational scaling constrains the model on those large scales, quite complementary to the X-ray luminosity. The deviation at small masses either indicates different assumptions about $f_{\rm gas}$, the gas temperature, or different selection effects of either the observational sample used to calibrate the model or to compare the scaling relation to. E.g., Mantz et al. (2010) determine their masses by adopting a constant value for $f_{\rm gas}$, in contrast to the approach adopted here which uses the observed $f_{\rm gas,500} - M_{500}$ relation given by Sun et al. (2009). Additionally, here, the *centrally included* temperature of Mantz et al. (2010) is used throughout all the work, while Mantz et al. (2010) use the *centrally excised* temperature to calculate $Y_{\rm X}$. This assumption also impacts the scatter of the $Y_{\rm X} - M$ relation. In fact, the use of the *centrally included* temperature results in a scatter of $\sigma_{yx} \approx 0.11$ (see table 6.3 where the $Y_{\rm X}$ scaling relations obtained here are reported), significantly higher than the value of $\sigma_{yx} = 0.052$ found by Mantz et al. (2010).

In the bottom panel of figure 6.2, the $Y_{\rm SZ} - M_{500}$ relation (calculated as in equation 3 of Battaglia et al., 2011) is compared to the observed scaling relation of Planck Collaboration et al. (2011). Their sample contains clusters up to $z \approx 0.45$ and has a median of $z \approx 0.15$; hence, the comparison is done with the MultiDark snapshot $z = 0.16$ (containing 11419 clusters above the adopted mass cut) which however is not used throughout the rest of the work. The model reproduces the data remarkably well, except for the high-mass end where simulations have a weaker constraining power due to the comparably small box size in comparison to the survey volume of *Planck*. In table 6.4, the SZ scaling relations for different redshifts are reported. The corresponding scatter of $\sigma_{yx} \approx 0.11$ compares well with the *Planck* result of $\sigma_{yx} \approx 0.1$.

Redshift z	A	B	σ_{yx}
0	-9.18 ± 0.07	1.61 ± 0.01	0.109
0.1	-8.85 ± 0.07	1.59 ± 0.01	0.109
0.2	-8.82 ± 0.08	1.59 ± 0.01	0.109
0.4	-8.79 ± 0.10	1.59 ± 0.01	0.108
0.61	-8.65 ± 0.14	1.59 ± 0.01	0.109
0.78	-8.36 ± 0.18	1.57 ± 0.01	0.109
1	-8.28 ± 0.26	1.57 ± 0.02	0.109

Table 6.3: $Y_{\rm X,500} - M_{500}$ scaling relations in the form of $\log_{10}\ (E(z)\ Y_{\rm X,500}\ /\ h_{70}^{-2.5}\ {\rm M}_\odot\ {\rm keV}) = A + B\ \log_{10}\ (E(z)\ M_{500}\ /\ h_{70}^{-1}\ {\rm M}_\odot)$. The relation scatter σ_{yx} is also shown.

Redshift z	A	B	σ_{yx}
0	-27.93 ± 0.07	1.60 ± 0.01	0.109
0.1	-27.74 ± 0.07	1.59 ± 0.01	0.109
0.16	-27.76 ± 0.08	1.59 ± 0.01	0.109
0.2	-27.65 ± 0.08	1.59 ± 0.01	0.109
0.4	-27.57 ± 0.10	1.59 ± 0.01	0.108
0.61	-27.50 ± 0.13	1.59 ± 0.01	0.109
0.78	-27.15 ± 0.18	1.58 ± 0.01	0.109
1	-27.01 ± 0.26	1.58 ± 0.02	0.109

Table 6.4: $Y_{\rm SZ,500} - M_{500}$ scaling relations in the form of $\log_{10}\ (E(z)^{-2/3}\ Y_{\rm SZ,500}\ /\ h_{70}^{-2.5}\ {\rm Mpc}^2) = A + B\ \log_{10}\ (E(z)\ M_{500}\ /\ h_{70}^{-1}\ {\rm M}_\odot)$. The relation scatter σ_{yx} is also shown.

6.1.4 X-ray Luminosity Function

The XLF study has been somehow abandoned during the last years due to the difficulties of using the X-ray luminosity for cosmological purposes. The X-ray emissivity scales with the square of the gas density, which makes it subject to density variations and clumping. This implies large scatter that causes a large Malmquist bias and underlines the necessity of careful mock surveys that need to address all systematics.

Nevertheless, it provides a complementary check for the model built here. To this end, the *ROSAT* brightest cluster sample (BCS) XLF (Ebeling et al., 1997; with a median $z \approx 0.08$), which is in good agreement with results from the *ROSAT* ESO Flux-Limited X-ray (REFLEX; Böhringer et al., 2002) and HIFLUGCS (Reiprich & Böhringer, 2002), is taken as reference. Note that the

XLF is fully determined by the mass function and the $L_X - M_{500}$ relation after taking into account the observational biases. This means that applying the Malmquist bias corrected $L_X - M_{500}$ relation by Mantz et al. (2010) directly to the MultiDark mass function should yield an unbiased XLF. Figure 6.3 shows the bolometric and soft-band (0.1 − 2.4 keV) XLFs obtained in this way using the Mantz et al. (2010) results applied to the MultiDark $z = 0.1$ snapshot, the BCS XLFs (for which bolometric band there is only the Schechter fit available), and the bolometric XLF obtained from the MultiDark cluster sample at $z = 0.1$ through the model constructed here. While the soft-band XLF by Mantz et al. (2010) agrees well with the BCS data points, it deviates from the corresponding Schechter fit at low luminosities. This is also true in the bolometric band, where the Mantz et al. (2010) XLF and the model predictions agree well, but deviate from the BCS Schechter fit at low luminosities. This may be an artifact due to the use of Schechter fit instead of the data points or may point to incompleteness of the BCS sample. Note that the Poissonian errors of the XLF obtained from the MultiDark simulation are a lower limit as cosmic variance is neglected. Studies of the XLF will become again an important topic with the upcoming launch of the eROSITA satellite (see e.g. Cappelluti et al., 2011) and further studies in this direction are desirable.

Summarizing, the adopted phenomenological approach provides viable gas densities that reproduce the observed scaling relations of the ICM as well as the XLF. Thus, it can be applied in the following to model the CR population in galaxy clusters and to predict the radio and gamma-ray emission of the MultiDark-derived sample.

6.1.5 Cosmic Rays Modeling

In this section, a general model to calculate the cluster synchrotron (and gamma-ray) emission coming from secondaries of CR hadronic interactions with the ICM is built. A power-law CR proton distribution, $f(p)\mathrm{d}p = Cp^{\alpha}\mathrm{d}p$, is adopted, which is the effective one-dimensional momentum distribution (assuming isotropy in momentum space). To start, the synchrotron emissivity j_ν at frequency ν and per steradian of a steady-state electron population is provided (adapted from Pfrommer et al., 2008 and Enßlin et al., 2011),

$$j_\nu = A_\nu C(R) \rho_{\mathrm{gas}}(R) \frac{\epsilon_{\mathrm{B}}(R)}{\epsilon_{\mathrm{B}}(R) + \epsilon_{\mathrm{CMB}}} \left(\frac{\epsilon_{\mathrm{B}}(R)}{\epsilon_{B_{\mathrm{c}}}} \right)^{(\alpha-2)/4} , \tag{6.5}$$

where the abbreviations A_ν and $\epsilon_{B_{\mathrm{c}}}$ are defined in appendix A, ϵ_{CMB} is the CMB energy density, and $\epsilon_B = B^2/(8\pi)$ denotes the magnetic energy density. The magnetic field is assumed to scale with gas density as

$$B(R) = B_0 \left(\frac{\rho_{\mathrm{gas}}(R)}{\rho_{\mathrm{gas}}(0)} \right)^{\alpha_B} , \tag{6.6}$$

where B_0 is the central magnetic field and α_{B} a parameter representing the rate of decline of the magnetic field strength toward the cluster outskirts (see also section 4.3.3). The radio surface

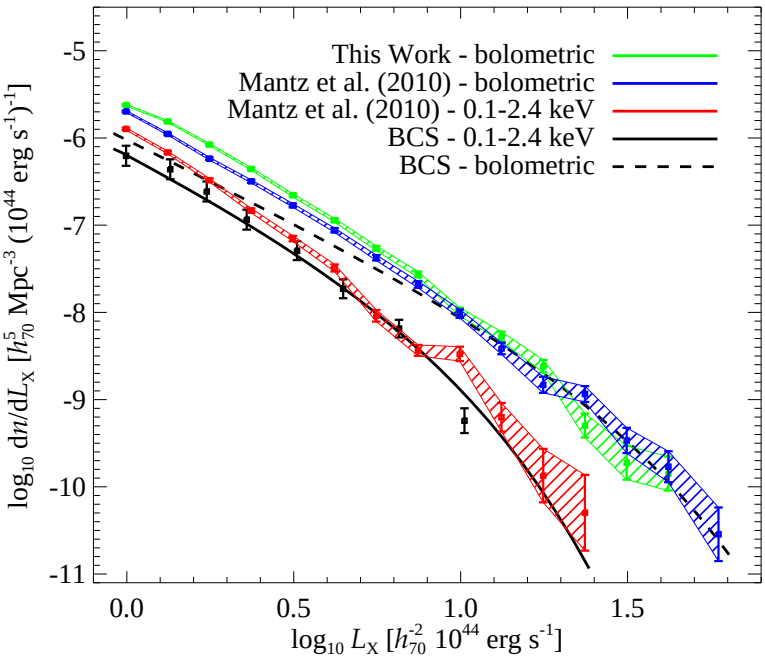

Figure 6.3: Bolometric X-ray luminosity function. Shown are the 0.1 – 2.4 keV data points, the 0.1 – 2.4 keV and bolometric Schechter fits of the BCS sample from Ebeling et al. (1997). The BCS sample is composed by clusters at $z \leq 0.3$ with a median of $z \approx 0.08$ and therefore is compared to the MultiDark $z = 0.1$ snapshot. The Mantz et al. (2010) 0.1 – 2.4 keV result well compares with the BCS data points but deviates from the corresponding Schechter fit. Finally, the Mantz et al. (2010) bolometric result and the bolometric prediction from the model constructed here are also shown. The XLFs are calculated in equally log-spaced mass bins; the reported error bars represent the Poissonian errors. Note that the comparison is limited in the luminosity range covered by the MultiDark sample, where the lowest part is cut because in that range the XLF rapidly drops due to the imposed mass cut.

brightness $S_\nu(R_\perp)$ and luminosity L_ν at a given frequency ν are given by

$$S(R_\perp) = 2\int_{R_\perp}^{\infty} j_\nu(R)\frac{R}{\sqrt{R^2 - R_\perp^2}}\mathrm{d}R\,, \tag{6.7}$$

$$L_\nu = 4\pi \int \mathrm{d}V\, j_\nu(R)\,. \tag{6.8}$$

The flux is given by $F_\nu = L_\nu/(4\pi D^2)$ where D is the luminousity distance of the considered object.

The CR distribution within galaxy clusters is governed by an interplay of propagation and advection. While the advection of CR by turbulent gas motions tends to result in centrally enhanced CR profiles, the propagation in form of CR streaming and diffusion tends to produce flat CR profiles. A full discussion of this issue is beyond the scope of this work and the reader is reminded

to Enßlin et al. (2011). Here the goal is to merge the result from the hydrodynamical cluster cosmological simulation of Pinzke & Pfrommer (2010), which provides a mass-scaling for the CR normalization, and the analytical result from Enßlin et al. (2011) where the above mentioned CR transport properties, neglected in the Pinzke & Pfrommer (2010) simulations for simplicity, are modeled.
Following closely Enßlin et al. (2011), when turbulent advection completely dominates the CR profile, this can be expressed as

$$C_{\rm simple}(R) = C_0 \left(\frac{P(R)}{P_0}\right)^{\frac{\beta_{\rm CR}}{\gamma}} , \tag{6.9}$$

where $\beta_{\rm CR} = (\alpha + 2)/3$, $\gamma = 5/3$ and $P(R) = n_{\rm e}(R) k_{\rm B} T(R)$ is the pressure. However, as explained before, both propagation and advection shape the CR profile and the ratio of their transport coefficients determines the exact shape. The treatment of this case is analytically developed in Enßlin et al. (2011) by solving the continuity equation for the CR density profile $\rho_{\rm CR}$. They found

$$\rho_{\rm CR}(R) = \rho_{\rm CR,0} \left(\frac{P(R)}{P_0}\right)^{\frac{1}{\gamma}} \exp\left(\frac{R}{R_*}\right) , \tag{6.10}$$

where $R_* = \gamma_{\rm tu} R_{\rm c}$, $\gamma_{\rm tu}$ is the turbulent parameter, and $R_{\rm c}$ is a characteristic radius where the turbulence is supposed to be injected which should be comparable to the cluster core radius. Assuming for simplicity that $P(R)/P_0 = n_{\rm e}(R)/n_0$, so neglecting the temperature dependence, and a standard β-profile for the electron density as:

$$n_{\rm e} = n_0 \left(1 + \frac{R^2}{R_{\rm c}^2}\right)^{-\frac{3\beta_{\rm cl}}{2}} , \tag{6.11}$$

the CR density profile $C_{\rm transport}(R) = C_0 (\rho_{\rm CR}(R)/\rho_{\rm CR,0})^{\beta_{\rm CR}}$ finally results to be

$$C_{\rm transport}(R) = C_0 \left(1 + \frac{R^2}{R_C^2}\right)^{-\beta_{\rm c}} \exp\left(\frac{R}{R_*}\beta_{\rm CR}\right) \tag{6.12}$$

for $R_- < R < R_+$, where $\beta_{\rm c} = 3\beta_{\rm cl}\ \beta_{\rm CR}/2\gamma$, while $C_{\rm transport}(R) = C_{\rm transport}(R_\pm)$ for $R < R_-$ and $R > R_+$ respectively. The solution for these radii is:

$$R_\pm = \frac{3\beta_{\rm cl}}{2\gamma} R_* \left(1 \pm \sqrt{1 - \left(\frac{2R_{\rm c}\gamma}{3\beta_{\rm cl}R_*}\right)^2}\right) . \tag{6.13}$$

Therefore, different CR transport cases are represented varying the value of the transport parameter $\gamma_{\rm tu}$; high $\gamma_{\rm tu}$ values correspond to the advection-dominated *simple* case while in case of $\gamma_{\rm tu} \approx 1$ the CR profile is flat. This is shown in appendix B for the two representative NCCC Coma and CCC Perseus cases, where it is also shown the result in case $C(R) = C_{\rm semi-analytical}(R) = \tilde{C}(R)\rho_{\rm gas}(R)/m_{\rm p}$ with $\tilde{C}(R)$ the mass-dependent universal normalization CR profile found in cosmological simulations of Pinzke & Pfrommer (2010). The CR profile driven by simulations is characterized by a more centrally peaked profile with respect to the analytical case. Note also

that the Perseus profile is much more centrally peaked with respect to Coma, which reflects their CCC and NCCC classification respectively.
The following steps are to i) generalize the above approach for the GNFW gas profiles obtained in section 6.1.2, and ii) merge the Enßlin et al. (2011) analytical approach with the $\tilde{C}$ universal CR normalization obtained from simulations in order to get a mass-scaling for the CR profiles. As explained in appendix B, in this case there is not an exact solution for the Enßlin et al. (2011) treatment of the problem. In fact, when trying to solve it analytically, one ends up with a 5-order equation. It is not practical to solve numerically such equation, and at the same time to discharge the unphysical solution, for the more than 10^4 MultiDark halos of the final sample used here. For simplicity, the Enßlin et al. (2011) formalism is used, after some modifications in order to adapt it to the case of this work. Therefore:

$$C_{\rm simple}(R) = C_0 \left(\frac{P(R)}{P_0}\right)^{\frac{\beta_{\rm CR}}{\gamma}} = C_0 \left(\eta(R)\right)^{\beta_{\rm CR}} , \tag{6.14}$$

where the advective CR profile $\eta(R) = (P(R)/P(0))^{1/\gamma}$ has been introduced (see Enßlin et al., 2011 for details). $\rho_{\rm CR}$ can be written as

$$\rho_{\rm CR}(R) = \rho_{CR,0}\ \eta(R)\ \exp\left(\frac{R}{R_*}\right) . \tag{6.15}$$

The *semi-analytical* mass-dependent universal normalization CR profile of Pinzke & Pfrommer (2010) is then introduced in the following way:

$$\eta(R) = \left(\frac{C_{\rm simple}(R)}{C_0}\right)^{1/\beta_{\rm CR}} = \left(\frac{C_{\rm final}(R)}{C_0}\right)^{1/\beta_{\rm CR}} \tag{6.16}$$

where $C_{\rm simple}(R)$ is re-defined as $C_{\rm final}(R) = \tilde{C}(R)P(R)$ of the final hybrid model, where $\tilde{C}(R)$ is the normalization CR profile of equation 22 of Pinzke & Pfrommer (2010), and $P(R) = n_{\rm e}(R)k_{\rm B}T(R)$. Here $T(R)$ represents the decline toward the cluster periphery expected by the fit to the universal temperature profile derived from cosmological cluster simulations (Pfrommer et al., 2007; Pinzke & Pfrommer, 2010). The last step is to generalize the case with one CR population with spectral index α, used up to here, to the case of Pinzke & Pfrommer (2010) where three different CR populations $\alpha_i = (2.15, 2.3, 2.55)$ are adopted. The whole formalism is easily extended to the three CR populations case by using sums over the three spectral indeces (see Pinzke & Pfrommer, 2010). This extension enters in the A_ν calculation, the $(\epsilon_{\rm B}(R)/\epsilon_{B_{\rm c}})^{(\alpha-2)/4}$ factor of equation 6.5, and into equation 6.14. While for the first two cases there are no problems, in the latter there would be. In fact, introducing a sum over α_i in equation 6.14 would make impossible to analytically reverse it to get $\eta(R)$ of equation 6.16. The three CR spectral indeces are therefore not introduced in this part and $\alpha = 2.3$ is used into equation 6.12.[6] However, the model is extended to three CR spectral indeces in the A_ν and $(\epsilon_{\rm B}(R)/\epsilon_{B_{\rm c}})^{(\alpha-2)/4}$ factors (see appendix A). In this way, when $\gamma_{\rm tu}$

[6]This choice does not affect the result. Varying α within $2.15-2.55$ leaves the radial shape and the normalization unchanged within 0.5%.

is high enough, e.g. 100 (1000), the radial shape and normalization of the semi-analytical model of Pinzke & Pfrommer (2010) is recovered at a 1% (0.1%) level.
Therefore, a new $C_{\rm transport}$ is obtained, which now shall be called $C_{\rm final}$, with all the needed ingredients, i.e. a mass-scaling CR normalization for the simulation derived cluster population, the general REXCESS derived GNFW gas profiles, the universal outer temperature decline and, least but not last, the $\gamma_{\rm tu}$ parameter which permits to explore different turbulent states of the clusters in the MultiDark sample.[7]
The top panel of figure 6.4 shows $C_{\rm final}$ for the NCCC and CCC cases, for different values of the $\gamma_{\rm tu}$ parameter. Additionally, in the bottom panel, the final model is compared with the analytical GNFW exact solution (see appendix B) and the pure semi-analytical cases for $\gamma_{\rm tu} = 100$ and normalized at $0.1 \times R_{200}$. As mentioned above, for high $\gamma_{\rm tu}$ values, the shape and normalization of the semi-analytical model of Pinzke & Pfrommer (2010) is recovered. Note therefore the more centrally peaked profile of the final model constructed here with respect to the analytical GNFW case. Indeed, the choice to introduce $\tilde{C}$ from the Pinzke & Pfrommer (2010) simulations in the model built here may introduce an overcooling problem. This can however be counteracted by changing the $\gamma_{\rm tu}$ and α_B values. The risk is that, when modeling a galaxy cluster, the final $\gamma_{\rm tu}$ value will be biased as the CR transport effects are degenerate with the initial CR profile, the α_B value, and other possible effects not considered here as e.g. cluster asphericity (see also next section).

6.2 Radio Surface Brightness Modeling

In this section, the CR model built in the previous section is used to reproduce the RH characteristics of some galaxy clusters. The final model includes a normalization parameter $g_{\rm CR}$ which acts just as a linear scaling for the emission and can be included in the calculation substituting A_ν with $A_{\nu,\rm final} = g_{\rm CR} A_\nu$ (see appendix A). Note that this parameter can be interpreted as the *maximum CR acceleration efficiency parameter* $g(\zeta_{\rm p,max})$ of Pinzke & Pfrommer (2010) *only* when $\gamma_{\rm tu} \approx 100$. Additionally, the CR-to-thermal pressure $X_{\rm CR} = P_{\rm CR}/P_{\rm th}$ will be used.[8]
Four galaxy clusters are taken as example. The giant radio halos of Coma (Deiss et al., 1997) and Abell 2163 (Feretti et al., 2001; Murgia et al., 2009) both merging NCCCs, and the radio-mini halos of Perseus (Pedlar et al., 1990) and Ophiuchus (Govoni et al., 2009; Murgia et al., 2009) both non-merging CCCs. The radio emission of these clusters is representative of a wide class of RHs and, additionally, Perseus, Ophiuchus and Coma are among the most promising clusters for gamma-ray observations (Pinzke & Pfrommer, 2010; Pinzke et al., 2011). Their main characteristics are detailed, together with the main parameters adopted for the modeling and the corresponding results, in table 6.5 at the end of this chapter. Figure 6.5 shows the corresponding

[7] In the final model, $R_{\rm c}$ of equation 6.13 becomes the characteristic radius of the GNFW gas profile of section 6.1.2, i.e. $R_{\rm c} = 0.2 \times R_{500}$, and $\beta_{\rm cl} = 0.8$ (changing the value of $\beta_{\rm cl}$ between e.g. 0.4 and 1.2 has no impact at all).

[8] The CR pressure is $P_{\rm CR} = \frac{g_{\rm CR} C_{\rm final} m_{\rm p} c^2}{6} \Sigma_{i=1}^{3} \Delta_i \beta_{1/(1+q^2)} \left(\frac{\alpha_i - 1}{2}, \frac{3-\alpha_i}{2}\right)$, where c is the speed of light, $q = 0.8$ (Pinzke & Pfrommer, 2010) and $\Delta_i = (0.767, 0.143, 0.0975)$ are the normalization factors found by Pinzke & Pfrommer (2010) (see also appendix A). The thermal pressure is $P_{\rm th} = n_{\rm gas} k_{\rm B} T$.

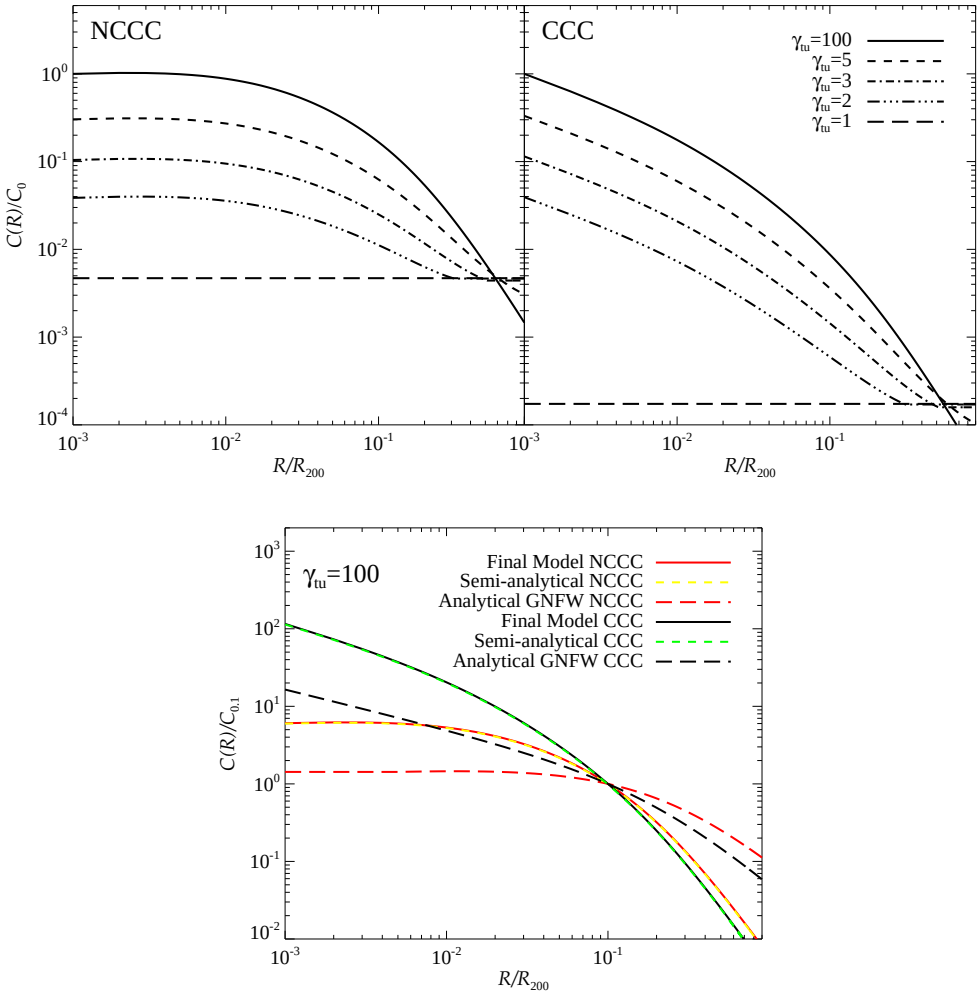

Figure 6.4: In the top panel, the final model $C_{\rm final}$ is shown for the NCCC and CCC cases and for different values of $\gamma_{\rm tu}$. $C_{\rm final}$ is normalized to $C_0 = C(0, \gamma_{\rm tu} = 100)$ where the CR populations are fixed to have a constant total CR number as in equation 36 of Enßlin et al. (2011) integrating up R_{200}. The bottom panel compares the $C_{\rm final}$ and pure semi-analytical cases (plugging in the GNFW gas profiles plus the temperature outer decrease) with the analytical GNFW case (with $\alpha = 2.3$) for $\gamma_{\rm tu} = 100$. In the latter plot, the CR profiles are normalized to $C_{0.1} = C(0.1R_{200})$.

surface brightness and CR-to-thermal pressure. Note that these clusters are modeled at 1.4 GHz and within R_{200}.

The Coma giant radio halo has a morphology remarkably similar to the extended X-ray thermal bremsstrahlung emission, although the radio peak seems to be displaced by about 0.05 deg with respect to the X-ray one and the radio emission declines more slowly going toward the cluster outskirts (Briel et al., 1992; Deiss et al., 1997). Note that it is clearly non-spherical, showing an elongation in the East-West direction. The full width half maximum (FWHM) of the Deiss

et al. (1997) radio observation beam is 0.156 deg, so almost two orders of magnitude larger than the X-ray observation of Briel et al. (1992).[9] A Gaussian smoothing is therefore applied to the theoretical surface brightness of equation 6.8 with $\sigma_{\rm smoothing} = FWHM_{\rm radio}/2.355$. Different values of $\alpha_{\rm B} = (0.3, 0.4, 0.5, 0.6, 0.7)$ and of the $\gamma_{\rm tu}$ parameter from 1 to 100 are investigated.[10] The central magnetic field is fixed to $B_0 = 5\ \mu$G (Bonafede et al., 2010) and $g_{\rm CR}$ is used as normalization factor to match the radio observations. The best fit to the data is obtained for $\gamma_{\rm tu} = 1$ and $\alpha_{\rm B} = 0.6$, however, values as high as $\gamma_{\rm tu} \approx 4$ can be accommodated. The total radio luminosity is reproduced within about 20%. The gamma-ray flux (see appendix C) within R_{200} for the best fit case and for energies above 100 MeV (100 GeV) is $F_\gamma = 4.1 \times 10^{-9}$ (1.5×10^{-12}) cm^{-2} s^{-1}. The $\gamma_{\rm tu} = 1$ case is therefore in tension with the limit recently set by *Fermi*-LAT (Zimmer et al., 2012) of $F_{\gamma,UL}(> 100\ {\rm MeV}) \approx 2.5 \times 10^{-9}$ cm^{-2} s^{-1}. Note that using a slightly higher $\gamma_{\rm tu}$ value, the prediction becomes again in agreement with gamma-ray observations. In fact, for $\gamma_{\rm tu} = 4$ one obtains $F_\gamma(> 100\ {\rm MeV}) = 9.6 \times 10^{-10}$ cm^{-2} s^{-1} (and $F_\gamma(> 100\ {\rm GeV}) = 3.6 \times 10^{-13}$ cm^{-2} s^{-1}).

The Abell 2164 giant radio halo is also closely correlated to the cluster thermal X-ray structure showing a slower decline going toward the cluster outskirts with respect to the bremsstrahlung emission (Feretti et al., 2001). It also appears to be non-spherical, being its shape elongated in the East-West direction. For the modeling, the surface brightness provided in Murgia et al. (2009) is used, where the radio image has a circular Gaussian beam with $FWHM_{\rm radio} = 62$"=0.017 deg. The position of radio and X-ray peaks is displaced by about 19" and Matteo Murgia has kindly provided the radio surface brightness computed with respect to the Reiprich & Böhringer (2002) X-ray position (however, it is almost unchanged). The $FWHM_{\rm radio}$ is larger than the resolution of the *ROSAT* satellite from which the gas density is taken. Once converted the angular sizes to physical sizes, the corresponding $\sigma_{\rm smoothing}$ is of the order of the Coma one because of the high distance of Abell 2163. Therefore, a Gaussian smoothing is applied also in this case. The same procedure as in Coma is followed, using again $B_0 = 5\ \mu$G. The best fit to the data, and also the only acceptable one, is obtained for $\gamma_{\rm tu} = 1$ and $\alpha_B = 0.3$, i.e. the flattest possible surface brightness. The total luminosity is recovered within about 15%. The corresponding gamma-ray flux within R_{200} for energies above 100 MeV (100 GeV) is $F_\gamma = 4.2{\times}10^{-10}$ ($1.5{\times}10^{-13}$) cm^{-2} s^{-1}, about two orders of magnitude lower than the upper limit obtained by *Fermi*-LAT (Ackermann et al., 2010a).

The Perseus diffuse radio emission is the best known example of radio-mini halo (Pedlar et al., 1990) and Perseus itself is surely one of the best studied clusters in X-rays (e.g. Churazov et al., 2003; Fabian et al., 2006b, 2011b). Also in the Perseus case, clear similarities between radio and thermal X-ray structures are found. The fitting procedure is done as before but now adopting $B_0 = 10\ \mu$G (see chapters 3 and 4 for a discussion on the Perseus, and generally on CCCs and NCCCs, magnetic fields). The best fit to the data is obtained for $\gamma_{\rm tu} = 3$ and $\alpha_{\rm B} = 0.4$, however, values as high as $\gamma_{\rm tu} \approx 100$, and as low as $\gamma_{\rm tu} = 2$, can be easily accommodated. The total luminosity is recovered within about 10%. The gamma-ray flux within R_{200} for the best

[9] Note therefore that the difference in position of the radio and X-ray peaks is negligible for the modeling.

[10] The CR number is fixed for $\gamma_{\rm tu} = 100$ using equation 36 of Enßlin et al. (2011), integrating up R_{200}, and then obliged to be the same at lower $\gamma_{\rm tu}$ values.

fit case and for energies above 100 MeV (100 GeV) is $F_\gamma = 1.4 \times 10^{-8}$ (5.1×10^{-12}) cm^{-2} s^{-1}. Adopting $\gamma_{\rm tu} = 100$ and $\alpha_B = 0.3$, the corresponding gamma-ray flux above 100 MeV (100 GeV) is $F_\gamma = 4.9 \times 10^{-9}$ (1.8×10^{-12}) cm^{-2} s^{-1}. Note that the central galaxy NGC 1275 flux above 100 MeV measured by *Fermi* is of about 2×10^{-7} cm^{-2} s^{-1} (Abdo et al., 2009), well above the values predicted here which however refer to the whole cluster. These predictions can be compared to the upper limit above 1 TeV, and for a region within 0.15 deg around the cluster center, recently obtained by Aleksić et al. (2012a). For the $\gamma_{\rm tu} = 3$ ($\gamma_{\rm tu} = 100$) case, a flux of $F_\gamma(> 1$ TeV, < 0.15 deg) $= 7.3 \times 10^{-14}$ (5.5×10^{-14}) cm^{-2} s^{-1} is obtained. This is well below the MAGIC collaboration upper limit of $F_{\gamma,{\rm UL}}(> 1$ TeV, < 0.15 deg) $\approx 1.4 \times 10^{-13}$ cm^{-2} s^{-1}. Note also that, in the case of $\gamma_{\rm tu} = 100$, a maximum CR acceleration efficiency parameter of 0.52 is obtained, about half of the value adopted by Pinzke & Pfrommer (2010).

The Ophiuchus cluster has been widely studied both in radio and X-rays in the last few years because of a claim of presence of a non-thermal hard X-ray tail (Eckert et al., 2008; Fujita et al., 2008; Govoni et al., 2009; Murgia et al., 2009; Pérez-Torres et al., 2009; Nevalainen et al., 2009; Murgia et al., 2010; Million et al., 2010). It was classified as a merging cluster by Watanabe et al. (2001), but more recently Fujita et al. (2008) did not found any evidence of merging and, on the contrary, classified it as one of the hottest clusters with a cool-core (see also Million et al., 2010). Its radio mini-halo displays similarities with the thermal X-ray emission. For the modeling, the surface brightness provided by Murgia et al. (2009) is used. The position of radio and X-ray peaks seems displaced by about 24". Again, Matteo Murgia has kindly provided the radio surface brightness computed with respect to the Reiprich & Böhringer (2002) X-ray position, however the change is not very significant. The modeling proceed as before, adopting a central magnetic field value of $B_0 = 10\,\mu$G. The best fit to the data is obtained for $\gamma_{\rm tu} = 5$ and $\alpha_B = 0.7$, however, values as high as $\gamma_{\rm tu} \approx 100$, and as low as $\gamma_{\rm tu} = 2$, can be easily accommodated. The total luminosity is recovered within about 20%. The gamma-ray flux within R_{200} for the best fit case and for energies above 100 MeV (100 GeV) is $F_\gamma = 1.2 \times 10^{-10}$ (4.3×10^{-14}) cm^{-2} s^{-1}. Adopting $\gamma_{\rm tu} = 100$ and $\alpha_B = 0.3$, the corresponding gamma-ray flux above 100 MeV (100 GeV) is $F_\gamma = 8.3 \times 10^{-11}$ (3.1×10^{-14}) cm^{-2} s^{-1}. The gamma-ray flux is, in both cases, about two orders of magnitude lower than the upper limit obtained by *Fermi*-LAT (Ackermann et al., 2010a). Note also that, in the case of $\gamma_{\rm tu} = 100$, a maximum CR acceleration efficiency parameter of 0.014 is obtained.

The following points need to be stressed:

1. The model parameter space for Coma and Abell 1263 giant halos is much more reduced than for the mini-halos cases. In fact, very low $\gamma_{\rm tu}$ values are needed in order to get acceptable fits. Higher $\gamma_{\rm tu}$ values would be expected for the merging NCCC cases (Enßlin et al., 2011). However, there are three main factors that render the merging NCCC fits not conclusive and can alleviate this problem. i) Primary electrons accelerated in outer shocks, not consider here, could have an important contribution in the RH emission. ii) Merging clusters are not spherical symmetric, which is the approximation made here, and this is clearly the case both for Coma and Abell 2163. Finally, iii) adopting the simulation-driven $\tilde{C}$ from Pinzke & Pfrommer (2010) in the hybrid CR model, may bring to a too steep central CR normalization which result in lower required $\gamma_{\rm tu}$ values with respect to a flatter

choice. To test this last point, the Coma surface brightness is fitted using a model without $\tilde{C}$ obtaining that values as high as $\gamma_{\rm tu} \approx 8$ can be accommodated. However, the $\gamma_{\rm tu} = 1$ case still represents the best fit model, it is indeed not affected by such arguments as the CR profile is always flat in this case. Despite these issues, the Coma and Abell 2163 RHs can be reproduced fairly well, solving previous problems of the *classical* hadronic model (see e.g. Donnert et al., 2010a).

2. RHs measurements set more stringent constraints on the hadronic model than gamma-ray observations, apart for the Coma case. Gamma-ray observations are a fundamental tool to disentangle between the hadronic and re-acceleration model. However, gamma-ray predictions should be scaled down with respect to previous results (Pinzke & Pfrommer, 2010; Pinzke et al., 2011) in light of the what is presented here (see also Enßlin et al., 2011).

3. The magnetic field values adopted here are perfectly in agreement with other observational constrains, solving previous tensions of the *classical* hadronic model (see e.g. Jeltema & Profumo, 2011). Indeed, different B_0 values could be adopted without entering in tension with other observational constraints with the exception of Coma for which a higher B_0 value would be in contradiction with Bonafede et al. (2010), while a lower one could result in a higher gamma-ray emission in contrast with the Zimmer et al. (2012) limit.

4. When considering the $\gamma_{\rm tu} = 100$ case, plausible only for Perseus and Ophiuchus, the $g_{\rm CR}$ parameter can be interpreted as the maximum CR acceleration efficiency used in Pinzke & Pfrommer (2010). This value should then be universal, i.e. it should be the same in all clusters. Here, $g_{\rm CR,Perseus} = 0.52$ and $g_{\rm CR,Ophiuchus} = 0.014$, as $B_0 = 10\ \mu$G is fixed in both cases and $g_{\rm CR}$ used as normalization. This discrepancy can be easily solved by increasing/lowering the Perseus/Ophiuchus central magnetic field (e.g. $B_{0,\rm Perseus} = 20\ \mu$G and $B_{0,\rm Ophiuchus} = 1\ \mu$G). Note however that, at this stage, this is not conclusive as any $\gamma_{\rm tu}$ value can virtually be chosen for both clusters.

5. With this reduced cluster sample, no definitive conclusion on the parameters used in the modeling can be drawn as many different choices could be done on the magnetic field, the $\gamma_{\rm tu}$ and $\alpha_{\rm B}$ parameters. This is particularly true for the analyzed mini-halos, for which almost all the ($\gamma_{\rm tu}$, $\alpha_{\rm B}$) parameter space is available (note also that the $\gamma_{\rm tu}$ and $\alpha_{\rm B}$ variables are of course degenerate). Such a study performed on all the knows RHs is highly desirable but beyond the scope of this work which instead investigates the LOFAR cluster survey potentiality.

The hadronic model built here reproduces the main characteristics of both giant and mini-halos without entering in tension with any existing observational constraint. As it will be shown in the next section, it can also reproduce the radio-to-X-ray scaling relation, solving previous issues of the *classical* hadronic model, and the radio-to-SZ scaling relation. It therefore fully accomplishes the initial purposes.

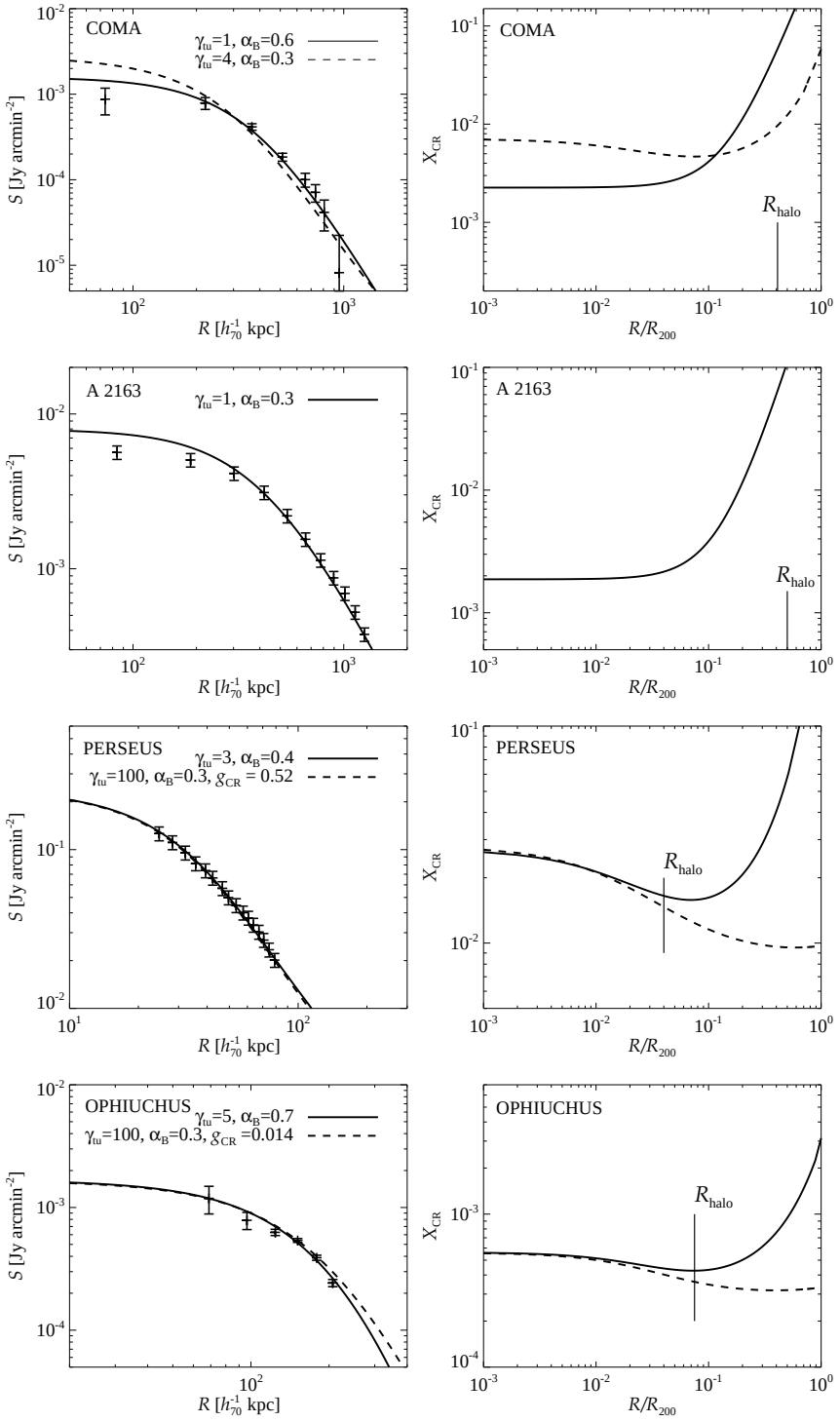

Figure 6.5: Surface brightness modeling of the Coma, Abell 2163, Perseus and Ophiuchus RHs. Left panels show the RHs azimuthal average surface brightness, while right panles show the corresponding CR-to-thermal pressure $X_{\rm CR}$. Note how different parameter values, giving almost the same surface brightness shape, result in very different $X_{\rm CR}$ profiles. In the Abell 2163 and Ophiuchus cases, 10% error bars are taken instead of the errors reported by Murgia et al. (2009). This is true also for Perseus, for which Pedlar et al. (1990) do not report errors.

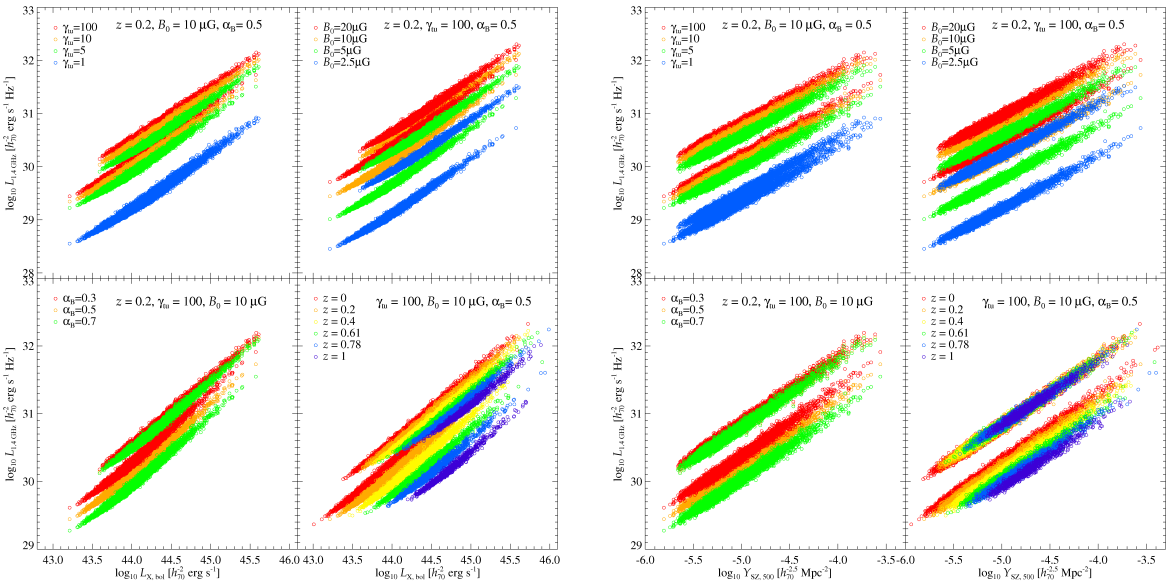

Figure 6.6: Radio-to-Xray and radio-to-SZ general scaling relations as predicted by the final CR model constructed here. The left panel shows how the $L_{1.4\ \mathrm{GHz}} - L_{\mathrm{X,bol}}$ relation varies changing different parameters. In the right panel, the same but for the $L_{1.4\ \mathrm{GHz}} - Y_{\mathrm{SZ,500}}$ relation. Note that in each plot there are two separated populations for each model realization, the top one is the CCC population while the bottom one is the NCCC population. The text in the plots indicates the parameters which are kept fixed. The g_{CR}-normalization parameter is fixed to 0.5 for all cases. See main text for details.

6.3 Radio Scaling Relations

An explained in chapter 1, there exist an apparent bimodality between the radio and X-ray cluster emission. Clusters with the same X-ray luminosity both host RHs and do not show any diffuse radio emission (e.g. Brunetti et al., 2009; Enßlin et al., 2011). More recently, a study of the radio-to-SZ scaling relation showed the absence of any kind of strong bimodality dividing the cluster population into radio-loud and radio-quiet clusters (Basu, 2012). In this section, these two scaling relations are investigated.

Figure 6.6 shows the general scaling relations of the final CR model of section 6.1.5 applied to the MultiDark sample. Both the radio-to-X-ray and the radio-to-SZ scaling relations are shown, varying different parameters as γ_{tu}, B_0, α_{B} and the redshift. The g_{CR}-normalization parameter is fixed to 0.5 for all cases, ensuring an average CR-to-thermal pressure at 2%-level (0.05%-level) within R_{500} ($R_{500}/2$). Here, the radio luminosity is calculated at 1.4 GHz within R_{500}.[11] The CR number is fixed for $\gamma_{\mathrm{tu}} = 100$ using equation 36 of Enßlin et al. (2011), integrating up R_{500}, and then obliged to be the same at lower γ_{tu} values; this will be the case also in the following. Note in particular how the different parameters affect in different ways the NCCC and CCC populations for the $L_{1.4\ \mathrm{GHz}} - L_{\mathrm{X,bol}}$ and $L_{1.4\ \mathrm{GHz}} - Y_{\mathrm{SZ}}$ relations. This is mainly the result of the different

[11] The mean (median) difference between calculating L_ν within R_{200} or R_{500} is 5.3% (5.6%).

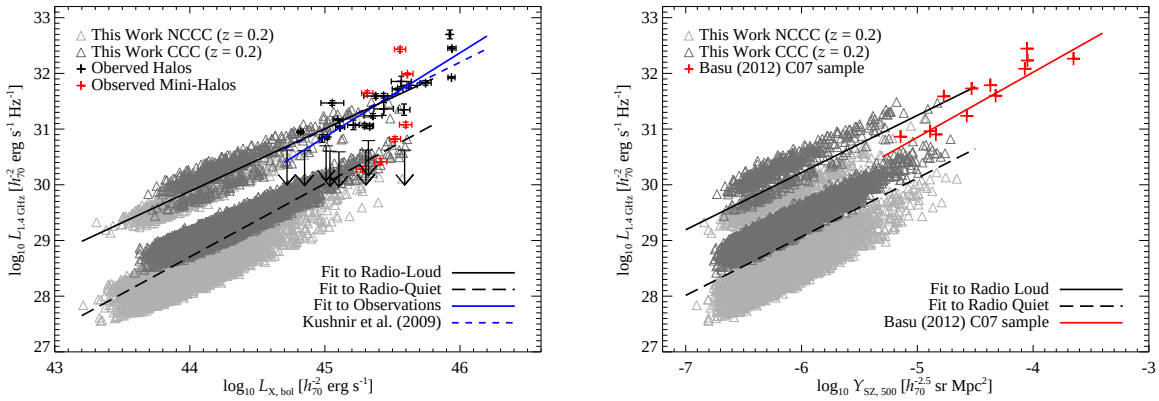

Figure 6.7: Radio-to-X-ray and radio-to-SZ scaling relation predictions from the final CR model (see main text for the details of the chosen parameters) compared with observations. *Left.* $L_{1.4\ \mathrm{GHz}} - L_{\mathrm{X,bol}}$ prediction compared to the observational sample constructed in appendix D. *Right.* $L_{1.4\ \mathrm{GHz}} - Y_{\mathrm{SZ}}$ prediction compared to the observational sample C07 from Basu (2012).

dependence on gas density of L_{X} and Y_{SZ}.

The model predictions should now be compared to observations. For this purpose, a particular realization of the model is chosen as representative. The MultiDark $z = 0.2$ sample (which well compares with the redshift of the observational samples, see below and appendix D) is artificially, and randomly, divided in radio-quiet and radio-loud clusters, with the latter being 10% of the total. Radio-quiet clusters are characterized by $\gamma_{\mathrm{tu}} = 1$ and randomly and uniformly distributed central magnetic fields B_0 in the intervals $[2.5, 5.5]\ \mu$G and $[5, 10]\ \mu$G for NCCCs and CCCs, respectively. Radio-loud clusters are characterized by randomly and uniformly γ_{tu} values in the intervals $[40, 80]$ and $[1, 5]$ for NCCCs and CCCs, respectively, and central magnetic field values in the intervals $[4.5, 7.5]\ \mu$G and $[7.5, 12.5]\ \mu$G for NCCCs and CCCs, respectively. The α_{B} value is fixed to 0.5. Also here, the g_{CR}-normalization parameter value is fixed to 0.5 for all the clusters, ensuring the median average CR-to-thermal pressure of about 2% (0.05%) within R_{500} ($R_{500}/2$). Note that these choices are not driven by any consideration apart the need to reproduce observations. Indeed, existing observations do no permit robust clues at all on which values should take these parameters in clusters, with possibly the only exception of the magnetic field. It is clear the need of large population studies of radio observed clusters in order to be able to draw robust hypothesis on the interplay of the different parameters in the modeling. Figure 6.7 shows how the model prediction compares with the observed radio-to-X-ray and radio-to-SZ scaling relations.

For comparison with the observed 1.4 GHz radio-to-X-ray scaling relation, the sample shown as black (halos) and red (mini-halos) crosses (plus some upper limits) in the left plot of figure 6.7 is constructed in appendix D. This sample is obtained from Brunetti et al. (2009), Enßlin et al. (2011), and Govoni et al. (2009) and has a median redshift of $z \approx 0.18$. The corresponding observational scaling relation in the form of $\log_{10} L_{1.4\ \mathrm{GHz}} = A + B\ \log_{10} L_{\mathrm{X,bol}}$ has $A = -50.433 \pm 2.226$ and $B = 1.803 \pm 0.049$, and a scatter of $\sigma_{yx} \approx 0.44$ (upper limits are not included in the fit

and units are as in figure 6.7). The reader is reminded to Brunetti et al. (2009) and Enßlin et al. (2011) for an extensive discussion on this topic. However, note that, as interestingly underlined also by Murgia et al. (2009), in contrast with radio halos, mini-halos seem to span a wide range of radio luminosity. The Perseus mini-halo (Y-axis highest red cross in the left plot of figure 6.7), for example, has a radio luminosity which is almost two order of magnitude higher than radio halos at the same X-ray luminosity. On the other hand, the Ophiuchus mini-halo (Y-axis lowest red cross in the left plot of figure 6.7), which is a representative of other few such examples recently detected in CCCs (i.e. A2029 and A1835), has a radio luminosity which is much lower, more typical of halos in merging clusters, and actually below the shown upper limits. Note also that the determination of the $L_{1.4} - L_{\rm X,bol}$ relation slope is not very robust because of the few known RHs and the uncertainties in the measurements both in the radio and X-rays. The recently detected mini-halos with very low luminosities are a clear example of the uncertainty and the large scatter that this relation may have. On the other hand, X-ray luminosities for the same object from e.g. *ROSAT* and *Chandra* can easily differ by a factor of few. The left panel of figure 6.7 additionally shows the Kushnir et al. (2009) slope prediction of ≈ 1.2, arbitrarily normalized for visual purposes, from their simple analytical hadronic model.

For the comparison to the observed 1.4 GHz radio-to-SZ scaling relation, the result obtained by Basu (2012) with the sample of radio halos from Cassano et al. (2007) (C07; median redshift of $z \approx 0.18$; note that no mini-halos are included) is taken as reference. For this sample, Basu (2012) quotes $Y_{\rm SZ}$ within the halo radii given by Cassano et al. (2007). These radii have a median of about 0.5 h_{70}^{-1} Mpc which well compares with the MultiDark $z = 0.2$ snapshot median $R_{500} \approx 0.4\ h_{70}^{-1}$ Mpc. For the C07 sample, Basu (2012) obtains a scaling relation in the form of $\log_{10} L_{1.4\ \rm GHz} = A + B\ \log_{10} Y_{\rm SZ}$ with $A = 29.7 \pm 0.8$ and $B = 1.17 \pm 0.18$, and a scatter of $\sigma_{yx} \approx 0.28$ (units are as in figure 6.7). Note however that this cannot be considered definitive, as for the radio-to-X-ray case, and these scaling relation determinations are likely going to be improved in the near future.

Figure 6.7 can now be analyzed. The normalization of the model can be arbitrarily varied changing $g_{\rm CR}$ as long as the resulting $X_{\rm CR}$ respects the current observational constraints (e.g. Aleksić et al., 2012a) and remains below few percents. As explained above, the choice of $g_{CR} = 0.5$ ensures average CR-to-thermal pressures at 2%-level within R_{500}, and therefore the available parameter space is quite wide. The model built here can both mimic a cluster radio bimodality or not, depending on the parameters adopted for the two artificial radio-loud and radio-quiet populations. However, note that the $L_{1.4\ \rm GHz} - L_{\rm X,bol}$ radio-loud and quiet population difference is larger than the $L_{1.4\ \rm GHz} - Y_{\rm SZ}$ one which exhibits more a sort of continuum going from the radio-loud CCCs to the radio-quiet NCCCs. This is because $L_{\rm X,bol}$ scales as $\rho_{\rm gas}^2$ while $Y_{\rm SZ}$ as $\rho_{\rm gas}$. As a consequence, the highly peaked gas profiles of CCCs have less impact on $Y_{\rm SZ}$ than on $L_{\rm X,bol}$. This can mimic the observed discrepancy of the presence of a bimodality in $L_{1.4\ \rm GHz} - L_{\rm X,bol}$ and the absence of it in $L_{1.4\ \rm GHz} - Y_{\rm SZ}$. Regarding the slope of the model, it is difficult to give a definitive determination because, again, this depends on the parameter values adopted and, particularly, to relative difference introduced between the NCCC/CCC and the radio-loud/quiet populations. However, note that the model $L_{1.4\ \rm GHz} - L_{\rm X,bol}$ slope is slightly shallower than the observed relation, more similar to the Kushnir et al. (2009) prediction, and that the model $L_{1.4\ \rm GHz} - Y_{\rm SZ}$ slope compares quite well with the observed one. The model is not additionally tuned to match

observations due to the many uncertainties and lack of robustness both in the observations and modeling at this stage

6.4 Radio Luminosity Function

Figure 6.8 shows the radio luminosity function (RLF) at 1.4 GHz, obtained from the representative realization of the final CR model detailed in the previous section, and compares it with observational results. As for the X-ray emission, the RLF is completely determined by the cluster mass function and the radio luminosity-to-mass relation, through $L_{1.4\ \mathrm{GHz}} - L_{\mathrm{X,bol}}$ or $L_{1.4\ \mathrm{GHz}} - Y_{\mathrm{SZ}}$, with the additional uncertainty of the fraction of radio-loud clusters. Therefore, figure 6.8 also shows the "true" RLFs obtained applying the $L_{1.4\ \mathrm{GHz}} - L_{\mathrm{X,bol}}$ and $L_{1.4\ \mathrm{GHz}} - Y_{\mathrm{SZ}}$ relations to the MultiDark $z = 0.2$ snapshot using their $L_{\mathrm{X,bol}}$ and $Y_{\mathrm{SZ,500}}$, as obtained from the phenomenological model, respectively. Pay attention that this is done using *only* the halos defined as radio-loud clusters, not all of them, and the cases for 100%, 25%, 10%, 5% and 1% radio-loud clusters are shown. As clear from figure 6.8, this is different from what is obtained with the model built here, where a fraction of radio-loud cluster is indeed defined, but the radio-quiet population is also contributing to the RLF, dominating at low luminosities. In fact, the top left plot of figure 6.8 also shows how the model RLF builds up from the quiet and loud populations for the 25% and 1% radio-loud cases.

In appendix D, an attempt to construct a RLF from existing X-ray flux-limited radio surveys is made. There exist two such studies, the cluster radio survey done with the National Radio Astronomy Observatory (NRAO) Very Large Array (VLA) sky survey (NVSS) at 1.4 GHz of Giovannini et al. (1999) and the one done with the Giant Metrewave Radio Telescope (GMRT) at 610 MHz by Venturi et al. (2007, 2008). For the latter, one can also construct a RLF at 1.4 GHz using the corresponding RHs follow-up measurements. The fractions of radio-loud clusters are about 6%, 18% and 24% for the NVSS 1.4 GHz, GMRT 610 MHz and GMRT 1.4 GHz samples, respectively. As explained in appendix D, the 1.4 GHz NVSS RLF (with a median redshift of $z \approx 0.18$) is finally taken as reference for the comparisons with observation. Note that the observational RLF determination is not very robust at this stage; the very different percent of radio-loud clusters found in different studies is indeed an indicator of this.

There is a general good agreement between the NVSS survey result and both the model RLF and the "true" RLFs, particularly for fraction of radio-loud clusters between 10% and 1%. The larger discrepancy seems to be present in the RLF obtained from the $L_{1.4\ \mathrm{GHz}} - L_{\mathrm{X,bol}}$ where the observed relation scatter is producing a high luminosity tail of objects contradicting the NVSS result. On the other side, the RLF obtained from the $L_{1.4\ \mathrm{GHz}} - Y_{\mathrm{SZ}}$ seems the one better matching the NVSS result. Note however that both facts may be artifacts due to the interplay of the two relation scatter and the still small statistic of the MultiDark $z = 0.2$ snapshot at very high masses. Figure 6.8 shows that it will be difficult to discriminate between different scenarios at high radio luminosities (or masses). Indeed, the bottom right plot of figure 6.8, where the model RLF and the "true" RLFs are compared at 10% radio-loud cluster fraction, suggests that the lower luminosity (mass) clusters will be the most useful in disentangling between different models. It is clear the key role of the upcoming LOFAR cluster survey for which predictions are presented

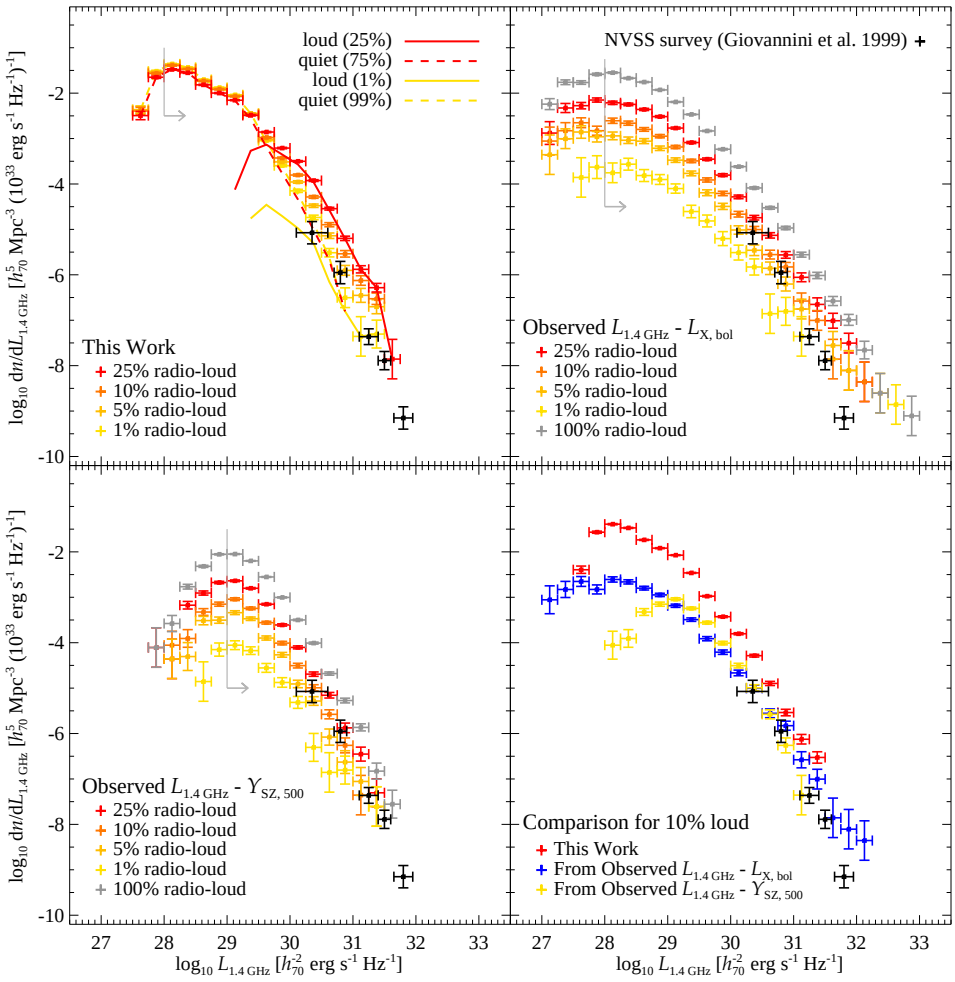

Figure 6.8: Radio Luminosity Function at 1.4 GHz. The top left panel shows the prediction of the final CR model (see main text for the details of the chosen parameters) for different percent of radio-loud clusters. Additionally shown is how the RLF builds up from the quiet and loud populations for the 25% and 1% cases. The top right panel shows the result obtained applying the observed $L_{1.4\ \mathrm{GHz}} - L_{\mathrm{X,bol}}$ directly to the MultiDark mass function at $z = 0.2$, using the $L_{\mathrm{X,bol}}$ of each halo as obtained from the phenomenological model, for different percent of radio-loud clusters. The bottom left panel shows the result obtained applying the observed $L_{1.4\ \mathrm{GHz}} - Y_{\mathrm{SZ,500}}$ directly to the MultiDark mass function at $z = 0.2$, using the $Y_{\mathrm{SZ,500}}$ of each halo as obtained from the phenomenological model, for different percent of radio-loud clusters. The bottom right panel shows the comparison between the three approaches for 10% of radio-loud clusters. The NVSS survey RLF (Giovannini et al., 1999) is also shown in all panels. Horizontal error bars represent the mass bins while the vertical error bars are Poissonian uncertainties. The light gray line with arrow shows the value above which the the RLF can be considered not affected by the low-luminosity decrease tail produced by the adopted mass cut (see section 6.1) and the scatter in the halo luminosities.

in the following. Note also the clear low-luminosity decrease in the RLFs that is an artifact due to the adopted mass cut (see section 6.1) and the scatter in the halo luminosities.
Figure 6.9 shows the predictions at 120 MHz obtained with the representative realization of the model detailed in the previous section with 10% of radio-loud clusters. Both the RLF (top left panel) and the cumulative number density (bottom left panel) are shown at the different MultiDark snapshots of table 6.1. Additionally shown is the expected LOFAR Tier 1 *point-source* flux limit of $F^{\rm PS}_{5\sigma} = 0.5$ mJy (Röttgering et al., 2012) converted to a luminosity limit at a given redshift. This flux limit is clearly underestimated for nearby RHs which extension in the sky can be as large as e.g. 1 deg in the Coma cluster case. In order to make more reliable predictions, in the following, the RH flux limit is calculated with the equation 10 of Cassano et al. (2010) taking R_{500} as halo extension and requiring the mean flux within the RH half-radius to be higher than $F^{\rm PS}_{5\sigma}$. This may result in an overestimation of the flux limit for CCCs, which radio emission is more centrally concentrated than NCCCs. The median R_{500} of the MultiDark sample is about 0.4 h_{70}^{-1} Mpc at all redshifts. This translates to a flux limit of about 30 mJy at $z = 0.1$, 7 mJy at $z = 0.2$ and 0.5 mJy, as the point-source value, at $z \approx 0.6$.
In order to make a more quantitative prediction, an analytical model which describes the evolving RLF is built. The 120 MHz RLF at different redshifts is fitted as a 2-order polynomial function in the form of $\log_{10} {\rm d}n/{\rm d}L_{120\ {\rm MHz}} = A_1 + A_2\ \log_{10} L_{120\ {\rm MHz}} + A_3\ (\log_{10} L_{120\ {\rm MHz}})^2$ (only luminosities higher then $\log_{10} L_{120\ 120{\rm MHz}} \geq 29.25$ are used in order to exclude the artificial low-luminosity decrease). An analytical form for the dependence of the three parameters A_i with respect to the redshift is obtained as $A_i = A_{i,0} + A_{i,1}\ (1 + z)$.[12] The right panels of figure 6.9 compare the RLF fits (top) and the cumulative number density (bottom) to the result obtained with the derived analytical model. The results obtained with the latter well compare with the prediction at a given redshift showing a significant deviation only at very high luminosities, and at very low luminosities for the highest considered redshifts, where however the very small statistic significantly affects the result.
This analytical model describing ${\rm d}N^2(L, z)/{\rm d}V_{\rm C}{\rm d}L$, where $V_{\rm C}$ is the comoving volume, is then used to calculate the total cumulative number of RHs in the sky above a given flux value F as

$$N(>F) = \int_{z_1}^{z_2} {\rm d}z \frac{{\rm d}V_{\rm C}}{{\rm d}z} \int_{L(F)}^{\infty} \frac{{\rm d}N^2(L, z)}{{\rm d}V_{\rm C}{\rm d}L} {\rm d}L\,, \tag{6.17}$$

where $L(F) = 4\pi D(z)^2 F$ and $D(z)$ is the luminosity distance computed from the corresponding redshift z. The result is shown in the left panel of figure 6.10 for the particular realization of the model described in the previous section with 10% fraction of radio-loud clusters (black solid thick line; only luminosities above $\log_{10} L_{120\ 120{\rm MHz}} \geq 29.25$ are integrated). The total is obtained integrating up to $z_2 = 2$ as above this value only few clusters survive the adopted mass cut and none would be detectable. The lower redshift limit (indicated as 0 in figure 6.10) is $z_1 = 0.018$ as the closer known RH, i.e. Perseus. Additionally shown is how the total result builds up in different redshift bins. This is compared to the RH total cumulative number obtained using *only* the 10% radio-loud clusters (black dashed thick line; this is done constructing the corresponding

[12]The values of these parameters are $A_{1,0} = -436.79$, $A_{1,1} = 109.75$, $B_{1,0} = 29.68$, $B_{1,1} = -7.17$, $C_{1,0} = -0.51$ and $C_{1,1} = 0.12$, and units are as the top left plot of figure 6.9.

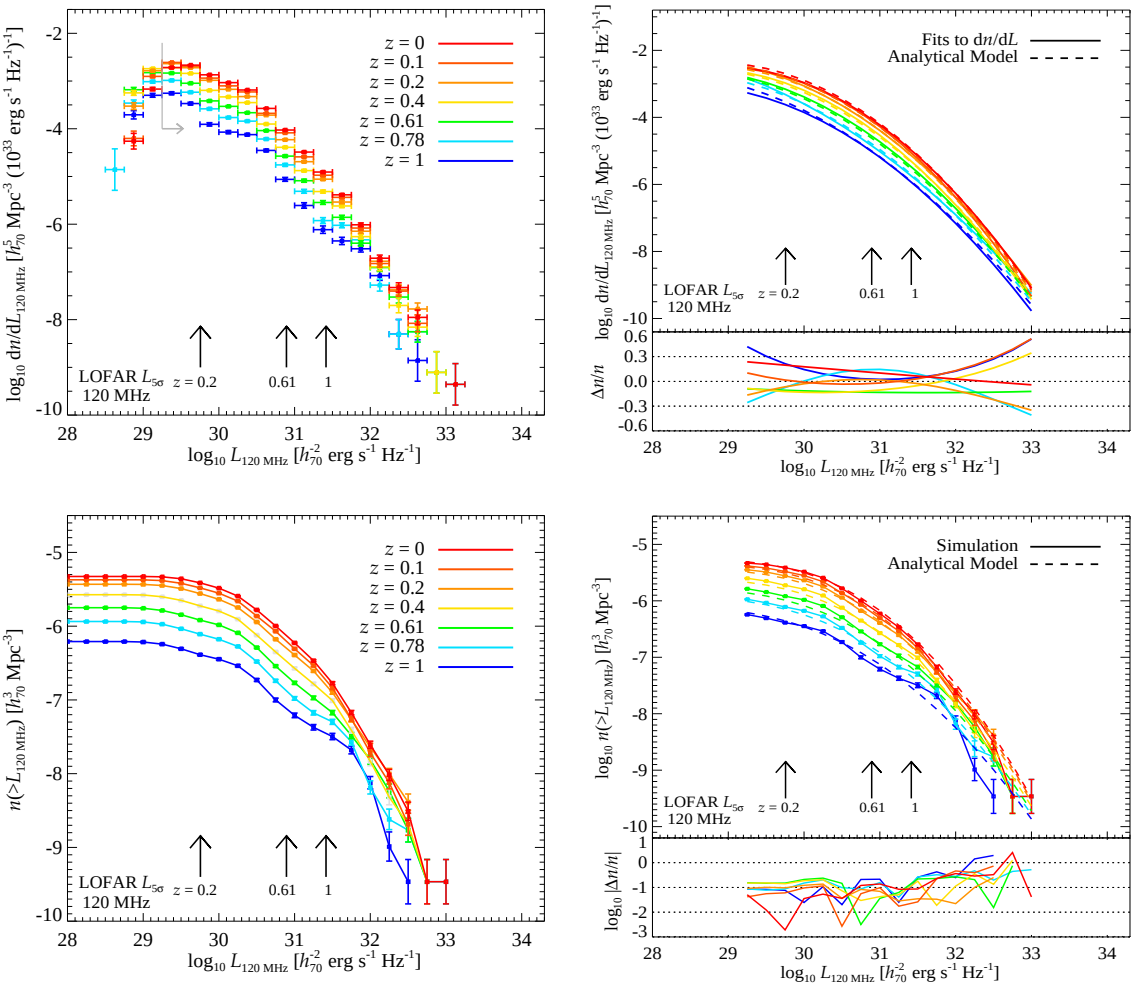

Figure 6.9: Radio luminosity function (top left panel) and cumulative number density (bottom left panel) at the different MultiDark samples of table 6.1 at 120 MHz for the model realization described in section 6.3 with 10% fraction of radio-loud clusters. By fitting the RLF with a 2-order polynomial function and modeling the 3 free parameters with respect to the redshift evolution, an analytical model for evolving RLF is obtained (see main text for details). The right panels show the comparison of the RLF fits (top) and the cumulative number density of the MultiDark samples (bottom) to the result obtained with the analytical model. The bottom panels of these two plots show the relative differences as $\Delta n/n = (n_{\rm analytical} - n_{\rm fit})/n_{\rm fit}$. Additionally shown is the LOFAR Tier 1 *point-source* flux limit of $F_{5\sigma}^{\rm PS} = 0.5$ mJy (Röttgering et al., 2012) converted to a luminosity limit at a given redshift. Horizontal error bars represent the mass bins while the vertical error bars are Poissonian uncertainties. The light gray line with arrow in the top left panel shows the value above which the the RLF can be considered not affected by the low-luminosity decrease tail produced by the adopted mass cut (see section 6.1) and the scatter in the halo luminosities.

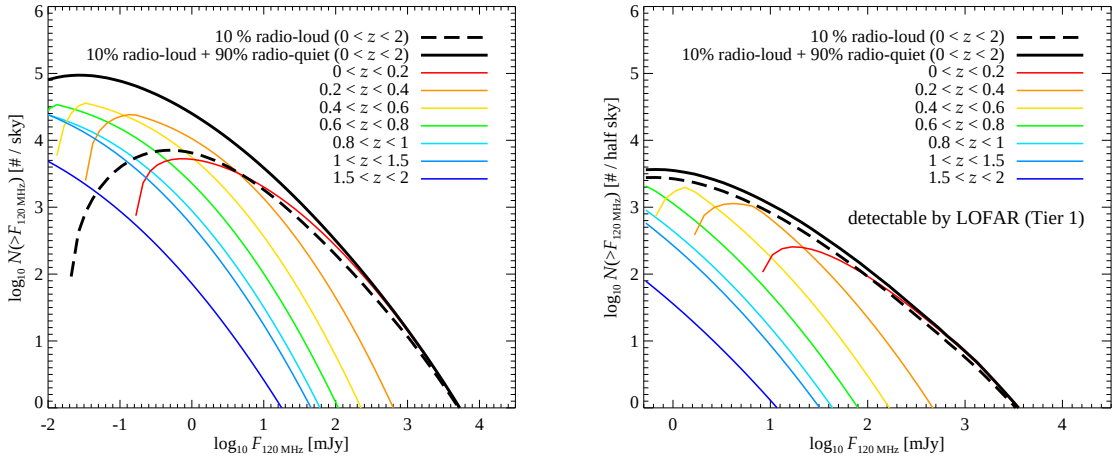

Figure 6.10: Cumulative number of RHs above a certain flux limit in all the sky at 120 MHz. Shown is the result of the model realization described in section 6.3 with 10% fraction of radio-loud clusters (black solid thick line) and the result obtained using *only* the 10% radio-loud clusters (black dashed thick line). Additionally shown is how the model total RLF (black solid thick line) builds up in different redshift bins. Note that the total number of (detectable) RHs would be dramatically reduced in the presence of a break in the model at some low mass-scale, or some sort of mass-dependence in the model parameters causing a lowering of the RH luminosities at low masses. *Left.* Total number of RHs in the sky. *Right.* Number of detectable RHs by the LOFAR Tier 1 survey considering its sky coverage (half sky) and flux limit at different redshifts, due to corresponding different source angular extensions, calculated with equation 10 of Cassano et al. (2010). The lower flux limit is taken to be $F^{\rm PS}_{5\sigma} = 0.5$ mJy. See main text for details.

RLF and repeating the above steps to build an analytical model, where only luminosities above $\log_{10} L_{120\ 120{\rm MHz}} \geq 30.75$ are integrated).

The right panel of figure 6.10 shows the total number of RHs that would be *detectable* by the LOFAR Tier 1 survey, where its sky coverage (about half sky) is taken into account. This is calculated with equation 6.17 taking $F = F_{\rm min}$ where $F_{\rm min}$ is calculated with the equation 10 of Cassano et al. (2010) as explained above. The lower flux limit is taken to be $F^{\rm PS}_{5\sigma}$, meaning that when $F_{\rm min} < 0.5$ mJy, i.e. at redshift above approximately $z = 0.6$, it is fixed at 0.5 mJy.

LOFAR Tier 1 at 120 MHz should be able to detect a total of about 3500 clusters hosting RHs above 0.5 mJy. The precise number is strongly dependent on the underling assumptions. There are two main uncertainties in the model constructed here: the fraction of radio-loud to radio-quiet clusters and the corresponding relative normalization (which in turn is the result of the interplay of the $\gamma_{\rm th}$, B_0, α_B, $g_{\rm CR}$, and therefore X_{CR}, parameters). The first is relevant only at medium-high luminosities, as can be seen for the 1.4 GHz RLFs in figure 6.9, and therefore would not dramatically impact the total number of (detectable) RHs because this is dominated by the low luminosities. The second uncertainty is assessed by comparing the total result of the model (black solid line) with the RLF obtained only from the radio-loud population (black dashed line).

Their difference somehow shows the uncertainty in the modeling for a fixed fraction of radio-loud clusters as all the configuration between the solid and dashed lines can be virtually realized changing the relative normalization of the loud and quiet populations.
The total number of (detectable) RHs is expected to be quite high. This is mainly due to neglecting an eventual mass-dependence in the model parameters and, more importantly, to the assumption that the model holds down to masses of about $M_{200} \approx 1.4 \times 10^{14}\ h_{70}^{-1}\ \mathrm{M}_{\odot}$ without any break. In fact, looking at the radio-to-X-ray and radio-to-SZ scaling relations of figure 6.7, one can see that most of the RHs in the MultiDark sample, also for the radio-loud population, lie at low masses and therefore at low luminosities unproved by current observations. The presence of a break at some low mass-scale, or some sort of mass-dependence in the model parameters causing a lowering of the RH luminosities, would eventually result in a dramatically reduced number of total (detectable) RHs. This would be more in agreement with recent predictions of a few to hundreds observable RHs by e.g. Cassano et al. (2010) and Sutter & Ricker (2011), while Enßlin & Röttgering (2002) also found that thousands of RHs would be detectable by future surveys. However, current information do not permit to make any reliable assumption in this sense.
Another relevant issue in such surveys is the identification of RHs and their hosting clusters (see also Cassano et al., 2010). RHs constitute a small part of the entire radio source population and therefore need to be distinguished from the emission produced by other sources. A good approach in this sense is to use X-ray samples of galaxy clusters. This underlines the importance of the future eROSITA mission also for the cluster non-thermal emission study as it is expected to detect around 10^5 clusters up to redshift $z \approx 1.3$ (see e.g. Cappelluti et al., 2011).
The results presented here show the potentiality of the LOFAR survey, and other future radio instruments, in determining the (120 MHz) RLF properties in a very broad range of luminosities. In particular, it should permit a robust determination of the number of clusters hosting RHs at a given luminosity (mass). This will be extremely helpful in determining the parameter values for the new hadronic model and eventually in elucidating the RH generation mechanism.

6.5 Conclusions

In this chapter, predictions for the RH population are presented assuming that RHs are generated by secondaries of the hadronic CR interactions with the ICM. A complete cosmological sample of galaxy clusters is built from the MultiDark N-body simulation (Prada et al., 2011) using seven snapshots from $z = 0$ up to $z = 1$ and selecting galaxy clusters by imposing a low mass cut at $M_{200} \approx 1.4 \times 10^{14}\ h_{70}^{-1}\ \mathrm{M}_{\odot}$.
First, a *phenomenological* model is constructed from the observed REXCESS cluster gas profiles (Croston et al., 2008) and cluster mass-to-gas fraction relation (Sun et al., 2009). This assigns a ICM gas density to a DM halo given only its total mass. In this way, a cosmological complete mock catalog of galaxy clusters is obtained such as it matches the observed $L_{\mathrm{X,bol}}$-to-mass, Y_{X}-to mass and Y_{SZ}-to-mass relations, and the X-ray luminosity function.
A new *hybrid* hadronic model for the CR distribution in clusters is then built merging previous results from simulations and analytical works. The semi-analytical mass-dependent universal normalization CR profile, obtained from the hydrodynamic cluster cosmological simulations of

Pinzke & Pfrommer (2010), is merged with the analytical model of Enßlin et al. (2011), which includes the treatment of CR transport processes. While CR advection tends to result in centrally enhanced CR profiles, the propagation in form of CR streaming and diffusion tends to produce flat CR profiles. The latter phenomena were not considered in previous works for sake of simplicity but turn out to be dramatically important. Note that the choice to adopt the Pinzke & Pfrommer (2010) simulation-derived universal profile, providing a mass-scaling, may introduce an overcooling problem. This can be counteracted by changing the $\gamma_{\rm tu}$ and α_B values, governing the CR transport processes and the magnetic field radial decline, respectively. However, the risk is that, when modeling a given galaxy cluster, the final $\gamma_{\rm tu}$ value may be biased as the CR transport effects are degenerate with the initial CR profile, the α_B value, and other possible effects not considered here as cluster asphericity and the contribution of primary electrons accelerated in outer shocks. Additionally, by adopting the result of Pinzke & Pfrommer (2010), which is parameterized with three CR spectral indexes $\alpha_i = (2.55, 2.3, 2.15)$, the possible CR transport effects on the CR spectral index are also neglected (see Enßlin et al., 2011 for details).

The Coma and Abell 2163 giant radio halos, and the Perseus and Ophiuchus radio mini-halos are modeled at 1.4 GHz. The new hybrid hadronic model can reproduce the surface brightness both of giant and mini-halos, solving problems of the *classical* hadronic model, and the total radio luminosity is recovered within a maximum of 20%. No tensions with existing observational constraints are found. Note that radio measurements put stringent constraints than corresponding gamma-ray observations, with the exception of the Coma cluster case. Gamma-ray measurements are fundamental to disentangle between the hadronic and re-acceleration models. The results presented here show however that gamma-ray predictions should be scaled down with respect to previous works (e.g. at least a factor of two for Perseus with respect to what used in chapter 3 and 4). Note in fact that the parameter space of the new hybrid hadronic model constructed here is largely extended with respect to previous models.

The radio emission of the clusters in the mock catalog is calculated, showing how different parameter choices in the CR modeling may affect the final result. A representative realization of the CR model is adopted and compared with existing observations. Thanks to the inclusion of the CR transport phenomena, the hadronic model built here can reproduce the apparent cluster bimodality observed in the radio-to-X-ray scaling relation (Brunetti et al., 2009; Enßlin et al., 2011) and, at the same time, it can reproduce the radio-to-SZ scaling relation recently presented by Basu (2012) which does not show any evidence of bimodality. This discrepancy may be only apparent as both results can here be reproduced with the same model.

The 1.4 GHz RLF is then calculated and compared with the observed one (Giovannini et al., 1999) finding a good agreement. The comparison between different RLFs illustrates that the low luminosity (mass) regime is the most promising range where to constrain different models by clearly determining the RH fraction against the total galaxy cluster population. Therefore, the 120 MHz RLF and cumulative number density are calculated in order to make predictions for the LOFAR cluster survey. The total cumulative number of RHs above a certain flux limit is obtained, showing that, under the assumptions made here, LOFAR Tier 1 at 120 MHz is expected to detect about 3500 RHs above 0.5 mJy. The precise number is strongly dependent on the underling assumptions and, in particular, to the assumption that the model holds down to masses of about $M_{200} \approx 1.4 \times 10^{14}\ h_{70}^{-1}\ \mathrm{M}_\odot$ without any break. Most of the RHs in the MultiDark

sample lie at low masses and therefore at low luminosities unproved by current observations. The presence of a break at some low mass-scale, or some sort of mass-dependence in the model parameters causing a lowering of the RH luminosities, would eventually result in a dramatically reduced number of total (detectable) RHs.
Concluding, this chapter shows the potentiality of observations by LOFAR, and other next-generation low-sensitivity radio instruments, in determining the RLF properties in a very broad range of luminosities. In particular, they should permit a robust determination of the number of clusters hosting RHs at a given luminosity (mass) and therefore elucidate the relation of the radio emission with cluster dynamical states in synergy with future X-ray missions like eROSITA. This will be extremely helpful in determining the parameter values for the new hadronic model built here and eventually in elucidating the RH generation mechanism.

Name	z	D	Δd	$L_{1.4\ \mathrm{GHz,\ obs}}$	Fit Parameters	$L_{1.4\ \mathrm{GHz,\ model}}$	References
		$[h_{70}^{-1}$ Mpc$]$	$[h_{70}^{-1}$ Mpc$]$	10^{31} $[h_{70}^{-2}$ erg s^{-1} Hz$^{-1}]$	γ_{tu}, α_{B}	10^{31} $[h_{70}^{-2}$ erg s^{-1} Hz$^{-1}]$	
Coma	0.023	101	2.15	0.72	1, 0.6	0.86	[1, 2, 3]
					4, 0.3	0.90	
A 2163	0.203	962	2.07	15.36	1, 0.3	13.43	[3, 4]
Perseus	0.018	78	0.15	4.40	3, 0.4	4.80	[3, 5, 6, 7]
					100, 0.3	3.97	
Ophiuchucs	0.028	121	0.41	0.19	5, 0.7	0.19	[3, 4]
					100, 0.3	0.23	

Table 6.5: Modeled radio halos and mini-halos. Top rows are giant radio halos, while the bottom are mini-halos. Δd represents the approximate dimension of the RH. $L_{1.4\ \mathrm{GHz,\ obs}}$ is the total luminosity at 1.4 GHz. M_{200} and R_{200} are taken from Reiprich & Böhringer (2002). The Coma ρ_{gas} and temperature are from Briel et al. (1992), while for A 2163 and Ophiuchus they are from Reiprich & Böhringer (2002). For Perseus, ρ_{gas} is from Churazov et al. (2003) and the temperature central dip is modeled as in Pfrommer & Enßlin (2004a). For all clusters, the outer temperature decrease is also adapted. Note that despite the fact that Ophiuchus is a CCC and has a central temperature dip, a constant temperature in the central part is used because the dip is important only below 30 h_{70}^{-1} kpc (see Million et al., 2010) and therefore it is not critical for the surface brightness modeling. The Fit Parameters column indicates the best fit values (top) and other permitted values for the modeling (bottom), and $L_{1.4\ \mathrm{GHz,\ model}}$ is the corresponding predicted total luminosity at 1.4 GHz within R_{200}. See the main text for details. References: [1] Deiss et al. (1997) [2] Briel et al. (1992) [3] Reiprich & Böhringer (2002) [4] Murgia et al. (2009) [5] Pedlar et al. (1990) [6] Churazov et al. (2003) [7] Pfrommer & Enßlin (2004a).

Part III

CONCLUSIONS AND FUTURE WORK

Chapter 7

Conclusions and Future Work

Morality is temporary,
wisdom is permanent.
Hunter S. Thompson

The topic of this PhD thesis is the study of non-thermal emission coming from CR and DM in clusters of galaxies. The main purpose is to gain a better understanding of the formation history of these objects and therefore of the Universe itself. My research work combines both observational and theoretical approaches, the former thanks to my participation in MAGIC gamma-ray experiment exploring the Universe at energies above 50 GeV. Here, the main contributions that this work brings to the above research field (see chapter 1) are summarized. At the end, I also detail some of the aspects that I consider important to be addressed in the near future.

A large part of this thesis is devoted to the search for the high-energy gamma-ray emission coming from the CR hadronic interactions in galaxy clusters. Such a discovery would dramatically help in disentangling between the hadronic and re-acceleration models of RHs, favoring the former. I leaded a deep observation campaign of the Perseus galaxy cluster with the MAGIC telescopes (described in detail in chapter 2) resulting in the longest observation ever of a cluster at VHE. The single-telescope observation performed in November-December 2008 for a total of about 25 hours is described in chapter 3 together with the implications for the possible CR-induded emission. This first observation is not enough sensitive to constrain emission models and only upper limits on the CR-to-thermal pressure, at a level of few percents, are obtained.
The MAGIC stereo observation campaign performed from October 2009 to February 2011 for a total of about 85 hours is described in chapter 4. During this campaign, VHE emission was discovered from the two Perseus cluster galaxies IC 310 and NGC 1275. This very deep observation permits, for the first time, to probe the underlying physics of cosmological hydrodynamic simulations of cluster formation by putting the strongest constraint to date to the CR-to-thermal pressure. This suggests the CR acceleration efficiency at structure formation shocks is lower than 50%, an optimistic but realistic value adopted in cosmological simulations, or the presence of non-negligible CR transport processes such as diffusion and streaming out of the cluster core region. Adopting a strong magnetic field everywhere in the radio-emitting region ($B >> B_{\rm CMB}$)

yields the minimum gamma-ray flux in the hadronic model of RHs. Depending on the assumed CR spectral index value, this flux is a factor of 2 to 18 below the MAGIC stereo upper limits. This puts the long-sought gamma-ray detection of clusters, in particular for Perseus, within the reach of deeper IACT campaigns with the possibility of scrutinizing the hadronic emission model of RHs.

As about 80% of the mass of galaxy clusters is in form of DM, these objects are also good candidates where to search for the secondary products of DM annihilation or decay. Amongst these secondary products, gamma-ray emission is expected at some level in many DM scenarios. This is investigated in chapter 3 for the Perseus cluster case using the MAGIC single telescope observation. The comparison with theoretical models is not very promising. In fact, with the assumed particle physics model, one of the most optimistic allowed scenarios with the neutralino as DM particle, boost factor values of the order of 10^4 are needed to reach the expected DM annihilation induced emission. Note, however, that possible contributions from internal bremsstrahlung, Sommerfeld enhancement as well as boost factors due to substructures are neglected in chapter 3. In fact, recent studies on the substructures effect in clusters show that their contribution is dramatically important, implying a flat DM annihilation emission profile out to the virial radius. This, together with the presence of the NGC 1275 signal at energies < 600 GeV in the MAGIC stereo data, calls for novel analysis techniques for DM searches in Perseus.

With the idea that extragalactic structures, such as galaxy clusters, are good DM candidates, in chapter 5 I investigate the potentiality of the NASA gamma-ray satellite *Fermi* in detecting a DM annihilation or decay induced signal from them. Using a constrained cosmological N-body simulation of the local Universe, provided by the CLUES project, I build all-skymaps of the density and density-squared DM distribution which are proportional to the DM decay and annihilation emission, respectively. In this kind of simulation, and therefore in the resulting all-skymaps, the main structures visible in the sky are well reproduced, such as the Virgo, Coma and Perseus clusters and the Great Attractor. Running 5-year *Fermi* observation simulations on these maps, for some representative DM models, permits to study the signal-to-noise all-skymaps. Eventually, I show that *Fermi* might detect DM induced gamma-ray emission from nearby galaxy clusters as well as from filaments of the cosmic web, particularly for some DM decay models.

The last part of the thesis is dedicated to the CR induced emission in clusters focusing on the radio domain. The next generation radio observatory, LOFAR, will play a fundamental role providing us with a galaxy cluster survey up to redshift $z \approx 1$. RH population studies will then permit the characterisation of the underlying physical mechanisms. I explore in detail this possibility for the hadronic model case in chapter 6. Basing on the observed cluster gas profiles and mass-to-gas fraction relation, a *phenomenological* model is constructed where a gas density can be assigned to a DM halo given only its total mass. This permits to create a cosmological complete cluster mock catalog from the MultiDark N-body simulation which well reproduces the observed X-ray cluster properties and statistics such as the observed $L_{\mathrm{X,bol}}$-to-mass, Y_{X}-to mass and Y_{SZ}-to-mass relations, and the X-ray luminosity function. I then construct a new *hybrid* hadronic model for the CR distribution in clusters, merging previous results from simulations and analytical works. In particular, it includes the treatment of CR transport processes. While CR advection tends to result in centrally enhanced CR profiles, the propagation in form of CR streaming and diffusion

tends to produce flat CR profiles. The latter phenomena are not considered in previous works for sake of simplicity but turn out to be dramatically important.
I show that this new hadronic model is able to match the observed RH properties of four representative cases (Coma, Abell 2163, Perseus and Ophiuchus) without entering in tension with any existing constraint. Note also that the corresponding gamma-ray predictions should be scaled down with respect to previous works (e.g. at least a factor of two for Perseus with respect to what considered in chapter 3 and 4). I then calculate the radio emission at 1.4 GHz for the clusters in the MultiDark mock catalog and compare them to observed scaling relations. Thanks to the inclusion of the CR transport phenomena, this new hadronic model can reproduce the apparent cluster bimodality observed in the radio-to-X-ray scaling relation. At the same time, it also reproduces the radio-to-SZ scaling relation which does not show any evidence of bimodality. As both results can be reproduced here with the same model, the corresponding observational discrepancy may be only apparent.
The 1.4 GHz RLF is then compared to the observed one, finding a good agreement. The comparison between different RLFs illustrates that the low luminosity (mass) regime is the most promising range where to constrain different models by clearly determining the RH fraction against the galaxy cluster population. Therefore, the 120 MHz RLF and cumulative number density are calculated, making prediction for the LOFAR cluster survey. I predict that the LOFAR Tier 1 cluster survey at 120 MHz should detect a total of about 3500 RHs above 0.5 mJy. The precise number depends on the underlying assumptions. Most of the RHs in my mock catalog lies at low masses and thus at low luminosities unproved by current observations. The presence of a break at some low mass-scale, or some sort of mass-dependence in the model parameters causing a lowering of the RH luminosities, would eventually result in a dramatically reduced number of total detectable RHs. However, current available information do not permit to make any reliable assumption in this direction. Eventually, I show that observations of LOFAR, and other next-generation low-sensitivity radio instruments, will be able to determine the RLF properties in a very broad range of luminosities. In particular, they should permit a robust determination of the number of clusters hosting RHs at a given luminosity (mass) and therefore elucidate the relation of the radio emission with cluster dynamical states. This will be extremely helpful in determining the parameter values for the new hadronic model constructed here and eventually in illustrating the RH generation mechanism.

Despite the important steps forward done in the last few years, it is not yet possible to say any conclusive word on the formation mechanism of RHs nor on the possible cluster CR induced gamma-ray emission. So far, the most constraining gamma-ray limit comes from the MAGIC observations of the Perseus galaxy cluster contained in chapter 3 and 4. Despite this large campaign, we are still far from the theoretical minimum gamma-ray flux and the parameter space for the hadronic model is still wide and far from being really constrained. In order to reach a deeper level of knowledge, additional IACT observations, of the order of hundred of hours, are needed. While this is a goal within the reach of current existing IACTs, there are many technical difficulties in such long-term observation campaigns given that they should be spread over many years. The planned next generation IACT instrument, CTA, is expected to have a much better sensitivity, particularly for extended sources, than existing IACTs. Therefore, I find fundamental

to study the feasibility and possible outcome of CTA cluster observations in elucidating the RH generation mechanism. The *Fermi* gamma-ray observations are also very important in this sense. *Fermi* has the advantage over existing IATCs of a full-sky survey and it can more easily deal with very extended sources. Integrating over 5 or more years, *Fermi* could indeed probe the expected cluster gamma-ray emission. Both IACTs and *Fermi* must be used in synergy in order to profit from their respective strengths and energy ranges.

We actually might be closer to some important insights on the non-thermal cluster emission in the radio regime where the LOFAR observatory is already in operation. A cluster survey is part of the LOFAR science key projects and will soon provide a large population of radio-observed galaxy clusters up to high redshift. The LOFAR predictions, provided in chapter 6 for the hadronic model, are only a beginning in this direction. The new hadronic model developed here is characterized by a much larger parameter space with respect to previous hadronic models and further work should be done investigating its full potential. Additionally, some open issues should be addressed in detail to understand their impact. In particular, the possible CR transport effect on the CR population spectral index, the contribute of primary electrons accelerated in outer shocks, which may be important over the total emission in the cluster outskirts, and cluster asphericity. The modeling of all know RHs in a comprehensive work will also help in understanding the hadronic model. Meanwhile, upcoming LOFAR results will permit to better characterize the model parameters and eventually to elucidate the RH generation mechanism.

The nature of DM is a pressing scientific question with very deep implications in almost all physics fields. After many efforts done in the past years, both with direct and indirect detection techniques, the theoretical window for the DM particle is eventually starting to narrow down. Observations of the secondary products of the DM annihilation or decay are a crucial way to understand the DM nature. Instruments in the gamma-ray regime are particularly well suited for these purposes because many DM candidates are expected to give rise to a very peculiar gamma-ray spectrum. In this sense, some observations have already been performed by existing IACTs and *Fermi*. It should be noted that our current knowledge places existing instruments, particularly ICATs, quite far from theoretical predictions, particularly for super-symmetric DM. Despite this, deep observation campaign on DM candidates should be continued as a possible positive outcome would be an incredible scientific breakthrough. Multi-frequency studies from radio to gamma-ray frequencies are also fundamental tools to investigate the DM nature.

From an astrophysical point of view, the full characterisation of the most promising objects for DM detection is vital. In particular, I found of fundamental importance to characterise the effect of DM substructures. Indeed, its impact on the DM induced emission can be dramatic, particularly for galaxy clusters. However, we are still far from a satisfactory knowledge of the DM substructure, therefore, its study by means of cosmological simulations as well as analytical work is fundamental.

According to the currently accepted cosmological scenario, structures grow hierarchically from small halos to larger ones and clusters of galaxies are the latest objects to form. Clusters have an enormous importance in cosmology because they represent an excellent way to test models on the origin and evolution of the Universe. The cluster population provides important information on cosmological parameters through its mass function, power spectrum and secondary CMB anisotropies. In order to make such studies, large and statistically complete cluster samples are

needed. X-ray surveys are still the most efficient way to detect clusters and to select well-defined samples. In fact, X-ray observations provide accurate measurements of many cluster physical parameters as the bremsstrahlung luminosity which is tightly correlated to the cluster gravitational mass, ICM density distribution and temperature. Therefore, most of the cosmological studies involve galaxy cluster samples based on X-ray observations. Besides the scope of probing cosmological models, the physical information that can be extracted from X-ray observations is also crucial in the understanding of the cluster non-thermal processes as shown in chapter 6. The future X-ray instrument eROSITA will be of maximum importance as it is expected to detect around about 10^5 clusters up to redshift 1.3. With such a large cluster sample, we will be able to strongly constrain the cosmological model and also to dramatically increase the knowledge of many cluster physical parameters. In this sense, the synergy with large mock-like cluster sample from N-body cosmological simulations is fundamental both for cosmology purposes and to study the non-thermal processes in galaxy clusters. Another instrument that is very important in this framework is the *Planck* satellite. The identification of the secondary anisotropies of the CMB, generated after the re-combination era, is crucial for cosmological studies. This is done identifying the distortions in the CMB spectrum caused by the thermal SZ effect. The SZ effect can be separated from the primary CMB anisotropies and used to study the cosmic structure evolution. In particular, the galaxy clusters that *Planck* detects via the SZ effect can be used as cosmological probes. Again, the synergy with N-body simulations is very important. The production of mock-like catalogs of SZ clusters and SZ all-sky maps are relevant tools for cosmology studies in conjunction with the *Planck* satellite results.

Concluding, the approaches used here open the road to many future applications in the radio, SZ, X-ray and gamma-ray fields. The study of non-thermal emission in galaxy clusters, combined with cosmological analyses of large cluster samples, will provide a deeper knowledge of the structure formation and eventually of the Universe evolution history.

Bibliography

Abdo, A. A., Ackermann, M., Ajello, M., et al. 2009, APJ, 699, 31

Abdo, A. A., Ackermann, M., Ajello, M., et al. 2010a, Physical Review Letters, 104, 091302

Abdo, A. A., Ackermann, M., Ajello, M., et al. 2010b, APJ, 712, 147

Abdo, A. A., Ackermann, M., Ajello, M., et al. 2010c, JCAP, 4, 14

Abramowitz, M. & Stegun, I. A. 1965, Handbook of mathematical functions with formulas, graphs, and mathematical tables, ed. Abramowitz, M. & Stegun, I. A.

Acciari, V. A., Aliu, E., Arlen, T., et al. 2009a, APL Letters, 706, L275

Acciari, V. A., Aliu, E., Arlen, T., et al. 2009b, Science, 325, 444

Acciari, V. A., Beilicke, M., Blaylock, G., et al. 2008, APJ, 679, 397

Acero, F., Aharonian, F., Akhperjanian, A. G., et al. 2009, Science, 326, 1080

Ackermann, M., Ajello, M., Allafort, A., et al. 2010a, APJ Letters, 717, L71

Ackermann, M., Ajello, M., Allafort, A., et al. 2010b, JCAP, 5, 25

Actis, M., Agnetta, G., Aharonian, F., et al. 2011, Experimental Astronomy, 32, 193

Aharonian, F., Akhperjanian, A., Beilicke, M., et al. 2003, A&A, 403, L1

Aharonian, F., Akhperjanian, A. G., Anton, G., et al. 2009a, A&A, 495, 27

Aharonian, F., Akhperjanian, A. G., Anton, G., et al. 2009b, A&A, 502, 437

Aharonian, F., Akhperjanian, A. G., Anton, G., et al. 2009c, APL Letters, 695, L40

Aharonian, F., Akhperjanian, A. G., Bazer-Bachi, A. R., et al. 2006a, Nature, 439, 695

Aharonian, F., Akhperjanian, A. G., Bazer-Bachi, A. R., et al. 2006b, Science, 314, 1424

Ajello, M., Rebusco, P., Cappelluti, N., et al. 2009, APJ, 690, 367

Albert, J., Aliu, E., Anderhub, H., et al. 2008a, APJ Letters, 685, L23

Albert, J., Aliu, E., Anderhub, H., et al. 2008b, Nuclear Instruments and Methods in Physics Research A, 588, 424

Albert, J., Aliu, E., Anderhub, H., et al. 2008c, APJ, 674, 1037

Albert, J., Aliu, E., Anderhub, H., et al. 2008d, APJ, 679, 428

Aleksić, J., Alvarez, E. A., Antonelli, L. A., et al. 2012a, A&A, 541, A99

Aleksić, J., Alvarez, E. A., Antonelli, L. A., et al. 2012b, A&A, 539, L2

Aleksić, J., Alvarez, E. A., Antonelli, L. A., et al. 2011, JCAP, 6, 35

Aleksić, J., Alvarez, E. A., Antonelli, L. A., et al. 2012c, Astroparticle Physics, 35, 435

Aleksić, J., Antonelli, L. A., Antoranz, P., et al. 2010a, APJ, 710, 634

Aleksić, J., Antonelli, L. A., Antoranz, P., et al. 2010b, APL Letters, 723, L207

Aliu, E., Anderhub, H., Antonelli, L. A., et al. 2009a, APJ, 697, 1299

Aliu, E., Anderhub, H., Antonelli, L. A., et al. 2009b, Astroparticle Physics, 30, 293

Anderson, B., Kuhlen, M., Diemand, J., Johnson, R. P., & Madau, P. 2010, APJ, 718, 899

Angel, J. R. P. & Stockman, H. S. 1980, ARA&A, 18, 321

Arvanitaki, A., Dimopoulos, S., Dubovsky, S., et al. 2009, Physical Review D, 79, 105022

Atwood, W. B., Abdo, A. A., Ackermann, M., et al. 2009, APJ, 697, 1071

Bagla, J. S. 2005, Current Science, 88, 1088

Basu, K. 2012, MNRAS, 421, L112

Battaglia, N., Bond, J. R., Pfrommer, C., & Sievers, J. L. 2011, ArXiv:1109.3709

Battaglia, N., Bond, J. R., Pfrommer, C., Sievers, J. L., & Sijacki, D. 2010, APJ, 725, 91

Becker, R. H., White, R. L., & Edwards, A. L. 1991, APJ Supplement, 75, 1

Begelman, M. C., Rees, M. J., & Blandford, R. D. 1979, Nature, 279, 770

Berezinsky, V. S., Blasi, P., & Ptuskin, V. S. 1997, APJ, 487, 529

Bergström, L. 2000, Reports on Progress in Physics, 63, 793

Bergström, L., Edsjö, J., & Zaharijas, G. 2009, Physical Review Letters, 103, 031103

Bergström, L. & Hooper, D. 2006, Physical Review D, 73, 063510

Bertone, G. 2010, Particle Dark Matter : Observations, Models and Searches, ed. Bertone, G. (Cambridge University Press)

Bertone, G., Hooper, D., & Silk, J. 2005, Physics Reports, 405, 279

Blasi, P. & Colafrancesco, S. 1999, Astroparticle Physics, 12, 169

Blasi, P., Gabici, S., & Brunetti, G. 2007, International Journal of Modern Physics A, 22, 681

Böhringer, H., Collins, C. A., Guzzo, L., et al. 2002, APJ, 566, 93

Böhringer, H., Tanaka, Y., Mushotzky, R., Ikebe, Y., & Hattori, M. 1998

Bonafede, A., Feretti, L., Murgia, M., et al. 2010, A&A, 513, A30+

Bonnarel, F., Fernique, P., Bienaymé, O., et al. 2000, A&A Supplement, 143, 33

Briel, U. G., Henry, J. P., & Boehringer, H. 1992, A&A, 259, L31

Bringmann, T., Bergström, L., & Edsjö, J. 2008, Journal of High Energy Physics, 1, 49

Broderick, A. E., Chang, P., & Pfrommer, C. 2011, ArXiv:1106.5494

Brown, A. M. & Adams, J. 2011, MNRAS, 413, 2785

Brunetti, G. & Blasi, P. 2005, MNRAS, 363, 1173

Brunetti, G., Cassano, R., Dolag, K., & Setti, G. 2009, A&A, 507, 661

Brunetti, G. & Lazarian, A. 2007, MNRAS, 378, 245

Brunetti, G. & Lazarian, A. 2011, MNRAS, 410, 127

Bullock, J. S., Kolatt, T. S., Sigad, Y., et al. 2001, MNRAS, 321, 559

Buttiglione, S., Capetti, A., Celotti, A., et al. 2010, A&A, 509, A6

Cappelluti, N., Predehl, P., Böhringer, H., et al. 2011, Memorie della Societa Astronomica Italiana Supplementi, 17, 159

Carilli, C. L. & Taylor, G. B. 2002, ARA&A, 40, 319

Cassano, R., Brunetti, G., Röttgering, H. J. A., & Brüggen, M. 2010, A&A, 509, A68

Cassano, R., Brunetti, G., Setti, G., Govoni, F., & Dolag, K. 2007, MNRAS, 378, 1565

Cavagnolo, K. W., Donahue, M., Voit, G. M., & Sun, M. 2009, APJ Supplemnet, 182, 12

Chen, C.-R., Mandal, S. K., & Takahashi, F. 2010, JCAP, 1, 23

Chen, Y., Reiprich, T. H., Böhringer, H., Ikebe, Y., & Zhang, Y.-Y. 2007, A&A, 466, 805

Churazov, E., Forman, W., Jones, C., & Böhringer, H. 2003, APJ, 590, 225

Cirelli, M., Panci, P., & Serpico, P. D. 2010, Nuclear Physics B, 840, 284

Clarke, T. E. 2004, Journal of Korean Astronomical Society, 37, 337

Clarke, T. E., Kronberg, P. P., & Böhringer, H. 2001, APL Letters, 547, L111

Clowe, D., Bradač, M., Gonzalez, A. H., et al. 2006, APJ Letters, 648, L109

Colafrancesco, S., Profumo, S., & Ullio, P. 2006, A&A, 455, 21

Coles, P. & Lucchin, F. 2002, Cosmology: The Origin and Evolution of Cosmic Structure, Second Edition, ed. Coles, P. & Lucchin, F.

Colin, P., Borla Tridon, D., Carmona, E., et al. 2009, ArXiv:0907.0960

Condon, J. J. & Broderick, J. J. 1988, Astronomical Journal, 96, 30

Condon, J. J., Cotton, W. D., & Broderick, J. J. 2002, Astronomical Journal, 124, 675

Croston, J. H., Pratt, G. W., Böhringer, H., et al. 2008, A&A, 487, 431

Cuesta, A. J., Jeltema, T. E., Zandanel, F., et al. 2011, APJ Letters, 726, L6

de Felice, F. & Clarke, C. J. S. 1990, Relativity on Curved Manifolds, ed. de Felice, F. & Clarke, C. J. S.

de Oña Wilhelmi, E. 2009, in American Institute of Physics Conference Series, Vol. 1112, American Institute of Physics Conference Series, ed. D. Bastieri & R. Rando, 16–22

Deiss, B. M., Reich, W., Lesch, H., & Wielebinski, R. 1997, A&A, 321, 55

Dennison, B. 1980, APL Letters, 239, L93

Dolag, K. & Enßlin, T. A. 2000, A&A, 362, 151

Domainko, W., Nedbal, D., Hinton, J. A., & Martineau-Huynh, O. 2009, International Journal of Modern Physics D, 18, 1627

Domingo-Santamaria, E., Flix, J., Rico, J., Scalzotto, V., & Wittek, W. 2005, in International Cosmic Ray Conference, Vol. 5, International Cosmic Ray Conference, 363–+

Domínguez, A., Primack, J. R., Rosario, D. J., et al. 2011, MNRAS, 410, 2556

Donnert, J., Dolag, K., Brunetti, G., Cassano, R., & Bonafede, A. 2010a, MNRAS, 401, 47

Donnert, J., Dolag, K., Cassano, R., & Brunetti, G. 2010b, MNRAS, 407, 1565

Douglas, J. N., Bash, F. N., Bozyan, F. A., Torrence, G. W., & Wolfe, C. 1996, Astronomical Journal, 111, 1945

Dubois, Y. & Teyssier, R. 2008, A&A, 482, L13

Dugger, L., Jeltema, T. E., & Profumo, S. 2010, JCAP, 12, 15

Dursi, L. J. & Pfrommer, C. 2008, APJ, 677, 993

Ebeling, H., Edge, A. C., Fabian, A. C., et al. 1997, APL Letters, 479, L101+

Eckert, D., Produit, N., Paltani, S., Neronov, A., & Courvoisier, T. J.-L. 2008, A&A, 479, 27

Edge, A. C., Stewart, G. C., & Fabian, A. C. 1992, MNRAS, 258, 177

Eisenstein, D. J., Weinberg, D. H., Agol, E., et al. 2011, Astronomical Journal, 142, 72

Enßlin, T., Pfrommer, C., Miniati, F., & Subramanian, K. 2011, A&A, 527, A99+

Enßlin, T. A., Biermann, P. L., Kronberg, P. P., & Wu, X.-P. 1997, APJ, 477, 560

Enßlin, T. A., Pfrommer, C., Springel, V., & Jubelgas, M. 2007, A&A, 473, 41

Enßlin, T. A. & Röttgering, H. 2002, A&A, 396, 83

Enßlin, T. A. & Vogt, C. 2006, A&A, 453, 447

Evans, N. W., Ferrer, F., & Sarkar, S. 2004, Physical Review D, 69, 123501

Fabian, A. C., Johnstone, R. M., Sanders, J. S., et al. 2008, Nature, 454, 968

Fabian, A. C., Sanders, J. S., Allen, S. W., et al. 2011a, MNRAS, 418, 2154

Fabian, A. C., Sanders, J. S., Allen, S. W., et al. 2011b, MNRAS, 418, 2154

Fabian, A. C., Sanders, J. S., Allen, S. W., et al. 2003, MNRAS, 344, L43

Fabian, A. C., Sanders, J. S., Taylor, G. B., et al. 2006a, MNRAS, 366, 417

Fabian, A. C., Sanders, J. S., Taylor, G. B., et al. 2006b, MNRAS, 366, 417

Felten, J. E. 1976, APJ, 207, 700

Feretti, L. 2003, in Astronomical Society of the Pacific Conference Series, Vol. 301, Astronomical Society of the Pacific Conference Series, ed. S. Bowyer & C.-Y. Hwang, 143–+

Feretti, L., Fusco-Femiano, R., Giovannini, G., & Govoni, F. 2001, A&A, 373, 106

Ferrari, C., Govoni, F., Schindler, S., Bykov, A. M., & Rephaeli, Y. 2008, Space Science Reviews, 134, 93

Fomin, V. P., Stepanian, A. A., Lamb, R. C., et al. 1994, Astroparticle Physics, 2, 137

Forman, W., Churazov, E., David, L., et al. 2003, ArXiv:0301476

Fornasa, M., Pieri, L., Bertone, G., & Branchini, E. 2009, Physical Review D, 80, 023518

Fujita, Y., Hayashida, K., Nagai, M., et al. 2008, Publications of the Astronomical Society of Japan, 60, 1133

Fujita, Y., Kohri, K., Yamazaki, R., & Kino, M. 2007, APL Letters, 663, L61

Galante, N., Acciari, V. A., Aliu, E., et al. 2009, ArXiv:0907.5000

Gao, L., Frenk, C. S., Jenkins, A., Springel, V., & White, S. D. M. 2012, MNRAS, 419, 1721

Giovannini, G., Feretti, L., Venturi, T., Kim, K. T., & Kronberg, P. P. 1993, APJ, 406, 399

Giovannini, G., Tordi, M., & Feretti, L. 1999, New Astronomy, 4, 141

Gitti, M., Brunetti, G., & Setti, G. 2002, A&A, 386, 456

Gómez-Vargas, G. A., Fornasa, M., Zandanel, F., et al. 2012, JCAP, 2, 1

Gottloeber, S., Hoffman, Y., & Yepes, G. 2010, ArXiv:1005.2687

Gottloeber, S. & Klypin, A. 2008, ArXiv:0803.4343

Govoni, F., Murgia, M., Markevitch, M., et al. 2009, A&A, 499, 371

Gregory, P. C. & Condon, J. J. 1991, APJ Supplement, 75, 1011

Han, J., Frenk, C. S., Eke, V. R., Gao, L., & White, S. D. M. 2012, ArXiv:1201.1003

Hartman, R. C., Bertsch, D. L., Bloom, S. D., et al. 1999, APJ Supplement Series, 123, 79

Heinz, S., Reynolds, C. S., & Begelman, M. C. 1998, APJ, 501, 126

Helder, E. A., Vink, J., Bassa, C. G., et al. 2009, Science, 325, 719

Hensley, B. S., Siegal-Gaskins, J. M., & Pavlidou, V. 2010, APJ, 723, 277

Hillas, A. M. 1985, in International Cosmic Ray Conference, Vol. 3, International Cosmic Ray Conference, ed. F. C. Jones, 445–448

Hinton, J. A. & Hofmann, W. 2009, A&A Annual Review, 47, 523

Hoffman, Y. & Ribak, E. 1991, APJ Letters, 380, L5

Hu, W. & Kravtsov, A. V. 2003, APJ, 584, 702

Jaffe, W. J. 1977, APJ, 212, 1

Jarosik, N., Bennett, C. L., Dunkley, J., et al. 2011, APJ Supplement, 192, 14

Jeltema, T. E., Kehayias, J., & Profumo, S. 2009, Physical Review D, 80, 023005

Jeltema, T. E. & Profumo, S. 2011, APJ, 728, 53

Jones, T. W. & Owen, F. N. 1979, APJ, 234, 818

Jubelgas, M., Springel, V., Enßlin, T., & Pfrommer, C. 2008, A&A, 481, 33

Kang, H. & Jones, T. W. 2005, APJ, 620, 44

Karlsson, N., Arlen, T., Aune, T., et al. 2009, ArXiv:0912.3807

Kataoka, J., Stawarz, Ł., Cheung, C. C., et al. 2010, APJ, 715, 554

Kempner, J. C., Blanton, E. L., Clarke, T. E., et al. 2004, in The Riddle of Cooling Flows in Galaxies and Clusters of galaxies

Keshet, U. 2010, ArXiv:1011.0729

Keshet, U. & Loeb, A. 2010, APJ, 722, 737

Kim, K.-T., Kronberg, P. P., & Tribble, P. C. 1991, APJ, 379, 80

Kiuchi, R., Mori, M., Bicknell, G. V., et al. 2009, APJ, 704, 240

Klypin, A., Hoffman, Y., Kravtsov, A. V., & Gottlöber, S. 2003, APJ, 596, 19

Klypin, A., Kravtsov, A. V., Valenzuela, O., & Prada, F. 1999, APJ, 522, 82

Knapp, G. R., Guhathakurta, P., Kim, D.-W., & Jura, M. A. 1989, APJ Supplement, 70, 329

Kravtsov, A. V., Klypin, A. A., Bullock, J. S., & Primack, J. R. 1998, APJ, 502, 48

Kravtsov, A. V., Klypin, A. A., & Khokhlov, A. M. 1997, APJ Supplement, 111, 73

Kravtsov, A. V., Vikhlinin, A., & Nagai, D. 2006, APJ, 650, 128

Krichbaum, T. P., Witzel, A., Graham, D. A., et al. 1992, A&A, 260, 33

Kuchar, P. & Enßlin, T. A. 2011, A&A, 529, A13+

Kuhlen, M., Diemand, J., & Madau, P. 2008, APJ, 686, 262

Kushnir, D., Katz, B., & Waxman, E. 2009, JCAP, 9, 24

Lal, D. V. & Rao, A. P. 2005, in Astronomical Society of the Pacific Conference Series, Vol. 345, From Clark Lake to the Long Wavelength Array: Bill Erickson's Radio Science, ed. N. Kassim, M. Perez, W. Junor, & P. Henning, 294

Lattanzi, M. & Silk, J. 2009, Physical Review D, 79, 083523

Li, T.-P. & Ma, Y.-Q. 1983, APJ, 272, 317

Libeskind, N. I., Yepes, G., Knebe, A., et al. 2010, MNRAS, 401, 1889

Loeb, A. & Waxman, E. 2000, Nature, 405, 156

Lopez Moya, M. 2007, PhD thesis, UCM Madrid

Lyutikov, M. 2006, MNRAS, 373, 73

Macciò, A. V., Dutton, A. A., & van den Bosch, F. C. 2008, MNRAS, 391, 1940

Mannheim, K. 1993, A&A, 269, 67

Mantz, A., Allen, S. W., Ebeling, H., Rapetti, D., & Drlica-Wagner, A. 2010, MNRAS, 406, 1773

Maraschi, L., Ghisellini, G., & Celotti, A. 1992, APJ Letters, 397, L5

Markevitch, M. 2006, in ESA Special Publication, Vol. 604, The X-ray Universe 2005, ed. A. Wilson, 723

Martin, P. G., Thompson, I. B., Maza, J., & Angel, J. R. P. 1983, APJ, 266, 470

Maza, J. 1979, PhD thesis, University of Toronto

McElroy, D. B. 1995, APJ Supplement, 100, 105

Meade, P., Papucci, M., Strumia, A., & Volansky, T. 2010, Nuclear Physics B, 831, 178

Million, E. T., Allen, S. W., Werner, N., & Taylor, G. B. 2010, MNRAS, 405, 1624

Miniati, F. 2002, MNRAS, 337, 199

Miniati, F. 2003, MNRAS, 342, 1009

Miniati, F., Ryu, D., Kang, H., & Jones, T. W. 2001, APJ, 559, 59

Mori, M. & Cangaroo Collaboration. 2001, in International Cosmic Ray Conference, Vol. 7, International Cosmic Ray Conference, 2831

Mücke, A., Protheroe, R. J., Engel, R., Rachen, J. P., & Stanev, T. 2003, Astroparticle Physics, 18, 593

Murgia, M., Eckert, D., Govoni, F., et al. 2010, A&A, 514, A76

Murgia, M., Govoni, F., Markevitch, M., et al. 2009, A&A, 499, 679

Navarro, J. F., Frenk, C. S., & White, S. D. M. 1996, APJ, 462, 563

Navarro, J. F., Frenk, C. S., & White, S. D. M. 1997, APJ, 490, 493

Neronov, A. & Aharonian, F. A. 2007, APJ, 671, 85

Neronov, A., Semikoz, D., & Vovk, I. 2010, A&A, 519, L6

Nevalainen, J., Eckert, D., Kaastra, J., Bonamente, M., & Kettula, K. 2009, A&A, 508, 1161

Nolan, P. L., Abdo, A. A., Ackermann, M., et al. 2012, APJ Supplement, 199, 31

Otte, N., A. Acciari, V. A., Aliu, E., et al. 2009, ArXiv:0907.4826

Papucci, M. & Strumia, A. 2010, JCAP, 3, 14

Parrish, I. J. & Quataert, E. 2008, APJ Letters, 677, L9

Pedlar, A., Ghataure, H. S., Davies, R. D., et al. 1990, MNRAS, 246, 477

Pérez-Torres, M. A., Zandanel, F., Guerrero, M. A., et al. 2009, MNRAS, 396, 2237

Perkins, J. S. 2008, in American Institute of Physics Conference Series, Vol. 1085, American Institute of Physics Conference Series, ed. F. A. Aharonian, W. Hofmann, & F. Rieger, 569–572

Perkins, J. S., Badran, H. M., Blaylock, G., et al. 2006, APJ, 644, 148

Petrosian, V., Bykov, A., & Rephaeli, Y. 2008, Space Science Reviews, 134, 191

Pfrommer, C. 2005, PhD thesis, München University

Pfrommer, C. 2008, MNRAS, 385, 1242

Pfrommer, C. & Dursi, L. J. 2010, Nature Physics, 6, 520

Pfrommer, C. & Enßlin, T. A. 2003, A&A, 407, L73

Pfrommer, C. & Enßlin, T. A. 2004a, A&A, 413, 17

Pfrommer, C. & Enßlin, T. A. 2004b, MNRAS, 352, 76

Pfrommer, C., Enßlin, T. A., & Springel, V. 2008, MNRAS, 385, 1211

Pfrommer, C., Enßlin, T. A., Springel, V., Jubelgas, M., & Dolag, K. 2007, MNRAS, 378, 385

Pfrommer, C., Springel, V., Enßlin, T. A., & Jubelgas, M. 2006, MNRAS, 367, 113

Pinzke, A. & Pfrommer, C. 2010, MNRAS, 409, 449

Pinzke, A., Pfrommer, C., & Bergström, L. 2009, Physical Review Letters, 103, 181302

Pinzke, A., Pfrommer, C., & Bergström, L. 2011, Physics Review D, 84, 123509

Planck Collaboration, Ade, P. A. R., Aghanim, N., et al. 2011, A&A, 536, A11

Prada, F., Klypin, A. A., Cuesta, A. J., Betancort-Rijo, J. E., & Primack, J. 2011, ArXiv:1104.5130

Prandini, E. 2011, PhD thesis, Universitá degli Studi di Padova

Pratt, G. W., Croston, J. H., Arnaud, M., & Böhringer, H. 2009, A&A, 498, 361

Primack, J. R. 2001, in COSMO-2000, ed. J. E. Kim, P. Ko, & K. Lee, 1–18

Profumo, S. & Jeltema, T. E. 2009, JCAP, 7, 20

Quataert, E. 2008, APJ, 673, 758

Rector, T. A., Stocke, J. T., & Perlman, E. S. 1999, APJ, 516, 145

Reimer, O., Pohl, M., Sreekumar, P., & Mattox, J. R. 2003, APJ, 588, 155

Reiprich, T. H. & Böhringer, H. 2002, APJ, 567, 716

Rephaeli, Y., Nevalainen, J., Ohashi, T., & Bykov, A. M. 2008, Space Science Reviews, 134, 71

Riebe, K., Partl, A. M., Enke, H., et al. 2011, ArXiv e-prints

Rolke, W. A., López, A. M., & Conrad, J. 2005, Nuclear Instruments and Methods in Physics Research A, 551, 493

Rosati, P., Borgani, S., & Norman, C. 2002, ARA&A, 40, 539

Röttgering, H., Afonso, J., Barthel, P., et al. 2012, Journal of Astrophysics and Astronomy, 34

Sánchez-Conde, M. A. 2009, PhD thesis, Universidad de Granada

Sánchez-Conde, M. A., Cannoni, M., Zandanel, F., Gómez, M. E., & Prada, F. 2011, JCAP, 12, 11

Sánchez-Conde, M. A., Prada, F., Łokas, E. L., et al. 2007, Physical Review D, 76, 123509

Sanderson, A. J. R., O'Sullivan, E., & Ponman, T. J. 2009, MNRAS, 395, 764

Sarazin, C. L. 1988, X-ray emission from clusters of galaxies (Cambridge Astrophysics Series, Cambridge: Cambridge University Press, 1988)

Sato, K., Furusho, T., Yamasaki, N. Y., et al. 2005, Publications of the Astronomical Society of Japan, 57, 743

Schlickeiser, R. 2002, Cosmic ray astrophysics (Springer. ISBN 3-540-66465-3)

Schlickeiser, R., Sievers, A., & Thiemann, H. 1987, A&A, 182, 21

Schuecker, P., Finoguenov, A., Miniati, F., Böhringer, H., & Briel, U. G. 2004, A&A, 426, 387

Seyfert, C. K. 1943, APJ, 97, 28

Sijbring, D. & de Bruyn, A. G. 1998, A&A, 331, 901

Sijbring, L. G. 1993, PhD thesis, Groningen University

Simon, J. D. & Geha, M. 2007, APJ, 670, 313

Springel, V., White, S. D. M., Frenk, C. S., et al. 2008, Nature, 456, 73

Strigari, L. E., Koushiappas, S. M., Bullock, J. S., & Kaplinghat, M. 2007, Physical Review D, 75, 083526

Sun, M., Voit, G. M., Donahue, M., et al. 2009, APJ, 693, 1142

Sutter, P. M. & Ricker, P. M. 2011, ArXiv:1110.2786

Taoso, M., Bertone, G., & Masiero, A. 2008, JCAP, 3, 22

Tavani, M. & AGILE Team. 2011, Nuclear Instruments and Methods in Physics Research A, 630, 7

Tavecchio, F. & Ghisellini, G. 2008, MNRAS, 385, L98

Taylor, G. B., Fabian, A. C., & Allen, S. W. 2002, MNRAS, 334, 769

Taylor, G. B., Gugliucci, N. E., Fabian, A. C., et al. 2006, MNRAS, 368, 1500

Totani, T. & Kitayama, T. 2000, APJ, 545, 572

Tremaine, S., Gebhardt, K., Bender, R., et al. 2002, APJ, 574, 740

Urry, C. M. & Padovani, P. 1995, Publications of the Astronomical Society of the Pacific, 107, 803

van Weeren, R. J., Röttgering, H. J. A., Brüggen, M., & Hoeft, M. 2010, Science, 330, 347

Venturi, T., Giacintucci, S., Brunetti, G., et al. 2007, A&A, 463, 937

Venturi, T., Giacintucci, S., Dallacasa, D., et al. 2008, A&A, 484, 327

Vermeulen, R. C., Readhead, A. C. S., & Backer, D. C. 1994, APJ Letters, 430, L41

Veron, P. 1978, Nature, 272, 430

Vestrand, W. T. 1982, Astronomical Journal, 87, 1266

Vikhlinin, A., Markevitch, M., Murray, S. S., et al. 2005, APJ, 628, 655

Vogt, C. & Enßlin, T. A. 2005, A&A, 434, 67

Voit, G. M. 2005, Reviews of Modern Physics, 77, 207

Völk, H. J., Aharonian, F. A., & Breitschwerdt, D. 1996, Space Science Reviews, 75, 279

Watanabe, M., Yamashita, K., Furuzawa, A., Kunieda, H., & Tawara, Y. 2001, Publications of the Astronomical Society of Japan, 53, 605

Weekes, T. C., Cawley, M. F., Fegan, D. J., et al. 1989, APJ, 342, 379

Weinberg, S. 1972, Gravitation and Cosmology: Principles and Applications of the General Theory of Relativity, ed. Weinberg, S.

White, R. L. & Becker, R. H. 1992, APJ Supplement, 79, 331

Willman, B., Geha, M., Strader, J., et al. 2011, Astronomical Journal, 142, 128

Yepes, G., Martínez-Vaquero, L. A., Gottlöber, S., & Hoffman, Y. 2009, in American Institute of Physics Conference Series, Vol. 1178, American Institute of Physics Conference Series, ed. C. Balazs & F. Wang, 64–75

Zandanel, F. 2007, Diploma thesis, Universitá degli Studi di Padova

Zavala, J., Springel, V., & Boylan-Kolchin, M. 2010, MNRAS, 405, 593

Zhang, L., Weniger, C., Maccione, L., Redondo, J., & Sigl, G. 2010, JCAP, 6, 27

Zimmer, S., Conrad, J., & Pinzke, A. 2012, in American Astronomical Society Meeting Abstracts, Vol. 219, American Astronomical Society Meeting Abstracts, 207.01

Zwicky, F. & Kowal, C. T. 1968, ”Catalogue of Galaxies and of Clusters of Galaxies”, Volume VI, ed. Zwicky, F., Herzog, E., & Wild, P.

Appendix A

Radio Emission Calculation

The factor A_ν for the synchrotron radio luminosity calculation of equation 6.5 is:

$$A_\nu = A_{\mathrm{E_{synch}}} \frac{16^{2-\alpha_\mathrm{e}} \sigma_\mathrm{pp} m_\mathrm{e} c^2}{(\alpha_\mathrm{e}-2)\sigma_\mathrm{T} \epsilon_{B_\mathrm{C}} m_\mathrm{p}} \left(\frac{m_\mathrm{p}}{m_\mathrm{e}}\right)^{\alpha_\mathrm{e}-2} \left(\frac{m_\mathrm{e}c^2}{\mathrm{GeV}}\right)^{\alpha_\mathrm{e}-1}, \tag{A.1}$$

with:

$$A_{\mathrm{E_{synch}}} = \frac{\sqrt{3\pi}}{32\pi} \frac{B_\mathrm{c} e^3}{m_\mathrm{e} c^2} \frac{\alpha_\mathrm{e} + \frac{7}{3}}{\alpha_\mathrm{e}+1} \frac{\Gamma\left(\frac{3\alpha_\mathrm{e}-1}{12}\right)\Gamma\left(\frac{3\alpha_\mathrm{e}+7}{12}\right)\Gamma\left(\frac{\alpha_\mathrm{e}+5}{4}\right)}{\Gamma\left(\frac{\alpha_\mathrm{e}+7}{4}\right)}, \tag{A.2}$$

where $\alpha_\mathrm{e} = \alpha + 1$ and Γ is the Gamma-function (Abramowitz & Stegun, 1965). $A_{\mathrm{E_{synch}}}$ is expressed in erg, and A_ν is expressed in erg cm^3 g^{-1} sr^{-1}.
The generalization of the radio luminosity calculation to three CR spectral indexes and the inclusion of the maximum CR acceleration efficiency parameter g_CR, following Pinzke & Pfrommer (2010), changes j_ν into:

$$\begin{aligned} j_{\nu,\mathrm{final}} &= g_\mathrm{CR} C(R) \rho_\mathrm{gas}(R) \frac{\epsilon_\mathrm{B}(R)}{\epsilon_\mathrm{B}(R) + \epsilon_\mathrm{CMB}} \\ &\times \Sigma_{i=1}^{3} \Delta_i A_{\nu,i} \left(\frac{\epsilon_\mathrm{B}(R)}{\epsilon_{B_\mathrm{c}}}\right)^{\frac{\alpha_i-2}{4}}, \end{aligned} \tag{A.3}$$

where the sum is over the three CR spectral indexes $\alpha_i = (2.55, 2.3, 2.15)$ with the corresponding factors $\Delta_i = (0.767, 0.143, 0.0975)$ found by Pinzke & Pfrommer (2010).

Appendix B

Cosmic Rays Modeling Details

In order to make some comparisons between $C_{\rm simple}$ and $C_{\rm transport}$, the NCCC Coma and the CCC Perseus cases are taken as reference. While for Coma the β-profile of equation 6.11 is a good approximation, and it is taken from Briel et al. (1992), for Perseus a double-β profile is needed. The following approximation is made: $P(R)/P_0 = n_{\rm e}(R)/n_0$, with $n_{\rm e}(R)$ both the double-β profile of Churazov et al. (2003) and the proper Perseus pressure profile as in section 6.2 (for Perseus, $R_{\rm c}$ is taken to be equal to the outer double-β profile core radius and $\beta_{\rm cl} = 0.8$). Note that the Enßlin et al. (2011) formalism is exact only for the approximation $P(R)/P_0 = n_{\rm e}(R)/n_0$ and in the case of a β-profile. There is not an exact analytical solution for the case of a double-β profile: one should use a numerical solution. In chapter 6, different choices for $P(R)/P_0$ are made, and a model that has to be applied to all the halos of the MultiDark sample is built. Numerically solutions are not used for each case. Instead, the Enßlin et al. (2011) formalism is adopted as a good approximation. The relevant parameters are $\gamma_{\rm tu}$, the exponential factor of equation 6.12, and the two radius $R_{\pm}$ that in general are very small/large so that the detail of $P(R)/P_0$ does not affect them critically. Indeed, other uncertainties, e.g. the assumption that the characteristic radius at which the turbulence is injected is the cluster core radius, are dominating and therefore with this approach the main CR transport effects are captured. The comparison between $C_{\rm simple}$ and $C_{\rm transport}$ is shown in figure B.1, where the result in case $C(R) = C_{\rm semi-analytical}(R) = \tilde{C}(R)\rho_{\rm gas}(R)/m_{\rm p}$, with $\tilde{C}(R)$ is the mass-dependent universal normalization CR profile found in cosmological simulations of Pinzke & Pfrommer (2010), is also shown. As expected, the CR profile driven by simulations is characterized by a more centrally peaked profile with respect to the analytical case. Note also the much more centrally peaked profile of Perseus with respect to Coma, which reflects their CCC and NCCC classification respectively, and the impact that have neglecting the temperature dependence in the Perseus case. Finally, the effect of varying the turbulent cluster state by means of $\gamma_{\rm tu}$ can be clearly appreciated.

In chapter 6, the Enßlin et al. (2011) approach needs to be generalized and merged with the $\tilde{C}$ universal CR normalization obtained from simulations. Also in this case there is not an exact solution for the Enßlin et al. (2011) treatment of the problem. In fact, when trying to solve it analytically, one ends up with a 5-order equation. It is not practical to solve numerically such equation, and at the same time to discharge the unphysical solution, for all the MultiDark halos. For simplicity, the approximation of using the Enßlin et al. (2011) formalism is made,

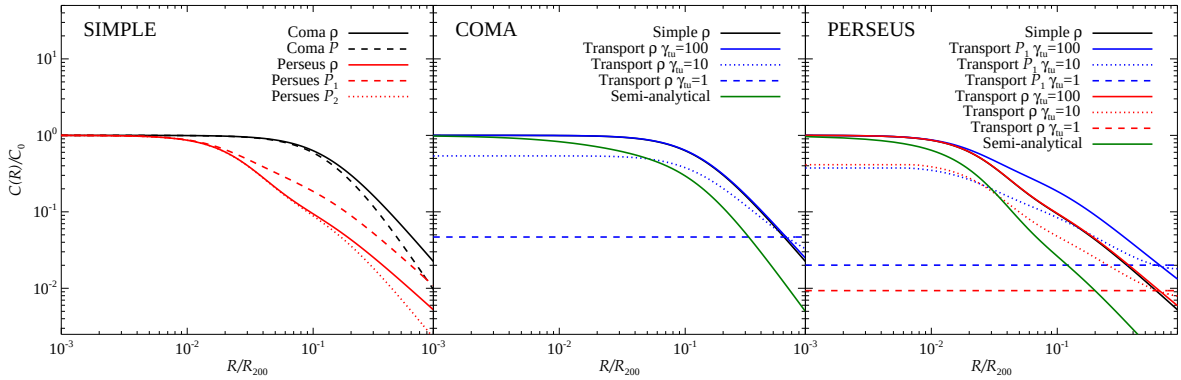

Figure B.1: Comparison of different CR profiles. The left panel shows $C_{\rm simple}$ for the Coma and Perseus cases both neglecting the temperature dependence (ρ) and considering it (P). The temperature profile of Coma has been modified so that it follows the characteristic decline toward the cluster periphery (Pfrommer et al., 2007; Pinzke & Pfrommer, 2010). Perseus is a CCC and it is characterized by a central dip in the temperature profile which may importantly affect the final CR profile, so the temperature profile as given in (Pfrommer & Enßlin, 2004a) (P_1) is adopted. Also shown is the case where only the characteristic decline toward the cluster periphery (P_2) is applied. The other two right panels show the *transport* case of Coma and Perseus for different values of $\gamma_{\rm tu}$ in comparison with the *simple* case. Additionally shown is the result in case of $C(R) = C_{\rm semi-analytical}(R) = \tilde{C}(R)\rho_{\rm gas}(R)/m_{\rm p}$ where $\tilde{C}(R)$ is the mass-dependent universal normalization CR profile found in cosmological simulations of Pinzke & Pfrommer (2010). The *simple* and *semi-analytical* profiles are normalized at $C_0 = C(0)$. The transport cases are normalized at $C_0 = C(0, \gamma_{\rm tu} = 100)$, where the CR populations are obliged to have a constant total CR number as in equation 36 of Enßlin et al. (2011) integrating up R_{200}. Finally, $\alpha = 2.3$.

after some modifications in order to adapt it to the case of chapter 6. In the case of taking just $P(R)/P_0 = n_{\rm e,GNFW}(R)/n_0$, with $n_{\rm e,GNFW}$ the profile of equation 6.1, there exist an exact solution following the Enßlin et al. (2011) treatment. Therefore, in order to qualitatively have an idea of how much is the error with the above described approach, figure B.2 compares the $C_{\rm transport}(R)$ of the GNFW exact solution and the approximate case where the Enßlin et al. (2011) formulae is used just adopting $P(R)/P_0 = n_{\rm e,GNFW}(R)/n_0$. In the second case, $R_- = 10^{-3}R/R_{200}$ in order to mimic the typical R_- value of the exact solution, otherwise a unphysical step feature would appear around $10^{-2}R/R_{200}$. This latter approximation is kept in the final model built in chapter 6. Note however that this modification does not change at all the model surface brightness and total luminosity. As clear from the figure, there is almost no appreciable difference between the two cases. The comparison shows that this approximated approach can be safely followed in order to derive a fully working model capturing the main CR transport effects.

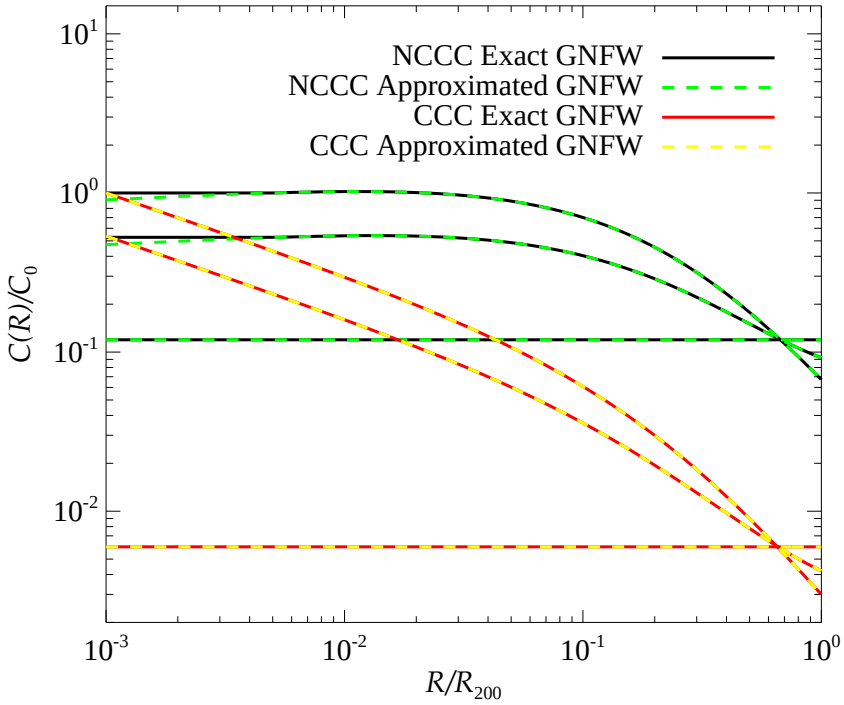

Figure B.2: Comparison of $C_{\rm transport}(R)$ for the GNFW exact solution and the approximated case where the Enßlin et al. (2011) formulae is used just with $P(R)/P_0 = n_{\rm e,GNFW}(R)/n_0$. Both the NCCC and CCC case for the respective GNFW profiles derived in section 6.1.2 are shown. From top to bottom: $\gamma_{\rm tu} = 100$, $\gamma_{\rm tu} = 10$ and $\gamma_{\rm tu} = 1$. The normalization is done at $C_0 = C(0, \gamma_{\rm tu} = 100)$ of the exact model where the CR populations are obliged to have a constant total CR number as in equation 36 of Enßlin et al. (2011) integrating up R_{200}. Note that the $C(0, \gamma_{\rm tu} = 100)$ value for the CCC case is identical between the exact and approximated model, while there is a small difference of about 9% in the NCCC case. Finally, $\alpha = 2.3$.

Appendix C

Gamma-ray Emission Calculation

The gamma-ray flux above a certain energy E_γ can be written as:

$$F_\gamma(E_\gamma) = \frac{1}{4\pi D^2} L_\gamma = 4\pi \int_0^{R_{500}} 2\pi S(R_\perp) R_\perp \mathrm{d}R_\perp \tag{C.1}$$

where $S(R_\perp)$ is the surface brightness:

$$S(R_\perp) = 2 \int_{R_\perp}^{\infty} j_\gamma(R) \frac{R}{\sqrt{R^2 - R_\perp^2}} \mathrm{d}R \tag{C.2}$$

with $j_\gamma(R) = A_\gamma \tilde{S}_\gamma(R)$ and $\tilde{S}_\gamma(R) = C(R)\rho_{\mathrm{gas}}(R)$. The parameter A_γ is (Pinzke & Pfrommer, 2010):

$$A_\gamma = g_{\mathrm{CR}} D_{\gamma,\mathrm{break}} \frac{4 m_{\pi^0} c}{3 m_{\mathrm{p}}^2} \Sigma_{i=1}^{3} \Delta_i \frac{\sigma_{\mathrm{pp,i}}}{\alpha_i \delta_i} \left(\frac{m_{\mathrm{p}}}{2 m_{\pi^0}} \right)^{\alpha_i} \times \\ \times \left[\beta_x \left(\frac{\alpha_i + 1}{2\delta_i}, \frac{\alpha_i - 1}{2\delta_i} \right) \right]_{x_1}^{x_2} \tag{C.3}$$

where $x_j = \left[1 + \left(\frac{m_{\pi^0} c^2}{2 E_{\gamma,j}} \right)^{2\sigma_i} \right]$, $[\beta_x(a,b)]_{x_1}^{x_2} = \beta_{x_2}(a,b) - \beta_{x_1}(a,b)$ and β denotes the incomplete Beta-function (Abramowitz & Stegun, 1965), and $\delta_i = 0.14\alpha_i^{-1.6} + 0.44$. The term $D_{\gamma,\mathrm{break}} = D_\gamma(E_\gamma, E_{\gamma,\mathrm{break}})$ represent diffusive CR losses due to escaping protons from the cluster at the equivalent photon energy for the break $E_{\gamma,\mathrm{break}}$ (see Pinzke & Pfrommer, 2010 for details). A_γ is expressed in $\mathrm{cm}^3\ \mathrm{s}^{-1}\ \mathrm{g}^{-1}$.

Appendix D

Observational Radio-to-X-ray Scaling relation and Radio Luminosity Function

For comparison with the observed 1.4 GHz radio-to-X-ray scaling relation, all the radio halos in the Enßlin et al. (2011) list are used and the corresponding X-ray bolometric luminosities taken from Brunetti et al. (2009). Four mini-halos from the Enßlin et al. (2011) list are used (excluding RXCJ1314.4-2515 and Z7160 because X-ray bolometric measurements are not present for them, and A2626 because its bolometric X-ray luminosity would place it as an extreme outlier with respect to the others). The Ophiuchus, A2029 and A1835 mini-halos are also added (Govoni et al., 2009). X-ray bolometric luminosities are taken form Reiprich & Böhringer (2002) for Perseus, A2142, A2029, PKS0745-191 and Ophiuchus, from Böhringer et al. (1998) for A2390, and from Cavagnolo et al. (2009) (ACCEPT: Archive of Chandra Cluster Entropy Profile Tables; http://www.pa.msu.edu/astro/MC2/accept/) for A1835. Mini-halos do not have errors on the X-ray bolometric luminosity and therefore a 10% error is assumed (this is true also for $L_{1.4\ \mathrm{GHz}}$ of all mini-halos apart A2390). The final observational sample of RHs has a median redshift or $z \approx 0.18$. Regarding the non-detected clusters in the Enßlin et al. (2011) list, only the 8 clusters for which ACCEPT bolometric X-ray luminosities are used. Figure 6.7, left panel, shows the corresponding radio-to-X-ray scaling relation $L_{1.4\ \mathrm{GHz}} - L_{\mathrm{X,bol}}$. The fit to observations, in the form of $\log_{10}(L_{1.4\ \mathrm{GHz}}/h_{70}^{-2}\ \mathrm{erg\ s^{-1}\ Hz^{-1}}) = A + B\ \log_{10}(L_{\mathrm{X,bol}}/h_{70}^{-2}\ \mathrm{erg\ s^{-1}})$, results in $A = -50.433 \pm 2.226$ and $B = 1.803 \pm 0.049$ and has a scatter of $\sigma_{yx} \approx 0.44$.

Additionally, in figure D.1, an attempt to construct a RLF from existing X-ray flux-limited radio surveys is made. There exist two such studies, the cluster radio survey done with the NVSS survey at 1.4 GHz of Giovannini et al. (1999) and the one done with GMRT at 610 MHz by Venturi et al. (2007, 2008). From both of them only RHs are selected, i.e. radio relics or other diffuse radio emissions of unclear classification are not considered. The 1.4 GHz NVSS survey contains 13 RHs out of 205 analyzed clusters and the 610 MHz GMRT survey contains 6 RHs out of the observed 34. The sample finally analyzed by Venturi et al. (2007, 2008) is composed by 50 clusters and a corresponding RLF at 1.4 GHz, using the 12 present RHs, can also be constructed with the existing 1.4 GHz follow-up measurements. The fractions of radio-loud clusters are about 6%, 18% and 24% for the NVSS 1.4 GHz, GMRT 610 MHz and GMRT 1.4 GHz samples, respectively. The corresponding median redshift is 0.18, 0.26 and 0.25. The RLF is calculated

using the classical V_{max} estimator (see e.g. Felten, 1976) correcting it for the incompleteness and sky coverage of the surveys. The most problematic aspect in obtaining these RLFs, apart the few available objects, is the calculation of a meaningful flux limit. This is calculated by fitting the upper envelope of the luminosity-distance distribution of the three populations, as shown in the insets of figure D.1, following the procedure adopted by Broderick et al. (2011). Note that it is particularly hard to calculate a meaningful flux limit for the GMRT survey due to its poor luminosity-distance RHs distribution. Therefore, the 1.4 GHz NVSS RLF is taken as reference. However, note that several issues can affect this result as e.g. the very reduced number of objects, and therefore the flux limit determination, and the Malmquist-Eddington bias. Indeed, the very different fraction of radio loud clusters obtained from different studies is a clear indicator of the large uncertainty in the RLF.

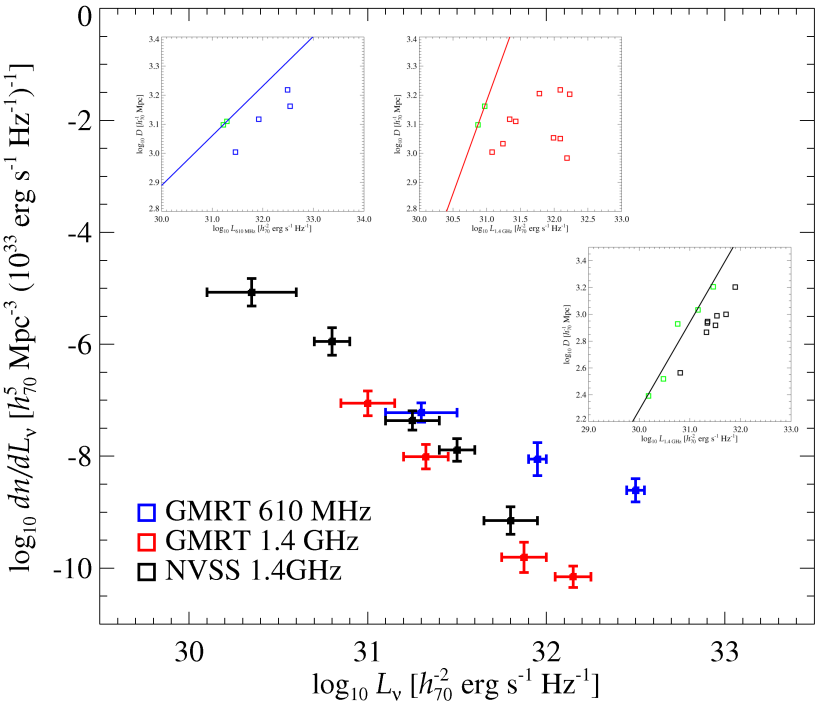

Figure D.1: Radio luminosity function obtained from existent observations. The three insets show the luminosity-distance distribution of the three samples (see main text for details) where the solid line is the fit to the upper envelope population, indicated in green, employed to calculate the flux limit for the classical V_{max} estimator. The choice of the upper envelope population is somehow arbitrary, particularly in the GMRT cases due to the poor luminosity–distance distributions. The horizontal error bars represent the mass bins while the vertical error bars are Poissonian uncertainties.

List of Figures

List of Tables

Acknowledgments

There are many persons that I would like to acknowledge here for many different reasons.
The first acknowledgment is for my PhD supervisor Paco Prada for the great guidance and the many opportunities you opened up for me. I suspect I owe you much more than I can recognize, above all the view of science and of how a scientist should be. I really learned a lot from you and I am very happy we shared these years.
Christoph Pfrommer deserves a very big acknowledgment too. Most of what I achieved in this thesis would have not been possible without your collaboration. It has been a pleasure to work with you these years and to learn from you. Many thanks for you patience with my always too long emails.
Thanks also to many colleagues and friends for the work we have done together, the help they gave me and the fun we had in various occasions. In particular, Miguel-Angel Sánchez-Conde, Alberto Dominguez, Anders Pinzke, Antonio Cuesta, Toño Montero-Dorta, Stefano Profumo, Tesla Jeltema, Miguel-Angel Perez-Torres, Mattia Fornasa, Germán Gómez-Vargas, Gustavo Yepes, Mirco Cannoni, Mario Gómez, Stefan Göttlober, David Cerdeño, Carlos Muñoz, Juan Cortina, Mosé Mariotti, Rajat Thomas and Federico Marinacci.
Thanks to the whole MAGIC collaboration for these fantastic years of work and fun. In particular, many thanks to Michele Doro, Saverio Lombardi, Pierre Colin, Elisa Prandini, Roberta Zanin, Karsten Berger, Marcos López, Julian Sitarek and Dominik Elsaesser. I want to give a special thank to Michele whom I first met as my diploma thesis co-supervisor, bombarding him of stupid questions, and ended up being a very good friend. Saverio also deserves a special thank for the too many hours of data we analyzed together, even if those were not the funniest of our hours together. Thanks also to all the magicians, and not, that shared with me many nights on the Roque, in particular: Michele, Roberta, Karsten, Nino, Alberto, Pepa, Javi, Reiko, Alicia, Andrea, Martin, Omar, Jan, Jens and Jelena.
Grazie alla mia famiglia che ha reso i miei sogni possibili. Grazie a mia madre Daniela e mio padre Eusebio per avermi cresciuto come hanno fatto e avermi insegnato a vivere, a loro che mai mettono in dubbio le mie capacitá. Grazie a mio fratello Ferruccio, a Silvia e alle mie nipotine Giada e Siria che mi fanno sempre ricordare che ci sono cose piú importanti di cui (pre)occuparsi. Grazie a Teresa, Arturo, Simona e Florio. Grazie a tutti quelli che ci sono sempre stati e a quelli che purtroppo non ci sono piú, le cui parole sono immortali nella mia fin troppo affollata testa e i cui racconti prometto rivivranno attraverso le mie parole.
Gracias a los amigos que han acompagñado estos años en Granada y que han hecho inolvidable esta experiencia. Gracias a Alberto por demasiadas cosas que no pueden ser resumidas ni en

una frase ni en un libro, quizás solo en un abrazo. Gracias a Laura por ser como es (y en particular por su habilidad en cantar...). Gracias a Alba que siempre me ha traído de vuelta a casa sano y salvo. Gracias a Kike por todas tus visitas y las mías en Madrid, ciudad que ahora amo como tu. Gracias a Miguel, el Pío, que ha dejado un gran vacío al volver a Canarias. Gracias a Vasi, Miriam, Pedro, Gabriella, William, Paqui, Bruno y Alberto G. y a mis compañeros de despacho Walter, Isa y Cristina. Gracias a todos los amigos del IAA, de la Universidad y de aquel fantástico Taller de Áltas Energías en Oviedo. Gracias a todos los que he conocido en Granada y en particular a aquellos que han compartido casa conmigo además de Alberto y Alba, los dos Mark y Javi.

Grazie ai miei amici nostrani, gli amici di Cibiana, di Feltre e "di Padova", troppi per metterli tutti qui e a cui ho giá dedicato pagine intere nella mia tesi di laurea. Grazie per essere cresciuti con me e avermi reso quello che sono. Grazie per esserci sempre. In tutti questi anni da emigrante la cosa piú difficile é stata vivere senza di voi giorno dopo giorno. Il vuoto che avete lasciato all'andarmene dall'Italia é colmato sola dai ricordi della vita vissuta assieme e dai nostri periodici re-incontri che mi rendono felice come un bambino e eccitato come una scolaretta. Grazie di cuore. Un grazie particolare a chi é venuto a trovarmi in terra straniera per affogare i nostri ricordi nell'alcool come solo noi sappiamo fare!

Grazie ad Alessandra, grazie in tutte le lingue, grazie per esistere ed essere come sei. Grazie per ogni singolo istante che abbiamo passato assieme da quando ci conosciamo. Grazie perché amandoti ho capito che non c'é niente di piú importante di questo che devo affannarmi a raggiungere, niente piú importante di averti ed amarti.

You know the only thing that's missing,
Is a little mouth harp blues,
And you know life's full of surprises,
You know we do that too.
Mötorhead